frontiers | Research Topics

Exploring roles of diagnostic ultrasonography in veterinary medicine

Edited by
Haney Samir, Ayman Abdel-Aziz Swelum and Mohamed M. M. Kandiel

Published in
Frontiers in Veterinary Science

ISSN 1664-8714
ISBN 978-2-83250-933-3
DOI 10.3389/978-2-83250-933-3

About Frontiers

Frontiers is more than just an open access publisher of scholarly articles: it is a pioneering approach to the world of academia, radically improving the way scholarly research is managed. The grand vision of Frontiers is a world where all people have an equal opportunity to seek, share and generate knowledge. Frontiers provides immediate and permanent online open access to all its publications, but this alone is not enough to realize our grand goals.

Frontiers journal series

The Frontiers journal series is a multi-tier and interdisciplinary set of open-access, online journals, promising a paradigm shift from the current review, selection and dissemination processes in academic publishing. All Frontiers journals are driven by researchers for researchers; therefore, they constitute a service to the scholarly community. At the same time, the *Frontiers journal series* operates on a revolutionary invention, the tiered publishing system, initially addressing specific communities of scholars, and gradually climbing up to broader public understanding, thus serving the interests of the lay society, too.

Dedication to quality

Each Frontiers article is a landmark of the highest quality, thanks to genuinely collaborative interactions between authors and review editors, who include some of the world's best academicians. Research must be certified by peers before entering a stream of knowledge that may eventually reach the public - and shape society; therefore, Frontiers only applies the most rigorous and unbiased reviews. Frontiers revolutionizes research publishing by freely delivering the most outstanding research, evaluated with no bias from both the academic and social point of view. By applying the most advanced information technologies, Frontiers is catapulting scholarly publishing into a new generation.

What are Frontiers Research Topics?

Frontiers Research Topics are very popular trademarks of the *Frontiers journals series*: they are collections of at least ten articles, all centered on a particular subject. With their unique mix of varied contributions from Original Research to Review Articles, Frontiers Research Topics unify the most influential researchers, the latest key findings and historical advances in a hot research area.

Find out more on how to host your own Frontiers Research Topic or contribute to one as an author by contacting the Frontiers editorial office: frontiersin.org/about/contact

Exploring roles of diagnostic ultrasonography in veterinary medicine

Topic editors

Haney Samir — Cairo University, Egypt

Ayman Abdel-Aziz Swelum — Zagazig University, Egypt

Mohamed M. M. Kandiel — Benha University, Egypt

Citation

Samir, H., Swelum, A. A.-A., Kandiel, M. M. M., eds. (2022). *Exploring roles of diagnostic ultrasonography in veterinary medicine*. Lausanne: Frontiers Media SA. doi: 10.3389/978-2-83250-933-3

Table of contents

05 Editorial: Exploring roles of diagnostic ultrasonography in veterinary medicine
Haney Samir, Ayman A. Swelum and Mohamed M. M. Kandiel

09 Case Report: Usefulness of Drip Infusion Cholangiography With Computed Tomography for the Diagnosis of Biloma in a Dog
Masahiro Tamura, Hiroshi Ohta, Nene Hasegawa, Kenji Hosoya and Mitsuyoshi Takiguchi

16 Relationship Between Somatic Cell Counts and Mammary Gland Parenchyma Ultrasonography in Buffaloes
Xinxin Zhang, Muhammad Jamil Ahmad, Zhigao An, Kaifeng Niu, Wei Wang, Pei Nie, Shan Gao and Liguo Yang

25 Exogenous L-carnitine Administration Ameliorates the Adverse Effects of Heat Stress on Testicular Hemodynamics, Echotexture, and Total Antioxidant Capacity in Rams
Hossam R. El-Sherbiny, Amr S. El-Shalofy and Haney Samir

34 Imaging Findings in Dogs and Cats With Presumptive Sclerosing Encapsulating Peritonitis
Bérengère C. H. Gremillet, Charles Porsmoguer, Géraldine Bolen, Frédéric Billen, Stéphanie Noël, Flore Brutinel and Valeria Busoni

43 Changes in Cardiac Function During the Development of Uremic Cardiomyopathy and the Effect of Salvianolic Acid B Administration in a Rat Model
Danfu Ma, Ahmed S. Mandour, Ahmed Elfadadny, Hanan Hendawy, Tomohiko Yoshida, Hussein M. El-Husseiny, Koji Nishifuji, Ken Takahashi, Zhenlei Zhou, Yanbing Zhao and Ryou Tanaka

54 Colonic Intramural Hematoma in a Cat: A Case Report
Ti-Chiu Hsu, Lee-Shuan Lin, Cheng-Shu Chung, Chuan Chiang, Hsien-Chieh Chiu and Ping-Hsun Huang

61 Color M-Mode Echocardiography for Non-Invasive Assessment of the Intraventricular Pressure in Dogs Before and After Ductus Arteriosus Occlusion: A Retrospective Study
Miki Hirose, Ahmed S. Mandour, Seijirow Goya, Lina Hamabe, Katsuhiro Matsuura, Tomohiko Yoshida, Momoko Watanabe, Kazumi Shimada, Akiko Uemura, Ken Takahashi and Ryou Tanaka

72 Histological and hemodynamic characterization of corpus luteum throughout the luteal phase in pregnant and non-pregnant buffalos in relation to nitric oxide levels based on its anatomical determination
Samer M. Daghash, Noha A. E. Yasin, Elshymaa A. Abdelnaby, Ibrahim A. Emam, Ayman Tolba and Yara S. Abouelela

89 Ultrasonographic and endoscopic guidance in diagnosis of Helicobacter gastritis presenting as a mass lesion in a dog: A case report
Thomas Gomes, Cecelia Harmon and Michael Nappier

96 Pulmonary thromboembolism due to immune-mediated hemolytic anemia in a cat: A serial study of hematology and echocardiographic findings
Tomohiko Yoshida, Ahmed S. Mandour, Manami Sato, Miki Hirose, Rina Kikuchi, Norihiro Komiyama, Hanan A. Hendawy, Lina Hamabe, Ryou Tanaka, Katsuhiro Matsuura and Akiko Uemura

104 Shear wave elastography measurements in dogs treated surgically for congenital extrahepatic portosystemic shunts
Merle Toom, Jimmy H. Saunders, Luc Duchateau, Goncalo Serrano, Hilde De Rooster, Nausikaa Devriendt and Emmelie Stock

112 Novel color M-mode echocardiography for non-invasive assessment of the intraventricular pressure in goats: Feasibility, repeatability, and the effect of sedation
Ahmed S. Mandour, Haney Samir, Tomohiko Yoshida, Katsuhiro Matsuura, Lina Hamabe, Kazumi Shimada, Hend A. Abdelmageed, Mohamed Elbadawy, Akiko Uemura, Ken Takahashi, Gen Watanabe and Ryou Tanaka

126 Hemodynamic effect of pimobendan following intramuscular and intravenous administration in healthy dogs: A pilot study
Masayuki Enokizono, Ahmed S. Mandour, Syunta Komeda, Seijirow Goya, Aki Takeuchi, Konosuke Katoh, Akira Yairo, Zeki Yilmaz, Kazumi Shimada and Ryou Tanaka

141 Comparison of thoracic ultrasonography and thoracic radiography between healthy adult horses and horses with bacterial pneumonia using a novel, objective ultrasonographic scoring system
Kate L. Hepworth-Warren, Nathan Nelson, Katarzyna A. Dembek and Kimberly A. S. Young

frontiers | Frontiers in Veterinary Science

TYPE Editorial
PUBLISHED 18 November 2022
DOI 10.3389/fvets.2022.1084676

OPEN ACCESS

EDITED AND REVIEWED BY
Sibylle Maria Kneissl,
University of Veterinary Medicine
Vienna, Austria

*CORRESPONDENCE
Haney Samir
Haneyvet360@yahoo.com;
Haneysamir600@yahoo.com;
Haneyvet360@cu.edu.eg

SPECIALTY SECTION
This article was submitted to
Veterinary Imaging,
a section of the journal
Frontiers in Veterinary Science

RECEIVED 30 October 2022
ACCEPTED 10 November 2022
PUBLISHED 18 November 2022

CITATION
Samir H, Swelum AA and Kandiel MMM
(2022) Editorial: Exploring roles of
diagnostic ultrasonography in
veterinary medicine.
Front. Vet. Sci. 9:1084676.
doi: 10.3389/fvets.2022.1084676

Editorial: Exploring roles of diagnostic ultrasonography in veterinary medicine

Haney Samir[1]*, Ayman A. Swelum[2] and Mohamed M. M. Kandiel[3]

[1]Department of Theriogenology, Faculty of Veterinary Medicine, Cairo University, Giza, Egypt,
[2]Department of Theriogenology, Faculty of Veterinary Medicine, Zagazig University, Zagazig, Egypt,
[3]Department of Theriogenology, Faculty of Veterinary Medicine, Benha University, Toukh, Egypt

KEYWORDS

blood flow, diagnostic ultrasonography, doppler, fertility, cardiology, internal medicine, surgery, veterinary practices

Editorial on the Research Topic
Exploring roles of diagnostic ultrasonography in veterinary medicine

Nowadays, ultrasound has become an important diagnostic tool, and its applications are proving more robust and tremendously beneficial in different aspects of veterinary practices. The advent of ultrasonography enables researchers and veterinarians to assess and monitor tremendous physiological and pathological events in the farm, companion, and wild animals (1). Because there is a growing demand for use of ultrasonography in studying, diagnosis, and monitoring many physiological events and diseases of animals, the goal of this special edition Research Topic is to shed light on the progress made in the past decade in applications of diagnostic ultrasonography in different aspects of physiological and pathological issues in the veterinary practices (reproduction, internal medicine, surgery, and cardiology). In this e-collection, 14 articles were published covering the aforementioned objectives and to provide direction and guidance to researchers in the field.

The study of Zhang et al. explored the usefulness of ultrasonography and Computer-assisted pixel assessment of the echotextural features of the mammary gland parenchyma in buffaloes during lactation at different somatic cell levels for diagnosing subclinical mastitis. In addition, this study found that examining the structures of the mammary gland parenchyma with vertical positioning showed better results than the horizontal direction. Similarly, in cows (2), it was reported that examining the vertical plane of the mammary gland was more suitable and could describe the significant correlation between echotextural variables and milk composition.

Tamura et al. described the usefulness of drip infusion cholangiography with computed tomography (DIC-CT) and abdominal ultrasonography for detecting the site of bile leakage in a dog with biloma [an encapsulated collection of bile outside or inside the biliary tract within the abdominal cavity; (3)]. Abdominal ultrasonography showed an enlargement of the gallbladder with the appearance of a kiwi-like pattern with residual

central echogenic bile, indicating gallbladder mucocele. The gallbladder wall was not affected but the common biliary duct was dilated. An accumulation of well-defined anechoic fluid was observed around the right liver lobes. The amount of accumulated fluid was much larger compared to the ascites.

El-Sherbiny et al. reported the pivotal roles of pulsed Doppler ultrasonography for the assessment of testicular blood flow in rams in subtropical conditions. This study showed that treatment of heat-stressed rams with L-carnitine (LC) exerted a significant improvement in testicular blood perfusion because of reductions of Doppler indices (resistive index: RI and pulsatility index: PI), which explain the elevation of arterial blood perfusion and decrease of the vessel resistance to blood flow (4–6). In addition, it highlighted the pivotal roles of assessing the echotexture changes of testicular parenchyma in the control and LC-treated rams by computer image analysis (7, 8).

Daghash et al. studied the usefulness of B-mode and color Doppler ultrasonography to monitor the developmental growth and hemodynamic changes of corpus luteum (CL) in buffalos from Day 5 till Day 40 after ovulation in pregnant and non-pregnant buffaloes. This study showed a significant elevation in CL area from Day 20 to Day 40 in pregnant buffalos compared to the non-pregnant ones with a marked elevation of plasma progesterone levels in the same group, which could indicate the importance of adequate CL area and diameter to establish the pregnancy. Concomitantly, CL blood flow increased, as evidenced by lowering Doppler indices values (8), in pregnant females compared to those in non-pregnant ones.

Gremillet et al. reported the imaging findings in seven dogs and two cats with a presumptive diagnosis of sclerosing encapsulating peritonitis (SEP). SEP is defined as a chronic inflammatory condition in which the small intestines are encased in a dense fibro collagenous membrane (9, 10). Radiographs imaging showed abnormal shape and distribution of small bowel loops. By ultrasonography, free fluid was visible in all animals, either distributed in the entire peritoneal cavity (7/9) or focally collected (2/9). Peritoneal effusion was echogenic (6/9) and loculated or partially loculated by thin echogenic septations (3/9), suggesting an inflammatory process. Bowel loops had a corrugated appearance in all animals suggesting the occurrence of adhesions and bowel inflammation.

Hsu et al. presented the invaluable uses of different imaging modalities such as radiography, ultrasonography, and computed tomography (CT) for differential diagnosis and monitoring the treatment of a rare case of colonic intramural hematoma in cats. Abdominal ultrasonography revealed the existence of a local heteroechogenic intramural mass located between the submucosal and muscular layers of the descending colon, causing severe compression and closure of the lumen of the colon. Cranial to the intramural colonic mass, colonic lymph nodes were enlarged. For efficient differential diagnosis (with abscess, hematoma, and colonic intramural neoplasia), ultrasonography maybe not be a suitable tool. Scanning by CT and cytological examinations was performed to provide more information and reach the final definitive diagnosis. The patient responded well to the surgical approach without recurrence.

Gomes et al. published an important case report of a golden retriever dog suffering from *Helicobacter spp*. gastritis with chronic vomiting. Abdominal ultrasonography revealed the presence of a cluster of multiple, round, and well-defined, hypoechoic foci of different sizes (∼0.7–1.8 cm) surrounded by gas within the lumen of the stomach. The histopathology of fundic cup biopsies showed large lymphocytic aggregates with mild multifocal inflammation of lymphocytes and eosinophils with few *Helicobacter*-like organisms on the surface of the epithelium. After appropriate treatment, the vomiting and fundic lesions were resolved on ultrasonographic examination. This case represented novel gross morphologic findings for *Helicobacter* spp. gastritis in dogs that responded well to the appropriate therapy and also highlighted how early intervention with advanced imaging can aid in diagnosis and treatment.

In equine, Hepworth-Warren et al. reported moderate sensitivity (66.7%) and high specificity (92.3%) of thoracic ultrasonography (TUS) for the identification of bacterial pneumonia in adult horses utilizing a TUS score system. In this study, ultrasonography was scored utilizing a novel scoring system evaluating several comet tails lesions, the presence or absence of pleural effusion, and/or pulmonary consolidation in each intercostal space. Ultrasonographic scores were significantly ($P = 0.01$) higher in the diseased group (median = 126) than in the control group (median = 20). Hence, TUS appears to be an acceptable stand-alone imaging tool for the diagnosis of bacterial pneumonia in horses when radiography is not practical.

Two-dimensional shear wave elastography (2D SWE) is an ultrasound technique that uses the technique of acoustic radiation force impulse to provide a quantitative assessment of tissue stiffness. In recent years, increased interest in this technique has developed in veterinary medicine due to its non-invasive nature, wide availability, and low cost (11). Interestingly, the study of Toom et al. aimed to compare liver stiffness values between dogs with the closed extrahepatic portosystemic shunt (EHPSS) and those with multiple acquired portosystemic shunts (MAPSS) after gradual surgical attenuation and to evaluate whether SWV could be used to determine EHPSS closure. The mean 2D SWV between dogs with closed EHPSS and those with MAPSS did not differ significantly in this study. However, these results could serve as a baseline and reference for future studies.

In veterinary cardiology, 5 papers were published in this e-collection. Mandour et al. explored the feasibility and repeatability of the color M-mode echocardiography (CMME) approach to measure different variables of the intraventricular pressure difference (IVPD) and intraventricular pressure gradients (IVPG) in goats and to explore the effect of sedation on the measured variables. This is the first study of the quantitative measurement of the IVPD and IVPG in goats using a novel CMME technique. The findings of the study, in conjunction

with conventional echocardiographic methods, might deepen understanding of the hemodynamic changes of the left ventricle in goats as well as other farm animals for further experimental and clinical studies.

Ma et al. aimed to assess the changes in cardiac function in experimental induced uremic cardiomyopathy (UC, induced diastolic dysfunction) rats and to assess the therapeutic efficacy of salvianolic acid B (Sal B) using IVPG and two-dimensional speckle tracking echocardiography (2DSTE) techniques. This study confirmed increased ventricular stiffness and fibrosis in UC rats which was potentially treated by Sal B through decreasing edema, inflammation, and fibrosis. However, Further studies may be needed to clarify the molecular mechanisms of Sal B for the treatment of UC.

Hirose et al. reported the usefulness of novel non-invasive assessment of the IVPD and IVPG by color M-mode echocardiography (CMME), a promising method in diagnosing diastolic function, before and after surgical occlusion of patent ductus arteriosus (PDA a congenital heart defect associated with increased preload) in dogs. The findings of this interesting study revealed matched response of IVPD and IVPG to the reduced preload rather than left ventricular relaxation. This result is an initial step in the clinical utility of CMME-derived IVPD and IVPG measurements in the diastolic function evaluation in dogs with PDA that warrants upcoming clinical investigations.

Yoshida et al. reported the pivotal roles of diagnostic imaging in the assessment and follow-up of the therapy of a case report of pulmonary thromboembolism (PTE) secondary to immune-mediated hemolytic anemia (IMHA) in cats. The echocardiographic assessment indicated an enlargement in the right ventricle and atrium, mild tricuspid regurgitation, and a recognized thrombus in the main pulmonary artery. Regenerative anemia and auto-agglutination tests were suggested on blood examination. Appropriate interventions using antithrombotic therapy and immunosuppressive therapy improved the case.

Enokizono et al. evaluated the cardiovascular effects of a single dose of intramuscular (IM) and intravenous (IV) administrations of pimobendane (Pim) in healthy dogs by monitoring the echocardiographic hemodynamic parameters for up to 120 min. This study indicated that IM injection of Pim enhanced left ventricular relaxation and contractility, causing vasodilation within a short time approximately in the same way as the IV route. However, further clinical studies should be performed to explore the effectiveness of IM injections of Pim in case of emergency.

Author contributions

HS conceptualized the idea and wrote the manuscript. AS and MK reviewed the manuscript with the first author. All authors reviewed the manuscript.

Acknowledgments

The authors appreciate the contributions of all authors in this e-collection. Also, we greatly thank the reviewers for their valuable comments.

Conflict of interest

The authors declare that the research was conducted in the absence of any commercial or financial relationships that could be construed as a potential conflict of interest.

Publisher's note

References

1. Samir H, Radwan F, Watanabe G. Advances in applications of color Doppler ultrasonography in the andrological assessment of domestic animals: A review. *Theriogenology.* (2021) 161:252–61. doi: 10.1016/j.theriogenology.2020.12.002

2. Schwarz T, Scheeres N, Małopolska MM, Murawski M, Agustin TD, Ahmadi B, et al. Associations between mammary gland echotexture and milk composition in cows. *Animals.* (2020) 10:2005. doi: 10.3390/ani10112005

3. Gould L, Patel A. Ultrasound detection of extrahepatic encapsulated bile: "Biloma". *AJR Am J Roentgenol.* (1979) 132:1014–5. doi: 10.2214/ajr.132.6.1014

4. Dickey RP. Doppler ultrasound investigation of uterine and ovarian blood flow in infertility and early pregnancy. *Hum Reprod Update.* (1997) 3:467–503. doi: 10.1093/humupd/3.5.467

5. El-Sherbiny H, Shahat A, Hedia M, El-Shalofy A. Effect of sexual maturation on testicular morphometry and echotexture and their association with intratesticular blood flow in ossimi rams. *Indian J Small Rumin.* (2022) 28:85–90. doi: 10.5958/0973-9718.2022.00034.4

6. El-Sherbiny HR, Fathi M, Samir H, Abdelnaby EA. Supplemental dietary curcumin improves testicular hemodynamics, testosterone levels, and semen quality in Baladi bucks in the non-breeding season. *Theriogenology.* (2022) 188:100–7. doi: 10.1016/j.theriogenology.2022.05.020

7. Brito L, Barth A, Wilde R, Kastelic J. Testicular ultrasonogram pixel intensity during sexual development and its relationship with semen quality, sperm production, and quantitative testicular histology in beef bulls. *Theriogenology.* (2012) 78:69–76. doi: 10.1016/j.theriogenology.2012.01.022

8. Samir H, Mandour AS, Radwan F, Swelum AA, Yoshida T, Tanaka R, et al. Diurnal rhythms in testicular blood flow, testicular morphometry and reproductive hormones in Shiba goats. *Reprod Fertil Dev*. (2022) 34:1043–51. doi: 10.1071/RD22139

9. Akbulut S. Accurate definition and management of idiopathic sclerosing encapsulating peritonitis. *World J Gastroenterol*. (2015) 21:675–87. doi: 10.3748/wjg.v21.i2.675

10. Machado NO. Sclerosing encapsulating peritonitis: review. *Sultan Qaboos Univ Med J*. (2016) 16:e142–51. doi: 10.18295/squmj.2016.16.02.003

11. Tamura M, Ohta H, Shimbo G, Osuga T, Sasaki N, Morishita K, et al. Usefulness of noninvasive shear wave elastography for the assessment of hepatic fibrosis in dogs with hepatic disease. *J Vet Intern Med*. (2019) 33:2067–74. doi: 10.1111/jvim.15598

frontiers in Veterinary Science

CASE REPORT
published: 07 March 2022
doi: 10.3389/fvets.2022.854042

Case Report: Usefulness of Drip Infusion Cholangiography With Computed Tomography for the Diagnosis of Biloma in a Dog

Masahiro Tamura[1,2], *Hiroshi Ohta*[1], *Nene Hasegawa*[1,2], *Kenji Hosoya*[3] *and Mitsuyoshi Takiguchi*[2*]

[1] *Department of Companion Animal Clinical Sciences, School of Veterinary Medicine, Rakuno Gakuen University, Ebetsu, Japan,* [2] *Department of Veterinary Clinical Sciences, Graduate School of Veterinary Medicine, Hokkaido University, Sapporo, Japan,* [3] *Veterinary Teaching Hospital, Graduate School of Veterinary Medicine, Hokkaido University, Sapporo, Japan*

Bilomas are encapsulated collections of bile outside or inside the biliary tract within the abdominal cavity. For diagnostic and therapeutic approaches, it is important to identify the origin of bile leaks from the biliary tract. This case report describes the usefulness of drip infusion cholangiography with computed tomography (DIC-CT) for detecting the site of bile leakage in a dog with biloma. A 10-year-old, castrated male Pomeranian dog was referred to our department for gastrointestinal signs. Abdominal ultrasonography detected gallbladder mucocele without evidence of defect on the wall and well-defined anechoic localized fluid accumulation around the right division of the liver. On the other hand, there was only a small amount of ascites in the abdominal cavity. The accumulated fluid collected through abdominocentesis had a bilirubin concentration of 11.4 mg/dl, which was more than twice as high as that in serum (0.4 mg/dl), but had absence of pyogenic bacteria. The DIC-CT with meglumine iotroxate showed two well-defined large fluid collections: one between right medial and lateral lobe and the other between the right lateral lobe and caudate process of caudate lobe. Three-dimensional DIC-CT views that the former was enhanced by the contrast agent and that it communicated with an intrahepatic bile duct of the right lateral lobe. Moreover, the DIC-CT images confirmed communication with each fluid collections. After 6 days of hospitalization, a decrease in the amount of accumulated fluid was confirmed, after which cholecystectomy was performed. The dog was discharged from the hospital without complications. No signs of bile leakage were observed on follow-up imaging on postoperative day 10. According to authors knowledge, this has been the first report to show that DIC-CT can be useful for determining the origin of bile leakage in dogs with bilomas.

Keywords: biloma, cholangiography, computed tomography, drip infusion, DIC-CT, dog, gallbladder mucocele

OPEN ACCESS

Edited by:
Haney Samir,
Cairo University, Egypt

Reviewed by:
Ahmed Elfadadny,
Tokyo University of Agriculture and Technology, Japan
Ahmed Abdelgalil,
Cairo University, Egypt

****Correspondence:***
Mitsuyoshi Takiguchi
mtaki@vetmed.hokudai.ac.jp

Specialty section:
This article was submitted to Veterinary Imaging, a section of the journal Frontiers in Veterinary Science

Received: *13 January 2022*
Accepted: *11 February 2022*
Published: *07 March 2022*

Citation:
Tamura M, Ohta H, Hasegawa N, Hosoya K and Takiguchi M (2022) Case Report: Usefulness of Drip Infusion Cholangiography With Computed Tomography for the Diagnosis of Biloma in a Dog. Front. Vet. Sci. 9:854042. doi: 10.3389/fvets.2022.854042

INTRODUCTION

Bilomas are encapsulated collections of bile outside or inside biliary tract within abdominal cavity (1). In humans, bilomas were reported to be results from abdominal trauma, spontaneous leakage of the biliary tree, or iatrogenic injury (2–5). Iatrogenic damage to the biliary tract is commonly associated with laparoscopic cholecystectomy (6). Bilomas in veterinary medicine has been

described to be developed after surgery of intrahepatic portosystemic shunt (7), cholecystectomy (8), and open liver biopsy (9) and associated with trauma (10). It is important for diagnosis and therapeutic approaches to identify the site of bile leakage. Although ultrasonography is widely used for the screening of biliary system, it is difficult to evaluate the intrahepatic and common biliary duct in detail (11).

Drip infusion cholangiography with computed tomography (DIC-CT) using meglumine iotroxate is a commonly used imaging technique for the evaluation of the anatomy of the biliary tree and to confirm its patency in human. Recently, its usefulness was also reported in dogs with gallbladder mucocele and cats with cholelithiasis (12, 13). However, there was no report to evaluate the bile leakage using DIC-CT. In this case report, we described the usefulness of the DIC-CT for the detection of the site of bile leakage in a dog with biloma.

CASE PRESENTATION

A 10-year-old, castrated male Pomeranian dog weighting 4.1 kg was referred to Hokkaido University Veterinary Teaching Hospital for examination due to history of lethargy, vomiting, and anorexia for 1–2 weeks. Several days prior to presentation, clinical signs had improved but mild gastrointestinal signs remained.

Physical examination at presentation was unremarkable, with the exception of slight abdominal discomfort, a heart and respiratory rate of 128 and 36/min, respectively, and a body temperature of 38.3 °C. Hematological abnormalities included mature neutrophilia (19.12×10^3 neutrophils/μl; reference interval, 2.95×10^3-11.64×10^3 neutrophils/μl) and monocytosis (1.45×10^3 monocytes/μl; reference interval, 0.16×10^3-1.12×10^3 monocytes/μl). Results of plasma biochemical analyses indicated elevated levels of total protein (7.8 g/dl; reference interval, 5.0–7.2 g/dl), blood urea nitrogen (39.1 mg/dl; reference interval, 9.2–29.2 mg/dl), and C-reactive protein (3.75 mg/dl; reference interval, 0.0–1.0 mg/dl); increased activity of alanine aminotransferase (174 IU/L; reference interval, 17–78 IU/L), alkaline phosphatase (>3,500 IU/L; reference interval, 47–254 IU/L), and gamma-glutamyl transpeptidase (124 IU/L; reference interval, 5–14 IU/L); and hyperphosphatemia (5.7 mg/dl; reference interval, 1.9–5.0 mg/dl) and hypercalcemia (12.8 mg/dl; reference interval, 9.3–12.1 mg/dl). Total bilirubin concentration was within reference limits (0.4 mg/dl; reference interval, 0.1–0.5 mg/dl). Prothrombin time and activated partial thromboplastin time was within normal limits, but fibrinogen

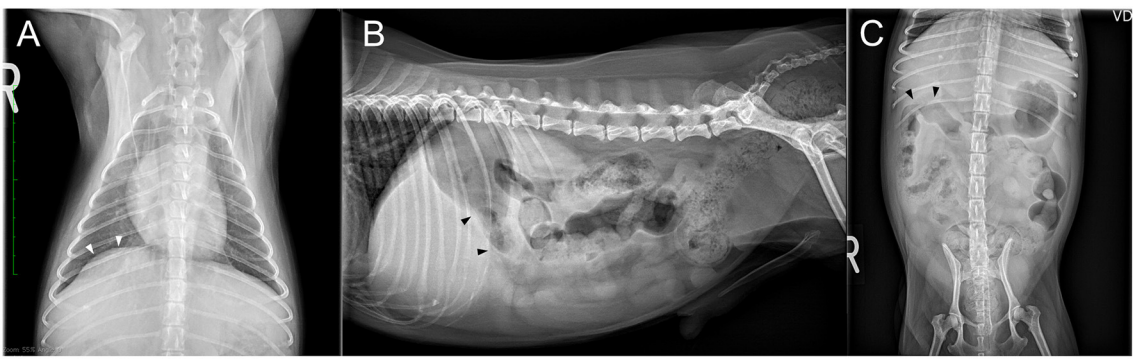

FIGURE 1 | Three thoracic and abdominal radiographs obtained from a dog with biloma on initial presentation. The right crus of the diaphragm was found to have been cranially displaced by one intercostal space relative to the left crus in the ventrodorsal view of the thorax [**(A)**; white arrow-head]. The pylorus of stomach was displaced caudally in the lateral **(B)** and ventrodorsal **(C)** radiographic views of the abdomen (black arrow-head).

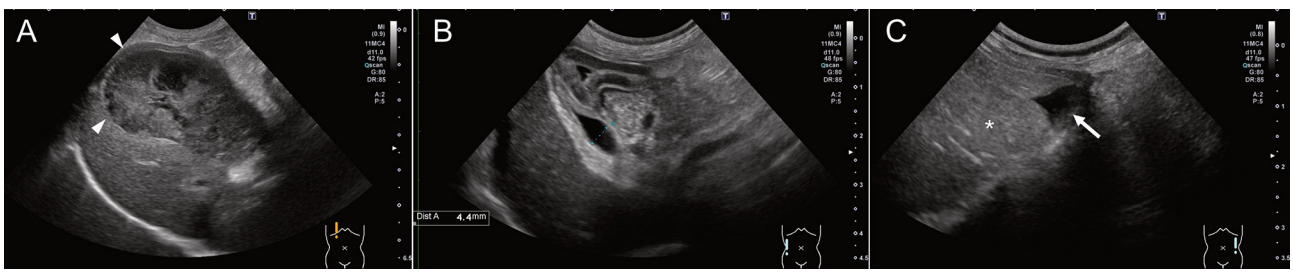

FIGURE 2 | Ultrasonographic findings. **(A)** The gallbladder showed a kiwi-like pattern and stella combination with residual central echogenic bile (white arrow-head), indicating gallbladder mucocele. **(B)** The common biliary duct dilation without echogenic sediment or debris was observed (4.4 mm). **(C)** A small amount of ascites (white arrow) was detected around the spleen (asterisk).

concentration was increased (502 mg/dl; reference interval, 113–385 mg/dl). The dog showed low serum thyroxine (T4) but normal serum free T4 and thyroid stimulating hormone.

Radiography showed that the right crus of the diaphragm was cranially displaced by one intercostal space relative to the left crus in the ventrodorsal view of the thorax (**Figure 1A**). The caudal displacement of the pylorus of the stomach was suspected in the lateral and ventrodorsal radiographic view of the abdomen (**Figures 1B,C**). The remaining abdominal organs and thoracic radiographs were normal.

Abdominal ultrasonographic examination revealed enlargement of the gallbladder, which showed a kiwi-like pattern and stella combination with residual central echogenic bile, indicating gallbladder mucocele (**Figure 2A**). No defect in the gallbladder wall was identified. Although common biliary duct dilation was observed (4.4 mm), no echogenic sediment or debris within the common biliary duct was observed (**Figure 2B**). A small amount of ascites was detected around the spleen and bladder (**Figure 2C**). Through the right intercostal approach, well-defined anechoic localized fluid accumulation was detected around the right liver lobes (**Figure 3A**). The amount of accumulated fluid was much larger compared to the ascites. No abnormality was found in other organs.

The localized fluid in the space within the right hepatic division was collected through abdominocentesis *via* the right intercostal space of the 10th−11th thoracic vertebra before CT examination and subsequently analyzed. The laboratory evaluation of fluid showed that it comparable to an exudate, with a total nucleated cell count of 11,500/μl and protein of 3.9 g/dl. Cytological examination revealed neutrophilia, despite the absence of pyogenic bacteria. The fluid accumulating around the right liver lobes had a bilirubin concentration of 11.4 mg/dl, which was more than twice as high as that in serum, and its glucose concentration was high compared to that in serum. Ascites could not be collected because of a small volume of effusion. The dog was diagnosed with gallbladder mucocele, and the localized bile fluid accumulation indicated the possibility of biloma around the right hepatic division.

To evaluate the bile leakage in the right hepatic division, DIC-CT was performed in accordance with previous studies (12, 13). A 22-gage over-the-needle catheter was inserted into the cephalic vein of the dog, and a dose of 100 mg iodine/kg meglumine iotroxate (Biliscopin; Bayer Schering Pharma, Berlin, Germany) was administered over 30 min. After administering the contrast agent, general anesthesia was induced using propofol (7 mg/kg, to effect intravenously) and maintained with isoflurane (minimum alveolar concentration of 1.3–1.5%) at 2 L/min of oxygen. CT images were obtained using an 80-slice CT scanner (Aquilion PRIME; Canon Medical Systems, Otawara, Tochigi). Initially, the dog was positioned and scanned in the ventral recumbent position with the following scanning parameters: X-ray tube potential of 80 kV, X-ray tube current of 200 mA, slice thickness of 0.5 mm, reconstruction interval of 0.5 mm, tube rotation time of 0.5 s, and helical detector pitch of 0.813. Apnea was induced during CT scans using a stop ventilator.

On DIC-CT in the ventral recumbent position, the contrast agent filled the intra and extrahepatic bile ducts, common bile duct, and duodenum, except for the gallbladder. The CT images showed two well-defined large fluid collections (**Figure 4A**): one between right medial and lateral lobe (3.6 × 1.7 × 2.4 cm) and the other between the right lateral lobe and caudate process of caudate lobe (3.0 × 0.9 × 3.2 cm). Three-dimensional DIC-CT views revealed that the former was enhanced by the contrast agent and that it communicated with an intrahepatic bile duct of the right lateral lobe (**Figures 4B,C**). The dog was then repositioned in dorsal recumbency and rescanned to evaluate the displacement of contrast agent. Accordingly,

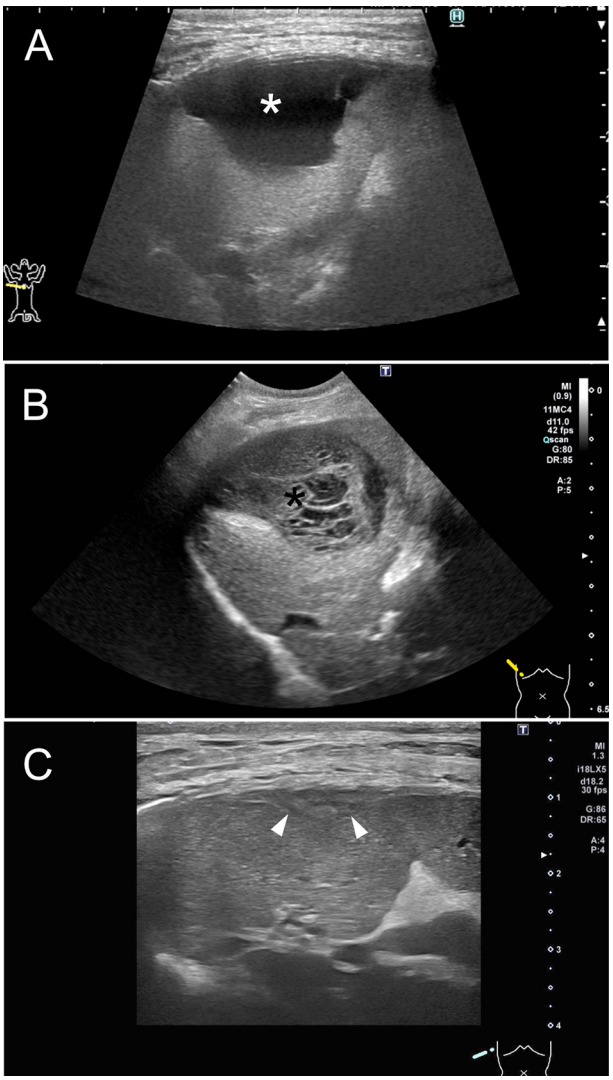

FIGURE 3 | Ultrasonography of the right liver lobes through a right intercostal approach from three different time points. **(A)** On initial presentation, well-defined anechoic localized fluid accumulation was detected around the right liver lobes. **(B)** On day 6, ultrasonography revealed that the size of biloma was stable, but its appearance had changed, showing a decreased fluid and organized echoic non-mobile collections, such as mucocele (black asterisk). **(C)** On postoperative day 10, abdominal ultrasonography was able to detect a trace level of biloma wall (white arrow-head) but no fluid accumulation around the right hepatic division.

the images showed that the leaked contrast agent fell dorsally through gravity (**Figure 4D**), and the DIC-CT images confirmed communication with each fluid collections. The dog showed no side reaction during and after DIC-CT. Thereafter, CT angiography using an intravenous injection of 600 mg iodine/kg iohexol (Omnipaque 300, GE Healthcare, Oslom Noeway) was performed for anatomical evaluation and surgical planning. From these findings, the dog was diagnosed with biloma caused by a leakage of the intrahepatic bile duct in the right lateral lobe.

We presumed that cholecystectomy was appropriate for the prevention of gallbladder rupture. Additionally, the right lateral hepatic lobectomy was considered for the treatment of bile leakage. However, conservative therapy with intravenous crystalloid fluid therapy, low molecular weight heparin (150 IU/kg as an intravenous continuous infusion for 24 h), and ampicillin (20 mg/kg, intravenous every 12 h) was performed before surgery due to following reasons: having mild clinical signs due to localized bile peritonitis and expecting the adhesion of intrahepatic bile duct, which may prevent lobectomy.

On day 6, ultrasonography revealed that the size of biloma was stable, but its appearance had changed such that the fluid decreased and organized echoic non-mobile collections, such as a mucocele, appeared (**Figure 3B**). Exploratory laparotomy was performed through the ventral midline approach with right paracostal incision. Exploration of the abdomen revealed severe adhesion between the right medial lobe of the liver and the abdominal wall, as well as between the gallbladder and omental

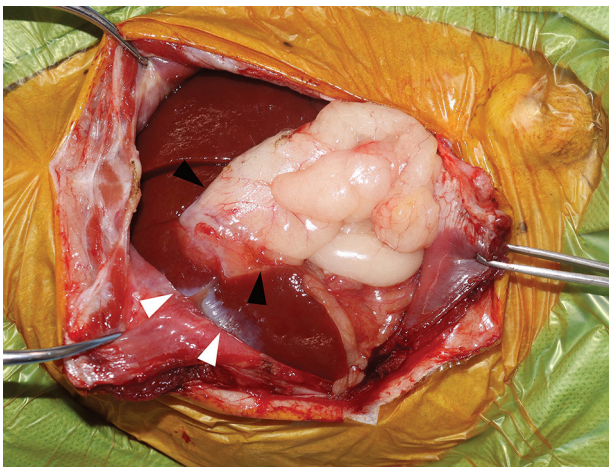

FIGURE 5 | Intraoperative findings. Image showing severe adhesion between the right medial lobe of the liver and the abdominal wall (white arrow-head) and between the gallbladder and omental fat (black arrow-head).

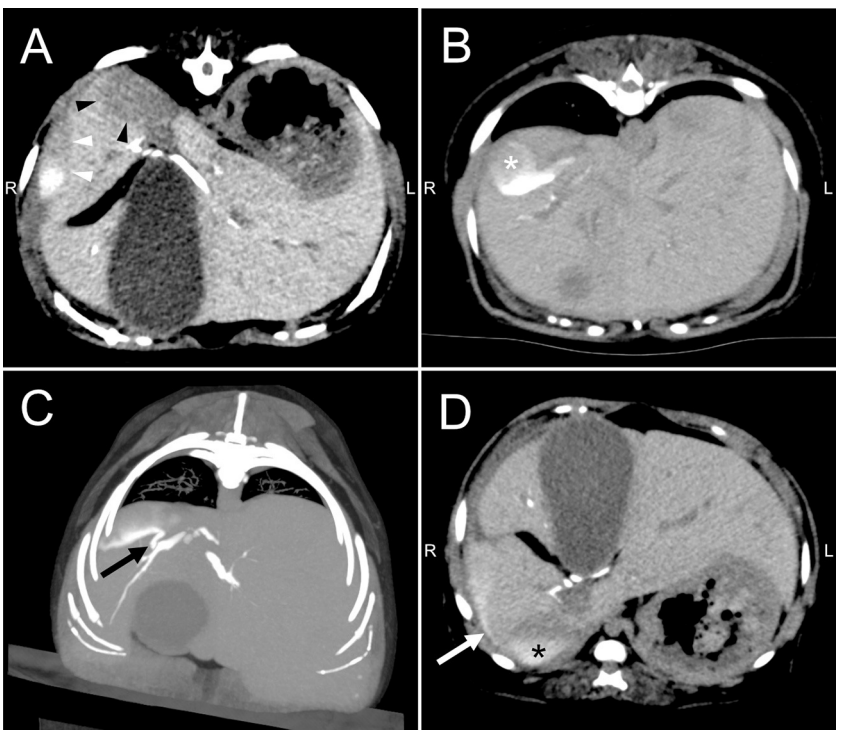

FIGURE 4 | Drip infusion cholecystocholangiography with computed tomography of the abdomen in a dog with biloma. **(A)** Transverse views revealed two well-defined large fluid collections, where one is in between right medial and lateral lobe (white arrow-head) and the other in between the right lateral lobe and caudate process of caudate lobe (black arrow-head). **(B)** The CT images showed that fluid collection was enhanced by the contrast agent (white asterisk) in the ventral recumbent position. **(C)** The reconstruction image showed communication between the fluid collection and intrahepatic bile duct of right lateral lobe (black arrow). **(D)** Drip infusion cholecystocholangiography with computed tomography images after repositioning to dorsal recumbency showed that the leaked contrast agent fell dorsally via gravity (white arrow) and confirmed communication between each fluid collections (black asterisk).

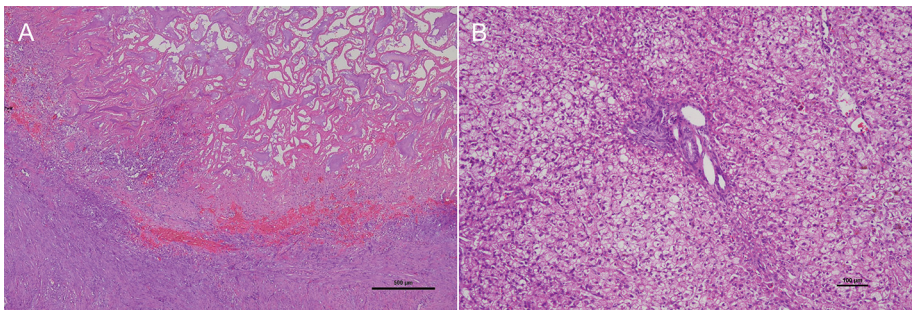

FIGURE 6 | Photomicrography of the hematoxylin and eosin-stained section of the gallbladder and liver. **(A)** A large viscous accumulation of mucus that filled and distended the gallbladder lumen and full thickness necrosis of the gallbladder wall. **(B)** Liver biopsy specimens revealed cytoplasmic vacuolation of hepatocytes without any inflammation and fibrosis of the hepatic parenchyma.

fat (**Figure 5**). Hepatic lobectomy was not performed due to the decrease in the amount of fluid within the biloma and the severe adhesion sealing intraoperatively. After cholecystectomy and liver biopsy, catheterization, and flushing of the common biliary duct was performed to confirm duct patency. The dog's recovery from general anesthesia was uneventful.

Tissues of the gallbladder and liver were submitted for histopathological analysis. Despite observing a large viscous accumulation of mucus that filled and distended the gallbladder lumen and full thickness necrosis of the gallbladder wall (**Figure 6A**), no findings of rupture were noted. Liver biopsy specimens revealed cytoplasmic vacuolation of hepatocytes without any inflammation and fibrosis of the hepatic parenchyma (**Figure 6B**). The dog was diagnosed with gallbladder mucocele with infarctions of the gallbladder and vacuolar hepatopathies.

Seven days after the surgery, the dog was in good condition and discharged from the hospital on the same day. The dog subsequently visited our hospital on postoperative day 10 for the removal of the skin sutures, during which abdominal ultrasonography detected a trace level of biloma wall and no fluid accumulation around the right hepatic division (**Figure 3C**). Seven months after the surgery, the dog was doing well without any recurrence of clinical signs determined via telephone contact with the owner.

DISCUSSION

We herein detail the experience with a rare case of biloma due to a leakage from intrahepatic bile duct in the right lateral lobe. To the best of our knowledge, this has been the first report describing the usefulness of DIC-CT for the detection of the bile leakage site within the intrahepatic duct in veterinary medicine.

A few reports have been available on bilomas in veterinary medicine, including three dogs and one cat with biloma. In one dog, biloma developed after surgical treatment of intrahepatic portosystemic shunt (7), whereas in the other dog, biloma was associated with trauma (hit by a car) (10). Moreover, biloma in a cat developed after open liver biopsy (9). Although one dog had also been diagnosed with biloma 12 days after cholecystectomy, this report has not been discussed during the causes of biloma (8). The current case had no history of biliary surgery, liver biopsy, or abdominal trauma, suggesting an unknown cause of biloma. Previous studies showed that the cause of bilomas in humans included spontaneous leakage of the intrahepatic bile duct (3, 4). The current dog may have developed biloma spontaneously. However, considering the histopathological diagnosis of gallbladder mucocele, the leakage of the intrahepatic duct in the right lateral lobe may have been caused by biliary obstruction due to the high viscosity of its contents.

DIC-CT provided valuable information regarding the localization of the bile leakage. This imaging technique has been used to assess the bile duct system in human patients, and its usefulness has also been recently reported in dogs with gallbladder mucocele and cats with cholelithiasis (12, 13). Nonetheless, the mentioned studies have focused on the evaluation of bile duct patency or the detection of extrahepatic bile duct obstruction secondary to its highly viscous contents or cholelithiasis. Dogs and cats with extrahepatic bile duct obstruction usually undergo cholecystectomy as well as intraoperative catheterization and flushing of the common bile duct (14). Conversely, hepatic lobectomy has been the treatment option for a leakage from intrahepatic bile duct provided that persistent bile leakage or major biliary injuries occur (15). However, hepatic lobectomy is highly invasive and carries increased risk of surgical complications, although it depends on the affected region of liver, especially in cases involving the right division of the liver as in our dog. Therefore, we performed DIC-CT to determine the bile leakage site given that this information was needed to establish a treatment plan and surgical approach. DIC-CT may be a useful method for evaluating bile leakage as well as bile duct patency.

Biliary rupture and subsequent bile peritonitis can be a clinically mild condition, or it can be a life-threatening condition (16, 17). Our dog presented with only mild gastrointestinal signs and a mild increase in C-reactive protein levels (3.75 mg/dl) at presentation. Bilomas are encapsulated collections of bile; hence, it is assumed that only a limited inflammatory response occurred in other organs.

The most common therapeutic approach in human patients with bilomas is percutaneous drainage (3, 4). Studies in veterinary medicine involving two dogs with bilomas who underwent percutaneous drainage showed that both dogs had good outcomes without such a surgical approach for biloma (8, 10). However, the current dog with biloma had been managed with supportive therapy and cholecystectomy. Without adequate medical management, the size or number of bilomas could have increased, and the clinical signs could have worsened, possibly necessitating aggressive drainage, or surgical treatment (18, 19).

A review of the literature on the use of iotroxate in 2,492 patients had shown that adverse reactions (e.g., anaphylaxis, urticaria, and respiratory distress) do occur in human patients following DIC-CT using meglumine iotroxate (20), but at relatively low rates (3.5%) (21). Additionally, previous studies have suggested that the rate of adverse reactions was three times lower with infusions at a constant rate than with bolus injections (21). Therefore, studies have proposed that the tolerance of intravenous biliary contrast agent can be improved when a slow infusion technique is used in humans (22, 23). Previously reported DIC-CT studies in dogs and cats had also used constant rate infusions over 30 min, with no significant side effects having been reported (12, 13). The current dog also did not show side effects after meglumine iotroxate infusion.

Overall, this case report showed that DIC-CT may be a useful method for detecting the bile leakage site within the intrahepatic duct. Further studies including a larger number of patients are needed to elucidate the usefulness and potential adverse reactions associated with DIC-CT.

DATA AVAILABILITY STATEMENT

The original contributions presented in the study are included in the article/supplementary material, further inquiries can be directed to the corresponding author/s.

ETHICS STATEMENT

The animal study was reviewed and approved by Hokkaido University Veterinary Teaching Hospital. Written informed consent was obtained from the owners for the participation of their animals in this study.

AUTHOR CONTRIBUTIONS

MT drafted this article and all co-authors carefully revised it. All authors contributed the management of this case, the conception of the work, and interpretation of data. All authors contributed to the article and approved the submitted version.

FUNDING

This open access publication fee was supported in part by funds of Rakuno Gakuen University.

ACKNOWLEDGMENTS

The authors wish to thank Dr. Yumiko Kagawa, an American College of Veterinary Pathologists board-certified pathologist, for her help with the interpretation of histopathological findings.

REFERENCES

1. Gould L, Patel A. Ultrasound detection of extrahepatic encapsulated bile: "Biloma". *AJR Am J Roentgenol.* (1979) 132:1014–5. doi: 10.2214/ajr.132.6.1014
2. Ferrusquía-Acosta JA. Álvarez-Navascués C, Rodríguez-García M. Giant biloma as a result of a blunt abdominal trauma: A case report. *Rev Esp Enferm Dig.* (2015) 107:768–9. doi: 10.17235/reed.2015.3886/2015
3. Fujiwara H, Yamamoto M, Takahashi M, Ishida H, Ohashi O, Onoyama H et al. Spontaneous rupture of an intrahepatic bile duct with biloma treated by percutaneous drainage and endoscopic sphincterotomy. *Am J gastroenterol.* (1998) 11:2282–4. doi: 10.1111/j.1572-0241.1998.00636.x
4. Bas G, Okan I, Sahin M, Eryilmaz R, Isik A. Spontaneous biloma managed with endoscopic retrograde cholangiopancreatography and percutaneous drainage: a case report. *J Med Case Rep*. (2011) 6:3. doi: 10.1186/1752-1947-5-3
5. Walker AT, Shapiro AW, Brooks DC, Braver JM, Tumeh SS. Bile duct disruption and biloma after laparoscopic cholecystectomy: imaging evaluation. *AJR Am J Roentgenol.* (1992) 158:785–9. doi: 10.2214/ajr.158.4.1532111
6. Bezzi M, Silecchia G, Orsi F, Materia A, Salvatori FM, Fiocca F, et al. Complications after laparoscopic cholecystectomy. Coordinated radiologic, endoscopic, and surgical treatment. *Surg Endosc.* (1995) 9:29–36. doi: 10.1007/BF00187881
7. Hunt GB, Mahoney P, Bellenger CR. Successful management of an iatrogenic biliary pseudocyst in a dog. *J Am Anim Hosp Assoc.* (1997) 33:166–70. doi: 10.5326/15473317-33-2-166
8. Lee N, Seo J, Park H, Yoon J. Diagnosis and successful percutaneous ultrasound-guided aspiration treatment of multiple bilomas in a dog. *J Small Anim Pract.* (2020) 61:321–2. doi: 10.1111/jsap.13133
9. Berry CR, Ackerman N, Charach M, Lawrence D. Iatrogenic biloma (biliary pseudocyst) in a cat with hepatic lipidosis. *Vet Radiol Ultrasound.* (1992) 33:145–9. doi: 10.1111/j.1740-8261.1992.tb01435.x
10. Soultani C, Patsikas M, Mylonakis M, Papazoglou L, Papadopoulou PL, Papakonstantinou PE, et al. Evaluation and treatment of a posttraumatic intrahepatic biloma in a dog. *J Am Anim Hosp Assoc.* (2011) 47:64–6. doi: 10.5326/JAAHA-MS-5710
11. Spillmann T, Happonen I, Kähkönen T. Fyhr T, Westermarck E. Endoscopic retrograde cholangio-pancreatography in healthy beagles. *Vet Radiol Ultrasound.* (2005) 46:97–104. doi: 10.1111/j.1740-8261.2005.00020.x
12. Hayakawa S, Sato K, Sakai M, Kutara K, Asano K, Watari T, et al. cholangiography in dogs with gallbladder mucocele. *J Small Anim Pract.* (2018) 59:490–5. doi: 10.1111/jsap.12832
13. Tanaka T, Akiyoshi H, Mie K, Shimazaki H, Ohashi F. Drip infusion cholangiography with CT in cats. *J Feline Med Surg.* (2018) 20:1173–6. doi: 10.1177/1098612X17738615
14. Mehler SJ. Complications of the extrahepatic biliary surgery in companion animals. *Vet Clin North Am Small Anim Pract.* (2011) 41:949–67. doi: 10.1016/j.cvsm.2011.05.009
15. Kapoor S, Nundy S. Bile duct leaks from the intrahepatic biliary tree: a review of its etiology, incidence, and management. *HPB Surg.* (2012) 2012:752932. doi: 10.1155/2012/752932
16. Bargellini P, Orlandi R, Paloni C, Rubini G, Fonti P, Peterson ME, et al. Evaluation of contrast-enhanced ultrasonography as a method for detecting gallbladder necrosis or rupture in dogs. *Vet Radiol Ultrasound.* (2016) 57:611–20. doi: 10.1111/vru.12404

17. Willard MD, Fossum T. Extrahepatic biliary disorders. In: Washabau RJ and Day M, editor. *Canine & Feline Gastroenterology*. St. Louis, MO: Saunders (2013). p. 933–6.
18. Ahluwalia JP, LaBrecque DR. A large biloma causing gastric outlet obstruction after a percutaneous liver biopsy. *J Clin Gastroenterol* (2004) 38:535–9. doi: 10.1097/01.mcg.0000123167.86324.ff
19. Kalfadis S, Ioannidis O, Botsios D, Lazaridis C. Subcapsular liver biloma due to gallbladder perforation after acute cholecystitis. *J Dig Dis*. (2011) 12:412–4. doi: 10.1111/j.1751-2980.2011.00523.x
20. Persson A, Dahlström N, Smedby O, Brismar TB. Three-dimensional drip infusion CT cholangiography in patients with suspected obstructive biliary disease: a retrospective analysis of feasibility and adverse reaction to contrast material. *BMC Med Imaging*. (2006) 6:1. doi: 10.1186/1471-2342-6-1
21. Nilsson U. Adverse reactions to iotroxate at intravenous cholangiography. A prospective clinical investigation and review of the literature. *Acta Radiol*. (1987) 28:571–5. doi: 10.3109/02841858709177403
22. Kwon AH, Inui H, Imamura A, Uetsuji S, Kamiyama Y. Preoperative assessment for laparoscopic cholecystectomy: feasibility of using spiral computed tomography. *Ann Surg*. (1998) 227:351–6. doi: 10.1097/00000658-199803000-00006
23. Okada M, Fukada J, Toya K, Ito R, Ohashi T, Yorozu A. The value of drip infusion cholangiography using multidetector-row helical CT in patients with choledocholithiasis. *Eur Radiol*. (2005) 15:2140–5. doi: 10.1007/s00330-005-2820-z

Conflict of Interest: The authors declare that the research was conducted in the absence of any commercial or financial relationships that could be construed as a potential conflict of interest.

Publisher's Note: All claims expressed in this article are solely those of the authors and do not necessarily represent those of their affiliated organizations, or those of the publisher, the editors and the reviewers. Any product that may be evaluated in this article, or claim that may be made by its manufacturer, is not guaranteed or endorsed by the publisher.

frontiers in Veterinary Science

ORIGINAL RESEARCH
published: 21 March 2022
doi: 10.3389/fvets.2022.842105

Relationship Between Somatic Cell Counts and Mammary Gland Parenchyma Ultrasonography in Buffaloes

Xinxin Zhang[1,2], *Muhammad Jamil Ahmad*[1,2], *Zhigao An*[1,2], *Kaifeng Niu*[1,2], *Wei Wang*[1,2], *Pei Nie*[1,2], *Shan Gao*[1,2] *and Liguo Yang*[1,2,3]*

[1] Key Laboratory of Animal Genetics, Breeding and Reproduction, Ministry of Education, College of Animal Science and Technology, Huazhong Agricultural University, Wuhan, China, [2] International Joint Research Centre for Animal Genetics, Breeding and Reproduction (IJRCAGBR), Huazhong Agricultural University, Wuhan, China, [3] Hubei Province's Engineering Research Center in Buffalo Breeding and Products, Wuhan, China

OPEN ACCESS

Edited by:
Ayman Abdel-Aziz Swelum,
Zagazig University, Egypt

Reviewed by:
Moez Ayadi,
University of Jendouba, Tunisia
Moustafa Mohamed Zeitoun,
Qassim University, Saudi Arabia
Dwijendra K. Gupta,
Jai Prakash Vishwavidyalaya, India

***Correspondence:**
Liguo Yang
yangliguo2006@qq.com

Specialty section:
This article was submitted to Veterinary Imaging, a section of the journal Frontiers in Veterinary Science

Received: 23 December 2021
Accepted: 02 February 2022
Published: 21 March 2022

Citation:
Zhang X, Ahmad MJ, An Z, Niu K, Wang W, Nie P, Gao S and Yang L (2022) Relationship Between Somatic Cell Counts and Mammary Gland Parenchyma Ultrasonography in Buffaloes. Front. Vet. Sci. 9:842105. doi: 10.3389/fvets.2022.842105

The aim of the present study was to determine whether the echotextural features of the mammary gland parenchyma in buffaloes during lactation at different somatic cell levels could be used to diagnose mastitis. This study was divided into two parts. In the first experiment, experimental buffaloes ($n = 65$) with somatic cell counts (SCC) tests ($n = 94$) in different seasons, including spring ($n = 22$), summer ($n = 24$), autumn ($n = 37$), and winter ($n = 11$), were used to obtain ultrasonic variables for each quarter of mammary gland that could best explain the corresponding somatic cell level. In the second part of the study, the first part's experimental results were verified by subjecting at least one-quarter udder of eight buffaloes to ultrasonography seven times during mid-July to mid-August for obtaining ultrasonic values at different somatic cell levels. The echo textural characteristics [mean numerical pixel values (NPVs) and pixel heterogeneity (pixel standard deviation, PSD)] were evaluated using 16 ultrasonographic images of each buffalo with Image ProPlus software. The effects of SCC, days in milk (DIM), scanning order (SO), season, as well as the scanning plane and udder quarter (SP + UQ) on both the PSD and NPVs of the mammary gland were significant ($p < 0.05$). The correlation coefficient between pre-milking sagittal PSD and somatic cell score (SCS) was the highest ($r = 0.4224$, $p < 0.0001$) with fitted linear model: $y = 0.19445x$ (dependent variable: SCS, independent variables: pre-milking sagittal PSD; $R^2 = 0.84$, $p < 0.0001$). In addition, SCC and ultrasonic of udder quarter were followed for 1 month, confirming that pre-milking sagittal PSD of mammary gland value could explain the SCC variation in milk. The current study demonstrated that the ultrasonographic examination of the udder could be one of the complementary tools for diagnosing subclinical mastitis in buffaloes.

Keywords: SCC, NPVs, PSD, ultrasonography, mastitis

INTRODUCTION

Buffalo is the second-largest milk-producing livestock, with an average of 118.162 million tons of buffalo milk per year over the last decade, according to the FAO statistical database (1). Like cows, mastitis is the most serious disease that causes economic loss in the buffaloes (2, 3). Although buffaloes are traditionally thought to be more resistant to mastitis than cows, some characteristics such as higher nutrient content in milk suitable for rapid microbial growth and pendulous udder with longer teats make buffaloes more prone to mastitis (2). In Nepal, the prevalence of subclinical mastitis is as high as 78% in buffalos and 55% in cows (4). Mastitis has a negative effect on milk composition (protein, fat, lactose, and mineral) (5, 6), curdling (7), milk yield (7), and conception rate (suppression to both corpus luteum (CL) diameter and function) (8) in buffaloes. Buffalos in developing countries are mostly raised on a small scale with adequate resources; limited quality research about health, management, nutrition, applied reproduction, and basic physiology (9) makes mastitis detection more difficult due to prevailing environmental and management conditions. Therefore, establishing the methods for early mastitis detection is significant for preventing and treating mastitis.

Early and accurate diagnosis of the disease is an essential part of treatment. Nowadays, many different methods for diagnosing mastitis are being practiced based on SCC and plate-culture techniques (10). SCC is an important indicator for judging subclinical udder infection; mastitis quarters included were defined as clinical mastitis or subclinical mastitis by SCC $\geq$ 200,000 cells/ml in the European Union, $\geq$250,000 cells/ml in Australia, and $\geq$150,000 cells/ml in New Zealand (11). Because of the significance of early diagnosis and early treatment, it is imperative to establish an economical, accurate, and rapid method for diagnosing mastitis on the farm (12).

Ultrasonography is a non-invasive technique that can examine udder for hematoma, abscess, inflammation, milk stones, tissue proliferation, congenital malformation, mucosal lesions, and foreign bodies (13). In recent years, ultrasound has been widely used to examine the anatomical structure of the mammary gland of various animals (14–16). Diagnostic ultrasonography has been employed to get the images of udder structures, including mammary glands with the mammary parenchyma, the lactiferous ducts, the mammary vessels, the teat (teat cistern and teat arteries), the supra-mammary lymph nodes, and the gland cistern (17). Several studies have investigated the relationship between the ultrasonography assessed mammary gland and SCC or mastitis (18–20). Ultrasound technology is considered an effective method for the rapid detection of mastitis.

Ultrasonography facilitates researchers in examining the same animals repeatedly and readily, providing grayscale and two-dimensional images of tissues in real time to evaluate their structure, echogenicity, and homogeneity. Therefore, the objective of this study was to develop a rapid method to detect mastitis by establishing the relationship between somatic cells and mammary echotextural characteristics in buffaloes.

MATERIALS AND METHODS

Experimental Animals

The present investigation was carried out in the buffalo farm of Jinniu Animal Husbandry Co. Ltd., China, from November 2020 to September 2021. The experimental animals were divided into two groups: experimental group (EG, $n = 65$, test-day records $= 94$) was tested in the first part and the validation group (VG, $n = 8$, test-day records $n = 54$) with at least one-quarter udder was tested in the second part to verify the results of the first part. All lactating buffaloes were housed in the free-stall pens and fed a total mixed rations (TMR) diet. DIM of all the buffaloes enrolled in this study were between 5 and 349 days with the parity between 1 and 6 and milked twice a day, morning and evening, in a parallel milking parlor (6×2). The milking machine parameters were set to an operational vacuum of 50 kPa, 64 ± 3 pulsation cycles/min at a ratio of 60:40, which were maintained every 3 months. Data for individual buffalo data were obtained from herd management software (Daily management system for buffalo V1.0).

Milk Sampling

All milk samples from the quarter mammary gland were collected on the morning of the ultrasound measurement, and the first few streams of milk were discarded before collection. Quarter-level SCC milk samples were collected in 50-ml sterile vials with preservatives added in advance that submitted to the Dairy Herd Improvement of Hubei testing center under -60°C conditions for SCC detection by somatic cytometer (CombiFoss FT+ FOSS Analytical, Hillerød, Denmark).

Mammary Gland Measurements

It was challenging to interpret the sensitivity difference between 5- and 7.5-MHz probes in examining the mammary parenchyma (21). Previously, Wang et al. (22) recommended using linear array transducers with high frequencies in conventional ultrasound examinations for superficial organs such as the udder. A high-frequency probe produces a good-quality ultrasound image (23). Hence, real-time B-mode ultrasonography (WED-3000-v, equipped with LNA/6.5 MHz rectal probe, Shenzhen Well; D Medical Electronics Co., Ltd., Guangdong, China) working at 7.5-MHz linear array transducer was used at a depth of 90 mm to examine the udder area of all four mammary glands in lactation buffalo. The same experienced operator did all mammary ultrasound examinations. Mammary ultrasound was consistently examined in the following order: left front, left rear, right rear, and right front using a probe coated with ultrasound gel to enhance contact against the animal's skin. Udders were clipped of excess hair to reduce the influence of hair on ultrasound scan results. The probe was placed directly in the middle of the udders. Ultrasonographic scans of the coronal and sagittal planes of each of the four quarters of the udder were taken immediately before and after milking (**Figure 1A**).

Each buffalo was scanned 16 times, and a total of 1,710 ultrasound images were captured and saved in bitmap (BMP) format. Subsequently, images were transferred using universal

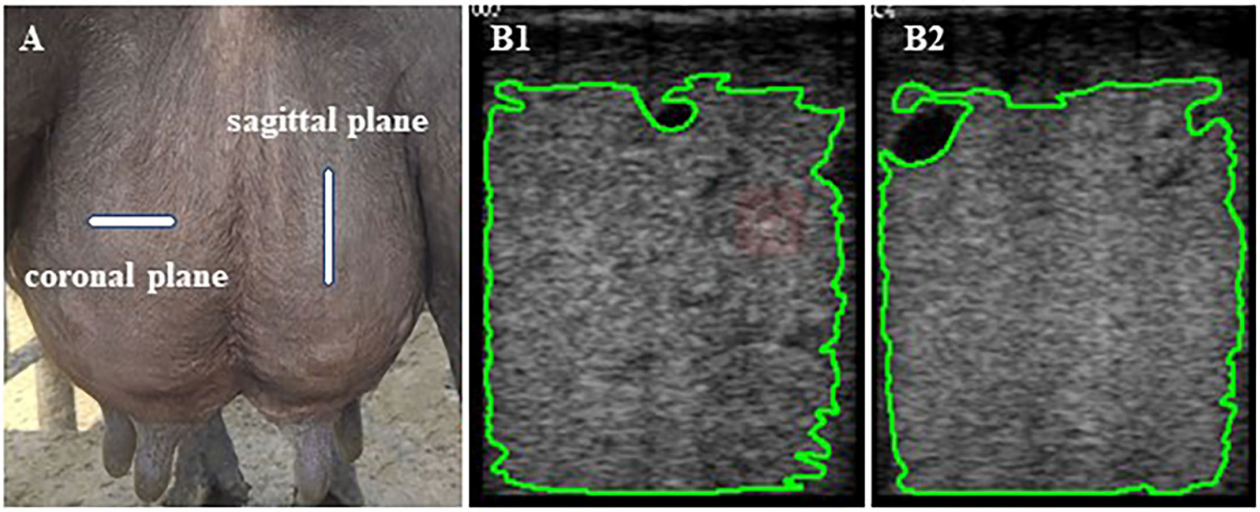

FIGURE 1 | (A) The probe is located on the coronal and sagittal planes surfaces of the udder quarters. **(B1,2)** The mammary parenchyma echotexture of the selected area of coronal **(B1)** and sagittal planes **(B2)** excluding the areas with lactiferous ducts, gland cisterns, and visible blood vessels formations was calculated using Image-Pro Plus software.

serial bus (USB) for computer analysis with USB software Image-Pro Plus 6.0 (National Institutes of Health, Rockville Pike, MD, USA) to analyze, process, and edit grayscale images by pixel value statistics and calculate area to get the intensity values. Areas with lactiferous ducts, gland cisterns, and visible blood vessel formations were not considered for the grayscale analysis (**Figure 1B**). Grayscale ultrasound images are composed of many luminance elements (pixels) corresponding to multiple acoustic interfaces within the detected tissues (24). Numerical pixel values (NPVs) were defined as a quantitative measure of pixel brightness, and pixel heterogeneity [pixel standard deviation (PSD)] was the standard deviation of NPV in the region of interest. The mean NPVs and pixel heterogeneity (PSD) values were calculated based on the brightness (absolute black, 0, to absolute white, 255) of the selected area of each ultrasound image (25). The echotextural characteristics of mammary gland parenchyma (pre-milking coronal NPVs, pre-milking sagittal NPVs, pre-milking coronal PSD, pre-milking sagittal PSD, post-milking coronal NPVs, post-milking sagittal NPVs, post-milking coronal PSD, and post-milking sagittal PSD) were obtained by combining ultrasonic image and computer software.

Ultrasonography of Udder Quarter at Different SCC Levels

To verify the echotextural variable's accuracy in detecting mastitis, at least one of the four udders of eight buffaloes of parity (2–5) with days in milk (DIM, 25–224), milk yield (MY mean, 6.01), and SCC tests ($n = 54$) was examined based on SCC tests (>200,000 cells/ml) of quarter milk samples. Mastitis can transfect to other quarter udder regions if not treated. Collecting milk samples and mammary glands ultrasound examination were carried out seven times at an interval of 6 and 1 day, respectively and followed up for 30 days to obtain mammary parenchyma echotexture images at different somatic cell levels.

Statistical Analysis

Factors Affecting Mammary Gland Echotexture

The data from 94 test-day records from 65 buffaloes were included in calculating the fixed effects using SAS's general linear model (GLM) procedure implemented in SAS version 9.4 (SAS Institute Inc., Cary, NC, USA) (26). The main effects are DIM, parity, season, SCC, scanning plane for each quarter, and scanning order (SO). The echotextural variables were determined by GLM as follows:

$$Y_{ijklmn} = \mu + DIM_i + Parity_j + Season_k + SCC_l + SO_m + (UQ + SP)_n + [SO \times (UQ + SP)]_{mn} + e_{ijklmn}$$

where Y_{ijklmn} is the NPVs or PSD; μ is the population mean of the model; DIM is fixed effect of lactation period ($i = 1$–4, the first class is DIM in 5–90 days and followed by classes of 90 days each, until the fourth class is 271–349 days); parity is fixed effect of the number of lactations ($j = 1$ to 3, primiparous were first levels, 2–3 parities were second levels, and 4–6 parities was the third level); season is fixed effect season of measurement [($k =$ Spring (April), Summer (July and August), Autumn (November), and Winter (January)]; SCC is fixed effect of somatic cell counts ($l =$ 1–5, 1:<200,000 cells/ml, 2: 200,000–500,000 cells/ml, 3:500,000–800,000 cells/ml, 4:800,000–5,000,000 cells/ml, and 5:>5,000,000 cells/ml); SO is fixed effect of SO ($m = 1$ to 2, before or after milking); UQ + SP is fixed effect of scanning plane for each quarter ($n =$ l to 8, sagittal vs. coronal within left front vs. left back vs. right back vs. right front udder quarter); SO × (UQ + SP) is the fixed effect of the interaction between SO and UQ + SP; and e_{ijklmn} is the random residual.

TABLE 1 | Factors affecting the echotextural characteristics of mammary gland parenchyma (NPVs and PSD).

Effect	PSD	NPVs
SCC (cells/ml)	<0.0001	0.0478
DIM/day	0.0101	<0.0001
Parity	0.4901	<0.0001
Season	<0.0001	<0.0001
UQ + SP	<0.0001	<0.0001
SO	0.0003	0.0406
SO × (UQ + SP)	0.2901	0.0283

NPVs, numerical pixel values; PSD, pixel standard deviation or pixel heterogeneity; SCC, SCC categories; DIM, days in milk; UQ + SP, fixed effect of scanning plane for each quarter; SO, fixed effect of scanning order; SO × (UQ + SP) is the fixed effect of the interaction between SO and UQ + SP.

Correlation Analysis and Linear Regression Between SCS and Mammary Gland Echotexture

For normality and homogeneity of the SCC variable, the transformation formula SCS = 3 + $\log_2$ (SCC/100,000) was used, using only data from the 94 test-day records from 65 buffaloes. Pearson correlations analysis was performed using the PROC CORR in SAS (version 9.4, SAS Institute Inc., Cary, NC, USA) (27). DIM, parity, and season were added to the process as a covariate based on factors affecting mammary gland parenchyma echotexture. According to the correlation analysis results, the general linear regression model was fitted by PROC REG procedure to determine the association between SCS (dependent variable) and mammary gland parenchyma echotexture (independent variables).

Changes of Mammary Gland Echotexture at Different SCC Levels

Mean values of mammary gland echotexture at different somatic cell levels (<200,000 cells/ml, 200,000–5,000,000 cells/ml, and >5,000,000 cells/ml) were obtained after 1-month follow-up and compared by ANOVA using SAS (version 9.4, SAS Institute Inc., Cary, NC, USA) (28). The data were visualized using the software package GraphPad Prism 6 (version 6.0c; GraphPad Software, Inc., La Jolla, CA, USA) (29).

RESULTS

Factors Affecting the Echo Textural Characteristics of Mammary Gland Parenchyma

Table 1 shows that the effects of SCC, DIM, SO, season, as well as the UQ + SP on both the PSD and NPVs of mammary glands were significant (PSD: SCC, $p < 0.0001$; DIM, $p = 0.0101$; SO, $p = 0.0003$; Season, $p < 0.0001$; UQ + SP, $p < 0.0001$; NPVs: SCC, $p = 0.0478$; DIM, $p < 0.0001$; SO, $p = 0.0406$; Season, $p < 0.0001$; UQ + SP, $p < 0.0001$). Whereas, parity and SO × (UQ + SP) on PSD were not found to have an effect on any of the measurements (parity, $p = 0.4901$; SO × (UQ + SP), $p = 0.2901$). Parity and SO × (UQ + SP) were found to have an effect on NPVs (parity, $p < 0.0001$ − SO × (UQ + SP), $p = 0.0283$).

TABLE 2 | The least square means of NPVs and PSD by SCC, DIM, season, UQ + SP, and SO categories for buffaloes (Mean ± SEM).

Effect	PSD	NPVs
SCC (cells/ml)		
<200,000	24.46 ± 0.24	61.38 ± 1.01
200,000–500,000	25.40 ± 0.31	59.81 ± 1.33
500,000–800,000	25.64 ± 0.44	61.51 ± 1.89
800,000–5,000,000	26.88 ± 0.23	63.91 ± 0.98
>5,000,000	27.12 ±0.37	62.54 ± 1.56
DIM/day		
5–90	26.56 ± 0.18	72.96 ± 0.76
91–180	25.75 ± 0.24	64.63 ± 1.03
181–270	25.85 ± 0.40	55.25 ± 1.69
271–349	25.43 ± 0.44	54.47 ± 1.85
Parity		
1	25.95 ± 0.24	57.05 ± 1.00
2–3	25.72 ± 0.21	63.57 ± 0.90
4–6	26.02 ± 0.33	64.87 ± 1.39
Season		
Spring (April)	25.37 ± 0.24	47.74 ± 1.01
Summer (July and August)	27.17 ± 0.28	64.04 ± 1.21
Autumn (November)	24.98 ± 0.24	66.18 ± 1.00
Winter (January)	26.07 ± 0.41	69.35 ± 1.75
UQ + SP		
Left front coronal	26.43 ± 0.34	60.11 ± 1.45
Left front sagittal	27.09 ± 0.34	60.38 ± 1.45
Left back coronal	24.57 ± 0.35	57.41 ± 1.48
Left back sagittal	24.68 ± 0.35	63.90 ± 1.50
Right back coronal	25.55 ± 0.33	63.73 ± 1.39
Right back sagittal	25.54 ± 0.33	68.38 ± 1.40
Right front coronal	25.83 ± 0.33	59.27 ±1.39
Right front sagittal	27.51 ± 0.33	61.45 ±1.39
SO		
Before milking	25.53 ± 0.22	62.73 ± 0.95
After milking	26.27 ± 0.22	60.93 ± 0.93

Mean PSD was the lowest in the SCC < 200,000 cells/ml and increases with SCC increase (24.46 vs. 25.40 vs. 25.64 vs. 26.88 vs. 27.12; **Table 2** and **Figure 2**). Mean PSD value of front half udder was larger than that of rear udder half, while mean NPV value was the opposite (PSD: 26.72 vs. 25.09; NPVs: 60.30 vs. 63.36; front half udder compared with rear udder half, respectively). During summer, PSD value was the highest compared with other seasons (summer: 27.17 vs. spring: 25.37 vs. autumn: 24.98 vs. winter: 26.07; $p < 0.05$). NPV value in spring was significantly lower than that in other seasons (spring: 47.74 vs. summer: 64.04 vs. autumn: 66.18 vs. winter: 69.35; $p < 0.05$). PSD were greater after than before milking, but NPVs were the opposite (PSD: 25.53 vs. 26.27, $p < 0.05$; NPVs: 62.73 vs. 60.93, $p < 0.05$; before compared with after milking, respectively). PSD and NPVs were highest between 5 and 90 days of lactation (PSD: 26.56; NPVs: 72.96).

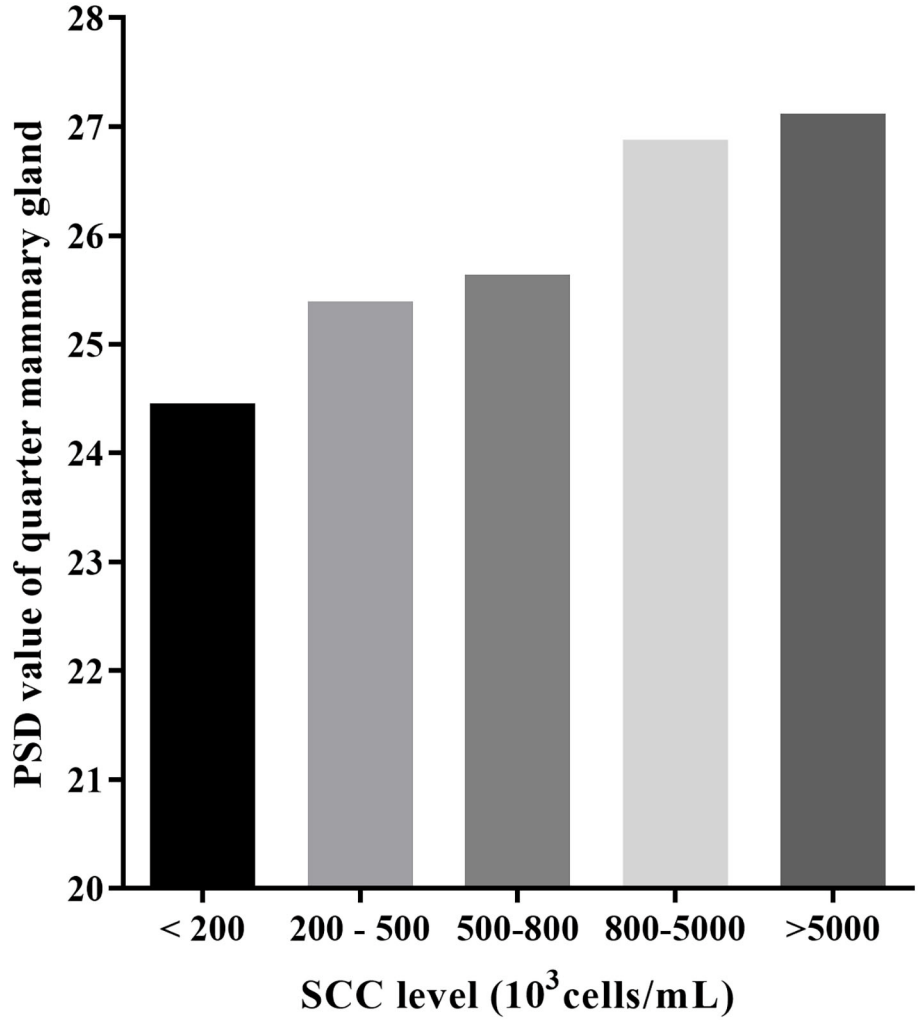

FIGURE 2 | The least square means of PSD by SCC categories for buffaloes.

The Relationship Between Echotextural Characteristics of Mammary Gland Parenchyma and SCS

Four PSD traits were highly significant and positively correlated with SCC among echotextural characteristics of the mammary gland parenchyma and SCC of the milk obtained in the period before and after milking, respectively ($p < 0.0001$), but non-significant with NPVs ($p > 0.05$), respectively (**Table 3**). The correlation coefficient between pre-milking sagittal PSD and SCS was the highest ($r = 0.4224$, $p < 0.0001$), compared with pre-milking coronal PSD ($r = 0.30734$, $p < 0.0001$), post-milking coronal PSD ($r = 0.27354$, $p < 0.0001$), and post-milking sagittal PSD ($r = 0.26595$, $p < 0.0001$). The high value of adjusted R^2 (0.82 to 0.84) indicated that the linear model of PSD fitting explained sufficient variability in SCC in milk. Pre-milking sagittal PSD had explained higher variation ($Y = 0.19445\times$, adjusted $R^2 = 0.84$) and fitted better than other models (**Table 4**).

Changes of Mammary Gland Echotexture of Quarter-Level at Different SCC Levels

All the data were reported as the average of the same SCC level in seven ultrasonic testing and SCC levels varied in 24 out of 32 mammary glands. The PSD value for most quarter udder increases with somatic cells (**Table 5** and **Figure 3**). A one-way ANOVA test was used to compare the pre-milking sagittal PSD values for different levels of SCC. The results showed that pre-milking sagittal PSD varied significantly ($p = 0.003$) between different levels of SCC. The pre-milking sagittal PSD value reached the lowest value at SCC < 200,000 cells/ml and significantly lower than other levels (SCC < 200,000: 24.85 vs. 200,000–5,000,000: 27.70 vs. SCC > 5,000,000: 28.12, $p < 0.01$).

DISCUSSION

The quality of feed, milking equipment, health conditions, and management systems of buffalo are all-inferior to those of

TABLE 3 | Pearson correlations coefficients between echotextural characteristics of mammary gland parenchyma and SCS ($n = 94$ test-day records).

Variable	*r*	*p*-value
Pre-milking coronal NPVs	0.00626	0.9129
Pre-milking coronal PSD	0.30734	<0.0001
Pre-milking sagittal NPVs	−0.00828	0.885
Pre-milking sagittal PSD	0.4224	<0.0001
Post-milking coronal NPVs	0.00126	0.9825
Post-milking coronal PSD	0.27354	<0.0001
Post-milking sagittal NPVs	0.02105	0.7128
Post-milking sagittal PSD	0.26595	<0.0001

TABLE 4 | The linear model between SCS and pre-milking sagittal, pre-milking coronal PSD, post-milking coronal PSD, and post-milking sagittal PSD.

Input variable	Adjusted R^2	Equation	*p*-Value
Pre-milking sagittal PSD	0.84	$Y = 0.19445x$	<0.0001
Pre-milking coronal PSD	0.82	$Y = 0.20065x$	<0.0001
Post-milking coronal PSD	0.82	$Y = 0.19165x$	<0.0001
Post-milking sagittal PSD	0.82	$Y = 0.18708x$	<0.0001

TABLE 5 | Descriptive statistics pre-milking sagittal PSD of the mammary gland in a single udder quarter using ANOVA analysis by SCC (54 test-day records for eight buffaloes).

Quarter-level udders	SCC (10^3 cells/ml)			*p*-Value
	<200	200–5,000	>5,000	
1	26.15	26.38	27.59	0.003
2	24.16	24.74	29.11	
3	22.23	25.03	24.38	
4	24.05	25.74	N	
5	25.98	26.09	N	
6	22.65	25.48	N	
7	25.51	N	26.48	
8	21.72	22.87	N	
9	24.04	24.38	26.22	
10	24.02	24.66	24.43	
11	23.81	25.81	27.04	
12	27.00	32.93	N	
13	22.79	N	29.22	
14	26.59	N	29.57	
15	24.13	N	27.25	
16	29.00	28.30	31.02	
17	25.90	34.54	N	
18	29.31	37.32	37.49	
19	27.28	28.21	N	
20	N	29.13	27.36	
21	N	28.99	31.61	
22	25.91	28.11	28.84	
23	20.89	N	25.65	
24	23.66	N	24.83	
Mean ± SEM	24.85 ± 0.47^b	27.70 ± 0.90^a	28.12 ± 0.78^a	

[ab]Pre-milking sagittal PSD means within the same row with different superscripts differ at $P < 0.05$.

N: There is no record of a match.

cows, which significantly affects the prevention, diagnosis, and treatment of mastitis in buffalo, especially at the farm level. California mastitis test for diagnosing mastitis has the advantage of being quick and easy to perform on the farm. However, it results in subjective and indirect determination, which instigates finding more accurate techniques (30). The effectiveness of ultrasound for detecting mastitis in buffalo was first confirmed (14). Ultrasound has been used as a diagnostic tool for several decades. However, its use in buffalo just started in the last decade, and there is a shortage of literature on the relationship between ultrasound and mastitis in buffaloes (31). The purpose of this study was to determine the relationship between mammary gland echotexture values and SCC in milk and finally to find a simple and accurate diagnosis method for buffalo mastitis. To the author's knowledge, this was the first attempt to correlate quantitative echotextural characteristics of the udder with SCC in buffaloes.

Udder fibrosis and atrophy due to chronic mastitis had hyperechoic cordial bands representing the fibrous tissues, replacing the glandular tissues in buffaloes (14). The ultrasonographic examination may explain internal structure changes in the mammary gland and teat tissue of animals with fibrosis and mastitis (14). The characteristic changes of mammary glandular parenchyma, teat, and the milk that occurred during all different mastitis phases show the different intensities of echogenicity (32). The grayscale intensity values of mammary parenchyma in pregnancy toxemia were significantly greater than in healthy controls. Not only in the mammary gland, pixel intensity and pixel heterogeneity in the testicular parenchyma was also related to male reproductive health (33, 34).

Currently, SCC, either from the whole udder or quarter, has been the best indicator of the mammary glands' inflammatory status (30, 35). A previous study has reported that the image of the udder with mastitis appeared as hyperechoic parenchyma in buffaloes (36). The current study showed a weak correlation between SCS and NPVs, which may be caused by mastitis, leading to local hyperechoic mammary ultrasound without a significant increase in the mean value of NPVs. According to various studies, the ultrasonography of normal mammary parenchyma depicts a homogenous structure (17, 37, 38). On the contrary, mammary glands with mastitis reveal non-homogenous regions in mammary gland parenchyma from hypo- to hyperechoic (23, 39). Believing that lack of milk secretion makes visualization of the mammary structures more complex, they suggested performing an ultrasound at least 2 h after milking for optimal visualization. These support the present study results; the correlation coefficient between PSD value and SCS was more significant before milking. In addition, SCC and ultrasonic of udder quarter were followed for 1 month, confirming that pre-milking sagittal PSD of mammary gland value could explain the SCC variation in milk.

The present study found that examining the structures of the mammary gland parenchyma with vertical positioning showed

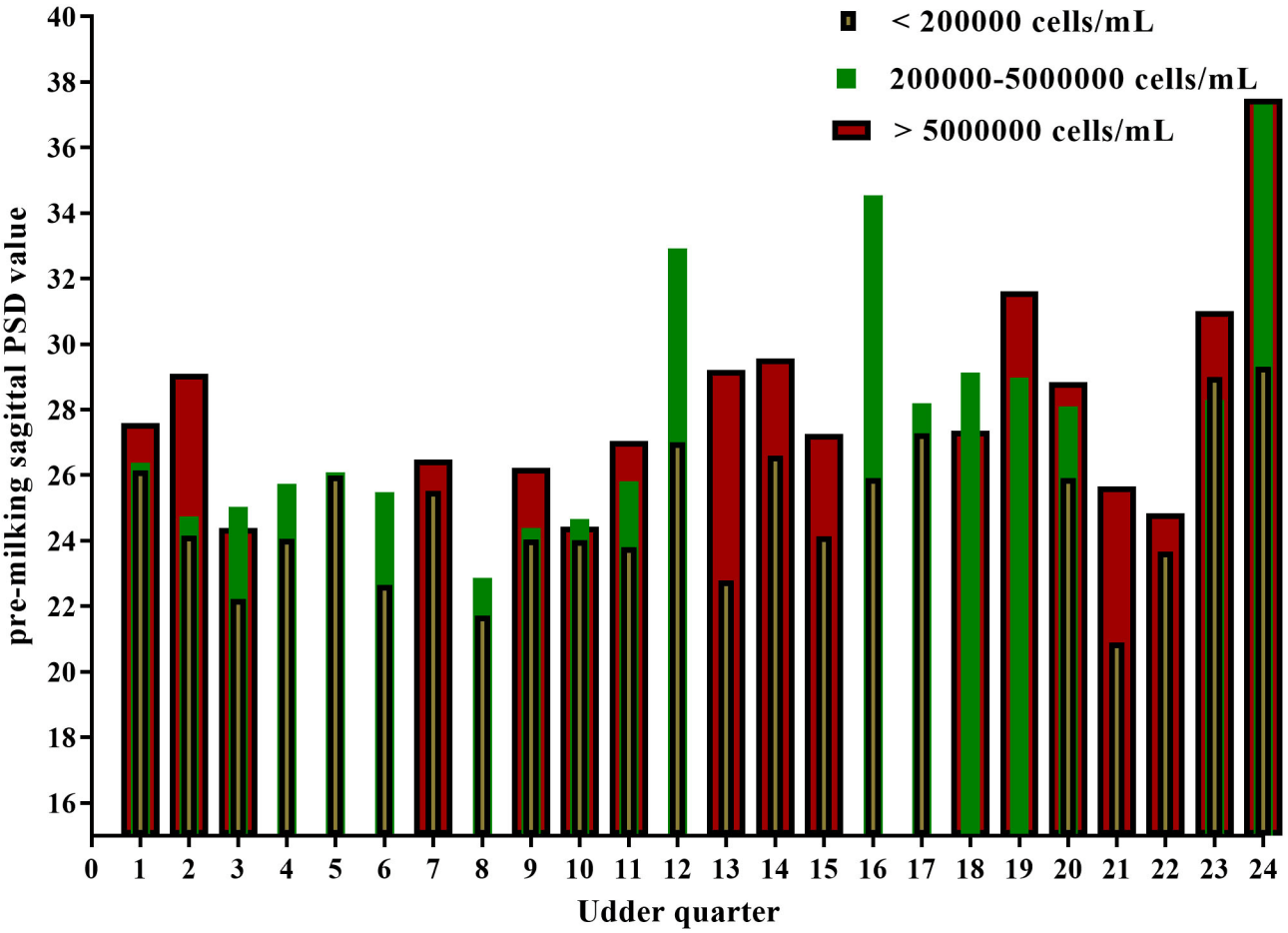

FIGURE 3 | Pre-milking sagittal PSD values of 24 quarter-level udders at different somatic cell levels.

better results than the horizontal direction, contradictory to findings in goats (39). However, Schwarz et al. (40) reported that examining the vertical plane of the mammary gland was more suitable and could describe the significant correlation between echotextural variables and milk composition (protein and lactose during both milking periods).

Our study showed that echotextural characteristics of the mammary parenchyma were influenced by many factors, including DIM, seasons, and measurement methods. Therefore, these factors should be considered while interpreting the ultrasonic-related effects. In our study, PSD values of the mammary gland were highest at 5–90 days of lactation and in summer. Coincidentally, Riekerink et al. (41) found that bulk milk SCC peaked in August to September during 4 consecutive years. Further, Morse et al. (42) found that clinical mastitis increases with increased temperature–humidity index value in summer. Hossein-Zadeh and Ardalan (43) reported that the odds of clinical mastitis increased in the first month of lactation. Early lactation mastitis occurs because of unresolved intramammary infections or the formation of intramammary infections during the dry period. A study in cows by Barkema et al. (44) shows that rear quarters were more likely than front quarters to have mastitis and high SCC. On the contrary, Hammer et al. (45) found that a quarter position is not associated with the risk of developing mastitis. However, the PSD value in the front quarters was higher than that in the rear quarters, which was confirmed in the study of Ali et al. (46), who found that the prevalence of mastitis was higher in the front quarters compared to the rear quarters in buffalo (prevalence of sub-clinical mastitis: front quarters 98/400 vs. rear quarters 85/400).

Interestingly, the results of our study showed that, before milking, the NPVs values were significantly higher than after milking, which was different from the results in cows (40). In agreement with current study findings, the PSD value of the mammary glands was larger after milking than before milking in Olkuska ewes (21). The variation in parenchymal echotexture can be explained by the differences in milk chemical composition and parenchymal tissue microstructure among different animals (21). The difference in the NPVs between dairy cows and buffaloes could be due to the much higher

milk yield of cows than buffalo [34.71 kg/days vs. 9.01 kg/days (47, 48)]. A small amount of buffalo milk as fluids with a high total solid and fat content (49) plays the role of an acoustic window and without significantly reducing mammary grayscale intensity values.

CONCLUSION

Despite the availability of different traditional and novel diagnostic tools for early mastitis diagnosis, there is no gold for testing as all tools have limitations; hence, a multifaceted approach is advised to improve udder health. Ultrasound is an economical, rapid tool for detecting mastitis on dairy farms. The PSD and NPVs of mammary were significantly associated with SCS, DIM, SO, season, as well as the scanning plane and udder quarter ($p < 0.05$). The correlation coefficient between pre-milking sagittal PSD and SCC was the highest ($r = 0.4224$, $p < 0.0001$). The pre-milking sagittal PSD of mammary gland value could explain the SCC variation in milk well. Computer-assisted pixel analysis of mammary gland ultrasonograms examination of the udder can aid in diagnosing subclinical mastitis in buffaloes. However, further research is needed to validate the current study's findings and statistical methods with large sample size and data.

DATA AVAILABILITY STATEMENT

The raw data supporting the conclusions of this article will be made available by the authors, without undue reservation.

ETHICS STATEMENT

The animal study was reviewed and approved by the Ethical Committee of the Hubei Research Center of Experimental Animals. Written informed consent was obtained from the owners for the participation of their animals in this study.

AUTHOR CONTRIBUTIONS

LY and XZ: conceptualization. XZ, ZA, KN, and WW: methodology. PN and SG: software and data curation. XZ and MA: investigation. XZ: writing—original draft preparation. MA: writing—review and editing. LY: supervision, project, and funding acquisition. All authors have read and agreed to the published version of the manuscript.

FUNDING

China Agriculture Research System of MOF and MAR supported this research work.

REFERENCES

1. FAO. *FAOSTAT*. (2021). Available online at: https://www.fao.org/faostat/en/#data/QCL (accessed January 15, 2022).
2. Fagiolo A, Lai O. Mastitis in buffalo. *Ital J Anim Sci.* (2007) 6:200–6. doi: 10.4081/ijas.2007.s2.200
3. Locatelli C, Piepers S, DeVliegher S, Barberio A, Supré K, Scaccabarozzi L, et al. Effect on quarter milk somatic cell count and antimicrobial susceptibility of Staphylococcus rostri causing intramammary infection in dairy water buffaloes. *J Dairy Sci.* (2013) 96:3799–805. doi: 10.3168/jds.2012-6275
4. Sah K, Karki P, Shrestha RD, Sigdel A, Adesogan AT, Dahl GE. Milk Symposium review: Improving control of mastitis in dairy animals in Nepal. *J Dairy Sci.* (2020) 103:9740–7. doi: 10.3168/jds.2020-18314
5. Uallah S, Ahmad T, Bilal M, Muhammad G, Rahman S. The effect of severity of mastitis on protein and fat contents of buffalo milk. *Pak Vet J.* (2005) 25:1–4. Avilable online at: http://www.pvj.com.pk/pdf-files/25_1/1-4.pdf
6. Ahmad T, Bilal M, Ullah S, Ur-rehman Z, Muhammad G. Impact of mastitis severity on mineral contents of buffalo milk. *Pakistan J Agric Sci.* (2007) 44:176–8. Avilable online at: https://pakjas.com.pk/papers/375.pdf
7. Tripaldi C, Palocci G, Miarelli M, Catta M, Orlandini S, Amatiste S, et al. Effects of mastitis on buffalo milk quality. *Asian-australas J Anim Sci.* (2010) 23:1319–24. doi: 10.5713/ajas.2010.90618
8. Mansour MM, Hendawy AO, Zeitoun MM. Effect of mastitis on luteal function and pregnancy rates in buffaloes. *Theriogenology.* (2016) 86:1189–94. doi: 10.1016/j.theriogenology.2016.04.009
9. Warriach H, Mcgill D, Bush R, Wynn P, Chohan K. A review of recent developments in buffalo reproduction—a review. *Asian-australas J Anim Sci.* (2015) 28:451. doi: 10.5713/ajas.14.0259
10. Martins SA, Martins VC, Cardoso FA, Germano J, Rodrigues M, Duarte C, et al. Biosensors for on-farm diagnosis of mastitis. *Front Bioeng Biotechnol.* (2019) 7:186. doi: 10.3389/fbioe.2019.00186
11. Ebrahimie E, Ebrahimi F, Ebrahimi M, Tomlinson S, Petrovski KR. A large-scale study of indicators of sub-clinical mastitis in dairy cattle by attribute weighting analysis of milk composition features: highlighting the predictive power of lactose and electrical conductivity. *J Dairy Res.* (2018) 85:193–200. doi: 10.1017/S0022029918000249
12. Ashraf A, Imran M. Diagnosis of bovine mastitis: from laboratory to farm. *Trop Anim Health Prod.* (2018) 50:1193–202. doi: 10.1007/s11250-018-1629-0
13. Szenczióvá I, Strapák P. Ultrasonography of the udder and teat in cattle: perspective measuring technique. *Slovak J Animal Sci.* (2012) 45:96–104. Available online at: http://www.vuzv.sk/slju/12-3/5-Szencziova-SJAS-3-2012review.pdf
14. Kotb EE, Abu-Seida AM, Fadel MS. The correlation between ultrasonographic and laboratory findings of mastitis in buffaloes (*Bubalus bubalis*). *Global Vet.* (2014) 13:68–74. doi: 10.5829/idosi.gv.2014.13.01.84171
15. Mantziaras G, Vasileiou NG, Ioannidi KS, Mavrogianni VS, Gougoulis DA, Fthenakis GC, et al. Use of contrast-enhanced ultrasonographic examination to evaluate health status of mammary glands of ewes at the end of a lactation period. *J Dairy Res.* (2018) 85:39–43. doi: 10.1017/S002202991800002X
16. Bonelli F, Orsetti C, Turini L, Meucci V, Pierattini A, Sgorbini M, et al. Mammary cistern size during the dry period in healthy dairy cows: a preliminary study for an ultrasonographic evaluation. *Animals.* (2020) 10:2082. doi: 10.3390/ani10112082
17. Barbagianni M, Mavrogianni V, Vasileiou N, Fthenakis G, Petridis I. Ultrasonographic examination of the udder in sheep. *Small Ruminant Res.* (2017) 152:86–99. doi: 10.1016/j.smallrumres.2016.12.009
18. Fasulkov I, Karadaev M, Vasilev N, Simeonov R, Urumova V, Mladenova E. Ultrasound and histopathological investigations of experimentally induced *Staphylococcus aureus* mastitis in goats. *Small Ruminant Res.* (2015) 129:114–20. doi: 10.1016/j.smallrumres.2015.05.018
19. Khoramian B, Vajhi A, Ghasemzadeh-Nava H, Ahrari-Khafi M, Bahonar A. Ultrasonography of the supramammary lymph nodes for diagnosis of bovine chronic subclinical mastitis. *Iran J Vet Res.* (2015) 16:75. doi: 10.22099/IJVR.2015.2928
20. Risvanli A, Dogan H, Safak T, Kilic MA, Seker I. The relationship between mastitis and the B-mode, colour Doppler ultrasonography measurements of supramammary lymph nodes in cows. *J Dairy Res.* (2019) 86:315–8. doi: 10.1017/S0022029919000530

21. Murawski M, Schwarz T, Jamieson M, Ahmadi B, Bartlewski PM. Echotextural characteristics of the mammary gland during early lactation in two breeds of sheep varying in milk yields. *Anim Reprod.* (2019) 16:853–8. doi: 10.21451/1984-3143-AR2019-0025
22. Wang Y-M, Fan W, Zhang K, Zhang L, Tan Z, Ma R. Comparison of transducers with different frequencies in breast contrast-enhanced ultrasound (CEUS) using SonoVue as contrast agent. *Br J Radiol.* (2016) 89:20151050. doi: 10.1259/bjr.20151050
23. Fasulkov I. Ultrasonography of the mammary gland in ruminants: a review. *Bulgarian J Vet Med.* (2012) 15:1–12. Available online at: http://tru.uni-sz.bg/bjvm/BJVM-March%202012%20p.01-12.pdf
24. Ahmadi B, Mirshahi A, Giffin J, Oliveira M, Gao L, Hahnel A, et al. Preliminary assessment of the quantitative relationships between testicular tissue composition and ultrasonographic image attributes in the ram. *Vet J.* (2013) 198:282–5. doi: 10.1016/j.tvjl.2013.06.001
25. Santos V, Simplício K, Sanchez D, Coutinho L, Teixeira P, Barros F, et al. B-mode and doppler sonography of the mammary glands in dairy goats for mastitis diagnosis. *Reprod Domest Anim.* (2015) 50:251–5. doi: 10.1111/rda.12479
26. Gall CA, Reif KE, Scoles GA, Mason KL, Mousel M, Noh SM, Brayton KA. The bacterial microbiome of Dermacentor andersoni ticks influences pathogen susceptibility. *The ISME Journal*. (2016) 10:1846–55. doi: 10.1038/ismej.2015.266
27. Melvin J, Heuwieser W, Virkler P, Nydam D, Wieland M. Machine milking–induced changes in teat canal dimensions as assessed by ultrasonography. *J Dairy Sci.* (2019) 102:2657–69. doi: 10.3168/jds.2018-14968
28. Bogaert H, De Koster J, Van Den Broeck W, Van Eetvelde M, Opsomer G. Effects of overconditioning on pancreatic insulin secretory capacity, fat infiltration, and the number and size of islets in dairy cows at the end of the dry period. *J Dairy Sci.* (2018) 101:11413–20. doi: 10.3168/jds.2018-14931
29. Wen R, Dong J, Wang Y, Wang L. Combination of color Doppler ultrasound and CT for diagnosing breast cancer. *Am J Transl Res.* (2021) 13:10771.
30. Fragkou I, Boscos C, Fthenakis G. Diagnosis of clinical or subclinical mastitis in ewes. *Small Rumin Res.* (2014) 118:86–92. doi: 10.1016/j.smallrumres.2013.12.015
31. Abu-Seida AM. Current status and prospect of ultrasonographic application in buffaloes. *Asian J Anim Vet Adv.* (2016) 11:144–57. doi: 10.3923/ajava.2016.144.157
32. Kotb E, El-Fattah A, Ola A, Azab AM, Leil AZ. Ultrasonography, histopathological udder alterations and bacteriological investigations for diagnosis of mastitic goats. *J Appl Vet Sci.* (2020) 5:77–86. doi: 10.21608/javs.2020.85593
33. Pozor M, Morrissey H, Albanese V, Khouzam N, Deriberprey A, Macpherson ML, et al. Relationship between echotextural and histomorphometric characteristics of stallion testes. *Theriogenology.* (2017) 99:134–45. doi: 10.1016/j.theriogenology.2017.05.031
34. De Souza Cunha DM, De Souza MB, Brito BF, Torres VL, Nunes TGP, Tavares SS, et al. Testicular morphological and ultrasonographic characterization of male gray brocket deers (*Mazama gouazoubira*) in different reproductive status. *Acta Scientiae Veterinariae.* (2019) 47:1712. doi: 10.22456/1679-9216.98311
35. Schukken YH, Wilson DJ, Welcome F, Garrison-Tikofsky L, Gonzalez RN. Monitoring udder health and milk quality using somatic cell counts. *Vet Res.* (2003) 34:579–96. doi: 10.1051/vetres:2003028
36. Rambabu K, Sreenu M, Kumar RS, Rao T. Ultrasonography of the udder and teat in buffaloes. *Buffalo Bull.* (2009) 28:5–10. Available online at: https://www.researchgate.net/publication/283112723_Ultrasonography_of_the_udder_and_teat_in_buffaloes
37. Flöck M, Winter P. Diagnostic ultrasonography in cattle with diseases of the mammary gland. *Vet J.* (2006) 171:314–21. doi: 10.1016/j.tvjl.2004.11.002
38. Franz S, Floek M, Hofmann-Parisot M. Ultrasonography of the bovine udder and teat. *Vet Clin North Am Food Anim Pract.* (2009) 25:669–85. doi: 10.1016/j.cvfa.2009.07.007
39. Fasulkov I, Georgiev P, Antonov A, Atanasov A. B-mode ultrasonography of mammary glands in goats during the lactation period. *Bulgarian J Vet Med.* (2010) 13:245–51. Available online at: https://www.researchgate.net/publication/272684140_B-MODE_ULTRASONOGRAPHY_OF_MAMMARY_GLANDS_IN_GOATS_DURING_THE_LACTATION_PERIOD
40. Schwarz T, Scheeres N, Małopolska MM, Murawski M, Agustin TD, Ahmadi B, et al. Associations between mammary gland echotexture and milk composition in cows. *Animals.* (2020) 10:2005. doi: 10.3390/ani10112005
41. Riekerink RO, Barkema H, Stryhn H. The effect of season on somatic cell count and the incidence of clinical mastitis. *J Dairy Sci.* (2007) 90:1704–15. doi: 10.3168/jds.2006-567
42. Morse D, Delorenzo M, Wilcox C, Collier RJ, Natzke R, Bray D. Climatic effects on occurrence of clinical mastitis. *J Dairy Sci.* (1988) 71:848–53. doi: 10.3168/jds.S0022-0302(88)79626-5
43. Hossein-Zadeh NG, Ardalan M. Cow-specific risk factors for retained placenta, metritis and clinical mastitis in Holstein cows. *Vet Res Commun.* (2011) 35:345–54. doi: 10.1007/s11259-011-9479-5
44. Barkema H, Schukken Y, Lam T, Galligan D, Beiboer M, Brand A. Estimation of interdependence among quarters of the bovine udder with subclinical mastitis and implications for analysis. *J Dairy Sci.* (1997) 80:1592–9. doi: 10.3168/jds.S0022-0302(97)76089-2
45. Hammer J, Morton J, Kerrisk K. Quarter-milking-, quarter-, udder-and lactation-level risk factors and indicators for clinical mastitis during lactation in pasture-fed dairy cows managed in an automatic milking system. *Aust Vet J.* (2012) 90:167–74. doi: 10.1111/j.1751-0813.2012.00917.x
46. Ali S, Hussain MA, Babar A, Rahim N. *A Study on The Prevalence and Associated Microorganisms of Subclinical Mastitis in Buffaloes at Swat, Khyber Pakhtunkhwa* (2020).
47. Hadrich J, Wolf C, Lombard J, Dolak T. Estimating milk yield and value losses from increased somatic cell count on US dairy farms. *J Dairy Sci.* (2018) 101:3588–96. doi: 10.3168/jds.2017-13840
48. Costa A, Neglia G, Campanile G, De Marchi M. Milk somatic cell count and its relationship with milk yield and quality traits in Italian water buffaloes. *J Dairy Sci.* (2020) 103:5485–94. doi: 10.3168/jds.2019-18009
49. Solanki P, Gupta VK. Manufacture of low lactose concentrated ultrafiltered-diafiltered retentate from buffalo milk and skim milk. *J Food Sci Technol.* (2014) 51:396–400. doi: 10.1007/s13197-013-1142-4

Conflict of Interest: The authors declare that the research was conducted in the absence of any commercial or financial relationships that could be construed as a potential conflict of interest.

Publisher's Note: All claims expressed in this article are solely those of the authors and do not necessarily represent those of their affiliated organizations, or those of the publisher, the editors and the reviewers. Any product that may be evaluated in this article, or claim that may be made by its manufacturer, is not guaranteed or endorsed by the publisher.

frontiers | Frontiers in Veterinary Science

ORIGINAL RESEARCH
published: 06 April 2022
doi: 10.3389/fvets.2022.860771

Exogenous L-carnitine Administration Ameliorates the Adverse Effects of Heat Stress on Testicular Hemodynamics, Echotexture, and Total Antioxidant Capacity in Rams

*Hossam R. El-Sherbiny, Amr S. El-Shalofy and Haney Samir**

Theriogenology Department, Faculty of Veterinary Medicine, Cairo University, Giza, Egypt

OPEN ACCESS

Edited by:
Valeria Pasciu,
University of Sassari, Italy

Reviewed by:
Ignacio Contreras Solís,
University of Sassari, Italy
Guilherme Rizzoto,
Ghent University, Belgium
Ricardo Costa,
Instituto de Zootecnia (IZ), Brazil

***Correspondence:**
Haney Samir
Haneyvet360@yahoo.com;
Haneysamir600@yahoo.com;
Haneyvet360@cu.edu.eg

Specialty section:
This article was submitted to Veterinary Imaging, a section of the journal Frontiers in Veterinary Science

Received: *23 January 2022*
Accepted: *03 March 2022*
Published: *06 April 2022*

Citation:
El-Sherbiny HR, El-Shalofy AS and Samir H (2022) Exogenous L-carnitine Administration Ameliorates the Adverse Effects of Heat Stress on Testicular Hemodynamics, Echotexture, and Total Antioxidant Capacity in Rams. Front. Vet. Sci. 9:860771. doi: 10.3389/fvets.2022.860771

Heat stress (HS) diminishes the testicular antioxidant defense systems, which adversely affect the testicular blood perfusion. Improving the testicular hemodynamics during HS conditions is of a great impact on the whole reproductive performance in rams. This study aimed to evaluate the ameliorative effects of L-carnitine (LC) on the testicular blood flow and echotextures and also on the total antioxidants (TAC) and nitric oxide (NO) concentrations in the serum during HS conditions in rams. Testicular blood flow was evaluated through scanning of the supra-testicular artery (STA) spectral patterns through pulsed Doppler ultrasonography [peak systolic velocity (PSV), end-diastolic velocity (EDV), time average maximum velocity (TAMAX), resistive index (RI), and pulsatility index (PI)], while the echotexture assessment of testicular parenchyma was performed by a computerized software program. Moreover, TAC and NO concentrations were assayed colorimetrically using the spectrophotometer. There were significant decreases ($P < 0.05$) in values of PSV at 48 and 168 h (23.45 ± 0.39 and 23.37 ± 1.41 cm/s, respectively), and TAMAX at 1, 48, and 168 h (17.65 ± 0.95, 17.5 ± 0.13, and 16.9 ± 1.05 cm/s, respectively) after LC administration compared to just before administration (31.92 ± 1.13 and 21.58 ± 0.92 cm/s, respectively). Values of RI and PI of the examined STA significantly decreased, especially at 1 h for RI (0.45 ± 0.02) and 1 and 48 h for PI (0.66 ± 0.06 and 0.65 ± 0.05, respectively) after LC treatment to 0 h (0.55 ± 0.03 and 0.84 ± 0.06, respectively). The EDV values did not show any significant ($P < 0.05$) changes in all the experimental time points. There were significant ($P < 0.05$) increases in the values of pixel intensity of the testicular parenchyma, especially at 1 and 168 h (78.71 ± 2.50 and 88.56 ± 4.10, respectively) after LC administration, compared to just before administration (69.40 ± 4.75). Serum NO levels tend to increase after LC administration ($P = 0.07$) concerning just before administration. While TAC values showed significant gradual increase and reached the highest values at 168 h (2.75 ± 0.58 mM/l) after

LC administration, compared to 0 h (1.12 ± 0.05 mM/l). In conclusion, exogenous LC administration ameliorates testicular hemodynamic disruptions, as measured by spectral Doppler ultrasonography, *via* augmentation of the rams' total antioxidant capacity under HS conditions.

Keywords: Doppler ultrasonography, heat stress, L-carnitine, nitric oxide, rams, total antioxidant capacity

INTRODUCTION

Global warming is one of the most common topics in the world public opinion these days, with many adverse environmental consequences, especially in the field of animal reproduction competence. Environmental thermal stress (TS) triggers oxidative stress (OS) cascade and deteriorates semen quality and fertilizing potential in rams (1, 2), Holstein bulls (3), Shiba goats (4), rabbit bucks (5), and buffalo bulls (6). In rams, elevated testicular temperature induces OS, which in turn diminishes both sperm motility and viability and increases total sperm abnormalities (7). Thermal stress initiates increases in antioxidant defense systems (8) followed by its decline in long-lasting TS *via* decrement of the mRNA expression of the mitochondrial superoxide dismutase (SOD)-1 with a subsequent decrease in SOD protein synthesis and activity, and more generation of superoxide anion (SOA) and cell apoptosis (9).

The positive association between arterial blood flow of the testes and its exocrine (sperm) and endocrine (testosterone hormone) functions has been reported in rams (10, 11), goat bucks (12), donkeys (13), and stud dogs (14). The main route through which testis could be enriched with oxygen and nutrients supply is the testicular artery (TA). Therefore, any alteration in the testicular blood perfusion affects both spermatogenesis and steroidogenesis, with subsequent loss of fertility (15, 16). Spectral Doppler ultrasound is a non-invasive reliable method for an organ function assessment *via* its blood flow measurement (13, 17). The use of testicular blood flow measurement as a potential predictor for male fertility has been applied in many species (14, 18, 19). Resistant index (RI), pulse index (PI), peak systolic velocity (PSV), end-diastolic velocity (EDV), and time-averaged maximum velocity (TAMAX) are the most commonly used parameters for providing a clear judgment on the organ hemodynamics (20).

Digital analysis of the testicular tissue B-mode ultrasound image [testicular echotexture (TE)] has become a useful tool for evaluating the male reproductive functions in different animal species (4, 21). The pixel matrix of the ultrasound image has a score from 0 to 255, with 0 assessed as black color, and 255 corresponds to white color with varying gray color in-between (21). Testicular histology (22), blood flow (4), and sperm-quality parameters (21) governed the degree of TE.

Decreased testicular blood perfusion in heat-stress conditions was reported in rams (10, 11) and goat buck (23). Several attempts have been reported to improve the testicular hemodynamics by administering exogenous treatments in rams and goat bucks with potential outcomes, that finally reflected on the whole male fertility, such as melatonin, gonadotropin-releasing hormone (GnRH), and luteinizing hormone (LH) (12, 19, 24, 25). L-carnitine (LC) is a vitamin-like bioenergetic amino acid that exists ubiquitously in different tissue types, such as heart, skeletal muscle, testes, and epididymis. LC has a substantial role in cell energy production *via* fatty acids (long-chain) transport through mitochondrial membranes and subsequent ATP synthesis *via* the β-oxidation process. Moreover, LC clears the mitochondrial matrix from the accumulated toxic acyl-CoA. L-carnitine protects the cell against OS *via* its antioxidative properties through free radicals (SOA, hydrogen peroxide) capturing and lipid peroxidation inhibition (26–28). Many studies have declared that LC enhances male fertility *via* improving reproductive hormones (29, 30), semen quality (28), antioxidant capacity (28, 31), and gene (GnRH and melatonin) modulation (28, 32, 33). Therefore, the authors postulated that LC administration to heat-stressed rams could alleviate the heat-stress-mediated testicular hemodynamics impairment and improve testicular functions. To the maximum of the authors' knowledge, studying the effect of LC on the rams' testicular hemodynamics in rams housed under heat-stress conditions has not been elucidated. Therefore, this study was aimed, for the first time, to investigate the effects of LC administration on testicular hemodynamics (RI, PI, EDV, PSV, and TAMAX), TE, serum nitric oxide, and total antioxidant concentrations in heat-stressed Ossimi rams.

MATERIALS AND METHODS

The experimental procedures of this study were carried out in the summer season (June–August 2021) at the farm of the Theriogenology Department, Faculty of Veterinary Medicine, Cairo University, Giza Governorate, Egypt (30.0276°N, 31.2101°E), following the accreditation of the ethical committee for animal use.

Animals and Care

Fifteen adult Ossimi rams (55.35 ± 3.5 kg body weight) and aged 3.5 ± 0.16 years, were used in this study. The inclusion criteria were adjusted based on the clinical, cardiovascular, and andrological fitness, based on physical and ultrasound examination. Rams that showed normal heartbeats, pulse rate, capillary refilling time, rectal temperature, and absence of hyperechogenic masses in the testicular ultrasonograms were favored the inclusion criteria. Therefore, only 15 rams were selected, for experimental procedures, out of 23 rams that were submitted to the above-mentioned examinations. Rams' housing was in the open air in a paddock belonging to

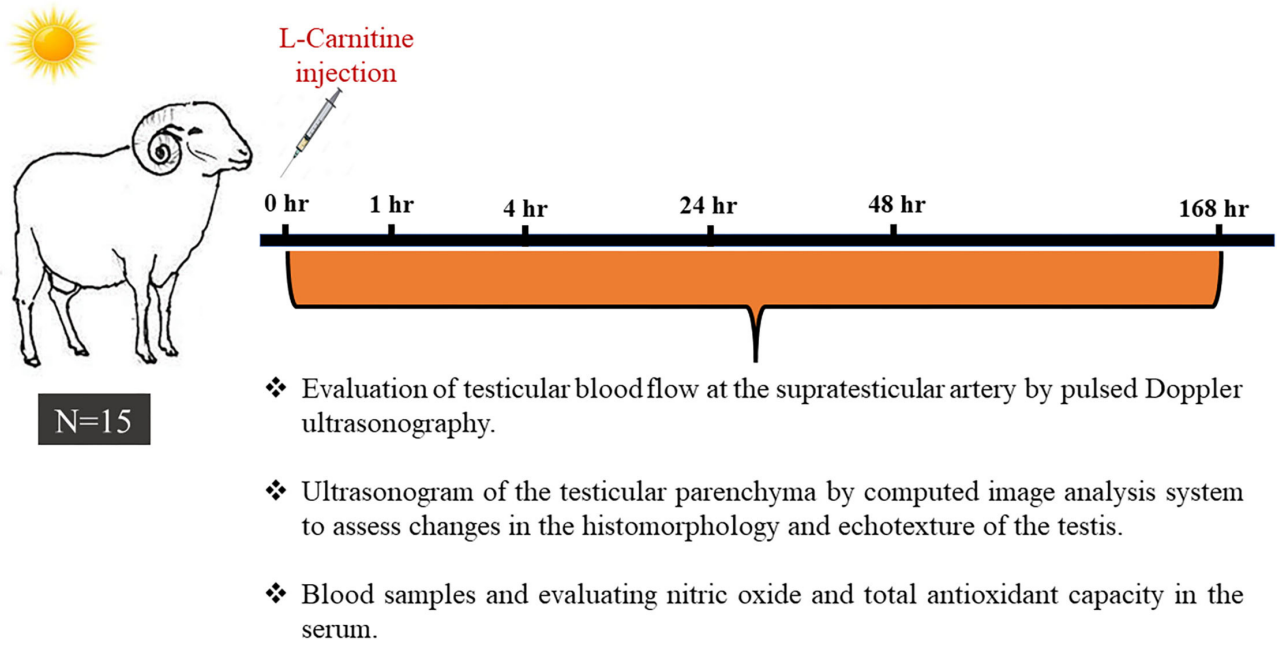

FIGURE 1 | A schematic diagram shows the experimental design, in which fifteen Ossimi rams exposed to environmental heat stress (temperature-humidity index = 32.5) were administered L-carnitine (LC; 20 mg/kg BW; IV) and underwent ultrasound examination and blood sampling just before L-carnitine administration (0 h) and 1, 4, 24, 48, and 168 h post-LC administration.

our department, subjected to normal environmental light, temperature, and humidity. The feeding regime was a mixed formula of concentrate pellets (14% crude protein and energy requirements of 6.39 MJ/kg diet) and green feed with *ad libitum* availability of fresh tape water. They were examined regularly during the experimentation with prophylactic vaccination and deworming programs against endemic diseases in Egypt.

Rams' Heat-Stress Assessment

The temperature (T) and relative humidity (RH) at each time point during the study were over 36°C and 60%, respectively, according to the Egyptian meteorological authority (Cairo, Egypt). The temperature-humidity index (THI) was calculated [THI = T – (0.31 – 0.31 RH) (T – 14.4)] following a previous study that described the relationship between sheep heat-stress and meteorological conditions (34). Based on the study mentioned later, the rams used in this study were subjected to severe environmental heat stress (THI $\geq$ 32.5).

Experimental Protocol

As explained in **Figure 1**, heat-stressed rams (n = 15) were examined sonographically either by spectral Doppler for the supra-testicular artery of the right and left testis and B-mode scanning of the testicular parenchyma or blood sampling just before (0 h) treatment with LC. Each ram was treated with a single intravenous (jugular vein) injection of LC [20 mg/kg body weight; Mepaco Corporation, Egypt; (35)] and examined at 1, 4, 24, 48, and 168 h after LC administration. The examination time points were selected based on the LC pharmacokinetics, especially the clearance time (36). All the experimental procedures, namely, testicular hemodynamic measurements and echotextures, nitric oxide assessment, and total antioxidant capacity assay, were repeated three times 2 weeks intervals during the same heat-stress conditions.

Obtaining Blood Samples and Biochemical Analysis

Blood samples (5 ml) were obtained from each ram through jugular venipuncture into plain tubes, just before ultrasonographic assessments at each time point. After centrifugation (15 min) of the drawn blood samples at 1,207 g, the serum samples were harvested and stored (−20°C) till further measurements of nitric oxide metabolites (NOMs) and total antioxidant (TAC) concentrations.

Concentrations of NOMs were measured using commercial kits (nitric oxide kit, Bio-diagnostic, Dokki, Egypt) using a spectrophotometer at 540 nm wavelength. The NOMs inter- and intra-assay coefficient variations were 6.9 and 5.3%, respectively, with assay sensitivity of 0.225 μmol/l in nitrites form (37).

Assessment of TAC was done using commercial kits (total antioxidant capacity, Bio-diagnostic, Dokki, Egypt) spectrophotometrically at a wavelength of 505 nm, based on a previous study (38). The assay rationale is the measurement of the suppressive ability of the sample on sodium benzoate conversion to thiobarbituric acid substances *via* reactive oxygen species (ROS) generated from Fenton's reaction (39).

Ultrasound Examination

During all the studied time points, sonographic measurements including pulsed-wave Doppler of the right and left

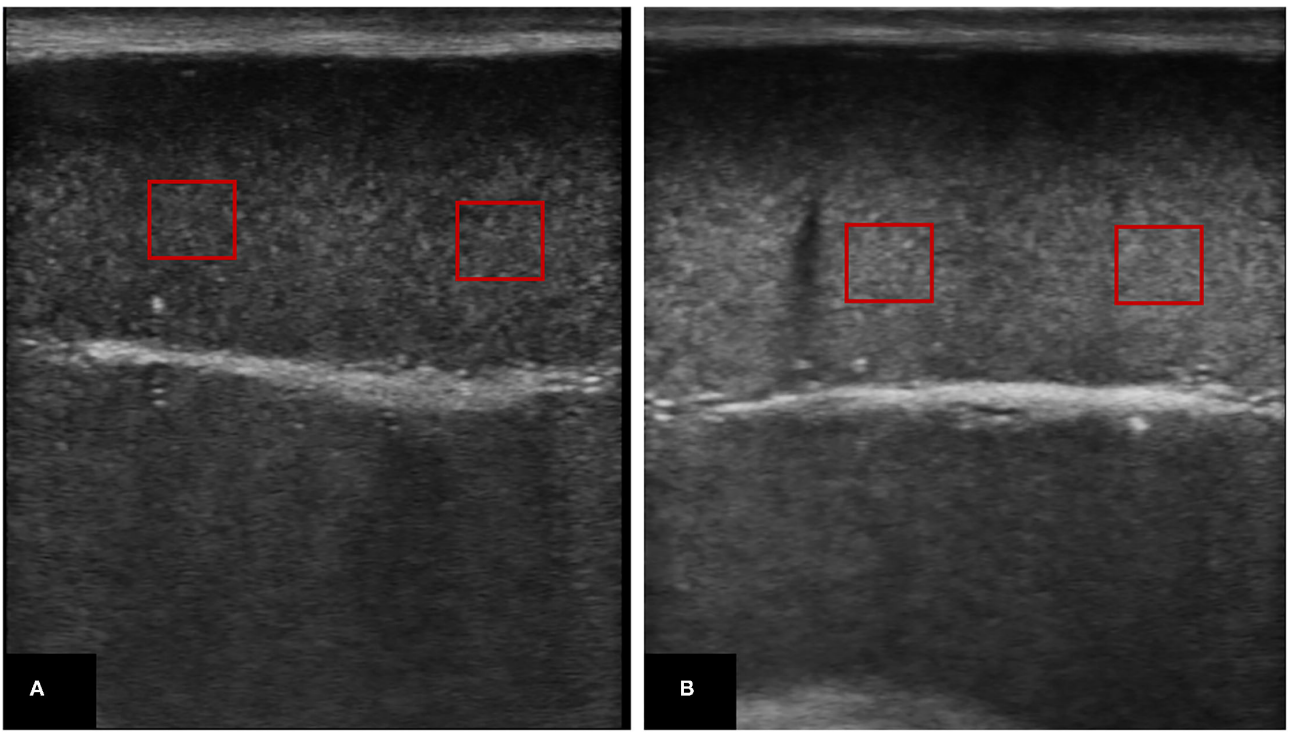

FIGURE 2 | Ultrasonograms of the testicular parenchyma in which echotextures were assessed by placing at least 3 squares (1 cm × 1 cm) and underwent computed digital analysis (Adobe Photoshop 64 CC software); **(A)** represents testicular parenchyma with low echotexture, whereas **(B)** represents higher echotexture.

supratesticular arteries (STAs) and TE were carried out by the same investigator. An ultrasound device (SonoScape E1V, SonoScape Medical Corp., China) supplied with a 7–14 MHz linear array probe was used for all ultrasonographic measurements. Following a previous study (23), the animals were restrained properly without any sedative agents administration, and the scrotal wool was shaved totally on both sides of each testis till the spermatic cord, and the transducer was loaded with a large amount of ultrasound gel for obtaining clear images for the testes and STA. Just before the testicular inlet, the rams' STA appeared tortuous and convoluted meshed with testicular veins. The instant spectral pattern of the STA (systole and diastole) governed the vessel's discrimination. After a clear view of the STA waveform, pulsed-wave Doppler was used for measurements of the following parameters: (1) PSV (cm/s); (2) EDV (cm/s); and (3) TAMAX (cm/s). From the later-mentioned Doppler parameters, both RI (RI = PSV – EDV/PSV) and PI (PI = PSV – EDV/average velocity) were calculated. All the device settings (brightness, focus, contrast, and gain) were adjusted and fixed throughout the study by the same investigator. The angle between the targeted vessel longitudinal axis and the Doppler beam was $\leq 60^{\circ}$ with 0.5 mm Doppler gate diameter and 50 MHz high-pass filters.

For TE assessment (22), a clear image, without artifacts, of the longitudinal and transverse aspects of both testes was frozen and saved for further digital computed analysis. The saved images were recalled and examined for testicular echogenicity (TE; the average number of pixels) and pixel heterogeneity (PH; the standard deviation of the pixels) utilizing image analysis software (Adobe Photoshop 64 CC software; Adobe Systems, 2016), by adjusting a 1 cm × 1 cm square in the testicular parenchyma (in 3 different areas) concerning the central positioning of the mediastinum testis (the most hyperechoic part of the testis) (**Figure 2**).

Statistical Analysis

The obtained data concerning the testicular hemodynamics (PSV, EDV, RI, PI, and TAMAX), TE and PH, and biochemical analysis (NOMs and TAC) are presented as means ± SEM. The normality and homogeneity of the results were tested using the Kolmogorov–Smirnov test and chi-squared test, respectively. The differences between rams regarding the right and left testes were nonsignificant; therefore, the obtained results were pooled, and the comparisons were done between the different studied time points. Repeated measures ANOVA test was used for discrimination of the differences among the means in the studied time points, and finally with Bonferroni *post hoc* test. GraphPad Prism5 software was used for all the studied statistical assessments. $P < 0.05$ was considered as statistically significant.

RESULTS

Effects of LC Administration on Blood Flow Hemodynamic Patterns

The temporal changes in testicular blood flow patterns of the STA of heat-stressed rams administered LC in this study are

TABLE 1 | Means ± SEM of the Doppler ultrasound measures of the supra-testicular arteries at the studied time points: just before LC treatment (0 h) and 1, 4, 24, 48, and 168 h post-treatment in Ossimi rams ($n = 15$).

Parameters	0 h	1 h	4 h	24 h	48 h	168 h
PSV (cm/s)	31.92 ± 1.13	24.95 ± 1.85	35.49 ± 2.61	29.61 ± 2.36	23.45 ± 0.39*	23.37 ± 1.41*
EDV (cm/s)	14.49 ± 0.88	13.80 ± 1.28	16.36 ± 0.74	14.36 ± 1.06	12.23 ± 0.49	11.18 ± 0.84
RI	0.55 ± 0.03	0.45 ± 0.02*	0.49 ± 0.05	0.47 ± 0.06	0.47 ± 0.03	0.52 ± 0.02
PI	0.84 ± 0.06	0.66 ± 0.06*	0.77 ± 0.12	0.74 ± 0.12	0.65 ± 0.05*	0.73 ± 0.04
TAMAX (cm/s)	21.58 ± 0.92	17.65 ± 0.95*	23.4 ± 0.59	20.23 ± 0.92	17.5 ± 0.13*	16.9 ± 1.05*

PSV, peak systolic velocity; EDV, end-diastolic velocity; RI, resistive index; PI, Pulsatility index; TAMAX, time average maximum velocity; LC, L-carnitine.
**Within the same row indicates a significant difference ($P < 0.05$).*

TABLE 2 | Means ± SEM of the pixel number and its standard deviation (testicular echogenicity and pixel heterogeneity) of the testicular parenchyma ultrasound B-mode images as analyzed using Photoshop program at the studied time points: just before LC treatment (0 h) and 1, 4, 24, 48 and 168 h post-treatment in Ossimi rams ($n = 15$).

Parameters	0 h	1 h	4 h	24 h	48 h	168 h
TE	69.40 ± 4.75	78.71 ± 2.50*	64.49 ± 2.44	65.42 ± 2.53	69.52 ± 3.91	88.56 ± 4.10*
PH	10.46 ± 0.48	9.32 ± 0.29	11.5 ± 0.53	11.2 ± 0.48	11.95 ± 0.64	11.34 ± 0.22

TE, testicular echogenicity; PH, pixel heterogeneity; LC, L-carnitine.
**Within the same row indicates a significant difference ($P < 0.05$).*

TABLE 3 | Effects of LC administration on serum NO and TAC concentrations of the heat-stressed rams at 1, 4, 24, 48, and 168 h after treatment vs. 0 h.

Parameters	0 h	1 h	4 h	24 h	48 h	168 h	*P*-value
NO (umol/L)	44.93 ± 1.57	53.09 ± 2.33	51.16 ± 3.23	54.94 ± 3.94	49.06 ± 4.99	52.89 ± 4.23	$P > 0.05$
TAC (mM/L)	1.12 ± 0.05	1.81 ± 0.22*	1.87 ± 0.06*	1.64 ± 0.25*	1.80 ± 0.13*	2.75 ± 0.58*	$P < 0.05$

NO, nitric oxide; TAC, total antioxidant capacity; LC, L-carnitine.
**Within the same row indicates a significant difference ($P < 0.05$).*

shown in **Table 1**. There were significant decreases ($P < 0.05$) in values of PSV at 48 and 168 h (23.45 ± 0.39 and 23.37 ± 1.41 cm/s, respectively) and TAMAX at 1, 48, and 168 h (17.65 ± 0.95, 17.5 ± 0.13, and 16.9 ± 1.05 cm/s, respectively) after LC administration compared to just before administration (31.92 ± 1.13 and 21.58 ± 0.92 cm/s, respectively). Regarding the LC administration effects on RI and PI values of the examined STA, there were significant ($P < 0.05$) decreases, especially at 1 h for RI (0.45 ± 0.02) and at 1 h (0.66 ± 0.06) and 48 h (0.65 ± 0.05) for PI after LC treatment compared to 0 h (RI: 0.55 ± 0.03, PI: 0.84 ± 0.06), whereas, the EDV values did not show any significant ($P < 0.05$) change in all the experimental time points.

Effects of LC Administration on Testicular Echogenic Properties

The changes in echogenicity of the testicular parenchyma after LC treatment concerning the studied time points in this study are given in **Table 2**. There were significant ($P < 0.05$) increases in the values of pixel intensity of the testicular parenchyma, especially at 1 and 168 h after LC administration (78.71 ± 2.50 and 88.56 ± 4.10, respectively), compared to just before administration (69.40 ± 4.75). While the PH of the testicular tissue did not exhibit any significant ($P < 0.05$) changes throughout the study time points.

Effect of LC Administration on Total Antioxidant Capacity and Nitric Oxide Concentrations

The serum total antioxidant capacity and nitric oxide levels in heat-stressed rams administered LC in this work are shown in **Table 3**. The NO levels in the rams' serum tended to increase ($P = 0.07$) after administration of LC compared to just before administration. Whereas the total antioxidant capacity showed significant ($P < 0.05$) gradual increases and reached the highest values at 168 h (2.75 ± 0.58 mM/l) after LC administration, compared to 0 h (1.12 ± 0.05 mM/l).

DISCUSSION

Male reproductive potential under HS conditions faces several obstacles, namely, sperm production decrement, OS, cellular apoptosis, steroidogenesis deficit, testicular hemodynamic disruption, and fertility decline (40). Several trials have been adopted to overcome the negative impact of heat stress in different species by using antioxidants (41–44). L-carnitine, a natural antioxidant, was used extensively in the perspective of cellular bioenergetics, glucose uptake, steroidogenesis, and antiapoptosis under different environmental conditions in different species (26, 29, 30, 35); however and interestingly, this

study is the first, according to the best of the authors' update, to use LC for alleviation the adverse effects of heat stress on testicular blood flow (TBF), TE, nitric oxide (NO), and total antioxidants (TAC) concentrations in Ossimi rams. This study showed that treatment of heat-stressed Ossimi rams with LC exerted a significant improvement in testicular blood perfusion. Interpretation of testicular blood flow enhancement is based on RI, PI, PSV, and TAMAX decreases, which explain the elevation of arterial blood perfusion and decrease of the vessel resistance to blood flow. These changes warrant higher testicular blood perfusion (45, 46). The way how LC improved TBF was not certainly clarified in this work; however, many pathways can describe these actions. First, LC may improve TBF through its cardioprotective effect on the myocardium, *via* the promotion of pyruvate oxidation, even at ischemic injury conditions, and helps the heart to recover properly, which affects directly the testicular irrigation with blood (47, 48). Moreover, LC protects the cardiac function through its antiapoptotic properties of the vascular endothelium, evidenced by upregulation of Bcl2 (antiapoptotic) and downregulation of BAX (apoptotic) genes and insulin-like growth factor-1 (49). It would be quite interesting to investigate different parameters of the cardiac and vascular performance regarding the possible testicular blood modulations induced by LC administration in further studies. Healthy vascular endothelial cells produce optimum nitric oxide (potent vasodilator) concentrations resulting in higher blood flow to the reproductive tract (47). Also, LC has a direct effect on NO production in the pulmonary endothelial cells *via* the carnitine acetyltransferase enzyme (50). In addition, LC deficiency induces mitochondrial dysfunction, lessens ATP production and vascular NO synthesis (51). Surprisingly, the differences in NO concentrations between the studied time points in this study were nonsignificant but tended to increase ($P = 0.07$). Earlier studies in men indicated that administration of LC either through oral or parenteral routes provoked NO bioavailability (52, 53). This discrepancy might be due to the differences in the dose (around 1 g/ram), frequency (single dose), and route of administration (IV) of LC treatment in this study compared to the aforementioned reports. The selected dose might be insufficient to elevate the NO concentration, as 1 g of LC may be enough for exerting antioxidant capacity and protecting the cellular components against lipid peroxidation (53), as proposed by the obtained results; whereas, for the elevation of NO, LC should be administered at a dose of at least 3 g daily (52). Second, the role of LC in mitochondrial functions should be considered, through fatty acid transfer, energy production, and removal of excess acyl-CoA, promoting optimum cellular functions in the whole body organs including heart and testes (26, 42, 48). Third, LC as a potent antioxidant protects the testicular cells from the free radicals (SOA and hydroxyl radicals) attacks by capturing them (26), these radicals stimulate the nitric oxide conversion to peroxynitrite (54), thus decreasing its bioavailability which, in turn, lead to decrease TBF. Fourth, LC may affect hypothalamic functions, manifested by elevated blood FSH and LH concentrations which, in turn, modulate testicular hemodynamics and functions (29, 32).

In Ossimi rams, decreased testicular blood flow was reported in the summer season (10). However, there were recent studies indicating a marked increase in testicular blood flow to compensate for increased testicular metabolism under HS conditions (55–57). Indeed, heat stress induces increases in testicular blood perfusion if the heat stress is locally induced on the testes directly (55, 57). However, in our experiment, the rams were exposed to thermal environmental conditions for about 3–4 weeks before the onset of the experiment (summer season). Second, our results may not be consistent with the findings in the above-mentioned literature, as these changes are dependent on whether the testicular temperature exceeded the core body temperature or not. In this study, rams were exposed to ambient temperature (>36°C) and relative humidity (>60%) with temperature-humidity index (32.5) that their effect might be generalized on different body systems. Moreover, the difference in rams' breed adaptability to the thermal conditions may be another factor that should be considered.

Studying the testicular echogenicity provides a complementary noninvasive testicular function evaluation through pixel intensity calculation (21). In this study, there was a significant change in TEs; these changes might be due to increased testicular perfusion with blood. Moreover, the relation between the testicular echogenic and hemodynamic changes has been reported (25) and changes in TE affect the testicular functions (10, 21, 23). Explanation of increases in TE observed at 1 h might be attributed to the higher vascular irrigation. A recent study proposed that higher cellular condensation and vascular irrigation are correlated with higher echogenic changes of the testicular parenchyma of rams, and *vice versa* (58). At 168 h, increases in TE might be attributed to the improvement of total antioxidant capacity compared to 0 h with subsequent amelioration of the OS status that may enhance the functionality of the cellular matrix of the testis including Sertoli, Leydig, and the spermatogenic cells (59).

Heat-stressed rams treated with LC, in this study, experienced significant ($P < 0.05$) higher concentrations of plasma TAC. These findings are in line with many studies conducted in different animal species (26, 53, 60). The improvement in reproductive antioxidant defense systems may be due to the increase in reduced glutathione concentration and activities of glutathione peroxidase, catalase, and SOD enzymes (28, 61, 62), which protect the reproductive organs' defense systems against ROS attacks.

The authors thought that comparing the studied parameters before and after administration of LC is appropriate to test the effects of LC on the same individual of rams (to avoid individual variations). Moreover, to validate the results, the experimental procedures were repeated three times at a 2-week interval in the same conditions. However, the inclusion of the control group in the experimental protocol and examination of a big number of rams may be important to be conducted in a further study. In addition, clarification of the effects of different doses, protocols, routes, and forms of LC on testicular functionality, semen quality, and molecular basics of how LC affects TBF in rams in adverse conditions are valuable to be conducted.

CONCLUSION

A single intravenous administration of LC improves testicular hemodynamics (by lessening RI and PI of supra-testicular arteries) and TEs and was followed by an increase in total antioxidants concentrations in Ossimi rams during the heat-stress conditions. However, further studies are needed to be conducted to clarify the effects of different doses, protocols, routes, and forms of LC on testicular functionality, semen quality, and molecular basics of how LC affects TBF in rams in adverse conditions.

DATA AVAILABILITY STATEMENT

The raw data supporting the conclusions of this article will be made available by the authors, without undue reservation.

ETHICS STATEMENT

The animal study was reviewed and approved by the Ethical Committee for Animal Use, Cairo University, Giza Governorate, Egypt.

AUTHOR CONTRIBUTIONS

HE-S: conceptualization, ultrasonographic examination, biochemical analysis, data curation, and manuscript writing. AE-S: conceptualization, experimental design and procedures, and manuscript editing. HS: conceptualization, Doppler examination, biochemical analysis, data validation, statistical analyses, and manuscript reviewing and editing. All authors contributed to the article and approved the submitted version.

REFERENCES

1. Alves MBR, de Andrade AFC, de Arruda RP, Batissaco L, Florez-Rodriguez SA, de Oliveira BMM, et al. Recovery of normal testicular temperature after scrotal heat stress in rams assessed by infrared thermography and its effects on seminal characteristics and testosterone blood serum concentration. Theriogenology. (2016) 86:795–805.e2. doi: 10.1016/j.theriogenology.2016.02.034
2. Shahat AM, Thundathil JC, Kastelic JP. Scrotal subcutaneous temperature is increased by scrotal insulation or whole-body heating, but not by scrotal neck insulation; however, all three heat-stress models decrease sperm quality in bulls and rams. *J Therm Biol.* (2021) 100:103064. doi: 10.1016/j.jtherbio.2021.103064
3. Al-Kanaan A, König S, Brügemann K. Effects of heat stress on semen characteristics of Holstein bulls estimated on a continuous phenotypic and genetic scale. *Livest Sci.* (2015) 177:15–24. doi: 10.1016/j.livsci.2015.04.003
4. Samir H, Nyametease P, Elbadawy M, Fathi M, Mandour AS, Radwan F, et al. Assessment of correlations and concentrations of salivary and plasma steroids, testicular morphometry, and semen quality in different climatic conditions in goats. *Theriogenology.* (2020) 157:238–44. doi: 10.1016/j.theriogenology.2020.08.002
5. Hashem N, Abd El-Hady A, Hassan O. Effect of vitamin E or propolis supplementation on semen quality, oxidative status and hemato-biochemical changes of rabbit bucks during hot season. *Livest Sci.* (2013) 157:520–6. doi: 10.1016/j.livsci.2013.09.003
6. Gonçalves AA, Garcia AR, Rolim Filho ST, da Silva JAR, de Melo DN, Guimarães TC, et al. Scrotal thermoregulation and sequential sperm abnormalities in buffalo bulls (Bubalus bubalis) under short-term heat stress. *J Therm Biol.* (2021) 96:102842. doi: 10.1016/j.jtherbio.2021.102842
7. dos Santos Hamilton TR, de Castro LS, de Carvalho Delgado J, de Assis PM, Siqueira AFP, Mendes CM, et al. Induced lipid peroxidation in ram sperm: semen profile, DNA fragmentation and antioxidant status. *Reproduction.* (2016) 151:379–90. doi: 10.1530/REP-15-0403
8. Rizzoto G, Kastelic J. A new paradigm regarding testicular thermoregulation in ruminants? *Theriogenology.* (2020) 147:166–75. doi: 10.1016/j.theriogenology.2019.11.019
9. Turrens JF. Mitochondrial formation of reactive oxygen species. *J Physiol.* (2003) 552:335–44. doi: 10.1113/jphysiol.2003.049478
10. Hedia M, El-Belely M, Ismail S, El-Maaty AMA. Monthly changes in testicular blood flow dynamics and their association with testicular volume, plasma steroid hormones profile and semen characteristics in rams. *Theriogenology.* (2019) 123:68–73. doi: 10.1016/j.theriogenology.2018.09.032
11. Hedia MG, El-Belely MS, Ismail ST, Abo El-Maaty AM. Seasonal variation in testicular blood flow dynamics and their relation to systemic and testicular oxidant/antioxidant biomarkers and androgens in rams. *Reprod Domest Anim.* (2020) 55:861–9. doi: 10.1111/rda.13696
12. Samir H, Nyametease P, Elbadawy M, Nagaoka K, Sasaki K, Watanabe G. Administration of melatonin improves testicular blood flow, circulating hormones, and semen quality in Shiba goats. *Theriogenology.* (2020) 146:111–9. doi: 10.1016/j.theriogenology.2020.01.053
13. Abdelnaby EA, Emam IA, Fadl AM. Assessment of the accuracy of testicular dysfunction detection in male donkey (Equus asinus) with the aid of colour-spectral Doppler in relation to plasma testosterone and serum nitric oxide levels. *Reprod Domest Anim.* (2021) 56:764–74. doi: 10.1111/rda.13916
14. Gloria A, di Francesco L, Marruchella G, Robbe D, Contri A. Pulse-wave Doppler pulsatility and resistive indexes of the testicular artery increase in canine testis with abnormal spermatogenesis. *Theriogenology.* (2020) 158:454–60. doi: 10.1016/j.theriogenology.2020.10.015
15. Kay G, Grobbelaar J, Hattingh J. Effect of surgical restriction of growth of the testicular artery on testis size and histology in bulls. *Reproduction.* (1992) 96:549–53. doi: 10.1530/jrf.0.0960549
16. Herwig R, Tosun K, Pinggera G-M, Soelder E, Moeller K, Pallwein L, et al. Tissue perfusion essential for spermatogenesis and outcome of testicular sperm extraction (TESE) for assisted reproduction. *J Assist Reprod Genet.* (2004) 21:175–80. doi: 10.1023/B:JARG.0000031251.57848.04
17. EL-Sherbiny H, EL-Shahat K, Abo El-Maaty A, Abdelnaby EA. Ovarian and uterine haemodynamics and their relation to steroid hormonal levels in postpartum Egyptian buffaloes. *Bulgarian J Vet Med*. (2020). doi: 10.15547/bjvm.2020-0091 [Online ahead of print].
18. Bollwein H, Schulze JJ, Miyamoto A, Sieme H. Testicular blood flow and plasma concentrations of testosterone and total estrogen in the stallion after the administration of human chorionic gonadotropin. *J Reprod Dev.* (2008) 54:335–9. doi: 10.1262/jrd.20014
19. Samir H, Sasaki K, Ahmed E, Karen A, Nagaoka K, El Sayed M, et al. Effect of a single injection of gonadotropin-releasing hormone (GnRH) and human chorionic gonadotropin (hCG) on testicular blood flow measured by color doppler ultrasonography in male Shiba goats. *J Vet Med Sci.* (2015) 14–0633. doi: 10.1292/jvms.14-0633
20. Viana J, Arashiro E, Siqueira L, Ghetti A, Areas V, Guimarães C, et al. Doppler ultrasonography as a tool for ovarian management. *Anim Reprod.* (2018) 10:215–22. Available online at: https://www.animal-reproduction.org/article/5b5a6049f7783717068b4694/pdf/animreprod-10-3-215.pdf
21. Brito L, Barth A, Wilde R, Kastelic J. Testicular ultrasonogram pixel intensity during sexual development and its relationship with semen quality, sperm production, and quantitative testicular histology in beef bulls. *Theriogenology.* (2012) 78:69–76. doi: 10.1016/j.theriogenology.2012.01.022
22. Giffin JL, Franks SE, Rodriguez-Sosa JR, Hahnel A, Bartlewski PM. A study of morphological and haemodynamic determinants of TE characteristics in the ram. *Exp Biol Med.* (2009) 234:794–801. doi: 10.3181/0812-RM-364
23. Samir H, Nyametease P, Nagaoka K, Watanabe G. Effect of seasonality on testicular blood flow as determined by color Doppler ultrasonography

and hormonal profiles in Shiba goats. *Anim Reprod Sci.* (2018) 197:185–92. doi: 10.1016/j.anireprosci.2018.08.027
24. El-Shalofy AS, Hedia MG. Exogenous oxytocin administration improves the testicular blood flow in rams. *Andrologia.* (2021) 53:e14193. doi: 10.1111/and.14193
25. El-Shalofy A, Hedia M, Kastelic J. Melatonin improves testicular haemodynamics, echotexture and testosterone production in Ossimi rams during the breeding season. *Reproduction in Domestic Animals.* (2021) 56:1456–63. doi: 10.1111/rda.14010
26. Hussein SA, Abd El-Hamid OM, Hemdan HS. Protective effect of L-carnitine on metabolic disorders, oxidative stress, antioxidant status and inflammation in a rat model of. *Int J Biol Chem.* (2014) 8:21–36. doi: 10.3923/ijbc.2014.21.36
27. Li J-L, Wang Q-Y, Luan H-Y, Kang Z-C, Wang C-B. Effects of L-carnitine against oxidative stress in human hepatocytes: involvement of peroxisome proliferator-activated receptor alpha. *J Biomed Sci.* (2012) 19:1–9. doi: 10.1186/1423-0127-19-32
28. Elokil AA, Bhuiyan AA, Liu H-Z, Hussein MN, Ahmed HI, Azmal SA, et al. The capability of L-carnitine-mediated antioxidant on cock during aging: evidence for the improved semen quality and enhanced testicular expressions of GnRH1, GnRHR, and melatonin receptors MT 1/2. *Poult Sci.* (2019) 98:4172–81. doi: 10.3382/ps/pez201
29. Abdel-Emam RA, Ahmed EA. Ameliorative effect of L-carnitine on chronic lead-induced reproductive toxicity in male rats. *Vet Med Sci.* (2021) 7:1426–35. doi: 10.1002/vms3.473
30. Aziz RLA, Abdel-Wahab A, El-Ela FIA, Hassan NE-HY, El-Nahass E-S, Ibrahim MA, et al. Dose-dependent ameliorative effects of quercetin and l-Carnitine against atrazine-induced reproductive toxicity in adult male Albino rats. *Biomed Pharmacother.* (2018) 102:855–64. doi: 10.1016/j.biopha.2018.03.136
31. El-Sherbini E-S, El-Sayed G, El Shotory R, Gheith N, Abou-Alsoud M, Harakeh SM, et al. Ameliorative effects of l-carnitine on rats raised on a diet supplemented with lead acetate. *Saudi J Biol Sci.* (2017) 24:1410–7. doi: 10.1016/j.sjbs.2016.08.010
32. Genazzani AD, Despini G, Czyzyk A, Podfigurna A, Simoncini T, Meczekalski B. Modulatory effects of l-carnitine plus l-acetyl-carnitine on neuroendocrine control of hypothalamic functions in functional hypothalamic amenorrhea (FHA). *Gynecol Endocrinol.* (2017) 33:963–7. doi: 10.1080/09513590.2017.1332587
33. Ahmed SD, Ahsan S, Burney SI. Male fertility: influence of testosterone, luteinizing hormone, and follicle-stimulating hormone on seminal free L-carnitine. *Hum Androl.* (2013) 3:76–80. doi: 10.1097/01.XHA.0000432480.17007.64
34. Papanastasiou D, Bartzanas T, Kittas C, editors. Relation between potential sheep heat-stress and meteorological conditions. In: *International Conference on Agricultural Engineering AgEng*, Zurich. (2014).
35. Kaçar C, Zonturlu AK, Karapehlivan M, ARI UÇ, Ögün M, Citil M. The effects of L-carnitine administration on energy metabolism in pregnant Halep (Damascus) goats. *Turk J Vet Anim Sci.* (2010) 34:163–71. doi: 10.3906/vet-0805-11
36. Rebouche CJ. Kinetics, pharmacokinetics, and regulation of L-carnitine and acetyl-L-carnitine metabolism. *Ann N Y Acad Sci.* (2004) 1033:30–41. doi: 10.1196/annals.1320.003
37. Abdelnaby EA, Emam IA, Salem NY, Ramadan ES, Khattab MS, Farghali HA, et al. Uterine hemodynamic patterns, oxidative stress, and chromoendoscopy in mares with endometritis. *Theriogenology.* (2020) 158:112–20. doi: 10.1016/j.theriogenology.2020.09.012
38. Fathi M, Salama A, El-Shahat K, EL-Sherbiny HR, Abdelnaby EA. Effect of melatonin supplementation during IVM of dromedary camel oocytes (Camelus dromedarius) on their maturation, fertilization, and developmental rates *in vitro*. *Theriogenology.* (2021) 172:187–92. doi: 10.1016/j.theriogenology.2021.05.021
39. Cortassa S, Aon MA, Winslow RL, O'Rourke B. A mitochondrial oscillator dependent on reactive oxygen species. *Biophys J.* (2004) 87:2060–73. doi: 10.1529/biophysj.104.041749
40. Nardone A, Ronchi B, Lacetera N, Ranieri MS, Bernabucci U. Effects of climate changes on animal production and sustainability of livestock systems. *Livest Sci.* (2010) 130:57–69. doi: 10.1016/j.livsci.2010.02.011
41. Sharma S, Ramesh K, Hyder I, Uniyal S, Yadav V, Panda R, et al. Effect of melatonin administration on thyroid hormones, cortisol and expression profile of heat shock proteins in goats (Capra hircus) exposed to heat stress. *Small Rumin Res.* (2013) 112:216–23. doi: 10.1016/j.smallrumres.2012.12.008
42. Ayyat MS, Abd El-Latif KM, Helal AA, Al-Sagheer AA. Interaction of supplementary L-carnitine and dietary energy levels on feed utilization and blood constituents in New Zealand White rabbits reared under summer conditions. *Trop Anim Health Prod.* (2021) 53:1–8. doi: 10.1007/s11250-021-02723-1
43. Shahat A, Rizzoto G, Kastelic J. Amelioration of heat stress-induced damage to testes and sperm quality. *Theriogenology.* (2020) 84–96. doi: 10.1016/j.theriogenology.2020.08.034
44. Fadl AM, Abdelnaby EA, El-Sherbiny HR. Supplemental dietary zinc sulfate and folic acid combination improves testicular volume and hemodynamics, testosterone levels and semen quality in rams under heat stress conditions. *Reprod Domest Anim.* (2022) 00:10. doi: 10.1111/rda.14096
45. Ginther O. *Ultrasonic Imaging and Animal Reproduction.* Cross plains: WI Equiservices Publishing. (1995).
46. Dickey RP. Doppler ultrasound investigation of uterine and ovarian blood flow in infertility and early pregnancy. *Hum Reprod Update.* (1997) 3:467–503. doi: 10.1093/humupd/3.5.467
47. Stanley WC, Lopaschuk GD, Hall JL, McCormack JG. Regulation of myocardial carbohydrate metabolism under normal and ischaemic conditions: potential for pharmacological interventions. *Cardiovasc Res.* (1997) 33:243–57. doi: 10.1016/S0008-6363(96)00245-3
48. Sharma S, Black SM. Carnitine homeostasis, mitochondrial function and cardiovascular disease. *Drug Discov Today.* (2009) 6:e31–9. doi: 10.1016/j.ddmec.2009.02.001
49. Mohamed MA. Impact of L-carnitine and cinnamon on insulin-like growth factor-1 and inducible nitric oxide synthase gene expression in heart and brain of insulin resistant rats. *Am J Biochem Biotechnol.* (2010) 6:204–12. doi: 10.3844/ajbbsp.2010.204.212
50. Sharma S, Sun X, Agarwal S, Rafikov R, Dasarathy S, Kumar S, et al. Role of carnitine acetyl transferase in regulation of nitric oxide signaling in pulmonary arterial endothelial cells. *Int J Mol Sci.* (2013) 14:255–72. doi: 10.3390/ijms14010255
51. Sharma S, Sud N, Wiseman DA, Carter AL, Kumar S, Hou Y, et al. Altered carnitine homeostasis is associated with decreased mitochondrial function and altered nitric oxide signaling in lambs with pulmonary hypertension. *Am J Physiol.* (2008) 294:L46–56. doi: 10.1152/ajplung.00247.2007
52. Bloomer RJ, Tschume LC, Smith WA. Glycine propionyl-L-carnitine modulates lipid peroxidation and nitric oxide in human subjects. *Int J Vitam Nutr Res.* (2009) 79:131–41. doi: 10.1024/0300-9831.79.3.131
53. Guzel NA, Orer GE, Bircan FS, Cevher SC. Effects of acute L-carnitine supplementation on nitric oxide production and oxidative stress after exhaustive exercise in young soccer players. *J Sports Med Phys Fitness.* (2015) 55:9–15. Available online at: https://www.minervamedica.it/en/journals/sports-med-physical-fitness/article.php?cod=R40Y2015N01A0009&acquista=1
54. Kissner R, Nauser T, Bugnon P, Lye PG, Koppenol WH. Formation and properties of peroxynitrite as studied by laser flash photolysis, high-pressure stopped-flow technique, and pulse radiolysis. *Chem Res Toxicol.* (1997) 10:1285–92. doi: 10.1021/tx970160x
55. Rizzoto G, Ferreira J, Garcia HM, Teixeira-Neto F, Bardella L, Martins C, et al. Short-term testicular warming under anesthesia causes similar increases in testicular blood flow in Bos taurus vs. Bos indicus bulls, but no apparent hypoxia. *Theriogenology.* (2020) 145:94–9. doi: 10.1016/j.theriogenology.2020.01.045
56. Rizzoto G, Hall C, Tyberg J, Thundathil J, Caulkett N, Kastelic J. Testicular hyperthermia increases blood flow that maintains aerobic metabolism in rams. *Reprod Fertil Dev.* (2019) 31:683–8. doi: 10.1071/RD17509
57. Adwell CB, Brito L, Oba E, Wilde R, Rizzoto G, Thundathil J, et al. Arterial blood flow is the main source of testicular heat in bulls and higher ambient temperatures significantly increase testicular blood flow. *Theriogenology.* (2018) 116:12–6. doi: 10.1016/j.theriogenology.2018.04.022
58. Hedia M, El-Shalofy A. Ageing affects plasma steroid concentrations and testicular volume, echotexture and haemodynamics in rams. *Andrologia.* (2022) 54:e14309. doi: 10.1111/and.14309

59. Camela ES, Nociti RP, Santos VJ, Macente BI, Murawski M, Vicente WR, et al. Changes in testicular size, echotexture, and arterial blood flow associated with the attainment of puberty in Dorper rams raised in a subtropical climate. *Reprod Domest Anim.* (2019) 54:131–7. doi: 10.1111/rda.13213
60. Shaker M, Houssen M, Abo-Hashem E, Ibrahim T. Comparison of vitamin E, L-carnitine and melatonin in ameliorating carbon tetrachloride and diabetes induced hepatic oxidative stress. *J Physiol Biochem.* (2009) 65:225–33. doi: 10.1007/BF03180575
61. Roy VK, Verma R, Krishna A. Carnitine-mediated antioxidant enzyme activity and Bcl2 expression involves peroxisome proliferator-activated receptor-γ coactivator-1α in mouse testis. *Reprod Fertil Dev.* (2017) 29:1057–63. doi: 10.1071/RD15336
62. Cao Y, Qu H-j, Li P, Wang C-b, Wang L-x, Han Z-w. Single dose administration of L-carnitine improves antioxidant activities in healthy subjects. *Tohoku J Exp Med.* (2011) 224:209–13. doi: 10.1620/tjem.224.209

Conflict of Interest: The authors declare that the research was conducted in the absence of any commercial or financial relationships that could be construed as a potential conflict of interest.

frontiers | Frontiers in Veterinary Science

ORIGINAL RESEARCH
published: 09 June 2022
doi: 10.3389/fvets.2022.891492

Imaging Findings in Dogs and Cats With Presumptive Sclerosing Encapsulating Peritonitis

Bérengère C. H. Gremillet, Charles Porsmoguer, Géraldine Bolen, Frédéric Billen, Stéphanie Noël, Flore Brutinel and Valeria Busoni*

Département des Animaux de Compagnie, Clinique Vétérinaire Universitaire, Université de Liège, Liège, Belgium

This retrospective case series describes imaging findings in seven dogs and two cats with a presumptive diagnosis of sclerosing encapsulating peritonitis (SEP) between 2014 and 2021. Peritoneal effusion was present in all animal patients. Sonographically, echogenic fluid with or without echogenic intraperitoneal septations, gathered or corrugated bowel loops, and abdominal lymphadenomegaly were suggesting an inflammatory process and the presence of adhesions. Gathering of the bowel with abdominal distension and/or signs of intestinal obstruction were major findings on radiographs. Abdominal fat stranding was an additional finding in animals undergoing a CT examination. Previous surgery, pregnancy, and the presence of a perforating foreign body were potential predisposing causes in 4/9 animals. Peritonitis was septic in 4/9 animals. As SEP is a rare condition but life threatening, this detailed description of imaging findings in a short case series can be useful for a presumptive diagnosis and surgical planning.

Keywords: feline, canine, diagnostic imaging, sclerosing encapsulating peritonitis, ultrasound, radiograph (X-ray), computed tomography

OPEN ACCESS

Edited by:
Haney Samir,
Cairo University, Egypt

Reviewed by:
Sami Akbulut,
İnönü University, Turkey
Ahmed Elfadadny,
Tokyo University of Agriculture and Technology, Japan
Ibrahim Emam,
Cairo University, Egypt
Danfu Ma,
Nanjing Agricultural University, China

****Correspondence:***
Bérengère C. H. Gremillet
b.gremillet@uliege.be

Specialty section:
This article was submitted to Veterinary Imaging, a section of the journal Frontiers in Veterinary Science

Received: *07 March 2022*
Accepted: *16 May 2022*
Published: *09 June 2022*

Citation:
Gremillet BCH, Porsmoguer C, Bolen G, Billen F, Noël S, Brutinel F and Busoni V (2022) Imaging Findings in Dogs and Cats With Presumptive Sclerosing Encapsulating Peritonitis. Front. Vet. Sci. 9:891492. doi: 10.3389/fvets.2022.891492

INTRODUCTION

Sclerosing encapsulating peritonitis (SEP), also referred as "chronica fibrosa encapsulata," "icing sugar bowel" or "fibroplastic peritonitis" in the literature, is defined as a chronic inflammatory condition often of unknown etiology in which the small intestines are encased in a dense fibrocollagenous membrane (1, 2). It is believed that this pathology results from low grade or subclinical peritonitis that eventually progressed to multiple adhesions and membrane formation, with sclerosing granulation or fibrous tissue encapsulation, and sometimes distortion of the viscera (1, 2).

This pathological entity is uncommon in dogs and rare in cats (3–16). Only few cases are published and beside three case series published in the 90's (3–6), the most recent cases enriching the veterinary literature are single case reports (8–16). In humans, SEP most commonly manifests as recurrent acute, subacute or chronic intestinal obstruction. Clinical presentation of SEP in animals is variable and rather nonspecific: most cases present with chronic peritoneal effusion with or without digestive signs, including vomiting, diarrhea, anorexia, and abdominal pain (4–7, 9–16). Some animals diagnosed with SEP are reported with a history of abdominal foreign bodies or chronic bacterial infections but most of the time the disease seems to be idiopathic (17). Therefore the designation primary idiopathic SEP as opposed to secondary SEP has been suggested (1, 2).

Because imaging is a routine part of the work-up of cases with abdominal symptoms, the objective of this retrospective study is to provide a detailed description of the most common imaging findings of SEP determined from a case series of dogs and cats having a final diagnosis of SEP at surgery.

MATERIALS AND METHODS

Case records from the Small Animal Veterinary Clinic of the University of Liège from 2014 to 2021 were reviewed. Animals with a final diagnosis of SEP based on macroscopic findings and/or histopathological analysis of biopsies at surgery were included in the retrospective study and their data (signalment, history, clinical findings, imaging reports and diagnostic images) reviewed. All included animals had undergone a comprehensive clinical examination and a diagnostic imaging investigation, including at least abdominal ultrasonography, with or without abdominal radiography or computed tomography (CT).

Ultrasound examination was performed in dorsal recumbency on awake animals using a fixed ultrasound machine equipped with high frequency (7.5–13 MHz) linear and/or curvilinear probes[1, 2, 3].

Radiographs included at least two orthogonal views: a latero-lateral projection and a ventro-dorsal projection. All radiographs were performed on awake animals maintained by human operators using a computed or direct radiography system 150 kV/800 mA[4, 5].

Abdominal CT angiography was performed in sternal recumbency, under general anesthesia after a transient period of hyperventilation to induce apnea and avoid motion artifacts. The animal was premedicated using butorphanol (0.3–0.4 mg/kg). Anesthesia was induced using propofol and followed by endotracheal intubation. Anesthesia was maintained using isoflurane gas and 100% oxygen. CT images were acquired using a multi-slice system with 16 or 64 slice detector[6]. Acquisition parameters used for the 16-multislice CT scanner were as follows: tube voltage 120 kV, reference tube current 200 mA, and pitch factor 0.8. Scan tube current was modulated by automatic exposure control (Care Dose, Siemens Medical Solutions, International). Image data sets were reconstructed using parameters of 200–300 mm field of view, 512 × 512 matrix, 1.5 mm slice thickness, and Br-20f reconstruction algorithm (window level 40 and window width 300) with filter back projection. For the 64-multislice CT scanner, acquisition parameters used were as follows: tube voltage 100 kV, reference tube current 260 mA, and pitch factor 0.6. Scan tube current was modulated by automatic exposure control (Care Dose, Siemens Medical Solutions, International). Image data sets were reconstructed using parameters of 100–200 mm field of view, 512 × 512 matrix, 0.75 mm slice thickness and Br-46 reconstruction algorithm (window level 88 and window width 404) with iterative reconstruction. Post-contrast images were acquired during the arterial, portal and venous phases after injection of 2 ml/kg of iodinated contrast medium (iohexol[7] or iopromide[8]) with an automated injector.

Abbreviations: CT, Computed tomography; SEP, sclerosing encapsulating peritonitis; FI, intact female; MN, neutered male; MI, intact male; N/A, not applicable.

[1]Aloka 3500 Prosound and Aloka Prosound SSD-Alpha10, Aloka Co. Ltd., Tokyo, Japan.

[2]Arietta 850 SE, Hitachi-Fujifilm, Mechelen, Belgium.

[3]Canon Aplio a, Sint-Stevens-Woluwe, Belgium.

[4]Agfa Musica DR 14s and CR35x, Mortsel, Belgium.

[5]X-ray table General Electric CGR, Diegem, Belgium.

[6]Siemens, Somatom 16 and Somatom Confidence 64, Erlangen, Germany.

RESULTS

Animals

Nine animals, seven dogs and two cats (D1-7, C1-2; **Table 1**), corresponded to selection criteria. Breed was variable in the canine patients. Five dogs were intact females, one intact male and one neutered male. Age ranged from 6 months to 10 years (median 1.5 year-old). Both feline patients were neutered male domestic shorthair, aged 6 and 7 years.

History and Clinical Findings

Two dogs had a recent surgery (uneventful antescrotal castration, and enterectomy) 2 weeks and 3 months before the diagnosis respectively. Two dogs had been pregnant, D1 with an unremarkable parturition 1 month before the diagnosis, and D2 with adhesions noticed by the referring veterinarian during C-section 10 months before. One dog had recently been adopted with an unknwon history (D6). The remaining four animals had an unremarkable clinical history.

Clinical signs at initial presentation included anorexia (6/9), lethargy (4/9), weight loss (4/9), abdominal distension (3/9), diarrhea (2/9), abdominal pain (1/9) and acute vomiting (1/9). D5 developed acute vomiting and diarrhea due to intestinal obstruction 1 month after the initial presentation and underwent enterotomy and ovariohysterectomy.

Bloodwork at initial presentation was available for 5/9 animals. Bloodwork was normal in one dog (D5). Four animals showed minor hematological or biochemical unspecific changes including mild to moderate neutrophilia (D1, D3, C1 and C2), mild lymphocytosis and monocytosis (C1), mild hyper- (D1, C2) or hypoglycemia (C1), pre-renal azotemia (C2), and mild hypoproteinemia and increase in alkaline phosphatase level (D3).

Radiographic and Ultrasonographic Findings

Two dogs (D1, D6) and one cat (C2) had abdominal radiographic examination and all animals underwent an abdominal ultrasonographic examination.

Radiographs showed increased abdominal volume in 2/3 animals (**Figure 1**). Reduced serosal detail and an abnormal geometric, plicated shape of intestinal gas content were present in all three animals, with bowel loops stacked in the central abdomen and surrounded by a large amount of fluid (2/3). These radiographic findings were considered suggestive of either the presence of a linear foreign body or multiple serosal adhesions.

[7]Omnipaque 300, General Electric Healthcare, Diegem, Belgium.

[8]Ultravist 300, Bayer Pharma, Diegem, Belgium.

TABLE 1 | Signalement, history and final diagnosis of the nine animals with sclerosing encapsulating peritonitis.

Patient	Age	Sex	Breed	History	Abdominal Radiographs	Abdominal Ultrasound	Abdominal CT	Final diagnosis and outcome
D1	1 y	FI	Belgian malinois	Pregnancy	- Abnormal intestinal gas distribution and plication	- Free anechoic abdominal fluid - Hyperechoic intraabdominal fat - Mechanical ileus - Moderate abdominal lymphadenomegaly	N/A	Septic peritonitis *(Staphylococcus pseudintermedius)*
D2	2 y	FI	23kg crossed-breed	Pregnancy	N/A	- Free echogenic abdominal fluid focally surrounding some bowel loops - Focally hyperechoic intraabdominal fat - Small intestine hypoperistaltism with stick-like foreign body - Moderate mesenteric and medial iliac lymphadenomegaly	N/A	Intestinal perforating foreign body
D3	10 m	MN	Belgian malinois	Antescrotal castration	N/A	- Echogenic partially loculated abdominal fluid - Hyperechoic intraabdominal fat - Encased bowel loops - Small intestine hypoperistaltism with uncertain intraluminal foreign body - Severe jejunal and medial iliac lymphadenomegaly - Mass-like tissue along the abdominal wall	N/A	Necrotic pancreatitis, Septic peritonitis (*Pseudomonas putida)*
D4	2 y	FI	Beagle	Perforating intestinal foreign body and enterectomy	N/A	- Anechoic right periovarian fluid focally surrounding some bowel loops and the ovary - Small round and distorted spleen surrounded by a thin echogenic capsule	N/A	Ovariectomy, lateral flank approach
D5	6 m	FI	Leonberger	-	N/A	- Free anechoic abdominal fluid - Encased bowel loops - Small intestine hypoperistaltism with intraluminal grass ball - Severe jejunal lymphadenomegaly, moderate medial iliac lymphadenomegaly - Mass-like tissue along the abdominal wall	- Mesenteric fat stranding	Intestinal obstruction by grass ball, Neutrophilic enteritis and lymphangiectasis
D6	10 y	MI	Dachshund	Adopted	- Abdominal distention - Abnormal intestinal gas distribution and plication - Homogeneous peripheral fluid opacity	- Free abdominal fluid - Hyperechoic intraabdominal fat - Encased bowel loops - Small intestine hypoperistaltism with uncertain intraluminal foreign body	- Free abdominal fluid - Encased bowel loops - Mesenteric fat stranding - Equivocal thickening and increased contrast enhancement of the peritoneum	Scrotal leydigoma

(Continued)

TABLE 1 | Continued

Patient	Age	Sex	Breed	History	Abdominal Radiographs	Abdominal Ultrasound	Abdominal CT	Final diagnosis and outcome
D7	1 y	FI	German shepherd	-	N/A	- Echogenic loculated abdominal fluid - Hyperechoic intraabdominal fat - Encased bowel loops - Moderate jejunal lymphadenomegaly - Mesenteric echogenic mass and duodenal mass	- Loculated abdominal fluid - Encased bowel loops - Mesenteric fat stranding	Low grade duodenal leiomyosarcoma. *Recheck ultrasound exam on day 478 after initial presentation:* mechanical ileus
C1	6 y	MN	Domestic shorthair cat	-	N/A	- Echogenic loculated abdominal fluid - Hyperechoic intraabdominal fat - Encased bowel loops - Severe mesenteric lymphadenomegaly, especially jejunal lymph nodes	- Loculated abdominal fluid - Encased bowel loops - Mesenteric fat stranding - Equivocal thickening and increased contrast enhancement of the peritoneum	Cocci and bacilli on peritoneal capsule
C2	7 y	MN	Domestic shorthair cat	-	- Abdominal distention - Abnormal intestinal gas distribution and plication - Homogeneous peripheral fluid opacity	- Free echogenic abdominal fluid - Hyperechoic intraabdominal fat - Encased bowel loops - Moderate abdominal lymphadenomegaly - Mass and nodular images within cllumped mesenteric fat - Suspected pseudomembranous cystitis	N/A	Pseudomembranous cystitis, Septic peritonitis (*Listeria monocytogenes)*

FI, intact female; MN, neutered male; MI, intact male; N/A, not applicable.

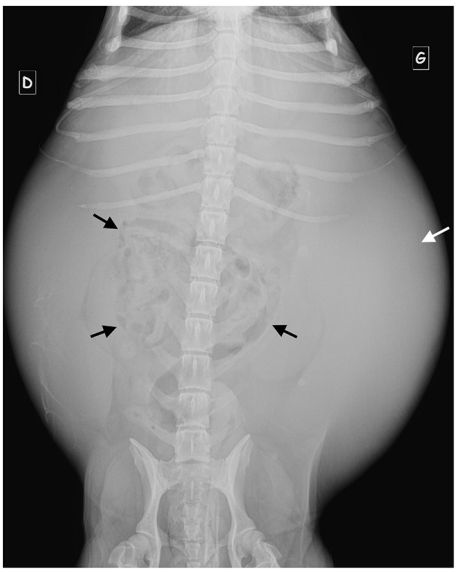

FIGURE 1 | Ventro-dorsal radiograph of D6. Note the severely increased abdominal volume, the central gathering of the small bowel loops (black arrows) with fluid opacity at the periphery of the peritoneal cavity (white arrow).

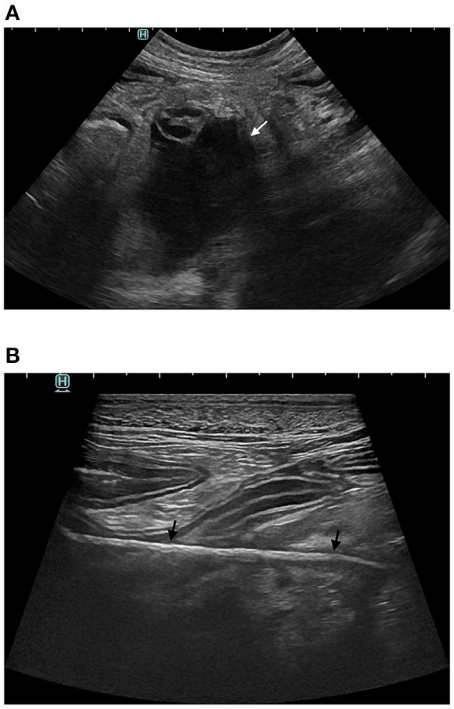

FIGURE 2 | Abdominal ultrasound of D2. **(A)** Echoic fluid filled cavity (white arrow) along a small bowel loop **(B)** Perforating intestinal stick-like foreign body (black arrows).

Sonographically free fluid was visible in all animals, either distributed in the entire peritoneal cavity (7/9) or focally collected (2/9). Peritoneal effusion was echogenic (6/9) and loculated or partially loculated by thin echogenic septations (3/9), suggesting an inflammatory process. Bowel loops had a plicated (7/9) and/or corrugated (7/9) appearance in all animals suggesting the occurrence of adhesions and bowel inflammation (**Figure 2**). In 6/9 animals the clumped bowel loops were encased and peritoneal fluid relegated separately in a different area of the abdominal cavity. In the two animals where peritoneal effusion was collected focally, the fluid was in close contact with a corrugated small bowel loop (in the area where a wooden foreign body was found perforating the bowel wall in D2 and in the right ovarian area concomitant with a periovarian effusion in D4) (**Figure 3**). Small bowel motility was considered reduced in 5/9 animals (D2 with a stick-like foreign body, D5 with grass ball, D1, D3 and D6 with uncertain intraluminal small foreign materials) and mechanical ileus occurred in 2/9 animals (D1 and D7, respectively on day 1 and day 478 after initial presentation). Intraabdominal fat was hyperechoic in 7/9 animals (focally in D2 surrounding the stick-like foreign body), suggesting steatitis. Moderate or severe abdominal visceral and/or parietal lymphadenomegaly was seen in 8/9 animals with the jejunal lymph nodes being predominantly involved in 4/9 animals.

Additional ultrasound findings were present in 5/9 animals. Two dogs (D3, D5) had thickened heterogeneous tissue mimicking a mass adherent to the abdominal wall at the site of laparotomy. D7 had an ovoid mesenteric echogenic mass unrelated to any abdominal organ and a small eccentric duodenal mass originating from the muscular layer. D4 had a small round distorted / folded spleen, surrounded by a thin echoigenic capsule. C2 had mass and nodular images (respectively $\geq$3 cm and $<$3 cm) within the clumped mesenteric fat and images of the bladder consistent with pseudomembranous cystitis.

CT Findings

Four animals underwent an abdominal CT (including contrast examination) (D5, D6, D7 and C1) for surgical planning.

Abdominal CT examinations confirmed the ultrasound findings in 4/4 animals. Free or loculated abdominal fluid (3–15 Hounsfield units) and encased bowel loops were confirmed in all three animals where this distribution had already been suspected based on radiographs and ultrasound (**Figures 4**, **5**). CT images also showed mesenteric fat stranding characterized by an increased linear or ill-defined attenuation in 4/4 animals. Extraluminal adhesions were suspected in 3/4 animals and in 2/4 animals an equivocal thickening and increased contrast enhancement of the peritoneum was noticed.

Surgical and Histopathological Findings

All nine animals underwent exploratory laparotomy. Surgery confirmed the presence of a thick capsule around the abdominal viscera (6/9), multiple serosal adhesions between small bowel loops (6/9) or between small bowel loops and ovary (1/9) or abdominal wall (2/9) (**Figure 6**). In the dog with the stick foreign body (D2) abdominal abscesses were present. Pancreatic necrosis was found in D3. Neutrophilic enteritis with associated mild lymphangiectasis was confirmed by histopathology in D5.

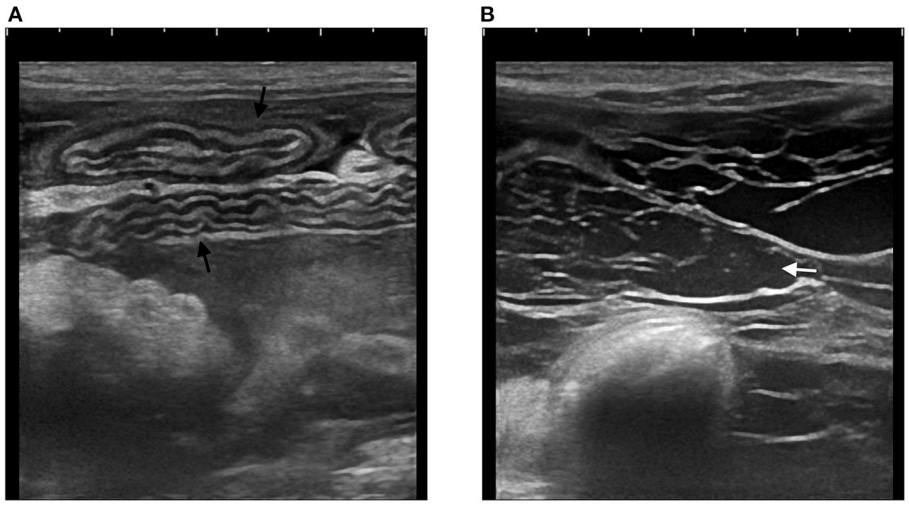

FIGURE 3 | Abdominal ultrasound of C1. **(A)** Multiple segments of corrugated small intestine (black arrows) **(B)** Echoic peritoneal fluid (white arrow) with multiple hyperechoic septations.

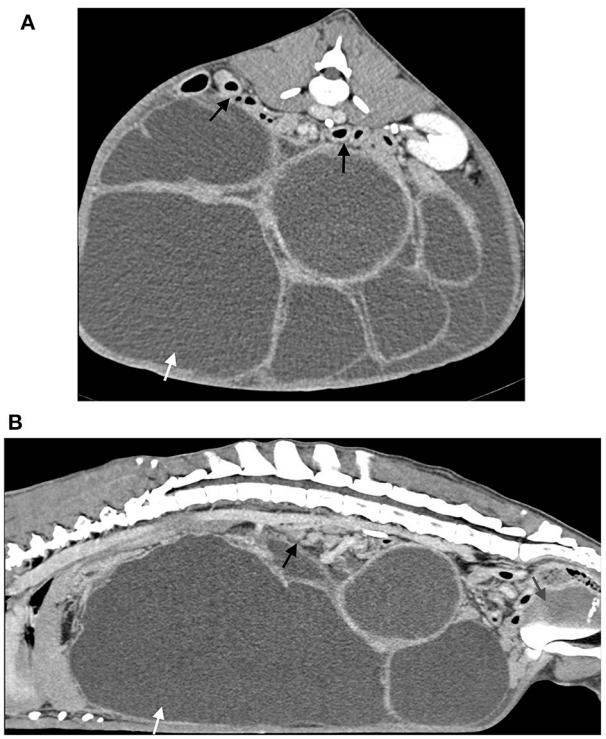

FIGURE 4 | Post-contrast CT acquisition of the abdomen of D7. **(A)** Transverse image, soft tissue window, at the level of the left kidney **(B)** Sagittal multiplanar reconstruction image, soft tissue window. A large amount of peritoneal fluid (white arrow) loculated by multiple hyperattenuating septations and dorsal gathering of the intestines is present (black arrows). Note also the mass effect of the fluid filled cavities and the secondary caudal displacement of the urinary bladder (gray arrow).

Neoplasia was confirmed in C2, D7 and D6, with respectively carcinomatosis associated to marked fibrosis, a low grade duodenal leiomyosarcoma and a scrotal leydigoma. Analysis of peritoneal fluid was performed in 5/9 animals and revealed a septic exudate in D1 (*Staphylococcus pseudintermedius*) and C2 (*Listeria monocytogenes*) and a non-septic modified transudate in D6, D7 and C1. Additionally, prior to referral, D6 had a positive bacterial culture (*Pseudomonas putida*) on peritoneal effusion. Fibrinous adhesions were submitted for histopathological analysis in 4/9 animals and confirmed either acute (C1 and D1) or chronic (C2 and D6) fibrinous neutrophilic inflammation. Cocci and bacilli were also present on the histopathological analysis of the fibrinous material in C1. Although most animals survived several months to years after initial admission (more than 3 to 20 months post diagnosis for 6/9 animals), 3/9 animals, including both cats, died or were euthanised within 7 days due to complications or lack of clinical improvement post-surgery.

DISCUSSION

This case series describes imaging findings in seven dogs and two cats with confirmed SEP. Most animals included were either juveniles or young adults (<3 years old). Previous reports show a wide age distribution demonstrating that juvenile (9, 12, 14, 16) as well as mature (7, 8, 10, 11, 13, 15) animals may be affected. Intact females were overrepresented (5/9) in contrary to previous reports which do not suggest any sex or neutered status influence (7, 8, 10–12, 15, 16).

SEP has been referred to be *idiopathic* or *secondary* depending on previous conditions that may be identified as potential trigger of peritoneal inflammation (1, 2). Foreign bodies and necrotic

FIGURE 5 | Late post-contrast CT acquisition of the abdomen of C1 (same case as **Figure 3**). **(A)** Transverse image, soft tissue window, at the level of the kidneys **(B)** Dorsal multiplanar reconstruction image, soft tissue window, at the level of the descending colon. There is central gathering of the intestines and a large amount of surrounding peritoneal fluid (white arrow). Fat stranding is also visible (black arrow).

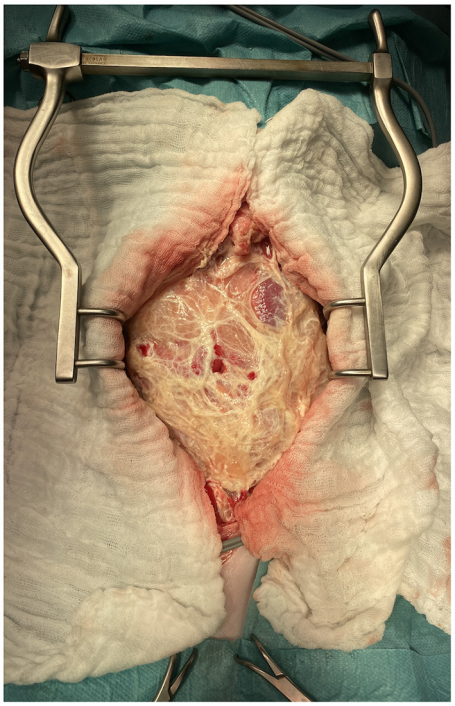

FIGURE 6 | Intraoperative picture of the laparotomy of C2 after abdominal wall incision. Note the thick fibrous membrane encapsulating the abdominal viscera.

neoplastic masses have been reported as potential initiating causes of abdominal inflammation in SEP (8, 10, 16). In the present case series one dog had undergone a previous abdominal surgery, one dog had a perforating foreign body and two had been pregnant prior or at the time of the diagnosis of SEP. Neoplasia was found in three other dogs (one carcinomatosis, one duodenal leyomyosarcoma and one scrotal leydigoma) and necrotic pancreatitis was found in one. These associated medical conditions may have been potential triggers for peritoneal inflammation. One dog had been castrated prior to the diagnosis of SEP (D6) and an ascending infection or systemic inflammation may have occurred.

The diagnostic imaging abnormalities in this case series predominantly involved the intestinal tract and peritoneal space. Intestinal findings most commonly involved plication and corrugation (consistent with the presence of adhesions in the absence of a foreign body) associated with peritoneal effusion and lymphadenomegaly. Sonographically, peritoneal fluid was often echogenic (6/9) and frequently associated with echogenic septae suggesting an inflammatory cause. This hypothesis is in accordance with previous descriptions in case reports (7, 8, 11, 12, 15, 16) and imaging text-books (18, 19). Thickening of the serosal surface and parietal peritoneum is also a sonographic finding described in textbooks (18, 19) but was not clearly seen in this retrospective case series.

Adhesions around and between small intestinal loops sometimes with an encapsulated visceral mass (6/9) was a common surgically finding. This characteristic encapsulation was seen as a gathering of small bowel loops in the central abdomen surrounded by fluid on radiographic, CT and ultrasonographic examinations of respectively 2/3, 3/4 and 5/9 animals. In two animals a mechanical ileus developed after the first onset of symptoms and this is similar to what is described in humans where mechanical ileus is reported as a consequence of adhesions and impaired bowel motility (1, 2).

Four cases had undergone a CT examination. Consistently with findings reported in literature (1, 2, 16), thickening of

the serosa or adhesions and peritoneal fat stranding were noticed on CT images. Fat stranding refers to an abnormal increased attenuation in fat because of edema and engorgement of lymphatics (20). In humans, fat stranding has been found to be very sensitive for peritoneal inflammation, being a key CT feature to differentiate uncomplicated from complicated appendicitis. Whereas mild inflammation causes a subtle hazy increased attenuation of the fat (ground-glass like), severe inflammation produces a reticular pattern (21, 22). In the animals where CT was performed linear/reticular fat stranding was present either in the entire peritoneal cavity or focally around the abnormal bowel loops. At contrast CT, two animals had serosal enhancement, and this is consistent with reports in human patients with SEP (2).

While the entire peritoneal cavity was involved in the majority of animals, two cases had focal ultrasound abnormalities with peritoneal effusion and hyperechoic fat being localized around an abnormal corrugated small bowel loop. These animals may either represent an earlier stage of the disease or simply better show the undergoing focal triggering process. However, if previous surgery is reported, animals with focal implication of the abdominal cavity may be difficult or impossible to distinguish from animals suffering of post-operative adhesions and not necessarily progressing to SEP.

The main limitations of this study are its retrospective nature and the small sample size. The complementary examinations were at the discretion of the clinician after consideration of the animal clinical presentation and owner budget. In particular, 5/9 animals did not have CT examination, 6/9 did not have abdominal radiographs and 5/9 did not have histopathological analysis of the peritoneal adhesions and membranes. However, because of the rarity of the disease, especially in cats (5, 6, 14), and its life threatening character a small case series assembling a detailed description of the most common imaging findings of SEP is considered useful to develop a better pre-surgical diagnosis in veterinary patients.

CONCLUSIONS

This small case series confirms findings previously reported in isolated SEP cases. As clinical presentation may be nonspecific, diagnostic imaging should be considered to exclude other disorders. Imaging findings of SEP in dogs and cats include abnormal shape and distribution of small bowel loops on radiographs, plicated and/or corrugated small bowel loops with echogenic loculated peritoneal effusion on ultrasound and fat stranding on CT.

DATA AVAILABILITY STATEMENT

The original contributions presented in the study are included in the article/supplementary material, further inquiries can be directed to the corresponding author.

ETHICS STATEMENT

The animal study was reviewed and approved by Comission d'Ethique Animale, Université de Liège. Written informed consent for participation was not obtained from the owners because this is a retrospective study using clinical datas. The Ethical Committee retrospectively approved the study (File number 22-2459) on the 11th of May 2022.

AUTHOR CONTRIBUTIONS

BG and VB contributed to conception and design of the study. BG and CP gathered database. BG organized the database and wrote the first draft of the manuscript. VB contributed to manuscript revision and wrote sections of the manuscript. All authors contributed to manuscript revision, read, and approved submitted version.

REFERENCES

1. Akbulut S. Accurate definition and management of idiopathic sclerosing encapsulating peritonitis. *World J Gastroenterol.* (2015) 21:675–87. doi: 10.3748/wjg.v21.i2.675
2. Machado NO. Sclerosing encapsulating peritonitis: review. *Sultan Qaboos Univ Med J.* (2016) 16:e142–51. doi: 10.18295/squmj.2016.16.02.003
3. Bellenger CR, Rothwell TLW. Sclerosing encapsulating peritonitis in a dog. *Aust Vet Pract.* (1991) 21:131–4.
4. Boothe HW, Lay JC, Moreland KJ. Sclerosing encapsulating peritonitis in three dogs. *J Am Vet Med Assoc.* (1991) 198:267–70.
5. Hardie EM, Rottman JB, Levy JK. Sclerosing encapsulating peritonitis in four dogs and a cat. *Vet Surg.* (1994) 23:107–14. doi: 10.1111/j.1532-950X.1994.tb00454.x
6. Setoguchi A, Kadosawa T, Nishimura R. Sclerosing encapsulating peritonitis in one dog and three cats. *Jpn J Vet Anesth Surg.* (1996) 27:79–89. doi: 10.2327/jvas.27.4_79
7. Adamama-Moraitou KK, Prassinos NN, Patsikas MN, Psychas V, Tsioli B, Rallis TS. Sclerosing encapsulating peritonitis in a dog with leishmaniasis. *J Small Anim Pract.* (2004) 45:117–21. doi: 10.1111/j.1748-5827.2004.tb00214.x
8. Etchepareborde S, Heimann M, Cohen-Solal A, Hamaide A. Use of tamoxifen in a German shepherd dog with sclerosing encapsulating peritonitis. *J Small Anim Pract.* (2010) 51:649–53. doi: 10.1111/j.1748-5827.2010.00998.x
9. Izawa T, Murai F, Akiyoshi H, Ohashi F, Yamate J, Kuwamura M. Encapsulating peritoneal sclerosis associated with abnormal liver development in a Young Dog. *J Vet Med Sci.* (2011) 73:697–700. doi: 10.1292/jvms.10-0503
10. Beck A, Stejskal M, Kurilj AG, Grabarevic Z. Necrotic omental lipoma in a dog as an unusual cause of sclerosing encapsulating peritonitis-a case report. *Vet Arh.* (2012) 82:391–9. doi: 10.24099/vet.arhiv
11. Barnes K. What Is Your Diagnosis? JAVMA. 2015 247. doi: 10.2460/javma.247.1.43
12. Veiga-Parga T, Hecht S, Craig L. Imaging diagnosis-sclerosing encapsulating peritonitis in a dog. *Vet Radiol Ultrasound.* (2015) 56:E65–9. doi: 10.1111/vru.12273
13. Santos ASO, Lemos LS, Viestel MAD, Rodrigues ABF, Almeida LG, Carvalho ECQ. Peritonite encapsulante esclerosante em cão (Canis familiaris): relato de caso. *Arquivo Brasileiro de Medicina Veterinária e Zootecnia.* (2017) 69:1203–5. doi: 10.1590/1678-4162-9235
14. Sonck L, van Brantegem L, Chiers K. Encapsulating peritoneal sclerosis: case report in a maine coon cat. *J Comp Pathol.* (2018) 158:126. doi: 10.1016/j.jcpa.2017.10.095
15. Carroll KA, Wallace ML, Hill TL, Bartges JW, Ruby JL, Mulder AT, et al. Pyloric outflow obstruction secondary to sclerosing encapsulating peritonitis in a dog. *Aust Vet J.* (2020) 98:11–6. doi: 10.1111/avj.12887

16. Isaac I, Carrera I, Martí J, Dibella A. Resolution of sclerosing encapsulating peritonitis in a young dog. *Vet Rec Case Rep*. (2020) 8:e001022. doi: 10.1136/vetreccr-2019-001022
17. Zachary JF. Alimentary system and the peritoneum. In: *Pathologic Basis of Veterinary Disease*. 6th ed. St Louis, MI: Elsevier (2017). p. 410.
18. Thrall DE. *Textbook of Veterinary Diagnostic Radiology*. 7th ed. Philadelphia, PA: Elsevier (2018).
19. Penninck D, D'Anjou MA. *Atlas of Small Animal Ultrasonography*. 2nd ed. New York, NY: John Wiley and Sons (2015).
20. Thornton E, Mendiratta-Lala M, Siewert B, Eisenberg RL. Patterns of fat stranding. *Am J Roentgenol.* (2011) 197:W1–14. doi: 10.2214/AJR.10.4375
21. Mittal MK, Dayan PS, Macias CG, Bachur RG, Bennett J, Dudley NC, et al. Performance of ultrasound in the diagnosis of appendicitis in children in a multicenter cohort. *Acad Emerg Med.* (2013) 20:697–702. doi: 10.1111/acem.12161
22. Pereira JM, Sirlin CB, Pinto PS, Jeffrey RB, Stella DL, Casola G. Disproportionate fat stranding: a helpful CT sign in patients with acute abdominal pain. *RadioGraphics.* (2004) 24:703–15. doi: 10.1148/rg.243035084

Conflict of Interest: The authors declare that the research was conducted in the absence of any commercial or financial relationships that could be construed as a potential conflict of interest.

frontiers | Frontiers in Veterinary Science

ORIGINAL RESEARCH
published: 16 June 2022
doi: 10.3389/fvets.2022.905759

Changes in Cardiac Function During the Development of Uremic Cardiomyopathy and the Effect of Salvianolic Acid B Administration in a Rat Model

Danfu Ma[1,2], Ahmed S. Mandour[2,3], Ahmed Elfadadny[4,5], Hanan Hendawy[2,6], Tomohiko Yoshida[2], Hussein M. El-Husseiny[2,7], Koji Nishifuji[4], Ken Takahashi[8], Zhenlei Zhou[1], Yanbing Zhao[1] and Ryou Tanaka[2]**

[1] College of Veterinary Medicine, Nanjing Agricultural University, Nanjing, China, [2] Departments of Veterinary Surgery, Faculty of Veterinary Medicine, Tokyo University of Agriculture and Technology, Tokyo, Japan, [3] Department of Animal Medicine (Internal Medicine), Faculty of Veterinary Medicine, Suez Canal University, Ismailia, Egypt, [4] Laboratory of Veterinary Internal Medicine, Division of Animal Life Science, Institute of Agriculture, Graduate School, Tokyo University of Agriculture and Technology, Tokyo, Japan, [5] Department of Animal Internal Medicine, Faculty of Veterinary Medicine, Damanhour University, Damanhour, Egypt, [6] Department of Veterinary Surgery, Anesthesiology, and Radiology, Faculty of Veterinary Medicine, Suez Canal University, Ismailia, Egypt, [7] Department of Surgery, Anesthesiology, and Radiology, Faculty of Veterinary Medicine, Benha University, Benha, Egypt, [8] Department of Pediatrics and Adolescent Medicine, Juntendo University Graduate School of Medicine, Bunkyo-Ku, Tokyo, Japan

OPEN ACCESS

Edited by:
Ayman Abdel-Aziz Swelum,
Zagazig University, Egypt

Reviewed by:
Amany Abdel-Rahman Mohamed,
Zagazig University, Egypt
Hani Mohamed,
Zagazig University, Egypt

***Correspondence:**
Zhenlei Zhou
zhouzl@njau.edu.cn
Ryou Tanaka
ryo@vet.ne.jp

Specialty section:
This article was submitted to Veterinary Imaging, a section of the journal Frontiers in Veterinary Science

Received: 27 March 2022
Accepted: 09 May 2022
Published: 16 June 2022

Citation:
Ma D, Mandour AS, Elfadadny A, Hendawy H, Yoshida T, El-Husseiny HM, Nishifuji K, Takahashi K, Zhou Z, Zhao Y and Tanaka R (2022) Changes in Cardiac Function During the Development of Uremic Cardiomyopathy and the Effect of Salvianolic Acid B Administration in a Rat Model. Front. Vet. Sci. 9:905759. doi: 10.3389/fvets.2022.905759

Background: Uremic cardiomyopathy (UC), the main cause of death in progressive chronic kidney disease (CKD), is characterized by diastolic dysfunction. Intraventricular pressure gradients (IVPG) derived from color m-mode echocardiography (CMME) and two-dimensional speckle tracking echocardiography (2DSTE) were established as novel echocardiographic approaches for non-invasive and repeatable assessment of cardiac function. Previously, salvianolic acid B (Sal B) showed the potential to alleviate concentric LV hypertrophy in the pressure overload model. The purpose of this study was to evaluate the changes in cardiac function in UC and assess the efficacy of Sal B therapy using IVPG and 2DSTE techniques.

Materials and Methods: Twenty-four rats underwent subtotal nephrectomy to produce progressive renal failure and were allocated equally into UC (n = 12) and Sal B-UC (n = 12) groups and monitored for 8 weeks. A sham-operated group was also included in this study (n = 12). Sal B was injected from weeks 4 to 8 in the Sal B-UC group. Conventional echocardiography, 2DSTE, and CMME were performed every 2 weeks post-operation, concomitantly with an evaluation of renal function. Histopathological and immunohistochemistry analyses were carried out to confirm the echocardiography findings.

Results: Renal failure and myocardial dysfunction were confirmed in the UC group from weeks 2 through 8. Eccentric and concentric hypertrophy was observed in the UC group, while the Sal B-UC group showed only eccentric hypertrophy. IVPG analysis did not reveal any significant differences between the groups. Edema, inflammation, fibrosis,

and immunohistochemical expression of CD3 infiltration were higher in the UC group compared with sham and Sal B-UC groups.

Conclusion: 2DSTE and IVPG explored the pathophysiology during the development of UC and indicated the incidence of myocardial dysfunction before ventricular morphological changes without intracardiac flow changes. This study confirmed increased ventricular stiffness and fibrosis in UC rats which was potentially treated by Sal B *via* decreasing edema, inflammation, and fibrosis.

Keywords: intraventricular pressure gradients, uremic cardiomyopathy, hypertrophy, strain, salvianolic acid

INTRODUCTION

Cardiovascular diseases are the leading cause of death in renal failure patients (1), with hypertrophy of the left ventricle (LV) the most prevalent cardiac disorder in this population. Left ventricular hypertrophy is closely related to heart failure (2). Although scientists termed cardiomyopathy related to renal failure as uremic cardiomyopathy (UC) in 1967, the pathogenesis of UC remains poorly understood due to its multifactorial etiology (3–5).

Multiple pathological pathways are involved in the development of UC. The UC-associated LV hypertrophy results from complex pressure overload, volume overload, and the uremic state itself. Systemic hypertension results in LV pressure overload, while LV volume overload occurs due to hypervolemia and anemia (6). While Pressure overload leads to concentric LV hypertrophy (7), volume overload results in eccentric LV hypertrophy. Hypertrophy of the LV is a beneficial adaptive response during the early stages of UC, but progressive LV overload leads to maladaptive cardiomyocyte alterations and death (4). The loss of cardiomyocytes leads to LV dilatation and eventually systolic dysfunction (3). Thus, different types of LV hypertrophy are observed in UC based on the forces acting on the LV (8).

Although conventional echocardiography enables longitudinal assessments of cardiac function, it lacks the sensitivity required for detecting diastolic dysfunction (9). Intraventricular pressure gradients (IVPG), the pressure gradients inside the ventricle that draw blood from the left atrium (LA) to the LV during diastole, have been strongly correlated with left atrial (LA) pressure and active relaxation (10). Our previous research proved that IVPG could be used as a serial cardiac function evaluation tool in rodent and dog models (11–13).

Strain is a dimensionless characteristic for measuring relative deformation. Two-dimensional speckle tracking echocardiography (2DSTE) enables the quantification of both regional strain and strain rate, resulting in promising novel parameters for describing myocardial function (14).

Currently, angiotensin-converting-enzyme inhibitors and Angiotensin II Receptor Blockers are used as the first-line therapeutic drugs in UC to counteract the RAAS effect. But the drawbacks of these drugs like hypotension, azotemia, and fatigue caught the attention (15). Nowadays, there is growing interest in herbal medicine as a replacement or supportive cardioprotective treatment. Salvianolic acid B (Sal B), a water-soluble active component of *Salvia miltiorrhiza Bunge*, also known as Danshen, is widely used in Asia to treat cardiovascular disease. Sal B is well tolerant in the general population (16) and could alleviate cardiac fibrosis *in vitro* and improve myocardial function in diabetic cardiomyopathy (17, 18). Sal B was proved to decrease the inflammation and fibrosis induced by the Angiotensin II (17), so anti-inflammation and antifibrosis are considered the main treatment mechanism in cardiovascular diseases (19). Recently, we demonstrated that 5 mg/kg Sal B comparatively improves cardiac function in rats with experimental LV hypertrophy (12). We select 5 mg/kg as the proper dose to treat UC based on a previous study because this dose showed proper effect and duration (20). To the best of our knowledge, no studies have investigated the utility of combining IVPG and 2DSTE in UC. In addition, the effect of Sal B on UC hemodynamics, myocardial function, and morphology is still unknown. In the current experiment, we investigated the usefulness of IVPG and 2DSTE in a UC model and explored the effect of Sal B as a potential treatment for UC. We hypothesized that different types of LV hypertrophy might contribute to the development of UC and that Sal B may alleviate the adverse effects of UC in the rat model.

MATERIALS AND METHODS

Animals and Ethical Approval

The experiment was conducted with 36 female Sprague Dawley rats, aged 3 months and weighing between 210 g and 250 g. All procedures followed the Guide for the Care and Use of Laboratory Animals (1994) and were approved by the Institutional Animal Care and Use Committee of the Tokyo University of Agriculture and Technology (Approval No. 31-36). The rats had free access to food and water and were housed at 20°C with a 12 h light/dark cycle.

Induction of Uremic Cardiomyopathy

A 5/6 nephrectomy was performed according to previously described procedures (21). Briefly, the rats were transferred into an anesthetic induction chamber, anesthesia was induced with 5% isoflurane until the rats reach deep anesthesia, then pentobarbital (40 mg/kg) was intraperitoneal injected. The left kidney was exposed by a left laparotomy under a surgical

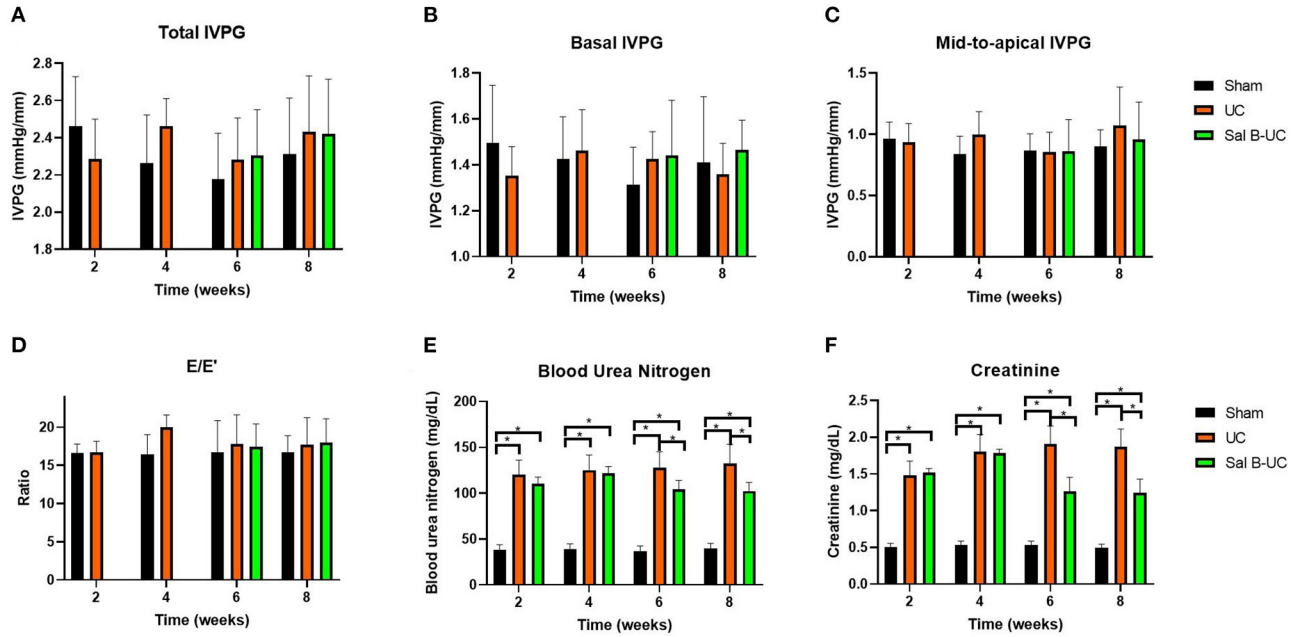

FIGURE 1 | Novel echocardiography and kidney function in uremic cardiomyopathy, sham operation, and Sal B-treated rats. Novel echocardiographic measurements in the sham, UC, and Sal B-UC groups. Two-way ANOVA was performed to test the differences between groups and time points, Tukey's *post-hoc* test used group comparisons. * Indicate a significant difference between groups, $p < 0.05$. **(A)** Total IVPG, the mix of basal and mid-to-apical intraventricular pressure gradients. **(B)** Basal IVPG, the basal intraventricular pressure gradients. **(C)** Mid-to-apical IVPG, the mid plus apex intraventricular pressure gradients. **(D)** E/E', ratio of E to E'. **(E)** creatinine. **(F)** BUN, blood urea nitrogen.

microscope (Leica M60, Wetzlar, Germany). The upper and lower kidney poles were electronically cauterized by a monopolar electrosurgical generator (Volleylab Force FX electro surgical Unit, Dublin, Ireland) and two 1 mm^2 Spongy Gelatin Absorbent (Huachen, Jiangxi, China) on the kidney bipolar wound, then the abdominal wall was closed. Because the whole surgery would take a proficient operator 25 min to complete and the effect of pentobarbital last more than 1 h, we provided two bags for the operated rats to prevent intra- and post-operative hypothermia until the anesthesia wore off. For intra- and post-operative pain management, butorphanol (0.5 mg/kg) and midazolam (0.5 mg/kg) was administrated if we observed pain after the surgical procedures (22). Signs of pain include hunched over ruffled, disheveled fur, squinty eyes, dull corneas, nose to the floor, and no eating or drinking. One week later, a total right nephrectomy was performed. The nephrectomized rats were divided into two groups: UC rats ($n = 12$) and Sal B-UC treated rats ($n = 12$); 12 rats were sham-operated and served as a control group.

Treatments

The Sal B-UC group was treated with Sal B from weeks 4 to 8 post-operation. Daily, 5 mg/kg of Sal B (Danshen DuofensuanYan 100 mg, GreenValley Inc, Shanghai, China) was injected into the abdominal cavity after the rats were tightly caged (**Supplementary Figure S1**). The UC rats received the same volume of normal saline by injection to limit the disturbance caused by the injection on the experimental results.

Blood Sampling and Renal Function Tests

Blood samples were drawn from every rat at weeks 2, 4, 6, and 8. After the rats were tightly caged, 2 ml of blood was collected from the tail vein using plain tubes. Blood samples were centrifuged at 3,500 rpm for 5 min, and clean non-hemolyzed serum was kept for analysis. The concentration of serum creatinine and blood urea nitrogen (BUN) were measured automatically by special kits (v-CRE-P and v-BUN-P, Fujifilm, Tokyo, Japan) and a Chemistry Analyzer (Dri-chem 7000V, Fujifilm, Tokyo, Japan).

Blood Pressure

Blood pressure was monitored using the oscillometric method (BP monitor for rats, Muromachi, Japan). The cuff was placed over the base of the rat's tail when the rat was tightly caged. Measurements were performed three times, and the average systolic, diastolic, and mean arterial blood pressures were recorded.

Echocardiography

Echocardiography was performed 2, 4, 6, and 8 weeks after right nephrectomy (ProSound F75 premier CV, Hitachi Healthcare System Inc, Tokyo, Japan). Isoflurane (2.5%) was administrated to rats by mask. Then we put the rats' right recumbency for short-axis echocardiograph parameter measurements, including IVSd,

TABLE 1 | Cardiac morphology of the investigated groups at 6 and 8 weeks.

Time	6 weeks			8 weeks			*p* of group	*p* of time
Group	Sham	UC	Sal B-UC	Sham	UC	Sal B-UC		
IVSd, mm	1.21 ± 0.17	1.57 ± 0.35*	1.39 ± 0.26	1.31 ± 0.16	1.67 ± 0.3*	1.57 ± 0.15†	0.000**	0.073
LVIDd, mm	7.53 ± 0.62	7.32 ± 0.27	7.93 ± 0.5‡	7.25 ± 0.58	7.32 ± 0.54	7.87 ± 0.69‡	0.007**	0.423*
LVPWd, mm	1.32 ± 0.27	1.78 ± 0.54*	1.43 ± 0.36	1.64 ± 0.33	1.95 ± 0.53	1.49 ± 0.46	0.004**	0.087
IVSs, mm	2.06 ± 0.39	2.29 ± 0.55	2.16 ± 0.46	1.96 ± 0.4	2.5 ± 0.52*	2.63 ± 0.19†	0.000**	0.042*
LVIDs, mm	4.34 ± 0.5	4.25 ± 0.38	4.48 ± 0.36	4.36 ± 0.46	3.93 ± 0.51†	4.13 ± 0.44	0.029*	0.028*
LVPWs, mm	2.32 ± 0.32	2.55 ± 0.72	2.39 ± 0.18	2.38 ± 0.43	2.88 ± 0.68*	2.95 ± 0.44†	0.009**	0.001**
FS %	42.59 ± 4.63	41.78 ± 4.99	43.58 ± 4.19	39.59 ± 7.6	46.45 ± 5.41*	47.67 ± 3.28†	0.003**	0.157
LVM (gm)	0.62 ± 0.11	0.91 ± 0.34*	0.79 ± 0.23	0.71 ± 0.11	0.99 ± 0.38	0.86 ± 0.24	0.011*	0.151
HW(g)	0.85 ± 0.09	1.17 ± 0.12*	1.09 ± 0.12†	0.88 ± 0.12	1.37 ± 0.12*	1.19 ± 0.12‡†	0.000**	0.001**
HW/BW(mg/g)	3.62 ± 0.19	5.11 ± 0.29*	4.61 ± 0.27‡†	3.62 ± 0.24	5.61 ± 0.31*	4.51 ± 0.34‡†	0.000**	0.000**
RWT	0.34 ± 0.07	0.46 ± 0.13*	0.36 ± 0.07†‡	0.41 ± 0.07	0.49 ± 0.09*	0.39 ± 0.06	0.000**	0.045*

*Echocardiographic measurements and longitudinal strain rate in the sham, UC, and Sal B-UC groups. Two-way ANOVA was performed to test the difference between groups and time points, and Tukey's post-hoc tests were used for group comparisons. Significance marks were fitted to compare data at each time point. * Indicates a significant difference between the sham and UC groups. The ** symbol indicates the significant difference of $p < 0.01$. † Indicates a significant difference between Sham and Sal B-UC groups. ‡ Indicates a significant difference between the UC and UC-Sal B groups. The significance level was $p < 0.05$. IVSd, interventricular septum diastolic diameter; LVIDd, left ventricular internal diastolic diameter; LVPWd, left ventricular posterior wall diastolic diameter; FS, fraction shorting; LVM, left ventricle mass; RWT, relative wall thickness; IVSs, interventricular septum systolic diameter; LVIDs, left ventricular internal systolic diameter; LVPWs, left ventricular posterior wall systolic diameter; FS, fraction shorting; LVM, left ventricle mass; RWT, relative wall thickness; HW, heart weight (g); HW/BW, heart weight (mg)/body weight (g). In this table, the two-way anova only include the data in 6 and 8 weeks. The full data including 2 and 4 weeks could be seen at* ***Supplementary Table S3****.*

TABLE 2 | Blood pressure and Doppler hemodynamic measurements in rats at 6 and 8 weeks.

Time	6 weeks			8 weeks			*p* of group	*p* of time
Group	Sham	UC	Sal B-UC	Sham	UC	Sal B-UC		
HR, BPM	298.74 ± 47.14	378 ± 56.29*	353.03 ± 42.92‡	310.23 ± 50.05	375.72 ± 45.1*	364.51 ± 45.82‡	0.000**	0.605
SAP, mmHg	93.41 ± 15	133.58 ± 13.56*	121.24 ± 9.45†	100.53 ± 15.25	144.12 ± 11.98*	126.75 ± 11.21†‡	0.000**	0.134
DAP, mmHg	73.75 ± 6.55	104.13 ± 9.8*	88.59 ± 9.82†‡	73.2 ± 5.63	123.93 ± 19.57*	106.18 ± 14.43†‡	0.000**	0.000**
MAP, mmHg	80.3 ± 6.17	113.94 ± 8.08*	110.36 ± 7.15†	82.31 ± 8.05	130.66 ± 13.52*	119.89 ± 8.4†‡	0.000**	0.000**
E, cm/s	105.58 ± 17.51	106.49 ± 10.79	103.26 ± 14.52	97.71 ± 16.91	106.47 ± 16.2	99.83 ± 19.44	0.054	0.371
E', cm/s	5.18 ± 1.06	6.32 ± 1.42*	6.06 ± 1.09	5.48 ± 0.6	6.16 ± 0.77	5.62 ± 0.53	0.024	0.674

*The echocardiographic measurements of the sham and UC groups. Two-way ANOVA was performed to test the difference between groups and time points, and Tukey's post-hoc tests were used for group comparisons. Significance marks were fitted to compare data at each time point. * Indicates a significant difference between the sham and UC groups, The ** symbol indicates the significant difference of $p < 0.01$, † Indicates a significant difference between Sham and Sal B-UC groups, ‡ Indicates a significant difference between the UC and Sal B-UC groups. The significance level was $p < 0.05$. HR, heart rate; SAP, systolic arterial pressure; DAP, diastolic arterial pressure; MAP, mean arterial pressure; E, the velocity of early mitral inflow; $E^{'}$, Peak velocity of early diastolic mitral annular motion as determined by pulsed-wave Doppler. In this table, the two-way anova only include the data in 6 and 8 weeks. The full data including 2 and 4 weeks could be seen at* ***Supplementary table S4****.*

LVIDd, LVPWd, IVSs, LVIDs, and LVPWs, using a 1–15 Mhz transducer (UST-52129, Hitachi Healthcare System Inc, Tokyo, Japan). The left ventricle mass (LVM) and relative wall thickness (RWT) were calculated with the following formulas (12):

$$LVM = [(LVIDd + LVPWd + IVSd)^3 - LVIDd^3] * 1.04$$

$$RWT = (IVSd + LVPWd)/LVIDd$$

Tissue Doppler Imaging and CMME for IVPG Analysis

Tissue Doppler imaging of the left parasternal (apical view) was performed, sampling transmitral E A flow velocity, $E^{'}$ septum(mitral valve root velocity), and $E^{'}$ lateral. The following formula was used to calculate $E/E^{'}$:

$$E/E^{'} = (E/E^{'}\ \text{lateral} + E/E^{'}\ \text{septum})/2$$

Color M-mode echocardiography (CMME) was performed in the transmitral flow window. To capture mitral inflow, the sample volume spanned from the orifice of the mitral valve to the LV apex, and the time-motion relation was sampled after the baseline changed to −64. The CMME image was analyzed using MATLAB (The MathWorks, Natick, MA). Prior machine settings (12) and an analysis algorithm have been described previously (23). Total IVPG was divided into two sections; Firstly, from the base of the LV near the mitral valve to one-third of the LV was termed the basal IVPG, and secondly, the gradient from the apex to two-thirds of the LV was termed the mid-to-apical IVPG (**Supplementary Figure S2**).

TABLE 3 | 2D-speckle tracking echocardiography measurements in rats at 6 and 8 weeks.

Time	6 weeks			8 weeks			*p* of group	*p* of time
Group	Sham	UC	Sal B-UC	Sham	UC	Sal B-UC		
APS	4.19 ± 0.41	2.97 ± 0.41*	3.12 ± 0.51‡	4.08 ± 0.48	3.04 ± 0.4*	2.68 ± 0.3‡	0.000**	0.348
MS	11.35 ± 1.12	7.81 ± 1.09*	8.3 ± 1.36‡	13.51 ± 1.6	8.9 ± 1.17*	8.64 ± 0.96‡	0.000**	0.030*
BS	11.97 ± 1.19	7.5 ± 1.05*	9.29 ± 1.52†‡	11.5 ± 1.36	7.08 ± 0.93*	7.5 ± 0.84‡	0.000**	0.098
APL	6.81 ± 0.67	6.55 ± 0.91	6.79 ± 1.11	7.45 ± 0.88	5.12 ± 0.67*	7.05 ± 0.79†	0.000**	0.503
ML	8.65 ± 0.86	6.55 ± 0.91*	6.23 ± 1.02†	9.23 ± 1.09	6.19 ± 0.81*	6.05 ± 0.67†	0.000**	0.971
BL	10.68 ± 1.06	5.86 ± 0.82*	7.48 ± 1.23†‡	7.72 ± 0.92	7.23 ± 0.95	7.05 ± 0.79	0.000**	0.101

*Longitudinal strain rate in the sham, UC, and Sal B-UC groups. Two-way ANOVA was performed to test the difference between groups and time points, and Tukey's post-hoc tests were used for group comparisons. Significance marks were fitted to compare data at each time point. * Indicates a significant difference between the sham and UC groups. The ** symbol indicates the significant difference of $p < 0.01$. † Indicates a significant difference between Sham and UC-Sal B groups. ‡ indicates a significant difference between the UC and UC-Sal B groups. The significance level was $p < 0.05$. APS, strain rate of the apical segment of the septum; MS, strain rate of the middle segment of the septum; BS, strain rate of the basal segment of the septum; APL, strain rate of the apical segment of the lateral free wall; ML, strain rate of the middle segment of the lateral free wall; BL, strain rate of the basal segment of the lateral free wall.*

In this table, the two-way anova only include the data in 6 and 8 weeks. The full data including 2 and 4 weeks could be seen at ***Supplementary Table S4****.*

Speckle Tracking Echocardiography

Loops of LV movement in four chambers (apical views) were acquired. Speckle tracking analysis was performed using an algorithm incorporated into EchoPAC PC DAS-RSI (Hitachi Aloka Co., Tokyo, Japan). The endocardium was traced manually for both end-systole and end-diastole phases. The software algorithm automatically divided each imaging plane of the LV into three equally circular sections: basal, midventricular, and apex on the septal and lateral aspects (**Supplementary Figure S3**). The longitudinal strain rate was obtained in six sections (14).

Histological Analysis

Heart tissue samples were collected from the three groups at the end of the study (weeks 8). We sectioned (4-μm), fixed the heart tissue samples in 10% neutral buffered formalin, and then embedded them in paraffin wax. The sections were cut, deparaffinized, rehydrated and then stained with Masson's trichrome and hematoxylin, and eosin (H&E). For statistical measurements, 36 sections (12 sections per group, each 4-μm thick) were used. The histopathological images were examined using image software (CellSens Standard; Olympus, Tokyo, Japan). The quantification of the histopathological score has been reported in detail before (24). Briefly, 36 sections (12 sections per group) were analyzed blindly by two histopathologists based on inflammatory cells infiltration (mononuclear cell), edema (interstitial edema between the cardiocytes), necrosis (degeneration and necrotic area), and myocytes arrangement (assembled or disassembled and direction of myocardial cells). The results of both investigators were averaged for all sections in the three groups and graded as 0 (none), 1 (mild), 2 (moderate), 3 (severe), or 4 (very severe) based on mononuclear cell infiltration, edema, necrosis, and myocyte arrangement. Fibrosis intensity was assessed at the interstitial level and perivascular area.

Immunohistochemical Staining of CD3

The same number of sections from each group were deparaffinized and rehydrated. Antigen retrieval was performed by incubating slides for 15 min at 95 °C in Tris-EDTA buffer (*pH* 9.0). Peroxidase blocking was achieved by treatment with 0.3% H_2O_2 diluted in methanol for 15 min. Nonspecific protein binding was inhibited by incubating the samples with 5% goat serum diluted in phosphate buffer saline with 0.1% Tween 20 for 2 h at room temperature, followed by overnight incubation with primary antibodies against monoclonal CD3 antibody (1:100, Invitrogen PA5-88511) at 4 °C. On the second day, the sections were incubated with horseradish peroxidase-conjugated secondary antibody for 1 h at room temperature. Antigen-antibody complexes were visualized after staining the samples with 3, 3′-diaminobenzidine. Cell nuclei were counterstained with hematoxylin. The frequency of CD3 cell infiltration was quantified for each of the three groups as the average number of CD3+ cells per 1 mm^2 of tissue.

Statistical Analysis

Data analysis was performed with a two-way analysis of variance (ANOVA) test with *post-hoc* contrasts by Tukey's honestly significant difference test using SPSS 26.0 (SPSS, Inc., Chicago, IL). The data are presented as mean ± standard deviation for all obtained parameters, and $p < 0.05$ were considered statistically significant.

RESULTS

Clinical Symptoms

Polyuria was defined as bedding being more wet than usual at routine cleaning. Polyuria was observed in the UC group 4 weeks after the operation. Polyuria was more evidenced in the UC group at 6 and 8 weeks (11/12, 12/12, respectively) than Sal-B (7/12, 6/12, respectively). Besides, swelling in the abdomen and limbs was noticed from 6 weeks in 50 % and 75% of rats from the UC group at 6 and 8 weeks, respectively, which indicated hypervolemia in the UC group. In contrast, no rats from sham and Sal-B groups showed clinical signs of swelling.

Renal Function Test

A significant increase ($p < 0.001$) in serum creatinine and BUN was observed in UC rats at the two- and four-week time points

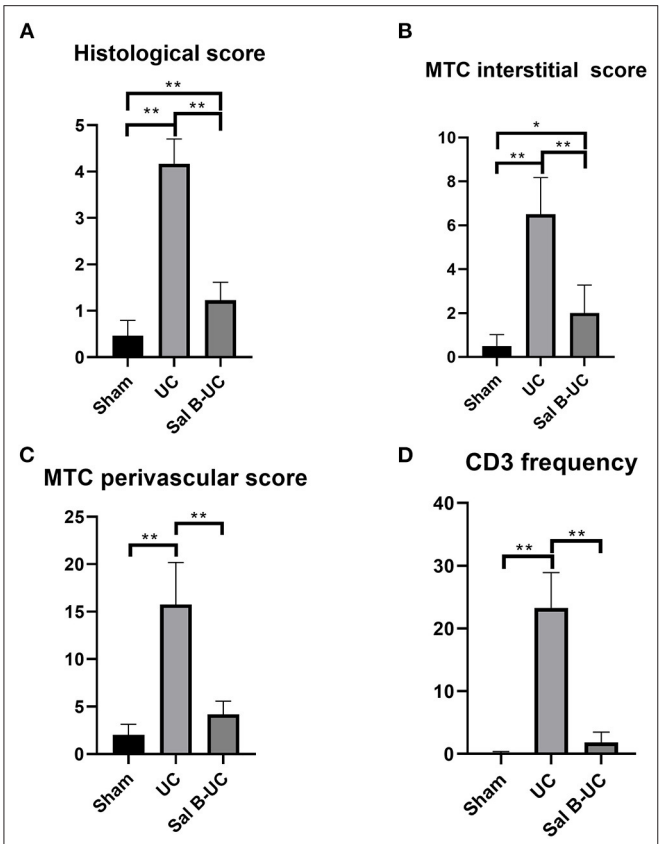

FIGURE 2 | Pathology score evaluation. **(A)** The histological score in the UC group was significantly higher than in the other groups. **(B)** Fibrosis intensity in the UC group was more than in the Sham and Sal B-UC groups as indicated by the blue staining of Masson's trichrome score. **(C)** Fibrosis in the perivascular area in the UC group was also high. **(D)** CD3+ T-lymphocyte frequency in the UC group was the highest among the three groups. The * symbol indicates the significant difference of $p < 0.05$. The ** symbol indicates the significant difference of $p < 0.01$.

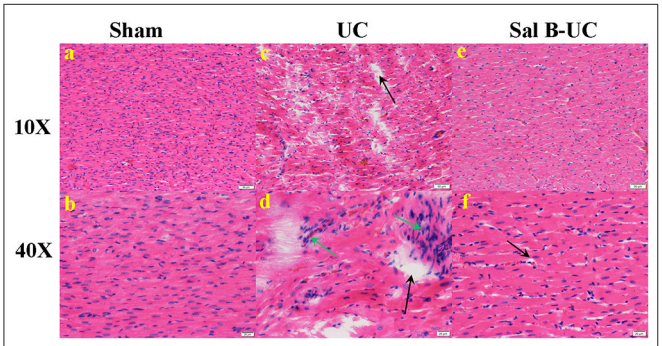

FIGURE 3 | Histological analysis. The histopathological images (10× and 40×) in the sham, UC, and Sal B-UC groups. **(A,B)** Myocytes are arrayed in parallel, with no inflammatory cell infiltration in the sham group. **(C,D)** Distorted cardiomyocytes, mononuclear cell infiltration (green arrow), and interstitial edema with necrosis (black arrow) in the UC group. **(E,F)** Mild edema with little inflammatory cell infiltration in the Sal B-UC group.

(**Figure 1**). Also, these biomarkers were significantly higher ($p < 0.001$) in the UC group than in the Sal B-UC group; nevertheless, serum creatinine and BUN were higher in the Sal B-UC group than in the sham group. And the percentage change analysis was shown in the **Supplementary Data**.

Conventional Echocardiography

Table 1 illustrates the cardiac morphology of the sham, UC group at 6 and 8 weeks in **Table 1**. Data collected at 2 and 4 weeks from sham and UC groups are presented in **Supplementary Tables S1A**. The UC group had higher IVSd, LVPWd, IVSs, LVPWS, and FS, but lower LVIDd and LVIDs, compared with the sham group. Moreover, the LVM and RWT were increased in the UC rats at all experimental intervals compared with the sham group. Based on these results, we confirmed that significant concentric LV hypertrophy occurred in the early stages of UC development. No difference was detected between the UC and Sal B-UC groups in IVSd, LVPWd, IVSs, LVPWS, FS, and LVIDs at the 6- and 8-week time points. Also, the observed IVSd and LVPWd values in the Sal B-UC group were < in the UC group but were still > in the sham group. In contrast, LVIDd, LVPWs, and FS were higher in the Sal B-UC group than in the UC group. Concentric hypertrophy was observed in the UC group at the two-, 6-, and 8-week time points because the LVM and RWT were significantly ($p = 0.001$ and $p < 0.001$) higher compared to the sham group. We noticed eccentric hypertrophy in the UC group at 4 weeks and in the Sal B-UC group at weeks 6 and 8. The LVM was increased in all groups at 8 weeks but the UC-SalB group showed the lowest value. These results indicate that Sal B delays the progressive development of hypertrophy.

Blood Pressure and Doppler Hemodynamic Results

Mitral inflow and TDI data are summarized in **Table 2.** Hemodynamic data collected at 2 and 4 weeks are presented in the **Supplementary Table S1B**. The HR in the UC group was higher than in the sham group at every time point. UC group showed higher blood pressure than the sham group. The Sal B-UC group showed lower systolic, diastolic, and mean arterial blood pressure than the UC. Systolic arterial blood pressure in the UC rats was higher than in the sham rats from the second week ($p < 0.001$). Also, no significant differences were detected in E, E', and E/E' between the three groups. IVPG data is illustrated in **Figure 1.** No difference was detected between the sham, UC, and Sal B-UC groups in total, basal, and mid-to-apical IVPG.

Speckle Tracking Echocardiography

The strain rates based on speckle tracking echocardiography are shown in **Table 3.** Strain rates collected at 2 and 4 weeks from sham and UC groups are presented in the **Supplementary Table S1C**. Compared with the sham group, the UC and Sal B-UC groups showed a significantly lower strain rate from the second to the eighth week ($p < 0.001$). In the UC group, once the strain rate had decreased in the mitral lateral segment in the second week, it did not show any further changes. The strain rate decreased in the second week in the middle lateral segment,

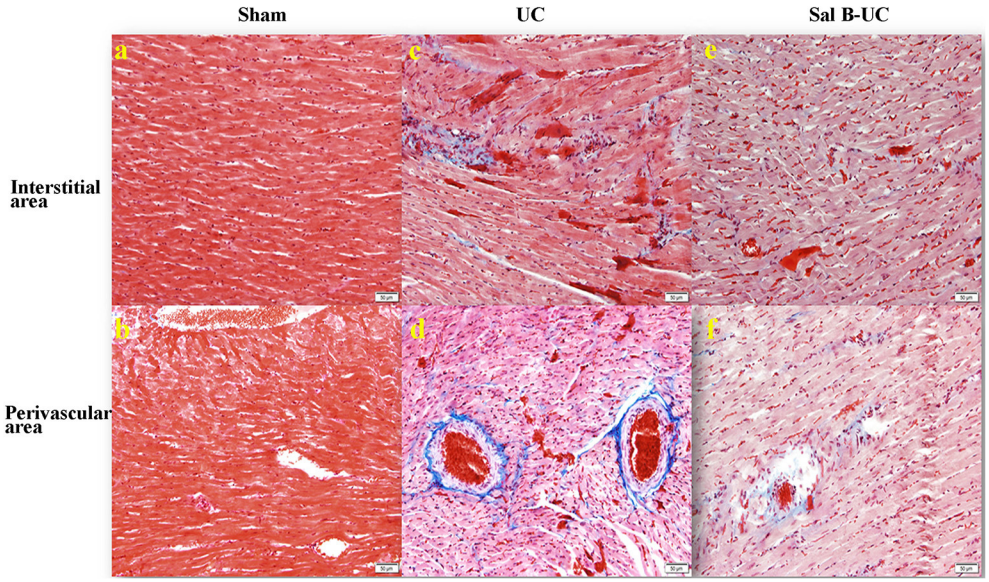

FIGURE 4 | Masson's trichrome staining. The Masson's trichrome images of the interstitial and perivascular area in the sham, UC, and Sal B-UC groups (50 μm). The light blue staining indicates the severity of cardiac fibrosis. In the sham group, fibrosis was not observed at either the interstitial level **(A)** or the perivascular area **(B).** In the UC group, severe fibrosis was observed at both interstitial levels **(C)** and the perivascular area **(D)**. In the Sal B-UC group, moderate light blue staining was present at the two levels **(E,F)**.

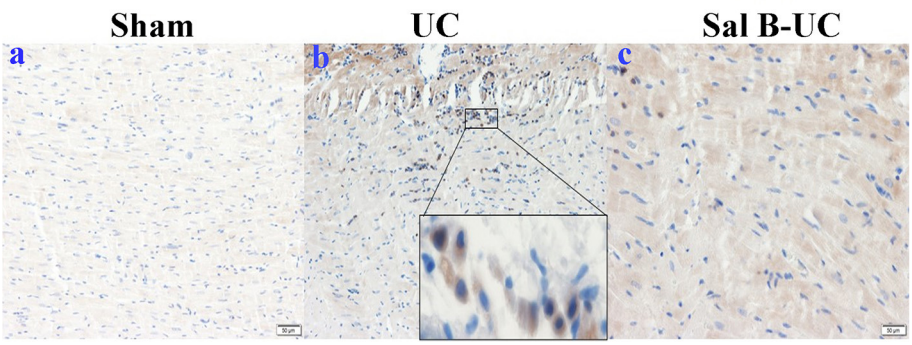

FIGURE 5 | Immunohistochemical (IHC) staining of CD3. The IHC staining of CD3 in the sham, UC, and Sal B-UC groups. CD3-T-lymphocytes were not recognized in the sham group **(A).** The number of CD3 infiltrations (brown color) was significantly increased in the UC group **(B).** A limited number of CD3+ was observed in the Sal B-UC group **(C)**.

and further diminished myocardial function was observed in the fourth week (p for time = 0.202). In the other five segments, the p-value for the time was <0.001, and the strain rate in the UC group decreased compared with the sham group, indicating fluctuating during UC development. The Sal B-UC group showed a similar level of myocardial movement to the UC group, and the strain rate in the Sal B-UC group was significantly lower than in the sham group ($p < 0.001$).

Histopathological Findings

To detect the cellular changes underlying the development of uremic cardiomyopathy in rats, we stained heart tissue with H&E and Masson's trichrome. The histopathological score was significantly higher ($p < 0.001$) in the UC group compared to the sham group (**Figure 2A**). A significant difference ($p < 0.001$) was observed between the Sal B-UC group and the sham group regarding their histopathological scores (**Figure 2B**). However, the score in the Sal B-UC group was much lower than the score of the UC group (**Figure 2C**). And we find CD3+ T-lymphocyte frequency in the UC group was the highest among the three groups (**Figure 2D**). The inflammatory changes in the UC group were represented in the form of inflammatory cell infiltration (especially mononuclear cell infiltration in **Figure 3**), severe degeneration and necrosis in cardiomyocytes, and increased size of cardiac myocytes compared to the other groups. Interstitial edema, as well as distorted cardiac muscle fibers, was also clearly observed in the UC group compared with the sham group. Inflammatory cell infiltration and interstitial edema were mild

in the Sal B-UC group. Besides, we evaluated fibrosis by using Masson's trichrome to stain the interstitial collagen fibers as well as perivascular collagen in the three groups. A greater intensity of bright blue collagen staining was detected in the UC group compared to the other two groups, as shown in **Figure 4**, indicating that fibrosis occurred at the interstitial and perivascular levels. In addition, the intensity of fibrosis in the Sal B-UC group was less than in the sham group.

Immunohistochemical Staining of CD3

To characterize the kinetics of inflammatory cell recruitment in uremic cardiomyopathy, an antibody against a marker CD3 (T cell inflammatory marker) was immunohistochemically stained in the three groups. The quantification of CD3+T-lymphocyte infiltration in the UC group was significantly increased ($p < 0.001$) compared to the other groups (**Figure 5**). Additionally, inflammatory cell recruitment was lower in the Sal B-UC group compared with the sham group. Accumulation of CD3 cells in the heart tissue of UC rats indicated that the molecular mechanism underlying disease progression had occurred.

DISCUSSION

This study aimed to evaluate cardiac status during the development of UC and assess the treatment effect of Sal B. While chronic kidney disease (CKD), a progressive pathological condition, is a precursor to UC, the pathophysiology of UC is poorly understood. Therefore, we designed this experiment using novel non-invasive techniques (IVPG and 2DSTE) to evaluate cardiac function in UC. These techniques allowed us to track cardiac changes during UC development. Furthermore, we used histopathological analysis to track the pathological changes occurring in UC. The results have given us a deeper understanding of UC pathophysiology. Additionally, we used herbal medicine as a replacement for cardioprotective treatments. The functional and pathological information about Sal B's treatment effect has helped to further our understanding of UC and its management.

Serum concentrations of BUN and creatinine are the gold standard for clinical diagnosis of CKD (25). A 5/6 subtotal nephrectomy is the primary avenue for investigating CKD (26), not only because this model directly decreases functional nephrons, but it is also relevant to clinical patients (21). In the present study, CKD was confirmed in UC rats by elevating BUN and creatinine concentrations from the second week after 5/6 nephrectomy until the endpoint of monitoring. Clinical symptoms like polyuria and hypervolemia support the diagnosis of CKD. Sal B-UC group showed less polyuria and hypervolemia, which indicate Sal B have treatment effect in UC. Sal B alleviate UC by reversing the elevated BUN and creatinine concentrations at 6 and 8 weeks. A Previous study revealed that the impaired kidney function was ameliorated by Sal B *via* a reduction in epithelial-mesenchymal transition-related proteins. Epithelial-mesenchymal transition in renal fibrosis was promoted by Sal B through autophagy activation (27).

We detected multiple types of ventricular geometry in UC. Concentric hypertrophy (elevated RWT and LVM) was observed in UC rats at the two-, 6-, and 8-week time points, but eccentric hypertrophy was also observed at the 4-week time point, evidenced by increased LVM and normalized RWT in the UC rats. This could be explained by the fact that pressure and volume overload dominate at different stages of UC development (28). The consequence of ventricular geometry change in UC makes staging UC based on geometry and intraventricular blood flow challenging, so multiple way analysis becomes necessary for UC diagnosis.

Patients with different types of hypertrophies show differing responses to the same drugs, indicating that different mechanisms are responsible for eccentric and concentric hypertrophy (8). In concentric LV hypertrophy, the sympathetic nervous system is overactivated. The activation of beta-adrenoceptors in the heart results in cardiomyocyte hypertrophy and progressive heart failure (29), which is considered the primary mechanism of concentric hypertrophy (30). The development of eccentric hypertrophy involves mechanical stress and activation of the sympathetic nervous system. The mechanical stress on the LV from pressure overload is stronger than that caused by volume overload (31).

The mechanism by which Sal B is believed to enact its therapeutic effect is similar to that of beta-blockers, which are the first-line therapeutic drugs for concentric hypertrophy. Previously, we have shown that Sal B protects against concentric LV hypertrophy caused by pressure overload and that it prevents further hypertrophy without a pressure-lowering effect (12). In the present study, Sal B showed a potential therapeutic effect against UC. The treatment effect of Sal B was confirmed by preventing the progression of UC because we observed a significantly different histopathology score between the Sal B-UC and sham groups and a dramatic difference in pathology score between the Sal B-UC and UC groups.

Myocardial dysfunction occurred from weeks two through eight. Administration of Sal B did not reverse the decreased longitudinal strain rate at week 6 or 8. The hypertrophy in UC rats was not apparent until week 6, which implies that myocardial dysfunction occurred before the changes in ventricular geometry (32). Furthermore, we found severe edema and inflammation in myocardial tissues and severe interstitial and perivascular fibrosis in the UC group, which confirmed our expectation: myocardial dysfunction was caused by edema, inflammation, and fibrosis in UC. However, edema, inflammation, and fibrosis in the Sal B-UC group were significantly lower than in the UC group ($p < 0.001$), but the strain rate was not significantly different. In other words, the inflammatory reaction was associated with myocardial dysfunction, while the severity of fibrosis was not related to myocardial function in UC. The difference between CD3 positive cells in UC and Sal B-UC indicates that the treatment effect of Sal B decreased the acute inflammatory reaction.

As we mentioned before, UC-associated LV hypertrophy results from complex pressure overload, volume overload, and the uremic state itself. Sal B alleviates UC by improving renal function, decreasing blood pressure, and reducing edema, inflammation, and fibrosis in the myocardial tissue. This pathophysiology mechanism indicates that cardiomyocyte is not the main target of Sal B treatment.

In the current work, resting HR was evaluated under equivalent anesthesia for all rats. Our previous work showed that HR had a weak influence on IVPG, so HR was not intentionally controlled (11). The resting HR in the UC group was higher than in the sham group at every time point following the operation. Elevated resting HR correlates with a higher risk of death (33), which indicates that cardiac function was damaged in the UC group. The impairment was not completely reversed by the Sal B administration.

No differences in IVPG were detected among the groups because IVPG is non-invasive technology concentrating on intracardiac flow, this result indicates that the flow was intact in UC. Basal IVPG correlates with E wave velocity, and mid-to-apical IVPG correlates with myocardial movement (10). Combined with the fact that E wave velocity, E', and E/E' also showed no differences between the groups, it is easily concluded that LA pressure was not elevated in the UC group. The usefulness of 2DSTE and IVPG for assessing cardiac function was confirmed in rats before (12, 13, 34). Myocardium dysfunction detected by STE combined with the fact that intracardiac flow was not disturbed in UC to provide us with an interesting conclusion: subtotal nephrectomy induced UC rat model could be used for cardiovascular drug selection. Because only the myocardium was affected in the UC rat model, the effect of medicine designed for myocardium-related diseases could be examined specifically. This information raises a question: did primary and secondary cardiovascular diseases like UC affect the myocardium differently? This will next stage of our research.

The main difference in the mechanism responsible for forming concentric and eccentric hypertrophy is the mechanical stress on the ventricle wall (8, 31). The changes in ventricular morphology indicate that mechanical stress fluctuates during the development of UC. Myocardial dysfunction occurred in the UC group from weeks two through eight, LV mass and RWT fluctuated, eventually leading to a variable but not a significantly different level of active relaxation in the UC group, confirmed by mid-to-apical IVPG.

Previously, scientists documented the structural and functional disorders of UC in mice (35, 36). Hamzaoui et al. pointed out the fact that different outcomes can be observed between two strains of mice emphasizes the importance of carefully comparing conclusions from the scientific literature (35). But the detailed echocardiography parameter and inflammatory markers have never been reported before. To our knowledge, this is the first study to document the detailed structural and functional outcomes of Sal B treatment in UC using echocardiography and histopathology. The data from this paper will be useful in further pharmacological and cardiovascular studies. For the veterinary field, this paper not only provided precious information about the pathophysiology of UC by novel ultrasound technique, but it will also encourage veterinarians to use this novel ultrasound technique in clinical practices in the future.

LIMITATIONS

Detailed molecular investigations were not performed in the current study. CD45 and RNA were not measured, because this research is concentrating on evaluating non-invasive cardiac function in UC.

CONCLUSION

Myocardial dysfunction occurs before ventricular morphological changes during the development of UC, and intracardiac flow was not affected in UC. Both eccentric hypertrophy and concentric hypertrophy were observed in UC, while only eccentric hypertrophy was observed in Sal B-treated rats. Sal B alleviates cardiomyopathy and prevents further development in the UC model. This study demonstrated increased ventricular stiffness and fibrosis in UC. Further studies are warranted to clarify the molecular pathways of Sal B for the treatment of UC.

DATA AVAILABILITY STATEMENT

The datasets presented in this study can be found in online repositories. The names of the repository/repositories and accession number(s) can be found in the article/**Supplementary Material**.

ETHICS STATEMENT

The animal study was reviewed and approved by Institutional Animal Care and Use Committee of the Tokyo University of Agriculture and Technology.

AUTHOR CONTRIBUTIONS

DM: conceptualization, methodology, software, writing—original draft, writing—review and editing, and visualization. AM and AE: methodology, software, and writing—review and editing. TY and KN: resources and data curation. HH: conceptualization and project administration. HE-H: investigation. KT: methodology and software. YZ: data and curation. ZZ and RT: project administration. All authors contributed to the article and approved the submitted version.

SUPPLEMENTARY MATERIAL

The Supplementary Material for this article can be found online at: https://www.frontiersin.org/articles/10.3389/fvets.2022.905759/full#supplementary-material

REFERENCES

1. Virani SS, Alonso A, Benjamin EJ, Bittencourt MS, Callaway CW, Carson AP, et al. Heart disease and stroke statistics-−2020 update: a report from the American heart association. *Circulation.* (2020) 141:e139–596. doi: 10.1161/CIR.0000000000000746
2. Kong P, Christia P, Frangogiannis NG. The pathogenesis of cardiac fibrosis. *Cell Mol Life Sci.* (2014) 71:549–74. doi: 10.1007/s00018-013-1349-6

3. Chamieh CEL, Liabeuf S, Massy Z. Uremic toxins and cardiovascular risk in chronic kidney disease: what have we learned recently beyond the past findings? *Toxins.* (2022) 14:280. doi: 10.3390/toxins14040280
4. Garikapati K, Goh D, Khanna S, Echampati K. Uraemic cardiomyopathy: a review of current literature. *Clin Med Insights Cardiol.* (2021) 15:1179546821998347. doi: 10.1177/1179546821998347
5. de Albuquerque Suassuna PG,Sanders-Pinheiro H, de Paula RB. Uremic cardiomyopathy: a new piece in the chronic kidney disease-mineral and bone disorder puzzle. *Front Med.* (2018) 5:20. doi: 10.3389/fmed.2018.00206
6. Alhaj E, Alhaj N, Rahman I, Niazi TO, Berkowitz R, Klapholz M. Uremic cardiomyopathy: an underdiagnosed disease. *Congest Heart Fail.* (2013) 19:E40–5. doi: 10.1111/chf.12030
7. Ganau A, Devereux RB, Roman MJ, de Simone G, Pickering TG, Saba PS, et al. Patterns of left ventricular hypertrophy and geometric remodeling in essential hypertension. *J Am Coll Cardiol.* (1992) 19:1550–8. doi: 10.1016/0735-1097(92)90617-V
8. Nauta JF, Hummel YM, Tromp J, Ouwerkerk W, van der Meer P, Jin X, et al. Concentric vs. eccentric remodelling in heart failure with reduced ejection fraction: clinical characteristics, pathophysiology and response to treatment. *Eur J Heart Fail.* (2020) 22:1147–55. doi: 10.1002/ejhf.1632
9. Kasner M, Westermann D, Steendijk P,Gaub R, Wilkenshoff U, Weitmann K, et al. Utility of doppler echocardiography and tissue doppler imaging in the estimation of diastolic function in heart failure with normal ejection fraction: a comparative doppler-conductance catheterization study. *Circulation.* (2007) 116:63–747. doi: 10.1161/CIRCULATIONAHA.106.661983
10. Iwano H, Kamimura D, Fox E, Hall M, Vlachos P, Little WC. Altered spatial distribution of the diastolic left ventricular pressure difference in heart failure. *J Am Soc Echocardiogr.* (2015) 28:597–605 e1. doi: 10.1016/j.echo.2015.01.002
11. Ma D, Matsuura K, Takahashi K, Shimada K, Yoshida T, Chantawong P, et al. Effect of mitral inflow pattern on intraventricular pressure gradients in hypertension rats. *J Hypertens.* (2019) 37:e157–8. doi: 10.1097/01.hjh.0000572016.82030.e6
12. Ma D, Mandour AS, Yoshida T, Matsuura K, Shimada K, Kitpipatkun P, et al. Intraventricular pressure gradients change during the development of left ventricular hypertrophy: effect of salvianolic acid B and beta-blocker. *Ultrasound.* (2021) 29:229–40. doi: 10.1177/1742271X20987584
13. Yairo A, Mandour AS, Matsuura K, Yoshida T, Ma D, Kitpipatkun P, et al. Effect of loading changes on the intraventricular pressure measured by color m-mode echocardiography in rats. *Diagnostics.* (2021) 11:1403. doi: 10.3390/diagnostics11081403
14. Dandel M, Lehmkuhl H, Knosalla C, Suramelashvili N, Hetzer R. Strain and strain rate imaging by echocardiography—basic concepts and clinical applicability. *Curr Cardiol Rev.* (2009) 5:133–48. doi: 10.2174/157340309788166642
15. Kostis JB, Shelton B, Gosselin G, Goulet C, Hood Jr WB, Kohn RM, et al. Adverse effects of enalapril in the studies of left ventricular dysfunction (SOLVD). SOLVD Investigators. *Am Heart J.* (1996) 131:350–5. doi: 10.1016/S0002-8703(96)90365-8
16. Yan YY, Yang YH, Wang WW, Pan YT, Zhan SY, Sun MY, et al. Post-marketing safety surveillance of the salvia miltiorrhiza depside salt for infusion: a real world study. *PLoS ONE.* (2017) 12:e0170182 doi: 10.1371/journal.pone.0170182
17. Wang C, Luo H, Xu Y, Tao L, Chang C, Shen X. Salvianolic acid B-alleviated angiotensin ii induces cardiac fibrosis by suppressing NF-kappaB pathway *in vitro*. *Med Sci Monit.* (2018) 24:7654–64. doi: 10.12659/MSM.908936
18. Li CL, Liu B, Wang ZY, Xie F, Qiao W, Cheng J, et al. Salvianolic acid B improves myocardial function in diabetic cardiomyopathy by suppressing IGFBP3. *J Mol Cell Cardiol.* (2020) 139:98–112. doi: 10.1016/j.yjmcc.2020.01.009
19. Wu Y, Xu S, Tian XY. The effect of salvianolic acid on vascular protection and possible mechanisms. *Oxid Med Cell Longev.* (2020) 2020:5472096. doi: 10.1155/2020/5472096
20. Chen YF, Jaw I, Shiao MS, Tsai TH. Determination and pharmacokinetic analysis of salvianolic acid B in rat blood and bile by microdialysis and liquid chromatography. *J Chromatogr A.* (2005) 1088:140–5. doi: 10.1016/j.chroma.2005.01.096
21. Santos LS, Chin EW, Ioshii SO, Tambara Filho R. Surgical reduction of the renal mass in rats: morphologic and functional analysis on the remnant kidney. *Acta Cir Bras.* (2006) 21:252–7. doi: 10.1590/S0102-86502006000400012
22. Tsukamoto A, Uchida K, Maesato S, Sato R, Kanai E, and Inomata T. Combining isoflurane anesthesia with midazolam and butorphanol in rats. *Exp Anim.* (2016) 65:223–30. doi: 10.1538/expanim.15-0113
23. Kobayashi M, Takahashi K, Yamada M, Yazaki K, Matsui K, Tanaka N, et al. Assessment of early diastolic intraventricular pressure gradient in the left ventricle among patients with repaired tetralogy of fallot. *Heart Vessels.* (2017) 32:1364–74. doi: 10.1007/s00380-017-1011-6
24. Shi K, Zhao W, Chen Y, Ho WT, Yang P, Zhao ZJ. Cardiac hypertrophy associated with myeloproliferative neoplasms in JAK2V617F transgenic mice. *J Hematol Oncol.* (2014) 7:25. doi: 10.1186/1756-8722-7-25
25. Smith GL, Shlipak MG, Havranek EP, Foody JM, Masoudi FA, Rathore SS, et al. Serum urea nitrogen, creatinine, and estimators of renal function: mortality in older patients with cardiovascular disease. *Arch Intern Med.* (2006) 166:1134–42. doi: 10.1001/archinte.166.10.1134
26. Gava AL, Freitas FP, Balarini CM, Vasquez EC, Meyrelles SS. Effects of 5/6 nephrectomy on renal function and blood pressure in mice. *Int J Physiol Pathophysiol Pharmacol.* (2012) 4:167–73 PMCID: PMC3466491
27. He Y, Lu R, Wu J, Pang Y, Li J, Chen J, et al. Salvianolic acid B attenuates epithelial-mesenchymal transition in renal fibrosis rats through activating Sirt1-mediated autophagy. *Biomed Pharmacother.* (2020) 128:110241. doi: 10.1016/j.biopha.2020.110241
28. Wang X, and Shapiro JI. Evolving concepts in the pathogenesis of uraemic cardiomyopathy. *Nat Rev Nephrol.* (2019) 15:159–75. doi: 10.1038/s41581-018-0101-8
29. Xu Q, Dalic A, Fang L, Kiriazis H, Ritchie RH, Sim K, et al. Myocardial oxidative stress contributes to transgenic beta(2)-adrenoceptor activation-induced cardiomyopathy and heart failure. *Br J Pharmacol.* (2011) 162:1012–28 doi: 10.1111/j.1476-5381.2010.01043.x
30. Zhao M, Fajardo G, Urashima T, Spin JM, Poorfarahani S, Rajagopalan V, et al. Cardiac pressure overload hypertrophy is differentially regulated by beta-adrenergic receptor subtypes. *Am J Physiol Heart Circ Physiol.* (2011) 301:H1461–70. doi: 10.1152/ajpheart.00453.2010
31. Mihl C, Dassen WR, Kuipers H. Cardiac remodelling: concentric versus eccentric hypertrophy in strength and endurance athletes. *Neth Heart J.* (2008) 16:129–33. doi: 10.1007/BF03086131
32. Winterberg PD, Jiang R, Maxwell JT, Wang B, Wagner MB. Myocardial dysfunction occurs prior to changes in ventricular geometry in mice with chronic kidney disease (CKD). *Physiol Rep.* (2016) 4:e12732. doi: 10.14814/phy2.12732
33. Böhm M, Swedberg K, Komajda M, Borer JS, Ford I, Dubost-Brama A, et al. Heart rate as a risk factor in chronic heart failure (SHIFT): the association between heart rate and outcomes in a randomised placebo-controlled trial. *Lancet.* (2010) 376:886–94. doi: 10.1016/S0140-6736(10)61259-7
34. Kitpipatkun P, Matsuura K, Shimada K, Uemura A, Goya S, Yoshida T, et al. Key factors of diastolic dysfunction and abnormal left ventricular relaxation in diabetic rats. *J Med Ultrason.* (2020) 47:347–56. doi: 10.1007/s10396-020-01021-x
35. Hamzaoui M, Djerada Z, Brunel V, Mulder P, Richard V, Bellien J, et al. 5/6 Nephrectomy induces different renal, cardiac and vascular consequences in 129/Sv and C57BL/6JRj

mice. *Sci Rep.* (2020) 10:1524. doi: 10.1038/s41598-020-58393-w

36. Kennedy DJ, Elkareh J, Shidyak A, Shapiro AP, Smaili S, Mutgi K, et al. Partial nephrectomy as a model for uremic cardiomyopathy in the mouse. *Am J Physiol Renal Physiol.* (2008) 294:F450–4. doi: 10.1152/ajprenal.00472.2007

Conflict of Interest: The authors declare that the research was conducted in the absence of any commercial or financial relationships that could be construed as a potential conflict of interest.

Publisher's Note: All claims expressed in this article are solely those of the authors and do not necessarily represent those of their affiliated organizations, or those of the publisher, the editors and the reviewers. Any product that may be evaluated in this article, or claim that may be made by its manufacturer, is not guaranteed or endorsed by the publisher.

frontiers | Frontiers in Veterinary Science

CASE REPORT
published: 17 June 2022
doi: 10.3389/fvets.2022.913862

Colonic Intramural Hematoma in a Cat: A Case Report

Ti-Chiu Hsu[1,2], *Lee-Shuan Lin*[1,2,3,4*], *Cheng-Shu Chung*[5,6], *Chuan Chiang*[7], *Hsien-Chieh Chiu*[8] *and Ping-Hsun Huang*[8]

[1] *Laboratory of Veterinary Diagnostic Imaging, Department of Veterinary Medicine, College of Veterinary Medicine, National Pingtung University of Science and Technology, Pingtung, Taiwan,* [2] *Division of Diagnostic Imaging, Veterinary Medical Teaching Hospital, National Pingtung University of Science and Technology, Pingtung, Taiwan,* [3] *School of Dentistry, College of Dental Medicine, Kaohsiung Medical University, Kaohsiung, Taiwan,* [4] *Department of Medical Imaging and Radiological Sciences, College of Health Sciences, Kaohsiung Medical University, Kaohsiung, Taiwan,* [5] *Laboratory of Veterinary Surgery, Department of Veterinary Medicine, College of Veterinary Medicine, National Pingtung University of Science and Technology, Pingtung, Taiwan,* [6] *Division of Small Animal Surgery, Veterinary Medical Teaching Hospital, National Pingtung University of Science and Technology, Pingtung, Taiwan,* [7] *UniCore Animal Hospital, Taipei City, Taiwan,* [8] *Tzuoo Ann Animal Hospital, Taipei City, Taiwan*

Colonic intramural hematoma is a rare condition in humans and companion animals. Its clinical presentation in cats has not previously been reported. An 8-year-old male American shorthair cat presented with acute onset of constipation and anorexia for 3 days. Laboratory examination indicated mild elevation of alanine aminotransferase, globulin, and total protein levels. Complete blood count was normal. Radiographs revealed a soft tissue opacity mass located caudodorsally to the urinary bladder, causing narrowing of the descending colonic lumen. Sonography showed a heteroechogenic intraluminal mass containing liquefied content between the submucosal and muscular layers of the descending colon. On computed tomographic images, the mass contained two different attenuated contents with an interface. Colonoscopy was then performed for intestinal biopsy, and the contents observed in the intraluminal mass were drained *via* surgical evacuation and considered as blood clots. Supportive medical treatment, including antibiotics and fecal softener, was administered, and the clinical signs resolved uneventfully. Mild chronic proctitis without apparent malignancy was confirmed histopathologically, and no recurrence was observed after more than 14 months, and thus a colonic intramural hematoma was presumptively diagnosed. The information provided by multimodal imaging of the mass was essential for the diagnosis and determination of the treatment in this case.

Keywords: cat, colonic intramural hematoma, colonoscopy, computed tomography, ultrasonography

OPEN ACCESS

Edited by:
Haney Samir,
Cairo University, Egypt

Reviewed by:
Hossam R. El-Sherbiny,
Cairo University, Egypt
Ibrahim Emam,
Cairo University, Egypt

***Correspondence:**
Lee-Shuan Lin
linleeshuan@gmail.com

Specialty section:
This article was submitted to Veterinary Imaging, a section of the journal Frontiers in Veterinary Science

Received: *06 April 2022*
Accepted: *16 May 2022*
Published: *17 June 2022*

Citation:
Hsu T-C, Lin L-S, Chung C-S, Chiang C, Chiu H-C and Huang P-H (2022) Colonic Intramural Hematoma in a Cat: A Case Report. Front. Vet. Sci. 9:913862. doi: 10.3389/fvets.2022.913862

INTRODUCTION

Colonic intramural hematoma is rare in humans and animals and occurs mostly secondary to blunt abdominal trauma, anticoagulant therapy, coagulopathies, or intestinal neoplasia in humans (1). In humans, spontaneous colonic hematoma is most commonly associated with blunt trauma (2). Risk factors include bleeding diathesis, such as those experienced by patients undergoing anticoagulant therapy or with coagulopathies (3). Few cases secondary to synchronous colon cancer for patients who underwent hemicolectomy have also been reported (1, 4). Rarely, it occurs secondary to vaginal delivery (5). Clinically, colonic intramural hematoma usually causes lower abdominal pain, lethargy, anorexia, and constipation in humans. The diagnosis of colonic intramural hematoma in

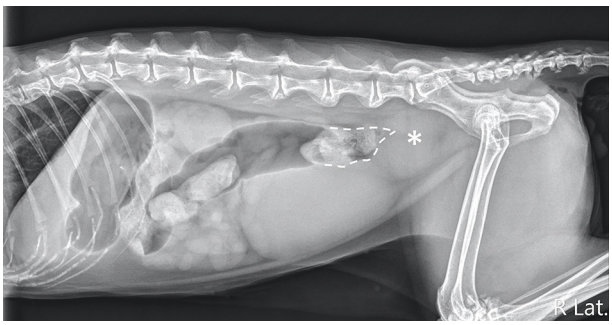

FIGURE 1 | Right lateral projection of the abdomen. An ovoid-shaped, soft-tissue opacity mass (asterisk) caudodorsal to the urinary bladder was noted, causing a narrowing of the descending colonic lumen (dotted line).

humans is mainly based on radiology, such as contrast-enhanced computed tomography (CT) (1). Treatment may vary from case to case, including surgical and conservative management; however, its clinical presentation, diagnosis, and treatment outcome have not been previously described in cats. Therefore, this report aimed to present the multimodal imaging findings of colonic intramural hematoma in a cat and to describe the successful treatment with surgical evacuation.

CASE DESCRIPTION

An 8-year-old neutered male American shorthair cat was referred to the Unicore Animal Hospital because of decreased defecation for 1 week and acute onset of constipation with anorexia 3 days prior. Physical examination revealed no apparent colonic narrowing on rectal palpation.

Laboratory examination was performed for preanesthetic evaluation and revealed mild elevated levels of alanine aminotransferase (152 U/L; reference range, 12–130 U/L), globulin (5.9 g/dl; reference range, 2.8–5.1 g/dl), and total protein (9.3 g/dl; reference range, 5.7–8.9 g/dl). The complete blood count was normal.

Abdominal radiography (MODEL BLR-500A; Toshiba, Tochigi, Japan) of the right lateral, left lateral, and ventrodorsal projections was performed while the cat was awake, and a large, well-defined, ovoid-shaped, soft tissue opacity mass was observed caudodorsal to the urinary bladder at the sixth lumbar vertebra to the sacrum level, causing dorsal displacement, and narrowing of the descending colon (**Figure 1**). The mass was approximately 3.1 cm in height and 3.6 cm in length in the right lateral abdominal projection. Dilation of the colon was observed, with gas accumulation cranial to the narrowed location. Radiographic differential diagnoses included a colonic intraluminal neoplasia/foreign body, an intramural neoplasia/abscess/hematoma, or an extramural neoplasia/granuloma. Considering the rapid progression of the disease, abscesses and hematomas were mostly suspected.

Abdominal ultrasonography was performed with an ultrasound device (Vivid E80; GE Healthcare, IL, USA) equipped with a linear transducer (11 L-D, GE Healthcare; 4–10 MHz), and the patient was positioned in dorsal recumbency under general anesthesia. The sagittal and transverse planes of ultrasonographic

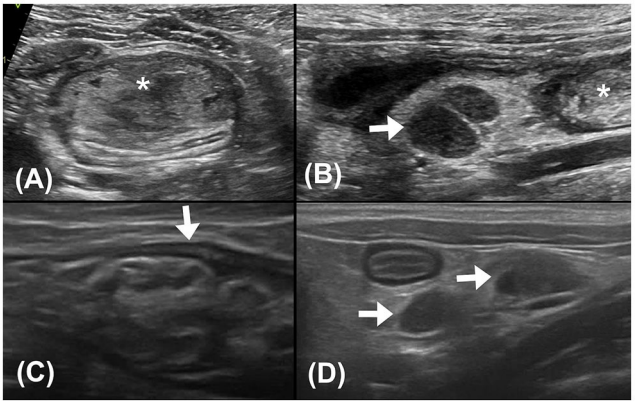

FIGURE 2 | (A) Transverse plane ultrasound image of the descending colon. A hyperechoic mass (asterisk) with heteroechogenicity between the submucosal and muscular layers of the descending colon was seen. **(B)** Sagittal plane ultrasound image of the colonic lymph nodes (0.6 cm in thickness and 0.9 cm in length). The colonic lymph nodes (arrow) adjacent to the mass (asterisk) appeared enlarged and hypoechogenic. **(C)** Follow-up sagittal plane ultrasound image of the descending colon 2 weeks after surgical evacuation. No mass effect was noted at the affected site. The intestinal layering (arrow) was relatively normal, with a thickened and corrugated mucosal layer. **(D)** Follow-up sagittal plane ultrasound image of colonic lymph nodes 2 weeks after surgical evacuation. The colonic lymph nodes (arrows) were smaller (0.4 cm in thickness and 0.7 cm in length) and with homogeneous echogenicity.

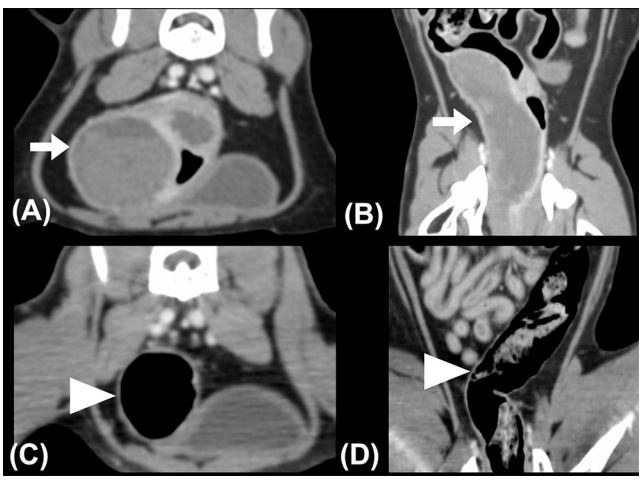

FIGURE 3 | (A) Transverse and **(B)** dorsal plane CT images revealed intramural masses (arrows) in the descending colon. Hyperattenuating contents accumulated on the gravity-dependent side of the mass, exhibiting two different layers within the mass with a clear interface. The whole descending colon was deviated to the right on the pre-treatment CT images. **(C)**Transverse and **(D)** dorsal plane CT images obtained 1-month post-treatment. Normal colonic intestinal layering was noted, while the colonic lymph nodes (not shown) appeared normal in size and attenuation. The descending colon was located in the left caudal abdominal cavity. The patient's right side is shown on the left image.

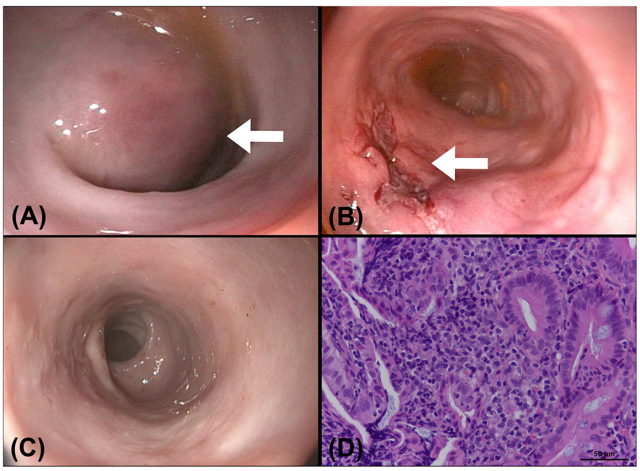

FIGURE 4 | A colonoscopy was performed after a CT examination. **(A)** A round submucosal mass (arrow) with an intact mucosa was noticed at the descending colon, causing narrowing of the colonic lumen. **(B)** The colonoscopic image obtained after surgical evacuation of the contents in the mass: the incision wound (arrow) was kept open for drainage of the remaining blood clots. **(C)** Image of a follow-up colonoscopy 1 month after evacuation: the incision wound was well-healed, and no recurrence was seen. **(D)** Pathology of the colonic specimen showed chronic proctitis and lymphoid hyperplasia of the colon. A small number of lymphocytes and plasma cells with fewer neutrophils are noted multifocally in the lamina propria of colon (H&E stain, bar = 50 μm, 400×).

images revealed a focal heteroechogenic intramural mass located between the submucosal and muscular layers of the descending colon (∼2.6 cm in width and 1.3 cm in height), causing extreme compression and occlusion of the colonic lumen. The intramural mass was liquefied and floating. Enlarged colonic lymph nodes were observed cranial to the intramural colonic mass, indicating hypoechogenicity (0.6 cm in thickness and 0.9 cm in length). Considering the location and echogenicity of the mass, colonic intramural neoplasia with regional colonic lymphadenopathy was mainly suspected, whereas abscess and hematoma could not be completely excluded (**Figures 2A,B**).

A triple-phase CT examination (Discovery 690; GE Healthcare, IL, USA) was performed to obtain further information. On CT images, a large, fluid-to-soft tissue attenuating mass was noted between the submucosal and serosal layers, arising from the middle portion of the descending colon, extending caudally to the distal descending colon immediately cranial to the rectum, and spanning approximately 8 cm in length. The colonic intramural mass contained two different attenuating contents with an interface at all three phases: hyperattenuating materials (40–60 Hounsfield Unit, HU) accumulating on the gravity-dependent side and lower attenuating contents (30–40 HU) on the upper side (**Figures 3A,B**). Ultrasound-guided fine-needle aspiration was performed, and ∼8 ml of non-agglutinated blood was drained. The tentative diagnosis was intraluminal hematoma based on cytologic results.

Lactulose (2 ml per time, SID, PO) was prescribed for 1 week to resolve constipation. The cat underwent colonoscopy (EVIS EXERA III, CLV-190, PCF-PH190L, Olympus Corporation, Tokyo, Japan) 1 week later at the Tzuoo Ann Animal Hospital, and a mass with an intact mucosal surface and spotty oozing blood was observed (**Figure 4A**). A speculum was used to approach the mass from the anus and make an incision with a scalpel because it was difficult to penetrate the mass with biopsy forceps. A large number of blood clots were aspirated from the mass. A cotton swab was used to confirm the integrity of the outer intestinal wall and intestinal biopsies of the lesions were sampled with Blakesley nasal forceps (N2990, STORZ, Tuttlingen, Germany). Colonoscopy was reperformed to ensure that there was no active bleeding after surgical evacuation and biopsy (**Figure 4B**). Histologically, the specimens revealed that mucosal architectures and multiple hyperplastic lymphoid foci were noted at the junction of the mucosa and submucosa. A small number of multifocal lymphocytes and plasma cells were also noted in the lamina propria, with fewer neutrophils. The patient was diagnosed as chronic proctitis with lymphoid hyperplasia (**Figure 4D**).

After colonoscopy, amoxicillin (20 mg/kg, BID, PO), lysozyme (17 mg/kg, BID, PO), L-glutamine (27 mg/kg, BID, PO), tranexamic acid (20 mg/kg, BID, PO), and lactulose (2 ml per time, SID, PO) were prescribed for 2 weeks. Constipation resolved after surgical evacuation, only scant blood was observed in the stool for 4 days. No apparent defecation difficulty, anorexia, or abdominal pain was noted. Follow-up ultrasonography (MyLab^{TM} Class C, LA435, 6–18 MHz, Esaote, Italy) performed 2 weeks later at the Tzuoo Ann Animal Hospital revealed that the affected colon appeared to display normal layering with thickened and corrugated mucosa. The colonic lymph nodes showed homogeneous echogenicity and smaller size than before (0.4 cm in thickness and 0.7 cm in length; **Figures 2C,D**). A follow-up CT (Aquilion, Toshiba Medical Systems Corporation, Tochigi, Japan) (**Figures 3C,D**), colonoscopy (**Figure 4C**), and laboratory examination were performed 1 month later, and showed no mass effect or abnormality during the examinations, while globulin content returned to normal levels and blood coagulation was normal. No relative clinical signs were noted in follow-up telephone interviews after 14 months. The timeline of medical interventions is illustrated in **Figure 5**.

DISCUSSION

Intestinal intramural hematoma is rare in companion animals, and only five cases have been reported in dogs in three previous studies (6–8). Based on our knowledge, this is the first report describing intestinal intramural hematoma in cats. Intestinal intramural hematomas may occur in any part of the intestine. Small intestinal intramural hematomas in dogs are mostly associated with pancreatitis or anticoagulant therapy, resulting in upper abdominal pain and vomiting. In the literature on human patients, the small intestine is affected much more frequently than the large intestine, due to the fixed position of

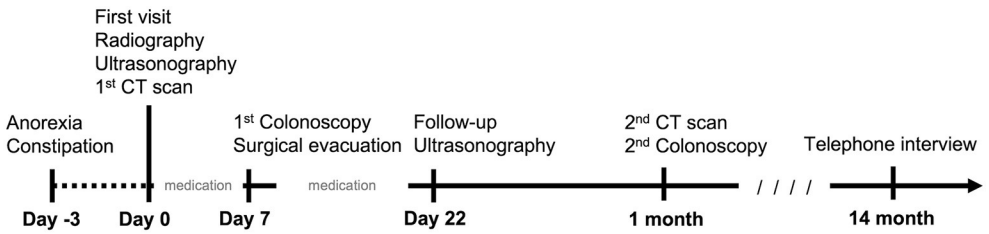

FIGURE 5 | A brief timeline of the medicine intervention in the cat. Clinical signs presented 3 days prior to first visit. Radiography, ultrasonography, and CT examination were performed on the same day of the first visit. Palliative medication was administrated for 7 days. The surgical intervention was performed 7 days later. Post-operative medicine was administrated for 2 weeks. The patient revisited on day 22. A follow-up CT scan and colonoscopy were conducted 1 month later. After 14 months, a final telephone interview was conducted.

the duodenum anterior to the vertebral column, the force of a blow tends to shear the duodenum held in this fixed position in traumatic cases (6, 9). Additionally, pancreatic disease has been associated with intramural hematoma of the duodenum (9, 10). Colonic intramural hematomas are mostly caused by blunt abdominal trauma, anticoagulant therapy, coagulopathies, or intestinal neoplasia, and large colonic hematomas lead to colonic obstruction, resulting in lower abdominal pain, decreased defecation, vomiting, nausea, and abdominal distention (1). No colonic intramural hematoma has been reported in dogs or cats. In our case, the hematoma was located in the descending colon, causing obstruction of the colonic lumen and resulting in a progressively decrease in defecation and acute onset of constipation with anorexia.

Anticoagulant therapy, foreign bodies, coagulopathies, and secondary blunt abdominal trauma are common causes of colonic hematoma in humans (11). Hematological examination showed a normal coagulopathy function and no clinical history of associated anticoagulation therapy in our case, and no specific findings regarding foreign bodies were noted in the whole digestive system. However, blunt abdominal trauma could not be completely excluded, although it might not have been noticed by the owner. Colonic intramural hematoma induced by blunt abdominal trauma appeared with no apparent cutaneous wound on the first day in human patients, but the acute onset of lower abdominal pain and constipation occurred 1 day later, which is similar to the acute onset of constipation in our case (1, 11). In the veterinary literature for dogs and horses, small intestinal intramural hematomas are usually noted within the tunica muscularis or between the submucosa and tunica muscularis; whereas large intestinal intramural hematomas in houses are usually located in the submucosa (6, 8, 12–14). The intestinal mucosa contains numerous blood and lymph vessels, and hematomas are produced at the tunica muscularis and submucosal layer upon tearing of the terminal artery vessels as they leave the mesentery to penetrate the muscular layer of the intestinal wall, which may explain why the colonic intramural hematoma in this cat was located between the submucosa and muscular layer on ultrasonographic images (15–18). However, in our case, only the mucosa and submucosa could be pathologically evaluated because an invasive procedure for full-thickness intestinal biopsy was not performed at the owner's request.

In our case, a large soft tissue opacity mass was noted in the caudal abdomen, causing dorsal deviation and extreme occlusion of the descending colon and leading to megacolon, which is mostly associated with constipation. Considering the location, the mass was mainly suspected to have arisen from the distal descending colon. However, radiographs only show the location of the mass and cannot differentiate whether it is intraluminal, intramural, or extramural mass. Considering the acute onset of clinical signs, hematoma, abscess, and foreign body were suspected and the likelihood of a granuloma is lower (19). Neoplasia could not be completely excluded, due to the variable duration of onset of clinical signs (20–22). Further diagnostic imaging examinations are required to identify the origin of the mass.

This cat showed a heterogeneous echoic, liquefied mass between the submucosal and muscular layers in the descending colon with regional colonic lymphadenopathy. The echogenicity was similar to that observed in feline colonic neoplasia or feline gastrointestinal eosinophilic sclerosing fibroplasia (FGESF); however, inconsistent with the loss of layering, our case showed intact intestinal layering (23–25). Fluid-filled contents may indicate an abscess; however, homogeneous or anechoic contents are more commonly seen in abscesses (24, 26, 27). In our case, radiographic and ultrasonographic findings together confirmed a colonic intramural mass between the submucosal and muscular layers, but differentiation from the hematoma sonographically was difficult, as similar lesions might also present in intramural neoplasia, abscesses, and FGESF. Considering the large extent of the mass and multiple colonic lymphadenopathies, a more comprehensive examination, such as CT, was performed to provide more information.

On CT images, a large, well-capsuled, soft-tissue attenuating mass was noted in the submucosal and serosal layers of the distal descending colon, causing severe narrowing of the colonic lumen. The mass was nonenhancing and showed stratified contents with a clear interface, 30–40 and 40–60 HU in the upper and lower layers, respectively, similar to that seen in the human literature (28). This interface was only seen on CT images but not on ultrasonography, which might be caused by precipitation of lysed and fragmented clots upon

ventral recumbency of the patient during CT scans. Cytological examination revealed abundant red blood cell contents without platelets, consistent with previous chronic hemorrhage (29). A clear interface with different attenuations was also observed in large intracranial hematomas in humans, although the lesion locations were different (30). In our case, triple-phase contrast was performed, and the mass showed no enhancement and intact mucosal and serosal intestinal layers in the arterial, portal, and delayed phases, which was similar to the characteristics of the human colonic intramural hematoma on CT images and further excluded the suspicion of intestinal neoplasia and FGESF (11, 31–33). Abscesses were also excluded due to higher attenuation of contents in the mass (24). The CT image in our case provided a more complete visualization of the abdomen than ultrasonography and radiography and was helpful in excluding intestinal perforation and active bleeding to determine whether emergency surgery was necessary.

The relationship between the timing of hematoma and image characteristics is well known in the human literature; however, it is less well described in animals. In humans, hematomas present variable echogenicity and density at different times on ultrasonographic and CT images (31, 34). Immediately after the hemorrhage (on day 1), freshly extravasated blood is mostly anechoic on ultrasonography and exhibits mixed 40–80 HU signals on CT images, which can be attributed to the formation of a meshwork of fibrin fibrils and globin molecules (3, 31). During week 1, as the hematoma matures, clot retraction ensues, the hematoma shows mostly heterogeneous echogenicity on ultrasonographic images and shows 50–80 HU signals on the CT image, which is similar to what was seen in our case (31, 34). The hematoma gradually becomes more hypoechogenic on ultrasonographic images and hypoattenuating (∼10–50 HU) on CT images after the acute phase due to chemical breakdown of globin molecules and lysis of clots over the weeks (31, 34). The intramural mass in our case showed heterogeneous echogenicity on ultrasonography and intermediate attenuation on CT images; therefore, we speculated that the hematoma was formed within 1 week, and this time period also coincided with the onset of clinical signs.

In humans, the treatment of intramural colonic hematoma includes conservative and surgical treatment, whereas descriptions in animals are limited. The optimal management of colonic intramural hematoma depends on the differences in etiologies and the patient's general condition in humans. Conservative treatment is typically used, especially when coagulopathy is the cause (1, 3). Surgical intervention includes surgical excision and surgical evacuation. Surgical excision, such as in hemicolectomy, is often required in cases showing failure of conservative treatment, peritonitis, hemoperitoneum, and intractable bleeding; whereas surgical evacuation may be considered in cases without mucosal perforation (18). Evacuation solely by colonoscopy is rarely seen in the literature because it is difficult to detect and sample colonic intramural hematoma in deeper layers, such as the muscular layer (6, 35). Surgical evacuation of the hematoma by laparotomy is more feasible, because it can facilitate a direct approach of the lesion and ensure there is no oozing after evacuation. Complications of surgical evacuation include hemoperitoneum, peritonitis, and intestinal perforation (18). In our case, ultrasonography revealed the location of the mass was between the submucosal and muscular layers, and the thickness of the mass was more than 1.3 cm, thus we considered incision from the mucosal surface for surgical evacuation was safe. The distal location of the hematoma enabled the anal approach; therefore, surgical evacuation from the anus with a speculum was performed. A cotton swab was used to ensure that the outer colonic layers were not injured or perforated. The wound was not closed for the drainage of the remaining blood clots. After surgery, antibiotics and hemostatic medicine were administered, and the clinical signs, including appetite, spirits, defecation, and abdominal pain, were followed up to ensure that there were no postsurgical complications. No recurrence or complication was noted for more than 14 months; therefore, we considered that this was a sporadic disease in this cat, and surgical evacuation was feasible in this situation.

There are several limitations to our case report. First, no full-thickness biopsy was performed in our case to confirm the origin of the hematoma. Second, the cause of hematoma in this cat is still unknown, thus the incidence of recurrence cannot be estimated. Last, although the outcome of surgical evacuation was good in the current case, as an individual case study, the contraindication of surgical evacuation cannot be fully confirmed.

CONCLUSION

In conclusion, our report describes the multimodality imaging findings and their clinical relevance in a rare case of feline colonic intramural hematoma. The mass appeared as a large mass affecting the descending colon on radiographs, an intraluminal mass between the submucosal and muscular layers with heteroechogenicity and liquified contents on ultrasonography, and showing almost non-enhancing and stratified contents on CT images. Ultrasonography provides a more precise layering location, whereas enhancement and density in CT images can offer more definitive information regarding the diagnosis and formation of the hematoma. The patient responded well to surgical evacuation of the hematoma using the anal approach. No recurrence was noted for more than 14 months. The multimodal imaging findings in this case were invaluable for differential diagnosis and determining the optimal course of treatment.

DATA AVAILABILITY STATEMENT

The original contributions presented in the study are included in the article/**Supplementary Material**, further inquiries can be directed to the corresponding author.

ETHICS STATEMENT

Ethical review and approval were not required for the animal study because this was a retrospective case report. Written informed consent was obtained from the owners for the participation of their animals in this study.

AUTHOR CONTRIBUTIONS

T-CH, L-SL, CC, H-CC, and P-HH contributed to image acquisition. T-CH, L-SL, and CC contributed to image interpretation. H-CC and P-HH performed the colonoscopy and surgical intervention. T-CH, L-SL, and C-SC contributed to manuscript editing. All authors reviewed and approved the final submitted manuscript.

FUNDING

This publication was supported by the Southern Taiwan Science Park Bureau, Ministry of Science and Technology, Taiwan, ROC under contract 110CB-1-04.

ACKNOWLEDGMENTS

We would like to thank Dr. Jian-Nan Chen for the image acquisition of the follow-up ultrasonography, and Dr. Yi-Chia Li for pathology image acquisition.

SUPPLEMENTARY MATERIAL

The Supplementary Material for this article can be found online at: https://www.frontiersin.org/articles/10.3389/fvets.2022.913862/full#supplementary-material

Supplementary Video I | Ultrasonographic images of the colonic intramural hematoma and colonic lymphadenopathy.

REFERENCES

1. Wang J, Sun X, Shi H, Cao D. Intramural hematoma of colon: case report of 2 cases. *Medicine (Baltimore).* (2020) 99:e19404. doi: 10.1097/MD.0000000000019404
2. Samir R, Hashem MB, Badary HA, Bahaa A, Bakheet N. Perspectives and management strategies for acute colonic intramural hematoma. *Int J Gen Med.* (2022) 15:2861. doi: 10.2147/IJGM.S294884
3. Kwon K, Cheung DY, Seo Y, Kim SB, Bae KN, Kim HJ, et al. Supportive management resolved a colonic intramural hematoma in an anticoagulant user. *Intern Med.* (2014) 53:1505–9. doi: 10.2169/internalmedicine.53.2358
4. Ninomiya I, Sakai Y, Koizumi K, Kohchi I, Kazami A, Fujimoto S, et al. Synchronous colon cancers associated with a submucosal hematoma. *Gastrointest Endosc.* (2002) 56:926–9. doi: 10.1067/mge.2002.129590
5. Bacalbaşa N, Bohîlţea R, Dumitru M, Turcan N, Cîrstoiu ML. Subserosal hematoma of the sigmoid colon after vaginal delivery. *J Med Life.* (2017) 10:76. doi: 10.26416/Gine.15.1.2017.507
6. Heng HG, Huang A, Baird DK, Mitsui I, Parnell NK. Imaging diagnosis–spontaneous intramural canine duodenal hematoma. *Vet Radiol Ultrasound.* (2010) 51:178–81. doi: 10.1111/j.1740-8261.2009.01648.x
7. Padalkar M, Savage M, Cohen EB. Small intestinal intramural hematoma secondary to a migrating wire foreign body in a dog. *Vet Radiol Ultrasound.* (2018) 59:E61–5. doi: 10.1111/vru.12485
8. Moore R, Carpenter J. Intramural intestinal hematoma causing obstruction in three dogs. *J Am Vet Med Assoc.* (1984) 184:186–8.
9. Hughes CE, Conn JJ, Sherman JO. Intramural hematoma of the gastrointestinal tract. *Am J Surg.* (1977) 133:276–9. doi: 10.1016/0002-9610(77)90528-1
10. Hayashi K, Futagawa S, Kozaki S, Hirao K, Hombo Z. Ultrasound and CT diagnosis of intramural duodenal hematoma. *Pediatr Radiol.* (1988) 18:167–8. doi: 10.1007/BF02387565
11. Torres US, Cesar DN, D'Ippolito G. Computed tomography and magnetic resonance imaging findings in a case of colonic intramural hematoma after mild blunt abdominal trauma. *J Comput Assist Tomogr.* (2016) 40:896–8. doi: 10.1097/RCT.0000000000000534
12. Kobluk CN, Smith DF. Intramural hematoma in the jejunum of a mare. *J Am Vet Med Assoc.* (1988) 192:379–80.
13. Speirs VC, van Veenendaal JC, Christie BA, Lavelle RB, Gay CC. Obstruction of the small colon by intramural haematoma in three horses. *Aust Vet J.* (1981) 57:88–90. doi: 10.1111/j.1751-0813.1981.tb00454.x
14. Pearson H, Waterman AE. Submucosal haematoma as a cause of obstruction of the small colon in the horse: a review of four cases. *Equine Vet J.* (1986) 18:340–1. doi: 10.1111/j.2042-3306.1986.tb03647.x
15. Ettinger SJ, Feldman EC, Cote E. *Textbook of veterinary internal medicine-ebook, 8th ed.* Elsevier Health Sciences (2017). p. 3827
16. Miller MJ, McDole JR, Newberry RD. Microanatomy of the intestinal lymphatic system. *Ann N Y Acad Sci.* (2010) 1207 Suppl 1:E21–8.
17. Calabuig R, Ortiz C, Sueiras A, Vallet J, Pi F. Intramural hematoma of the cecum: report of two cases. *Dis Colon Rectum.* (2002) 45:564–6. doi: 10.1007/s10350-004-6240-y
18. Alzeerelhouseini HIA, Abuzneid YS, Aljabarein OY. Delayed presentation of intramural cecal hematoma with challenges in the treatment. A case report and review of the literature. *Int J Surg Case Rep.* (2021) 82:105884. doi: 10.1016/j.ijscr.2021.105884
19. Tyrrell D, Beck C.Survey of the use of radiography vs ultrasonography in the investigation of gastrointestinal foreign bodies in small animals. *Vet Radiol Ultrsound.* (2006) 47:404–8. doi: 10.1111/j.1740-8261.2006.00160.x
20. Joudrey SD, Robinson DA, Blair R, Mclaughlin LD, Gaschen L. Perianal neuroendocrine tumor with suspected lymph node metastasis causing colonic compression and subsequent megacolon. *Can Vet J.* (2015) 56:240.
21. Leroy BE, Lech ME. Prostatic carcinoma causing urethral obstruction and obstipation in a cat. *J Feline Med Surg.* (2004) 6:397–400. doi: 10.1016/j.jfms.2004.04.005
22. Arteaga TA, Mcknight J, Bergman PJ, A. review of 18 cases of feline colonic adenocarcinoma treated with subtotal colectomies and adjuvant carboplatin. *J Am Anim Hosp Assoc.* (2012) 48:399–404. doi: 10.5326/JAAHA-MS-5807
23. Rivers BJ, Walter PA, Feeney DA, Johnston GR. Ultrasonographic features of intestinal adenocarcinoma in fivecats. *Vet Radiol Ultrasound.* (1997) 38:300–6. doi: 10.1111/j.1740-8261.1997.tb00859.x
24. Nemoto Y, Haraguchi T, Shimokawa Miyama T, Kobayashi K, Hama K, Kurogouchi Y, et al. Pancreatic abscess in a cat due to Staphylococcus aureus infection. *J Vet Med Sci.* (2017) 79:1146–50. doi: 10.1292/jvms.17-0026
25. Weissman A, Penninck D, Webster C, Hecht S, Keating J, Craig LE. Ultrasonographic and clinicopathological features of feline gastrointestinal eosinophilic sclerosing fibroplasia in four cats. *J Feline Med Surg.* (2013) 15:148–54. doi: 10.1177/1098612X12464224
26. Lee M, Kang JH, Chang D, Na KJ, Yang MP. Pancreatic abscess in a cat with diabetes mellitus. *J Am Anim Hosp Assoc.* (2015) 51:180–4. doi: 10.5326/JAAHA-MS-6122
27. Penninck D, d'Anjou M-A. *Atlas of Small Animal Ultrasonography*. 2nd ed. John Wiley & Sons (2015). p. 50.
28. Nozu T. Idiopathic spontaneous intramural hematoma of the colon: a case report and review of the literature. *Clin J Gastroenterol.* (2009) 2:161–5. doi: 10.1007/s12328-008-0061-9
29. Cowell RL, Tyler RD, Meinkoth JH, DeNicola DB. *Diagnostic Cytology and Hematology of the Dog and Cat-E-Book,* 4th ed. Elsevier Health Sciences (2007). p. 108.
30. Parizel PM, Makkat S, Van Miert E, Van Goethem JW, van den Hauwe L, De Schepper AM. Intracranial hemorrhage: principles of CT and MRI interpretation. *Eur Radiol.* (2001) 11:1770–83. doi: 10.1007/s003300000800
31. Plojoux O, Hauser H, Wettstein P. Computed tomography of intramural hematoma of the small intestine: a report of 3 cases. *Radiology.* (1982) 144:559–61. doi: 10.1148/radiology.144.3.6980432
32. Wisner E, Zwingenberger A. *Atlas of Small Animal CT and MRI,* 1st ed. John Wiley & Sons (2015). p. 539. doi: 10.1002/9781119421399

33. Thieme ME, Olsen AM, Woolcock AD, Miller MA, Simons MC. Diagnosis and management of a case of retroperitoneal eosinophilic sclerosing fibroplasia in a cat. *JFMS Open Rep.* (2019) 5:2055116919867178. doi: 10.1177/2055116919867178
34. Wicks JD, Silver TM, Bree RL. Gray scale features of hematomas: an ultrasonic spectrum. *AJR Am J Roentgenol.* (1978) 131:977–80. doi: 10.2214/ajr.131.6.977
35. Kwon CI, Kim DH, Hong SP. Immediate endoscopic management of an intramural hematoma developed during colonoscopy. *Clin Endosc.* (2017) 50:508–9. doi: 10.5946/ce.2017.037

Conflict of Interest: The authors declare that the research was conducted in the absence of any commercial or financial relationships that could be construed as a potential conflict of interest.

Publisher's Note: All claims expressed in this article are solely those of the authors and do not necessarily represent those of their affiliated organizations, or those of the publisher, the editors and the reviewers. Any product that may be evaluated in this article, or claim that may be made by its manufacturer, is not guaranteed or endorsed by the publisher.

frontiers | Frontiers in Veterinary Science

ORIGINAL RESEARCH
published: 12 July 2022
doi: 10.3389/fvets.2022.908829

Color M-Mode Echocardiography for Non-Invasive Assessment of the Intraventricular Pressure in Dogs Before and After Ductus Arteriosus Occlusion: A Retrospective Study

Miki Hirose[1†], Ahmed S. Mandour[1,2†], Seijirow Goya[3], Lina Hamabe[1], Katsuhiro Matsuura[1], Tomohiko Yoshida[1], Momoko Watanabe[1], Kazumi Shimada[1], Akiko Uemura[4], Ken Takahashi[5] and Ryou Tanaka[1*]*

[1] Department of Veterinary Surgery, Tokyo University of Agriculture and Technology, Tokyo, Japan, [2] Department of Animal Medicine (Internal Medicine), Faculty of Veterinary Medicine, Suez Canal University, Ismailia, Egypt, [3] Department of Bioresource Sciences, Nihon University, Fujisawa, Japan, [4] Division of Veterinary Research, Department of Veterinary Surgery, Obihiro University of Agriculture and Veterinary Medicine, Obihiro, Japan, [5] Department of Pediatrics and Adolescent Medicine, Juntendo University Graduate School of Medicine, Bunkyo, Japan

OPEN ACCESS

Edited by:
Haney Samir,
Cairo University, Egypt

Reviewed by:
Carlos Fernando Agudelo,
University of Veterinary and Pharmaceutical Sciences Brno, Czechia
Samar Elsharkawy,
Cairo University, Egypt

***Correspondence:**
Ahmed S. Mandour
dr_mandour@vet.suez.edu.eg
Ryou Tanaka
ryo@vet.ne.jp

[†] These authors have contributed equally to this work

Specialty section:
This article was submitted to Veterinary Imaging, a section of the journal Frontiers in Veterinary Science

Received: 31 March 2022
Accepted: 06 June 2022
Published: 12 July 2022

Citation:
Hirose M, Mandour AS, Goya S, Hamabe L, Matsuura K, Yoshida T, Watanabe M, Shimada K, Uemura A, Takahashi K and Tanaka R (2022) Color M-Mode Echocardiography for Non-Invasive Assessment of the Intraventricular Pressure in Dogs Before and After Ductus Arteriosus Occlusion: A Retrospective Study. Front. Vet. Sci. 9:908829. doi: 10.3389/fvets.2022.908829

Background: Novel non-invasive evaluation of the intraventricular pressure differences and gradients (IVPD and IVPG) by color M-mode echocardiography (CMME) is a promising method in diastolic function evaluation. Patent ductus arteriosus (PDA) is a congenital heart defect which is associated with increased preload. The present work provides a clinical trial for the assessment of IVPD and IVPG changes in dogs before and after surgical occlusion of PDA.

Materials and Methods: A total of 12 client-owned dogs were enrolled in this study. PDA was confirmed using echocardiography, and all dogs underwent PDA occlusion. Conventional echocardiography and CMME were conducted on each patient on the operation day (Pre-PDA) and 48 h after its occlusion (Post-PDA). The total IVPD and total IVPG, as well as segmental intraventricular pressure (basal, mid-to-apical, mid, and apical) were measured from Euler's equation using specific software (MATLAB). Data were analyzed for variability and for the difference between pre- and post-PDA. The effect of PDA occlusion on the measured variables was calculated using biserial ranked correlation (rc).

Results: There was a significant reduction in end-diastolic volume, fraction shortening, stroke volume, and mitral inflow velocities (early and late) after PDA closure. CMME was feasible in all dogs, and the CMME indices showed moderate variability, except for the apical segment of IVPD and IVPG. After PDA closure, in comparison with the pre-PDA occlusion, there was a significant reduction in total IVPD (2.285 ± 0.374 vs. 1.748 ± 0.436 mmHg; $P = 0.014$), basal IVPD (1.177 ± 0.538 vs. 0.696 ± 0.144 mmHg; $P = 0.012$), total IVPG (1.141 ± 0.246 vs. 0.933 ± 0.208 mmHg; $P = 0.032$), and basal IVPG (0.578 ± 0.199 vs. 0.377 ± 0.113 mmHg; $P = 0.001$); meanwhile, mid, mid-to-apical, and apical segments of both IVPD and IVPG showed non-significant difference.

The magnitude of PDA occlusion on the measured variables was clinically relevant and associated with a large effect size on total and basal IVPD and IVPG (rc > 0.6).

Conclusion: The current clinical study revealed matched response of IVPD and IVPG to the reduced preload rather than left ventricular relaxation. This result is an initial step in the clinical utility of CMME-derived IVPD and IVPG measurements in the diastolic function evaluation in dogs with PDA that warrants further clinical studies.

Keywords: dog, ductus arteriosus, Doppler echocardiography, intraventricular pressure, diastole, overloading

INTRODUCTION

During the fetal life, the vascular tunnel, known as "ductus arteriosus," shunts the blood between the aorta and the main pulmonary artery to bypass the immature nonfunctional fetal lungs. At birth, the abrupt increase in the blood oxygen content and the reduction in the blood prostaglandin levels stimulate the closure of the duct. In dogs, functional closure of the ductus occurs 4 days post-partum and becomes complete at 7–8 days of age (1–3). However, hypoplasia and asymmetry of the ductal architecture result in patent ductus arteriosus (PDA), which is the most frequently reported congenital cardiac defect that affects a wide range of dog breeds. PDA is accounted for 20–30% of the congenital heart defects in dogs depending on geographical screening (4). PDA is routinely diagnosed on clinical examination with echocardiography which shows volume overloading (5, 6). Depending on the size of the PDA, the clinical signs of PDA are variable ranging from no or mild symptoms to severe congestive heart failure signs including dyspnea, continuous heart murmurs, abnormal pulses, and exercise intolerance. The PDA in dogs can be managed medically or occluded surgically through a transvenous catheter or *via* thoracotomy. Rapid interference for surgical occlusion of the PDA tunnel is preferable before overt clinical symptoms and irreversible heart damage (2).

Recently, CMME-derived intraventricular pressure differences (IVPD) and intraventricular pressure gradients (IVPG) have been invented as promising tools for cardiac function examination. Studies revealed the utility of IVPD and/or IVPG for the diagnosis of diastolic dysfunction. The feasibility of the novel approach has been utilized in various experimental animal models (7–13), as well as in some human studies (14–16). Recent studies showed that non-invasive IVPG could be an indicator of heart failure in children as well as in dogs receiving chemotherapy (12, 15). IVPG also explained the mechanism underlying diastolic dysfunction in the tetralogy of Fallot, which was associated with reduced suction force as indicated by reduced mid-to-apical IVPG (14). Another study suggested that IVPD and IVPG indices could reflect the preloading conditions (9). However, more studies are still needed for the validation of IVPD/IVPG in the clinical setting.

Current cardiovascular research focuses on the development of non-invasive diagnostics for diastolic dysfunction. This is because heart failure with preserved ejection fraction (HFpEF) is known to account for half of the patients diagnosed with end-stage heart failure, and the accurate diagnostic methods are challenging and have not yet been established (17). Evaluation of diastolic function using conventional echocardiography is limited as the measurements are affected by the heart rate and arrhythmias. A combination of various echocardiographic techniques is necessary to avoid overestimation of the echocardiographic measurements (18). Additionally, the practical usage of a reliable cardiac catheterization method is invasive and requires perioperative procedures, including anesthesia, and surgical techniques (19, 20). To our knowledge, there are no reports of clinical studies which have focused on the importance of IVPD and IVPG analysis obtained from CMME in canine congenital heart disease. PDA is a good example of volume overloading, which resulted in a profound left to right shunt from the aorta to the pulmonary artery leading to left side dilatation, increased end-diastolic pressure, myocardial failure, and overt pulmonary edema (6, 21). We hypothesize that the hemodynamic and contractility changes which occur before and after PDA closure could be detected by the measurement of IVPD and IVPG using CMME. The present study aims to provide a short-term evaluation of IVPD/IVPG changes in dogs with PDA.

MATERIALS AND METHODS

Animals and Study Protocol

A total of 12 client-owned dogs echocardiographically diagnosed with PDA and underwent transvascular PDA occlusion were enrolled in this study. The study was carried out between January 2018 and April 2021 at the Animal Medical Center, Tokyo University of Agriculture and Technology, Japan. Before enrollment, the informed consent was collected from all owners.

Clinical Examination and Diagnosis of PDA

Diagnosis and decision for the surgical treatment of PDA were determined through a comprehensive clinical evaluation including detailed medical history, physical examination (including cardiac auscultation, mucous membrane color, breathing condition, etc.), as well as thoracic radiography, electrocardiography, and echocardiography. On cardiac auscultation, grade IV continuous left basilar systolic murmur was detected in all cases. Specific objects/parameters to be evaluated before surgery were as follows: signalment (age, breed, sex, and body weight), anatomical characterization of PDA, existence and severity of heart failure, as well as systolic and/or diastolic dysfunction.

PDA Closure

Patent ductus arteriosus occlusion was performed *via* intercostal thoracotomy under general anesthesia. All preoperative, intraoperative, and postoperative procedures were conducted as described in previous reports (22–24). All dogs were sedated with buprenorphine hydrochloride (Lepetan; Otsuka Pharmaceutical Co., Ltd., Tokyo, Japan, 0.02 mg/kg, intravenously), midazolam hydrochloride (Dormicum; Astellas Pharma Inc., Tokyo, Japan, 0.2 mg/kg, intravenously), and atropine sulfate (Atropine sulfate; Tanabe Seiyaku Co., Ltd., Saitama, Japan, 25 μg/kg, intravenously). After tracheal intubation, anesthesia was induced with propofol (Propofol Mylan; Mylan Seiyaku, Tokyo, Japan, 4 mg/kg, intravenously) and was maintained by isoflurane inhalation (Isoflurane for Animal Use; Intervet, Osaka, Japan, end-tidal concentration of 1.5 ± 0.1%). The ductus arteriosus was occluded using a double hemostatic clip (DS titanium ligation clip, Aesculap, Japan). During surgery, transesophageal echocardiography was performed with ProSound SSD-α10 (Hitachi Aloka Medical, Ltd., Japan) using a sector probe (UST-52119S, Hitachi Aloka Medical, Ltd., Japan). Postoperative confirmation of hemostatic clip and leakage was assessed by Doppler echocardiography.

Conventional Echocardiography

Standard echocardiography was performed on all unsedated dogs at the baseline on the operation day before surgical occlusion of the PDA (Pre-PDA) and 48 h after its occlusion (Post-PDA). The echocardiography was performed using ALOKA prosound α10 (Hitachi Aloka Medical, Ltd., Japan) with a 5-MHz phased array transducer probe (UST52108, Hitachi Aloka Medical, Ltd., Japan). Dogs were placed in lateral recumbency and the conventional echocardiographic examination from the standard right and left cardiac windows was recorded using a well-known standard echocardiographic technique (25). The following measurements were reported from the right parasternal short-axis view at the papillary muscle level: left ventricle (LV) end-diastolic and end-systolic diameters (LVIDd, LVIDs), interventricular septal thickness in diastole and systole (IVSd, IVSs), LV free wall thickness in diastole and systole (LVPWd, LVPWs), LV end-diastolic and end-systolic volume (EDV, ESV), and fraction shortening (FS). From the right parasternal short-axis view at the base of the heart in late systole, the left atrium diameter (LADs), aortic diameter (Ao), and the left atrial diameter to aortic diameter ratio (LA/Ao) were obtained by two-dimensional echocardiography. Also, the right ventricular outflow tract (RVOT) was measured by pulsed-wave Doppler echocardiography of the main pulmonary artery. On the left apical view, the left ventricular outflow tract (LVOT) and mitral inflow velocity indices (early velocity, Ev; late velocity, Av) were measured using pulsed-wave Doppler echocardiography, while tissue Doppler imaging (TDI) was used to measure the annular tissue velocity indices. The TDI measurements include systolic velocity (Sm) as well as early and late diastolic tissue velocities (Em and Am) from IVS (septal, Sep) and LVPW (free wall, FW). The corresponding ratio between Em/Am, as well as E and Em (E/Em) from IVS and LVPW was then calculated.

Color M-Mode Echocardiography for Assessment of IVPD and IVPG

The whole echocardiography protocol including CMME was performed within 15 min in which the CMME was traced within 5 min. To avoid the stress-related erroneous imaging, the examination was temporarily stopped when there was an abrupt increase in respiratory and heart rates. The ultrasound probe was set to trace IVPG from the left apical two-chamber view with proper visualization of the entire mitral inflow tract to the LV apex. To increase the Nyquist limit, a prior machine setting including sweep speed of 300 mm/s and color baseline shift was adjusted at −64. During image processing for IVPD and IVPG using the MATLAB, the time from aortic valve opening to its closure, the time from the beginning of Q wave to the start of early mitral inflow (E wave), and the time from the start of Q wave to the peak E wave were collected from conventional echocardiography and manually inserted into the dialog boxes of the MATLAB. Five high-quality images of consecutive heartbeats were selected and analyzed separately by the same observer, and the average measurement of each patient was considered for the analysis.

The IVPD and IVPG derived from CMME were calculated based on the previously validated IVPD measurements technique (14, 26, 27). IVPD was calculated from the Euler equation after processing images obtained *via* the CMME using MATLAB (The MathWorks, Natick, MA, USA) as follows:

$$(\partial P)/(\partial s) = -\rho((\partial v)/(\partial t) + v(\partial v)/(\partial s)).$$

where ∂ is the change in element followed, P is the pressure, ρ is the constant blood density (1,060 kg/m^3), v is the velocity, s is the position along with the color M-mode line, and t is the time. The IVPG values were derived from the IVPD according to the following formula (14, 26–28):

$$\text{IVPG (mmHg/cm)} = \text{IVPD/LV length}.$$

The IVPG and IVPD were automatically divided into basal, mid-to-apical, mid, and apical segments, which are corresponding to their location in the LV (11, 12, 14).

Statistical Analysis

The sample size of dogs before and after the closure of PDA was measured based on the outcomes and calculations performed with the G*Power 3.1.9.2 software (University Kiel, Germany, 1992–2014) (29) assuming a moderate effect of PDA occlusion on CMME variables according to Cohen with 0.37 effect size (30). The normality of the data was tested by the Shapiro–Wilk test and the 95% coefficient of variations (CV) and 95% confidence interval (CI) of means were reported. Wilcoxon matched-pairs signed-rank test was used to compare all echocardiographic data before and after PDA occlusion using GraphPad Prism Version 8 (GraphPad Software Inc., San Diego, CA, USA). Analyzed variables showing $P < 0.05$ were considered statistically significant. Spearman's rank correlation was measured between conventional cardiac parameters and CMME indices. To examine the effect of PDA closure on the obtained parameters, the effect size for non-parametric data was calculated by rank-biserial correlation (rc) using a free JASP software program. Interpretation of the effect size was done based on rc values as

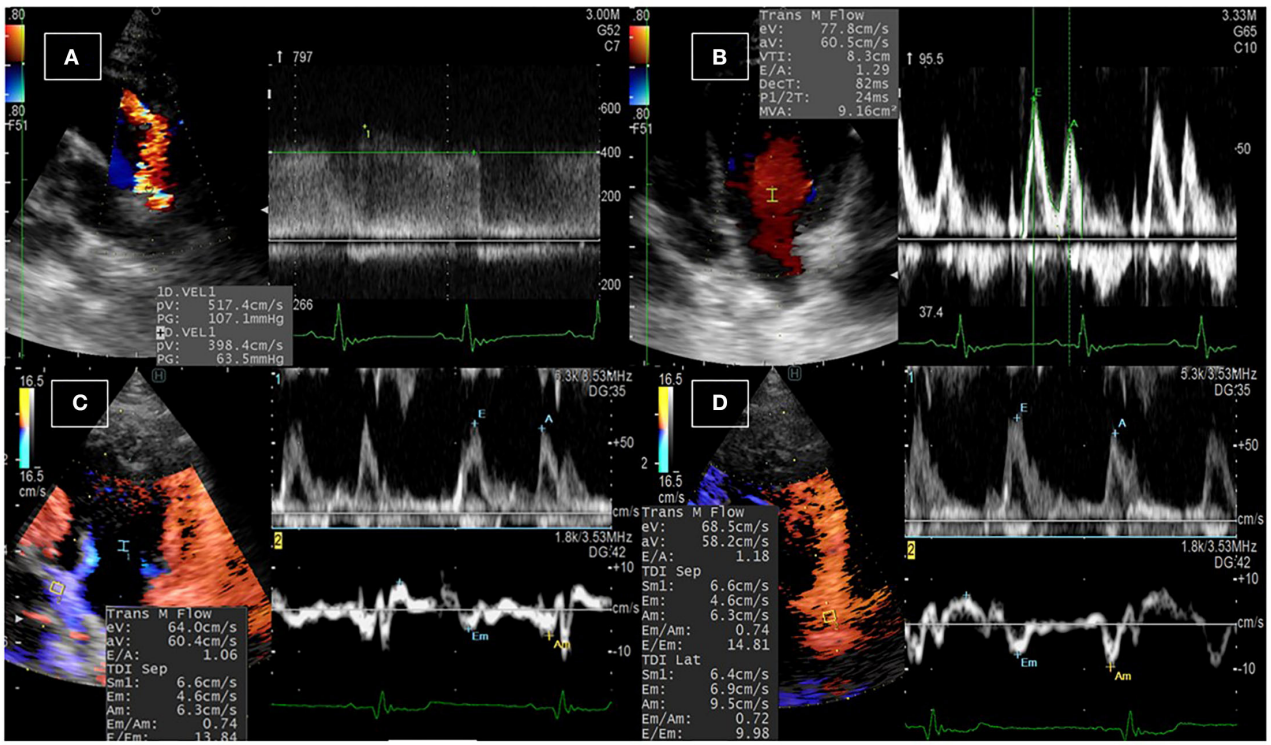

FIGURE 1 | Conventional echocardiographic examination in dogs with PDA. **(A)** The PDA shunt was detected upon echocardiographic examination from the left parasternal short-axis view at the base of the heart using color Doppler echocardiography, and the velocity of the blood flow across the shunt was detected using continuous-wave Doppler echocardiography. **(B)** Pulsed-wave Doppler echocardiography of the transmitral flow was used to measure the early and late diastolic peaks. **(C,D)** Dual Doppler imaging of the transmitral flow and the tissue Doppler imaging at the septal **(C)** and the free **(D)** wall of the left ventricle to measure the early inflow velocity to early tissue velocity (E/Em) ratio.

follows (31): small effect (rc $\geq$ 0.1), medium effect (rc $\geq$ 0.4), and large effect (rc $\geq$ 0.6).

RESULTS

Clinical Findings and Outcomes

Twelve small breed dogs underwent surgical treatment for PDA. Five dog breeds were included in this study: Pomeranians (33.3%, $n = 4$), Chihuahua (25%, $n = 3$), Maltese (16.7%, $n = 2$), Mix (16.6%, $n = 2$), and Toy Poodles (8.3%, $n = 1$). Overall, seven males (58.3%) and 5 females (41.7%) were included. On the day of diagnosis, the median BW was 1.49 kg (range: 0.92–2.16) and the median age was 4.5 months (range: 2–7). One dog had diarrhea and was prescribed anti-diarrhea medicine and antibiotics by the referring clinic before surgery. Also, one dog showed cough and another one had polyuria and polydipsia. No dog showed severe symptoms of heart failure or received other medication.

Conventional Echocardiography

Figure 1 illustrates the conventional echocardiographic findings in dogs diagnosed with PDA. The left–right PDA shunt was detected from the left cranial parasternal location after obtaining the heart base in the short axis. **Table 1** shows functional measurements of conventional echocardiography. The data revealed a significant increase in IVSd and LVPWd thickness, and a significant reduction in LVIDd, heart rate, EDV, FS, and mitral inflow waves (Ev and Av). By TDI, Sm of the septum and the E/Em of the free wall were significantly reduced. The effect size on the aforementioned heart function parameters was large (rc > 0.6). Before the operation, the median of PDA velocity was 532.3 cm/s (range: 436.3–594.9 cm/s). The following abnormalities were observed in the postoperative settings: mitral regurgitation (MR) was found in eight dogs (median MR velocities: 571.5 cm/s, dp/dt: 3,123.7 mmHg/s); pulmonary regurgitation (PR) in four dogs (median PR: 146.0 cm/s); and tricuspid regurgitation (TR) in one dog (TR velocity: 169.6 cm/s). All dogs were discharged from the hospital 48 h after showing hemodynamic stability.

Color M-Mode Echocardiography

The CMME was successfully performed in all dogs (**Figure 2**). All dogs showed standard spectral mitral inflow waves of CMME with the opening and closure of the mitral valve. The obtained IVPD and IVPG results from MATLAB yielded five different indices, total, basal, mid-to-apical, mid, and apical. **Table 2** shows the descriptive statistics of CMME variables in dogs before and after PDA occlusion. All CMME data were normally distributed, except mid-to-apical IVPD. The variability of CMME data from pre- and post-PDA was separately calculated, which showed a

TABLE 1 | Echocardiographic measurements in dogs before and after PDA occlusion.

Variables	Pre-PDA	Post-PDA	*P*-value	Effect size
IVSd	3.90 (2.50–4.40)	4.55 (3.70–5.100	0.007	−0.879
LVIDd	22.65 (16.40–32.20)	19.55 (14.20–25.20)	0.001	1.000
LVPWd	3.35 (3.00–4.80)	4.05 (3.30–7.60)	0.006	−0.927
IVSs	5.70 (4.10–12.10)	6.45 (4.10–10.00)	0.331	−0.364
LVISd	13.00 (9.50–20.10)	12.60 (8.30–18.50)	0.266	0.394
LVPWs	6.35 (4.40–7.60)	6.70 (5.30–7.90)	0.100	−0.561
HR	150.0 (103-166.00)	130.0 (66.0–162.0)	0.014	0.818
EDV	11.5 (4.40–33.00)	7.50 (2.90–16.00)	0.001	1.000
ESV	2.2 (0.80–8.10)	2.0 (0.60–6.40)	0.528	0.218
FS%	42.2 (28.00–55.50)	34.7 (20.90–57.20)	0.034	0.692
LADs	12.65 (1.60–18.40)	11.0 (6.30–16.70)	0.096	0.485
Ao	9.10 (1.20–10.90)	9.2 (7.90–10.40)	0.783	0.145
LA/Ao	1.44 (1.01–1.75)	1.10 (0.79–1.74)	0.106	0.455
RVOT	7.70 (7.50–7.90)	8.6 (4.70–11.90)	0.002	0.621
LVOT	9.15 (5.70–10.90)	9.05 (4.20–11.70)	0.835	−0.127
Ev	97.70 (77.80–124.50)	74.90 (51.40–104.50)	0.001	1.000
Av	67.85 (58.10–89.80)	43.35 (32.30–68.10)	0.001	1.000
Sm Sep	7.90 (4.40-9.50)	6.60 (3.20–9.50)	0.040	0.667
Em Sep	8.70 (6.30–12.60)	6.90 (4.50–10.60)	0.066	0.603
Em/Am Sep	1.35 (1.04–2.22)	1.18 (0.59–2.34)	0.424	0.182
E/Em Sep	10.77 (8.10–19.02)	10.20 (8.84–13.79)	0.077	0.515
S FW	7.90 (5.00–10.70)	7.25 (3.70–9.90)	0.436	0.269
Em FW	12.90 (5.70–17.80)	11.25(7.10–16.90)	0.226	0.410
Em/Am FW	2.0 (0.99–8.98)	1.95 (1.49–3.25)	0.470	−0.242
E/Em FW	7.28 (5.31–17.53)	5.54 (4.20–7.41)	0.003	0.879

Values are presented as median (data range). The comparison was done between the obtained echocardiographic measurements in the same individuals before and after PDA occlusion. $P < 0.05$ was considered statistically significant.

rc, ranked biserial correlation. LVIDd, LV end-diastolic diameters; LVIDs, LV end-systolic diameters; IVSd, interventricular septal thickness in diastole; IVSs, interventricular septal thickness in systole; LVPWd, LV free wall thickness in diastole; LVPWs, LV free wall thickness in systole; EDV, end-diastolic volume; ESV, end-systolic volume; EF, ejection fraction; FS, fractional shortening; LA/Ao, left atrial diameter to aortic diameter ratio; RVOT, right ventricular outflow tract; LVOT, left ventricular outflow tract; HR, heart rate; Ev, the early diastolic velocity of mitral inflow; Av, the late diastolic velocity of mitral inflow; E/A early to late mitral inflow ratio; S, systolic annular velocity, Em, early tissue annular tissue velocity; Am, late annular tissue velocity; Em/Am, early to late annular tissue velocity ratio. Sep, septal wall; FW, free wall.

E/Em early mitral inflow to early tissue velocity ratio.

comparable 95% CV. All IVPD and IVPG indices obtained from pre- and post-PDA showed moderate variability (95% CV < 25%), except for the apical IVPD and apical IVPG (95% CV = 36.9 and 44.8, respectively). The variability of IVPD and IVPG data between heart cycles was not significant.

Effect of PDA Closure on IVPD and IVPG Measurements

Figures 3, **4** represent the results of the IVPD and IVPG indices before and after PDA occlusion. The data revealed a significant reduction in total IVPD (Mean ± SD: 2.285 ± 0.373 vs. 1.748 ± 0.436 mmHg; $P = 0.014$), basal IVPD (1.177 ± 0.538 vs. 0.696 ± 0.144 mmHg; $P = 0.012$), total IVPG (1.141 ± 0.246 vs. 0.933 ± 0.208 mmHg; $P = 0.032$), and basal IVPG (0.578 ± 0.199 vs. 0.377 ± 0.113 mmHg; $P = 0.001$) after PDA closure. The percentage of reduction in total IVPD, basal IVPD, total IVPG and basal IVPG after PDA closure were 23.5% (0.537 mmHg), 40.9% (0.481 mmHg), 18.23% (0.208 mmHg), and 34.8% (0.201 mmHg), respectively. In addition, there were non-significant increases in apical IVPD (0.198 ± 0.157 vs. 0.253 ± 0.180 mmHg) and apical IVPG (0.107 ± 0.088 vs. 0.131 ± 0.089 mmHg) after PDA closure compared with the baseline ($P > 0.05$). Also, there was no significant change in the mid and mid-to-apical IVPD and IVPG. Regarding the effect size, the differences in the observed data (Pre- and Post-PDA) were clinically relevant and showed association with a large effect size on total IVPD (rc = 1.0), basal IVPD (rc = 0.889), total IVPG (rc = 0.944), and basal IVPG (rc = 1.0).

Correlation Between IVPD/IVPG Indices and Echocardiographic Measurements

The correlation results are presented in **Table 3**. Total IVPD was correlated positively with Ev ($r = 0.470$, $P = 0.021$). Basal IVPD was trended positive with E/Em free wall ($r = 0.450$, $P = 0.071$). Mid-to-apical IVPD was correlated with ESV ($r = 0.422$, $P = 0.040$) and Ev ($r = 0.424$, $P = 0.040$). Apical IVPD was positively correlated with ESV ($r = 0.677$, $P = 0.001$) and negatively with FS ($r = -0.502$, $P = 0.017$). Basal IVPG was correlated with LA/Ao ($r = 0.446$, $p = 0.033$). Mid-to-apical IVPG was correlated with LVIDd ($r = 0.418$, $P = 0.042$), EDV ($r = 0.434$, $P = 0.034$), and ESV ($r = 0.541$, $P = 0.032$). Apical IVPG was correlated with Em of the free wall ($r = 0.454$, $P = 0.026$). Em/Am free wall was negatively correlated with basal IVPD and basal IVPG, and was positively correlated with mid-to-apical IVPD, apical IVPD, mid-to-apical IVPG, and apical IVPG. Neither body weight nor HR was significantly correlated with CMME indices.

DISCUSSION

In congenital heart disease like PDA, it is important to consider diastolic function and preload separately to understand the pathophysiology and to formulate a treatment plan (32, 33). To date, IVPD and IVPG evaluation *via* CMME is still at the research stage, and the widespread use of such novel methods requires intensive experimental and clinical trials (7, 12, 15). Recent studies have begun to reveal the efficiency of CMME-derived IVPD and IVPG indices for the evaluation of cardiac function. However, this is the first clinical study that explored the short-term changes in IVPD and IVPG in dogs before and rapidly after PDA occlusion.

Regarding conventional echocardiographic parameters, PDA occlusion resulted in a significant reduction of LVIDd, HR, EDV, FS, Ev, Av, Sm septum, and E/Em free wall, as well as a mild non-significant decline in Em and E/Em at the interventricular septum. These changes have been previously reported following PDA closure, and temporal systolic dysfunction may occur in

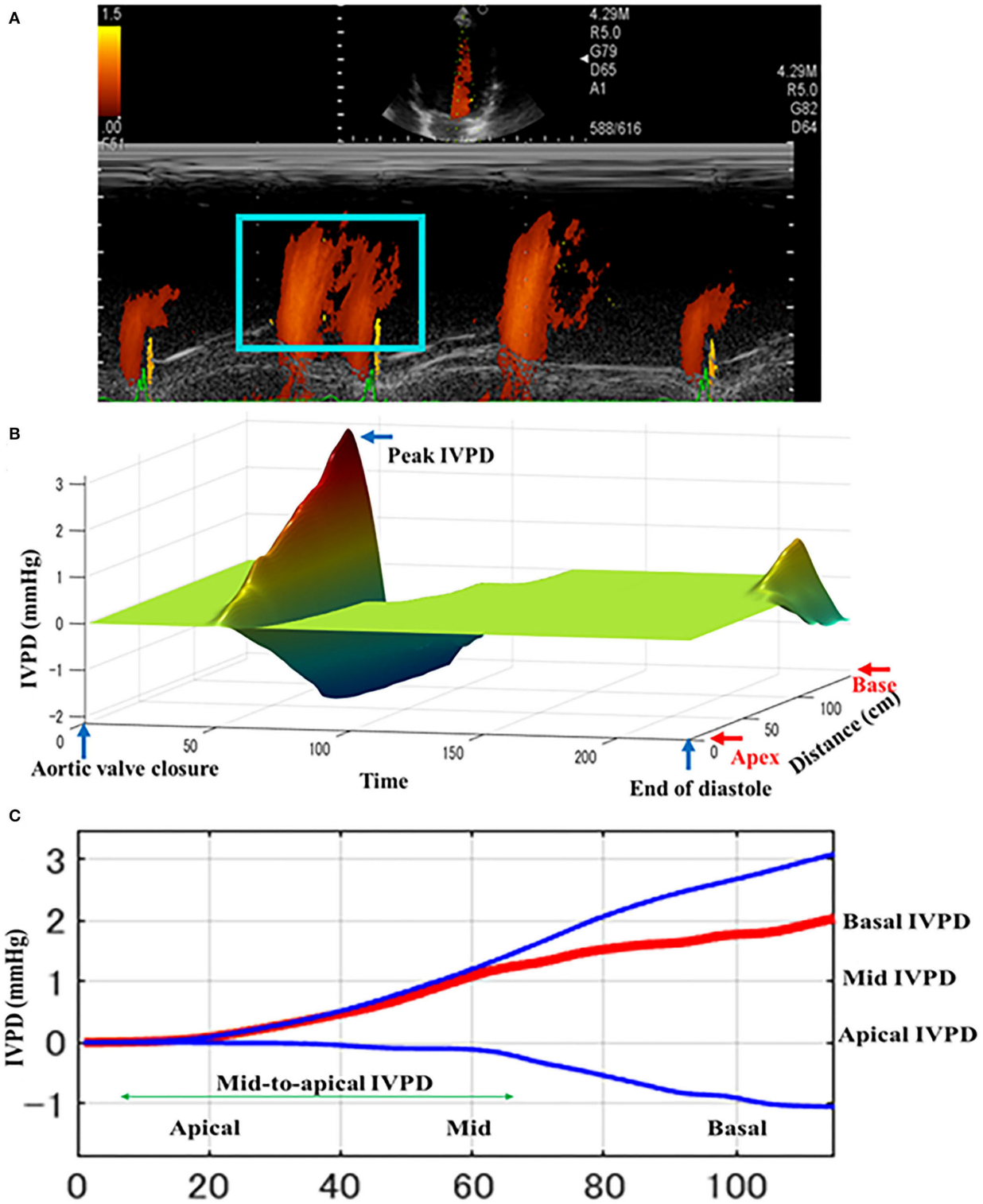

FIGURE 2 | Schematic illustration of intraventricular difference (IVPD) measured by Color m-mode echocardiography (CMME) in dogs before PDA occlusion. The mitral inflow was firstly optimized from the left apical four-chamber view. After that, the machine setting for CMME to measure IVPD (IVPG) was switched on and photos were captured **(A)**. Offline saved photos were further processed by MATLAB software for IVPD and IVPG calculation. The three-dimensional profile of IVPD was calculated after extraction of the velocity, temporal, and spatial elements from the region of interest (blue box) **(B)**. Spatial distribution of the IVPD along the entire left ventricle from the base toward the apex **(C)**. The top (blue), middle (red), and bottom (blue) lines represent inertial, total, and convective IVPD, respectively.

TABLE 2 | Variability and normality of CMME indices before and after PDA occlusion.

Variables	Pre-PDA			Post-PDA		
	Mean ± SD	95% CI (L-U)	95% CV	Mean ± SD	95% CI (L-U)	95% CV
Total IVPD	2.21 ± 0.37	1.82–2.61	16.8	1.74 ± 0.29	1.82–2.61	16.89
Basal IVPD	1.14 ± 0.24	0.80–1.47	21.3	0.72 ± 0.16	0.80–1.47	21.63
Mid-to-apical IVPD	1.13 ± 0.24	0.90–1.35	21.3	1.00 ± 0.20	0.90–1.35	20.40
Mid IVPD	0.91 ± 0.17	0.75–1.08	18.8	0.77 ± 0.15	0.75–1.08	18.96
Apical IVPD	0.19 ± 0.07	0.09–0.29	36.9	0.25 ± 0.08	0.09–0.29	32.72
Total IVPG	1.12 ± 0.21	0.94–1.29	18.5	0.94 ± 0.18	0.94–1.29	18.90
Basal IVPG	0.54 ± 0.10	0.42–0.67	18.8	0.39 ± 0.08	0.42–0.67	21.34
Mid-to-apical IVPG	0.56 ± 0.11	0.46–0.66	19.1	0.57 ± 0.11	0.46–0.66	19.89
Mid IVPG	0.47 ± 0.10	0.40–0.54	20.8	0.43 ± 0.08	0.40–0.54	19.24
Apical IVPG	0.099 ± 0.044	0.044–0.155	44.8	0.133 ± 0.059	0.044–0.155	44.6

The intraventricular pressure difference (IVPD) and intraventricular pressure gradients (IVPG) indices before and after occlusion of the patent ductus arteriosus (PDA) in dogs (n = 12). CV, coefficient of variation; CI, confidence interval (lower and upper limit).

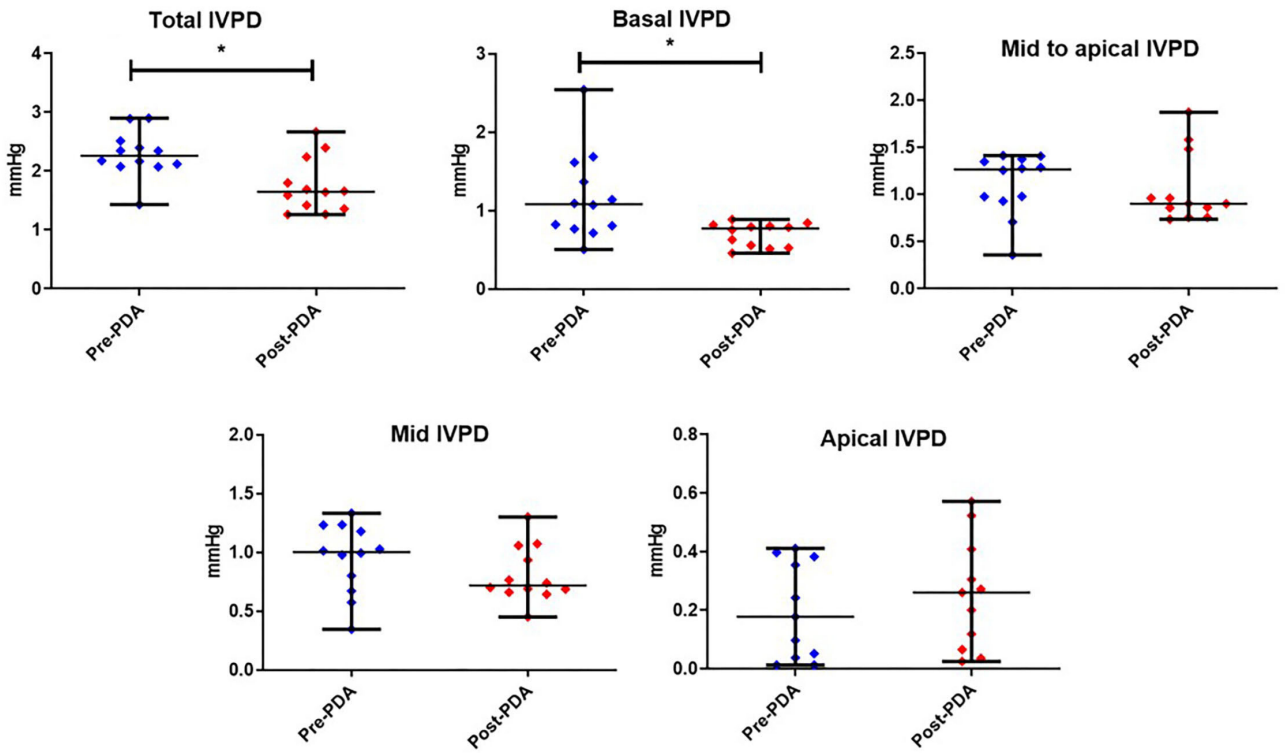

FIGURE 3 | CMME-derived intraventricular pressure difference (IVPD) variables before and after occlusion of the patent ductus arteriosus (pre-PDA, post-PDA) in dogs ($n = 12$). Dots plots showing the median and range. *indicates the statistical significance ($P < 0.05$).

some dogs which seems to be clinically unimportant (5, 6, 34). Based on Frank-Starling's Law, the contractility of the LV is increased secondary to elevated preload through the existing shunt *via* stretching of the muscle fibers to maintain effective systemic circulation. Therefore, reduction of the loading condition of the LV after PDA closure reduces myofibrillar stretching and contractility. In human PDA cases, a severe reduction in the preoperative FS has been reported to be a risk factor for postoperative death (35). Unlikely, postoperative mortalities are less encountered in dogs diagnosed with PDA, as they are usually admitted at <1 year of age before any significant reduction in the FS%. In this study, the FS% was

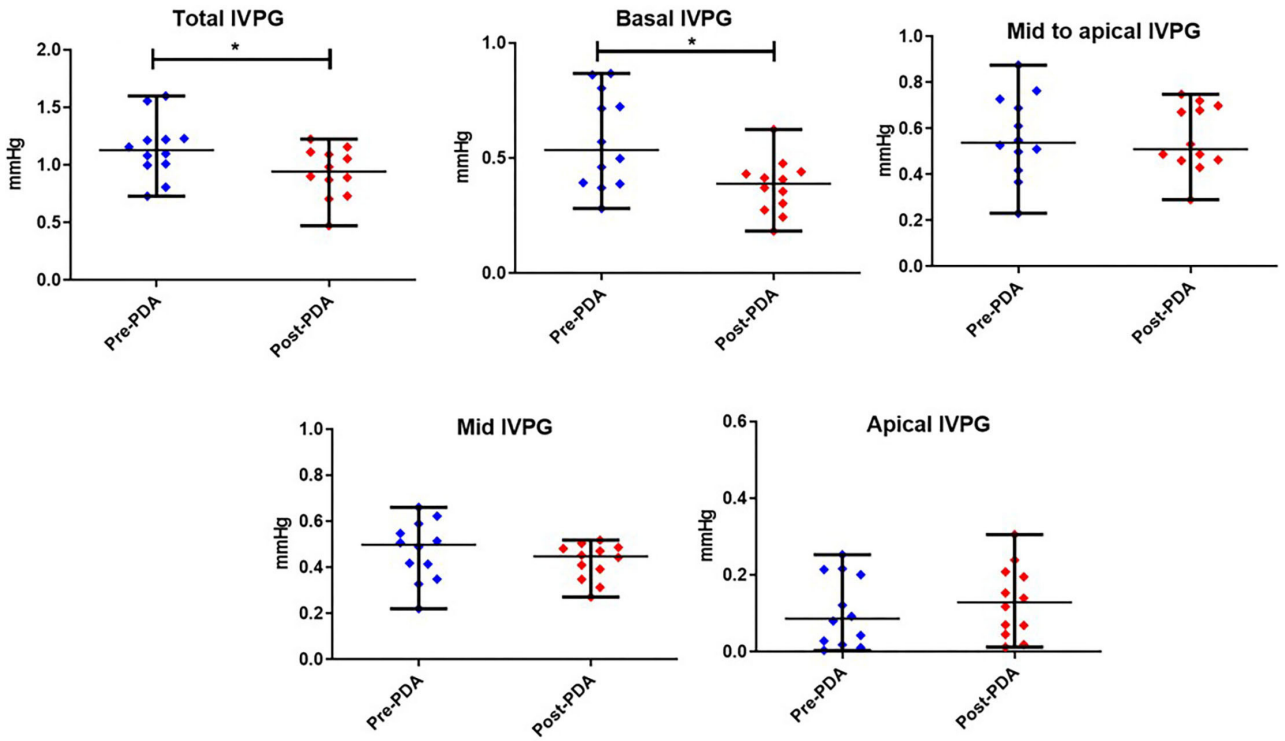

FIGURE 4 | Dots plots showing the median and range of the intraventricular pressure gradients (IVPG) indices Pre-and Post-PDA closure in dogs ($n = 12$). *reveals the statistical significance ($P < 0.05$).

TABLE 3 | Correlation between CMME indices and echocardiographic measurements.

Variables	HR	BW	LVIDd	EDV	ESV	FS%	LA/Ao	Ev	Em FW	Em/Am FW	E/Em FW
Total IVPD	0.007	0.095	0.211	0.192	0.193	−0.087	0.140	0.470*	−0.024	0.148	0.462
Basal IVPD	−0.115	−0.337	0.003	−0.017	−0.251	0.219	0.237	0.131	−0.192	−0.392*	0.450
Mid-to-apical IVPD	0.261	0.059	0.272	0.267	0.422*	−0.270	−0.219	0.424*	0.157	0.458*	0.225
Mid IVPD	0.051	−0.089	0.177	0.162	0.044	0.026	−0.163	0.213	−0.149	0.146	0.380
Apical IVPD	0.312	0.024	0.241	0.257	0.677*	−0.502*	−0.204	0.345	0.426*	0.533*	−0.161
Total IVPG	−0.263	−0.160	0.334	0.334	0.166	0.055	0.288	0.241	−0.038	−0.247	0.263
Basal IVPG	−0.290	−0.272	0.196	0.185	−0.179	0.307	0.446*	0.044	−0.089	−0.489*	0.108
Mid-to-apical IVPG	0.121	−0.053	0.418*	0.434*	0.541*	−0.248	−0.080	0.258	0.314	0.434*	−0.087
Mid IVPG	0.028	−0.148	0.317	0.319	0.119	0.086	−0.016	0.182	0.187	0.190	−0.010
Apical IVPG	0.215	0.047	0.351	0.370	0.703*	−0.420*	−0.074	0.281	0.454*	0.473*	−0.254

Spearman's correlation between conventional echocardiographic parameters and color M-mode echocardiographic indices.
**indicates significant correlation ($P < 0.05$).*

>35% (median of 41.9%), except for one case in which the FS was 28.0%, indicating no reduction of preoperative FS%. The reduction of the Em (for the septum) could be explained by the fact that it can be affected by HR and preload (36). In addition, Em velocity may not reflect the function of the entire ventricle, as it is highly angle-dependent and also vastly influenced by the cardiac translational movement and tethering (17).

Color M-mode echocardiography can be used to separately evaluate the diastolic function and cardiac preload. The feasibility of CMME for the assessment of IVPD and IVPG has already been reported in dogs (11, 12). As in previous studies, IVPD and IVPG were calculated using a program in MATLAB, which was further modified from previous reports (14, 16, 26–28). To enable a detailed evaluation of the pathophysiology of each fraction of IVPD and IVPG in the LV, the LV was divided into three sections

according to its anatomical localization, which collectively or partially reflects specific LV function, which implies that IVPD and IVPG can be interpreted comprehensively (26). In this study, CMME was feasible in all dogs and showed moderate variability (95% CV <25%) in all indices except for the apical IVPD and apical IVPG. Those results could be attributed to variable loading conditions that can be influenced by different factors in dogs including age, body weight, and breed of dogs (11). Since all the echocardiographic data were collected without prior sedation, body movements may have resulted in data variability. The higher variability in the apical segment was previously reported (37), which could be explained by variation in the color resolution of the upper part of CMME images compared with the lower part.

In the current study, there was a significant decrease in total and basal IVPD and IVPG post-PDA compared with pre-ligation measurements. This is presumably due to the reduction in the loading status secondary to decreased preload in the dogs post-PDA (9). This explanation is supported by the observed reduction in LVIDd, Ev, and E/Em, which are known as conventional indicators of the preload (25). The apical segment of IVPD and IVPG, on the other hand, increased slightly but not significantly in our study. Additionally, there were no significant changes in mid and mid-to-apical IVPD or IVPG. Generally, PDA closure showed a synchronous decrease in the LV preload and increment in the afterload. The increase in afterload is related to the low-resistance pulmonary circulation compared to the LV outflow (34, 38, 39). A temporal reduction in heart function following PDA ligation was previously reported (5). We assumed a decrease in mid and/or mid-to-apical segments of LV pressure obtained *via* CMME as an indication of LV active relaxation after PDA closure (7). However, this was not proved in our study, which may be due to the small size group, absence of CHF in our patients, and lack of long-term follow-up by CMME. In other words, 48 h was insufficient to observe significant changes in LV active relaxation by CMME. A previous human study required long-term follow-up for recovery of cardiac function after PDA closure (38). In addition, the recovery of diastolic function after PDA closure is slow and difficult to assess (40). Therefore, long-term observations of IVPD and IVPG may allow better assessment of changes in LV mitigation capacity. Based on our results, we believe that left ventricular relaxation capacity is less susceptible to sudden hemodynamic changes that may be detectable by CMME over a longer time of patient follow-up.

In our study, there were some correlations between the CMME-derived indices and conventional echocardiographic parameters, particularly those that are important for diastolic function, as previously observed in other studies (7, 9–12, 16, 37). The IVPD and IVPG indices reported in the present study were comparable to previous reports in dogs and cats (11, 15, 37). A previous study reported CMME-derived IVPD and IVPG indices in a group of healthy small to large breed dogs of different ages and BW and found that the IVPD was influenced by the heart size (11). In our study, there was a significant correlation between mid-to-apical IVPG and LVIDd, which could be attributed to the narrow age and BW ranges of our group. Another feline study showed that the total IVPG was affected by HR (37), which was not found in our study. There was not much difference in the HR range between dogs in this study and cats in the other study (37). Unlike dogs, cats can become highly excited during the examination, and consequent fluctuation of the HR and increased systolic function may be noticed under the influence of a high sympathetic tone (37, 41). In our study, the correlation coefficient was almost weak. Therefore, proper interpretation of these relationships may be biased due to the small sample size and short-term follow-up, and we would like to accumulate a larger number of PDA cases throughout a longitudinal observation to increase the statistical power of our findings in the future.

Clinical Implications

This is the first clinical study to utilize CMME indices in dogs to compare the changes observed before and after PDA occlusion. The clinical relevance of the result is clear and has been associated with a large effect size on total and basal segments of IVPD and IVPG rather than mid-to-apical parts. The result of this study did not provide clear evidence of significant change in mid-to-apical IVPD/IVPG, the landmark for enhanced LV relaxation, because assessment after 48 h following PDA occlusion is too short to fully restore left ventricular diastolic function. This is likely due to the more rapid changes in hemodynamic rather than morphological changes in the cardiac function shortly after the PDA occlusion, and further longitudinal observation at different time points is necessary.

Limitations

The number of dogs included in the study is small; however, the provided data and their clinical relevance are quite solid. Since the PDA operation was performed *via* intercostal thoracotomy, neither catheterization nor angiography was performed for this study. A previous study showed that CMME-derived IVPD and IVPG were strongly correlated with *tau* measured by invasive catheterization, thus comparative assessment of IVPD between CMME and catheterization was not performed in this study (7, 12, 28). Besides, recent publications used CMME for non-invasive assessment of IVPD and/or IVPG that has been performed in dogs and cats without catheterization (15, 37).

CONCLUSION

A short-term observation of IVPD and IVPG reflects the changes in preload rather than myocardial relaxation, and a continuous follow-up at different time intervals following PDA occlusion warrants another study. Overall, CMME-derived IVPD and IVPG can be used for further evaluation of cardiac function in dogs, and the apical indices should be considered with caution.

DATA AVAILABILITY STATEMENT

The raw data supporting the conclusions of this article will be made available by the authors, without undue reservation.

ETHICS STATEMENT

The animal study was reviewed and approved by the Ethical Committee of the Animal Medical Center, Tokyo University of Agriculture and Technology. Written informed consent was obtained from the owners for the participation of their animals in this study.

AUTHOR CONTRIBUTIONS

MH, SG, and RT conceived and designed the experiment. RT, SG, and KS: surgical procedures. MH, ASM, KM, LH, KT, and TY: echocardiography and software analysis. MH and ASM: statistical analysis, manuscript drafting, and writing the final manuscript. LH, AU, KS, KT, and RT revised and edited the manuscript. All authors have read and agreed to the published version of the manuscript.

REFERENCES

1. Hew KW, Keller KA. Postnatal anatomical and functional development of the heart: a species comparison. *Birth Defects Res B Dev Reprod Toxicol.* (2003) 68:309al andReson. 1002/bdrb.10034
2. Buchanan JW, Patterson DF. Etiology of patent ductus arteriosus in dogs. *J Vet Intern Med.* (2003) 17:167fctus arterio1111/j.1939-1676.2003.tb02429.x
3. Hsu H-W, Lin T-Y, Liu Y-C, Yeh J-L, Hsu J-H. Molecular mechanisms underlying remodeling of ductus arteriosus: looking beyond the prostaglandin pathway. *Int J Mol Sci.* (2021) 22:3238. doi: 10.3390/ijms22063238
4. Oliveira P, Domenech O, Silva J, Vannini S, Bussadori R, Bussadori C. Retrospective review of congenital heart disease in 976 dogs. *J Vet Intern Med.* (2011) 25:477f congenital 1111/j.1939-1676.2011.0711.x
5. Hamabe L, Kim S, Yoshiyuki R, Fukayama T, Nakata TM, Fukushima R, et al. Echocardiographic evaluation of myocardial changes observed after closure of patent ductus arteriosus in dogs. *J Vet Intern Med.* (2015) 29:126tern Medluati1111/jvim.12517
6. Saunders AB, Gordon SG, Boggess MM, Miller MW. Long-term outcome in dogs with patent ductus arteriosus: 520 cases (1994–2009). *J Vet Intern Med.* (2014) 28:401f10. doi: 10.1111/jvim.12267
7. Nagueh SF. Heart failure with preserved ejection fraction: insights into diagnosis and pathophysiology. *Cardiovasc Res.* (2021) 117:999c1014. doi: 10.1093/cvr/cvaa228
8. Thomas JD, Choong CY, Flachskampf FA, Weyman AE. Analysis of the early transmitral Doppler velocity curve: effect of primary physiologic changes and compensatory preload adjustment. *J Am Coll Cardiol.* (1990) 16:644l Cardiolt. ,1016/0735-1097(90)90356-T
9. Nagueh SF. Left ventricular diastolic function. *JACC Cardiovasc Imag.* (2020) 13:228–44. doi: 10.1016/j.jcmg.2018.10.038
10. Flachskampf FA, Biering-Sctionmpf FA, Weyman AE. Analysis of the early transth OA. Cardiac imaging to evaluate left ventricular diastolic function. *JACC Cardiovasc Imag.* (2015) 8:1071–07115asco ev1016/j.jcmg.2015.07.004
11. Matsuura K, Shiraishi K, Sato K, Shimada K, Goya S, Uemura A, et al. Left ventricular vortex and intraventricular pressure difference in dogs under various loading conditions. *Am J Physiol Heart Circul Physiol.* (2019) 316:H88238. doi: 10.1152/ajpheart.00686.2018
12. Sasaki K, Ma D, Mandour AS, Ozai Y, Yoshida T, Matsuura K, et al. Evaluation of changes in the cardiac function before and after transcatheter edge-to-edge mitral valve repair in healthy dogs: conventional and novel echocardiography. *Anim Open Acc J MDPI.* (2021) 12:56. doi: 10.3390/ani12010056
13. Ma D, Mandour AS, Hendawy H, Yoshida T, El-Husseiny HM, Ozai Y, et al. Renovascular hypertension-induced cardiac changes in a rat model: feasibility of conventional and recent echocardiography. *J Hypertens.* (2021) 39:e40339:1rtens. e1097/01.hjh.0000749268.15046.a5
14. Ma D, Mandour AS, Yoshida T, Matsuura K, Shimada K, Kitpipatkun P, et al. Intraventricular pressure gradients change during the development of left ventricular hypertrophy: effect of salvianolic acid B and beta-blocker. *Ultrasound*. (2021) 29:229–40. doi: 10.1177/1742271X2098 7584
15. Matsuura K, Sato K, Shimada K, Goya S, Uemura A, Iso T, et al. Changes in left ventricular blood flow during diastole due to differences in chamber size in healthy dogs. *Sci Rep*. (2020) 10:1106. doi: 10.1038/s41598-019-57180-6
16. Matsuura K, Shiraishi K, Mandour AS, Sato K, Shimada K, Goya S, et al. The utility of intraventricular pressure gradient for early detection of chemotherapy-induced subclinical cardiac dysfunction in dogs. *Anim Open Access J MDPI.* (2021) 11:122. doi: 10.3390/ani11041122
17. Yairo A, Mandour AS, Matsuura K, Yoshida T, Ma D, Kitpipatkun P, et al. Effect of loading changes on the intraventricular pressure measured by color M-mode echocardiography in rats. *Diagnostics*. (2021) 11:403. doi: 10.3390/diagnostics11081403
18. Ma D, Mandour AS, Elfadadny A, Hendawy H, Yoshida T, El-Husseiny HM, et al. Changes in cardiac function during the development of uremic cardiomyopathy and the effect of salvianolic acid b administration in a rat model. *Front Vet Sci Vet Imag*. (2022) 9:905759. doi: 10.3389/fvets.2022.905759
19. Kobayashi M, Takahashi K, Yamada M, Yazaki K, Matsui K, Tanaka N, et al. Assessment of early diastolic intraventricular pressure gradient in the left ventricle among patients with repaired tetralogy of Fallot. *Heart Vessels*. (2017) 32:1364–74. doi: 10.1007/s00380-017-1011-6
20. Shigemitsu S, Takahashi K, Yazaki K, Kobayashi M, Yamada M, Akimoto K, et al. New insight into the intraventricular pressure gradient as a sensitive indicator of diastolic cardiac dysfunction in patients with childhood cancer after anthracycline therapy. *Heart Vessels*. (2019) 34:992s1001. doi: 10.1007/s00380-018-01332-7
21. Takahashi K, Nii M, Takigiku K, Toyono M, Iwashima S, Inoue N, et al. Development of suction force during early diastole from the left atrium to the left ventricle in infants, children, and adolescents. *Heart Vessels*. (2019) 34:296–306. doi: 10.1007/s00380-018-1239-9
22. Broaddus K, Tillson M. Patent ductus arteriosus in dogs. *Compendium.* (2010) 32:E3.
23. Takeuchi A, Uemura A, Goya S, Shimada K, Yoshida T, Hara S, et al. The utility of patent ductus arteriosus closure with hemostatic clip in dogs. *Pol J Vet Sci.* (2020) 23:255t Sc doi: 10.24425/pjvs.2020.1 33640
24. Ozai Y, Uemura A, Tanaka R, Takeuchi A, Hamabe L, Shimada K, et al. Clip ligation for treatment of patent ductus arteriosus occlusion in three cats. *J Vet Sci*. (2022) 23. (inpress). doi: 10.4142/jvs.21314
25. Tanaka R, Soda A, Saida Y, Sugihara K, Takashima K, Shibazaki A, et al. Evaluation of the efficacy and safety of coil occlusion for patent ductus arteriosus in dogs. *J Vet Med Sci.* (2007) 69:857fion of the 1292/jvms.69.857
26. De Madron E, Chetboul V, Bussadori C. *Clinical Echocardiography of the Dog and Cat-E-Book*. The Netherlands: Elsevier Health Sciences (2015).
27. Popovi6514ealth Sciencesnd Cat-E-Book y of coil occlusion for pate, et al. Scaling of diastolic intraventricular pressure gradients is related to filling time duration. *Am J Physiol Heart Circul Physiol.* (2006) 291:H762291: of of d1152/ajpheart.00081.2006
28. Yotti R, Bermejo J, Antoranz JC, Desco MM, Cortina C, Rojo-Alvarez JL, et al. A noninvasive method for assessing impaired diastolic suction

in patients with dilated cardiomyopathy. *Circulation.* (2005) 112:2921–9212:ationt1161/CIRCULATIONAHA.105.561340
29. Greenberg NL, Vandervoort PM, Firstenberg MS, Garcia MJ, Thomas JD. Estimation of diastolic intraventricular pressure gradients by Doppler M-mode echocardiography. *Am J Physiol Heart Circul Physiol.* (2001) 280:H250780: ofhy. Va1152/ajpheart.2001.280.6.H2507
30. Faul F, Erdfelder E, Buchner A, Lang AG. Statistical power analyses using G*Power 31: tests for correlation and regression analyses. *Behav Res Methods.* (2009) 41:1149–149:9tical p3758/BRM.41.4.1149
31. Cohen J. *Statistical Power Analysis for the Behavioral Sciences*. 2nd ed. Erlbaum (1988).
32. Fritz CO, Morris PE, Richler JJ. Effect size estimates: current use, calculations, and interpretation. *J Exp Psychol Gen.* (2012) 141:2al Morris PE,1037/a0024338
33. Ha J-W, Oh JK. Therapeutic strategies for diastolic dysfunction: a clinical perspective. *J Cardiovasc Ultrasound.* (2009) 17:86–95. doi: 10.4250/jcu.2009.17.3.86
34. Stauthammer CD, Tobias AH, Leeder DB, Krsize estimates: current use, calculations, and interpretation. cular pressure gradients bg interventional patent ductus arteriosus occlusion in dogs: 24 cases (2000-2006). *J Am Vet Med Assoc.* (2013) 242:1722–7222:et Med2460/javma.242.12.1722
35. Hou M, Qian W, Wang B, Zhou W, Zhang J, Ding Y, et al. Echocardiographic prediction of left ventricular dysfunction after transcatheter patent ductus arteriosus closure in children. *Front Pediatr.* (2019) 7:409. doi: 10.3389/fped.2019.00409
36. Firstenberg MS, Greenberg NL, Main ML, Drinko JK, Odabashian JA, Thomas JD, et al. Determinants of diastolic myocardial tissue Doppler velocities: influences of relaxation and preload. *J Appl Physiol.* (2001) 90:299hysiol of dias1152/jappl.2001.90.1.299
37. Matsuura K, Bach MBT, Takahashi K, Willesen JL, Koch J, Tanaka R. Non-invasive assessment of left ventricular relaxation property using color M-mode-derived intraventricular pressure gradients in cats. *J Vet Cardiol.* (2022) 41:236–48. doi: 10.1016/j.jvc.2022.03.006
38. Galal MO, Amin M, Hussein A, Kouatli A, Al-Ata J, Jamjoom A. Left ventricular dysfunction after closure of large patent ductus arteriosus. *Asian Cardiovasc Thoracic Ann.* (2005) 13:24c Andoi: 10.1177/021849230501300106
39. Abdel-Bary M, Abdel-Baseer KA, Abdel-Latif AF, Abdel-Naser MA, Nafie M, Eisa KM. Left ventricular dysfunction postsurgical patent ductus arteriosus ligation in children: predictor factors analysis. *J Cardiothorac Surg.* (2019) 14:168. doi: 10.1186/s13019-019-0990-z
40. Gupta SK, Krishnamoorthy K, Tharakan JA, Sivasankaran S, Sanjay G, Bijulal S, et al. Percutaneous closure of patent ductus arteriosus in children: immediate and short-term changes in left ventricular systolic and diastolic function. *Ann Pediatr Cardiol.* (2011) 4:139lCarddoi: 10.4103/0974-2069.84652
41. Abbott JA. Heart rate and heart rate variability of healthy cats in home and hospital environments. *J Feline Med Surg.* (2005) 7:195e Med doi: 10.1016/j.jfms.2004.12.003

Conflict of Interest: The authors declare that the research was conducted in the absence of any commercial or financial relationships that could be construed as a potential conflict of interest.

The handling editor HS declared a past co-authorship with the authors ASM and RT.

Publisher's Note: All claims expressed in this article are solely those of the authors and do not necessarily represent those of their affiliated organizations, or those of the publisher, the editors and the reviewers. Any product that may be evaluated in this article, or claim that may be made by its manufacturer, is not guaranteed or endorsed by the publisher.

frontiers | Frontiers in Veterinary Science

TYPE Original Research
PUBLISHED 28 July 2022
DOI 10.3389/fvets.2022.896581

OPEN ACCESS

EDITED BY
Sibylle Maria Kneissl,
University of Veterinary Medicine Vienna, Austria

REVIEWED BY
Karima Mahmoud,
National Research Centre, Egypt
Margherita Maranesi,
University of Perugia, Italy

*CORRESPONDENCE
Elshymaa A. Abdelnaby
elshymaa.ahmed@cu.edu.eg;
elshymaaahmed@yahoo.com

SPECIALTY SECTION
This article was submitted to Veterinary Imaging, a section of the journal Frontiers in Veterinary Science

RECEIVED 15 March 2022
ACCEPTED 29 June 2022
PUBLISHED 28 July 2022

CITATION
Daghash SM, Yasin NAE, Abdelnaby EA, Emam IA, Tolba A and Abouelela YS (2022) Histological and hemodynamic characterization of corpus luteum throughout the luteal phase in pregnant and non-pregnant buffalos in relation to nitric oxide levels based on its anatomical determination. *Front. Vet. Sci.* 9:896581. doi: 10.3389/fvets.2022.896581

Histological and hemodynamic characterization of corpus luteum throughout the luteal phase in pregnant and non-pregnant buffalos in relation to nitric oxide levels based on its anatomical determination

Samer M. Daghash[1], Noha A. E. Yasin[2], Elshymaa A. Abdelnaby[3]*, Ibrahim A. Emam[4], Ayman Tolba[1] and Yara S. Abouelela[1]

[1]Anatomy and Embryology Department, Faculty of Veterinary Medicine, Cairo University, Giza, Egypt, [2]Cytology and Histology Department, Faculty of Veterinary Medicine, Cairo University, Giza, Egypt, [3]Theriogenology Department, Faculty of Veterinary Medicine, Cairo University, Giza, Egypt, [4]Department of Surgery, Anaesthesiology and Radiology, Faculty of Veterinary Medicine, Cairo University, Giza, Egypt

This study aims to compare the complete growth and development of corpus luteum (CL) in domestic buffalos from day 5 until day 40 after ovulation either in pregnant or non-pregnant animals and whether luteal vascularity (LV) with progesterone (P4) and nitric oxide (NO) could determine luteal functionality or not. Pluriparous buffalos (*Bubalus bubalis*) were categorized as pregnant ($n = 6$) or non-pregnant ($n = 9$) after pregnancy check at day 25. Animals were subjected to ultrasound analysis to determine the CL area (cm^2) and LV. Blood sampling was performed following the Doppler examination. Ovarian tissue samples from non-pregnant buffalo genitalia ($n = 18$) and early pregnant buffalo genitalia ($n = 3$) were collected from great abattoirs. Luteal Doppler indices were lower in the pregnant group, while peak systolic velocity (PSV) was increased ($p < 0.05$) in the same pregnant females. Both P4 and NOMs were elevated ($p < 0.05$) in the pregnant group. There was a positive correlation ($p < 0.01$) between P4 and CL PSV. Based on our macroscopical examination, the CL of non-pregnant buffalos was classified into four stages. Histologically, stage I showed that CL was covered by a highly vascularized connective tissue (CT) capsule. It consisted of small and large lutein cells, whereas stage II was similar to stage I except for the presence of numerous fibroblast cells and vacuolated cells. Stage III was characterized by increasing the number of collagen fibers and the thickness of the blood vessels. Stage IV revealed thickening of the CT capsule and septae, regressed capillaries and arterioles, in addition to shrunken degenerated lutein cells. CL of pregnant buffalos revealed the same

structure as CL at stage II. CL area was increased in the pregnant group. The collective data suggested that evaluation of the luteal artery could be extremely helpful to determine the potential benefits of colored and pulsed Doppler in CL vascularization assessment in both luteal and early pregnancy phases.

KEYWORDS

buffalos, corpus luteum, Doppler, histology, pregnant

Introduction

Buffalos (*Bubalus bubalis*) are a common species in the Middle East (1) and Africa (2), and have great potential due to their critical role in farming and agriculture in those developing countries (3–5). One of the major restraints in the utilization of domestic buffalo reproductive capacity as compared to cattle has been its characteristically poorer reproductive functionality and efficiency (6) that is associated with silent heat, missing many behavioral signs, and lesser conception rates (7, 8). So, studying a basic reproductive pattern is of great importance for enhancing the reproductive efficiency of buffalos (9). The corpus luteum (CL) is the primary reproductive gland responsible for progesterone production, and is required for the establishment and progression of the gestation period; moreover, CL plays a critical role in many reproductive processes, such as successive implantation and embryonic development (10, 11). Histologically, CL consists of cells with a steroidogenic and non-steroidogenic nature (12). The steroidogenic cells, which are responsible for progesterone production, are composed of luteal cells (large and small cells that originate from both granulosa and theca cells), while the non-steroidogenic cells are composed of fibroblasts, endothelial cells, and macrophage (13, 14). Although luteal functions have been evaluated in many studies (15, 16), many specific regulatory factors related to luteal vascularization need future studies, especially in buffalos. The size of the CL at the mid-luteal phase of the estrous cycle ranged from 1 to 2 cm compared to that at pregnancy which ranged from 2 to 2.5 cm (17). Generally, the CL in buffalo is smaller compared to that in cattle (18) and associated with lower progesterone levels, which in turn may affect embryonic mortality (19, 20) and adversely impact the maintenance of pregnancy (21, 22). Some studies have reported that the adequate development of the CL in association with progesterone levels (P4) is needed to prevent embryonic mortality (23); in addition, pregnant buffalos reported a greater diameter of CL linked to a marked linear increase in plasma P4 levels that positively affects the luteal vascularity (LV) (24). Another study has reported a higher average timed velocity (TAV cm/sec) of the luteal artery in pregnant buffalos compared to non-pregnant buffalos (25). Moreover, lower pregnancy rates are observed with lower CL vascularization after 5 days of mating (26). The luteal and early normal pregnancy phases are associated with marked changes in the cardiovascular hemodynamic system, such as elevated blood flow volume and decreased Doppler indices, especially vascular resistance index (27, 28), as all these changes are followed by increased levels of nitric oxide (NO) and its metabolites (NOMs) in the form of nitrite and nitrate, which lead to the improved response of smooth muscle on NO reaction (29). Little is known about the histological structure of CL, using the Doppler technique that is based on the anatomical determination of the luteal artery, as well as characterization of each luteal stage in normal luteal and pregnant phases in Egyptian domestic buffalo. Therefore, this current study aimed to compare the complete growth and development of CL in domestic buffalos from day 5 until day 40 after ovulation either in pregnant or non-pregnant buffalo, and whether luteal vascularity (LV) with progesterone (P4) and nitric oxide (NO) could determine luteal functionality or not.

Materials and methods

Ethical approval

All experiments were performed according to the Veterinary Animal Care and Use Committee of the Faculty of Veterinary Medicine, Cairo University (Approval number Vet CU12/10/2021/363).

Animal housing and management

For the study, cyclic pluriparous ($n = 18$) Egyptian domestic buffalos (*Bubalus bubalis* aged 8–11 years, 3.5 ± 0.5 body condition score, 490 ± 30 kg) kept on a large animal farm in the Faculty of Veterinary Medicine at Giza square (30.0276°N, 31.2101°E) were used. Animals were maintained in open yards. All females were fed a mixed ration that consisted of 60% forage and 40% concentrate, containing dry matter and crude protein. To determine the female cyclicity, all buffalos underwent weekly ultrasound examination (1 time/week for 3 successive weeks) to evaluate the ovarian functionality using EXAGO, rectal ultrasound device (France), as the device is

equipped with a 6–12 MHz transrectal probe, before the start of examination procedures.

Time of synchronization and mating process

Synchronization was performed using the gonadotropin–prostaglandin–gonadotropin combination (GPG/ Ovsynch) protocol, which was previously conducted in cattle (30), and used in buffalo (31). The GPG program was started with the first intramuscular injection of GnRH (5 ml/animal; Receptal® 0.004 mg/ml, Msd Animal Health India) on day 0 followed by a single intramuscular injection of prostaglandin ($PGF_2\alpha$) per intramuscular injection (25 mg; Lutalyse®, Upjohn) on day 7 and a second GnRH was administered on day 9 as previously demonstrated in buffalos (31). All females underwent routine ultrasound assessment on day 11 after mating from the start of the GPG program and only those excited by a preovulatory follicle ≥1 cm (32) were used in the study ($n = 18$). All buffalos were examined randomly ($n = 18$); after that, nine buffalos were mated naturally 21 h after the second GnRH injection by an adult healthy bull aged from 9 to 10 years ($n = 5$) (33, 34). Mated buffalos were examined on day 25 for pregnancy after natural mating using the same ultrasound device at this day. Of nine females, only six became pregnant (GP I, Pregnant; $n = 6$), while the other three did not ($n = 3$); the second group were not mated and entered in the normal luteal phase after the ovulation process (GP II, Non-pregnant; $n = 9$). Furthermore, ultrasound assessments were done one-day post-mating to assure that all the animals underwent normal ovulation, which was confirmed by the disappearance of the largest follicle using B-mode ultrasound scanning (35, 36).

CL vascularization assessment

CL ultrasound assessment was conducted every day from day 5 after ovulation until day 40 using Doppler ultrasound portable device (ExaGO, rectal ultrasound device, France) performed with a 6–12 MHz transrectal probe with a device set as follows: velocity was automated at 25 cm/s, Doppler filter was 150 Hz, PRF was 3,500 kHz, and insonation angle was 40° (37). The procedure of CL examination was done once the ovary appeared on the ultrasound scanner and the image was frozen to measure the CL dimensions to estimate the CL area by equation [area = π*(a/2)*(b/2)], where a and b were the short and long axis of CL dimensions, respectively (26). To evaluate the CL blood flow perfusion, color Doppler mode was activated, and a sample window was placed on the CL tissue to show the colored area in blue (away from the probe) and red (toward probe) color maps, which were assessed by image analysis software program at different stages of the luteal phase and the first days of pregnancy (38).

CL Doppler parameter evaluations

Based on our anatomical determination of the luteal artery and at the level of clearly visualized CL, the spectral mode was activated to show the blood flow velocity of the luteal artery by the wave pattern that was presented only in the luteal artery, not on the luteal vein, as venous circulation assessment did not give any information due to the absence of spectral graph obtained from pulsed-wave Doppler mode (Figure 1). The spectral graph showed a Doppler measurements calculation automatically as resistance and pulsatility index (RI and PI), peak velocity point of contraction and end-diastolic point of relaxation (PSV and EDV cm/s), as well as time to perform maximum velocity (TAV cm/s; Figure 1). B-, color, and spectral modes videos (15 s duration /each) were saved and stored on the flash memory. If there was a cavity in the CL, the area of the CL was assessed by subtracting the cavity area from the whole CL area (39).

Blood sampling and hormonal assessment

Blood samples were obtained from the jugular vein of all buffalos from day 5 until day 40 following each Doppler examination. Plasma and serum samples were stored at −20 until hormone analysis. Progesterone (P4, EIA-1561) was analyzed using ELISA kits (DRG, Germany) by competitive assaying with inter and intra assays precisions of 9.96 and 5.4, respectively, and test sensitivity of 0.045 ng/ml. Serum samples were used in assaying the nitric oxide (NO) *via* its metabolites (NOMs; μmol/L) as previously examined in our laboratory (40, 41). The nitric oxide inter and intra assay coefficients were 1.17% and 1.09%.

Collection of tissue samples

Non-pregnant buffalo genitalia (ovaries bearing the CL) ($n = 18$) ($n = 2$ for vascular anatomical architecture and $n = 16$ for histological examination ($n = 4$ genitalia/each luteal stage) in addition to early pregnant buffalo genitalia ($n = 3$) were collected from great Cairo abattoirs within 3 months. The reproductive organs were transported on ice to the laboratory for examination within 15 min after exsanguinations. Stages of the estrous cycle were determined by macroscopic ovarian dating (color, consistency, size, vasculature of CL, and presence of follicles on the surface of the ovary) and then classified into early luteal [Stage I, ($n = 4$), 1–5 days] (Figure 2a) in which the CL appeared small, reddish, and soft; mid-luteal (stage II and

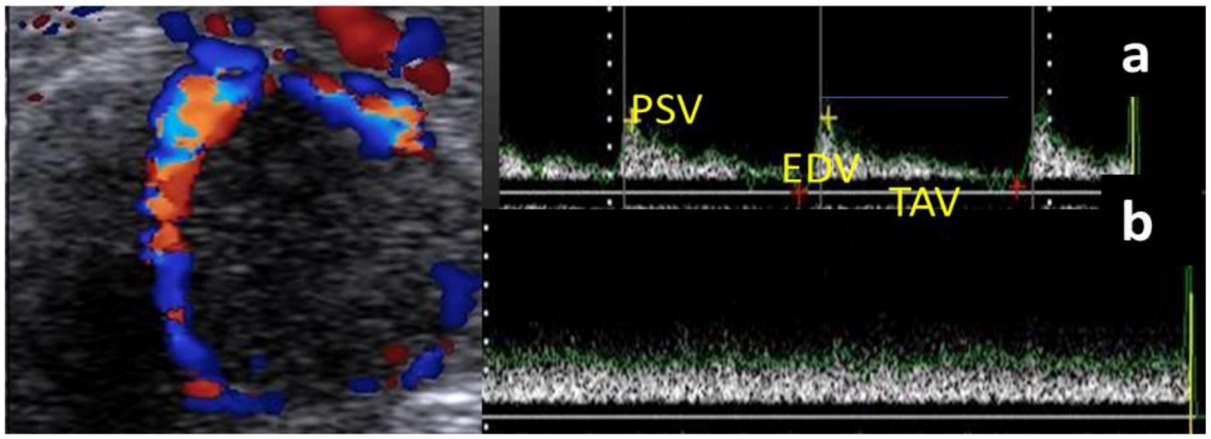

FIGURE 1
Ultrasonogram revealed the mature corpus luteum (CL) with its spectral wave of both luteal artery **(a)** and luteal vein **(b)** blood flow velocities. N.B: Luteal artery waveform characterized by a complete cardiac cycle in from of peak systolic (PSV; cm/s) and end diastolic velocities (EDV; cm/s) with time average to make maximum velocity (TAV; cm/s), while the vein wave was characterized by absence of cardiac cycle without any spectral graph.

stage III) in which the CL became large, brownish, and harder [Stage II, ($n = 4$), 6–10 days] (Figure 2b) and appeared fibrous, pale, and hard [Stage III, ($n = 4$), 11–16 days] (Figure 2c); and late luteal stage [Stage IV, ($n = 4$), 17–20 days] (Figure 2d). CL can be seen as fibrous, yellowish, and hard. While in pregnancy, CL became light reddish with enlargement of the uterine horn (Figure 2e). Additionally, this classification was also defined depending on Baithalu et al. (14).

Vascular anatomical architecture

Two specimens from non-pregnant genitalia were used to examine the vascular anatomical architecture for demonstrating the ovarian and luteal artery. Vessels were cannulated, flushed thoroughly with normal saline to remove any blood clots, and then injected with 60% gum milk latex emulsion colored red using ROTRING ink (42, 43). Then the specimens were kept in formalin 10% and 1% glycerine solution for 4 days before manual dissection. The photograph was taken by a digital camera and manipulated by Photoshop ccx64 version. After dissection, we found that the arterial supply of the buffalo ovary was the main ovarian artery, which trifurcated into ovarian, tubal, and uterine branches. The first one continued for a short distance craniolaterally and then divided into 3–4 twigs to enter the ovary from its attached border, the middle one was the luteal artery which was convoluted in its pathway until reached the ovary within the meso-ovarian ligament (Figure 3).

Histological examination

Samples of ovarian tissue containing CL from pregnant and non-pregnant buffalos were fixed in 10% neutral buffered formalin, dehydrated in ascending grades of ethanol, cleared in xylene, and finally embedded in paraffin wax. Paraffin sections (4–5 μm thick) were obtained and stained with hematoxylin and eosin, Crossman's trichrome stain, and periodic acid-Schiff (PAS) (44).

Statistical analysis

All data are presented as the mean ± SEM as all results are the first check for normality. An unpaired *t*-test was used for comparisons between the two groups at each time point. The statistical significance of progesterone and nitric oxide alterations, as well as luteal Doppler findings in both groups, was assessed by repeated-measures two-way analysis of variance (ANOVA) to study the effect of group, time, and their interaction. By this method, you can compare all 16 values (2*8) (interaction between the effect of group and time). All analyses were achieved by using SPSS software version 20. $p < 0.05$ indicates significant differences. Pearson's correlation coefficients between progesterone levels and CL Doppler parameters in all females (pregnant and non-pregnant) were calculated.

Results

Corpus luteum characterization in live animals and hormonal analysis

The luteal phase was divided into early (Figure 4), mid [stages II and III] (Figure 5), and late (Figure 6) stages in

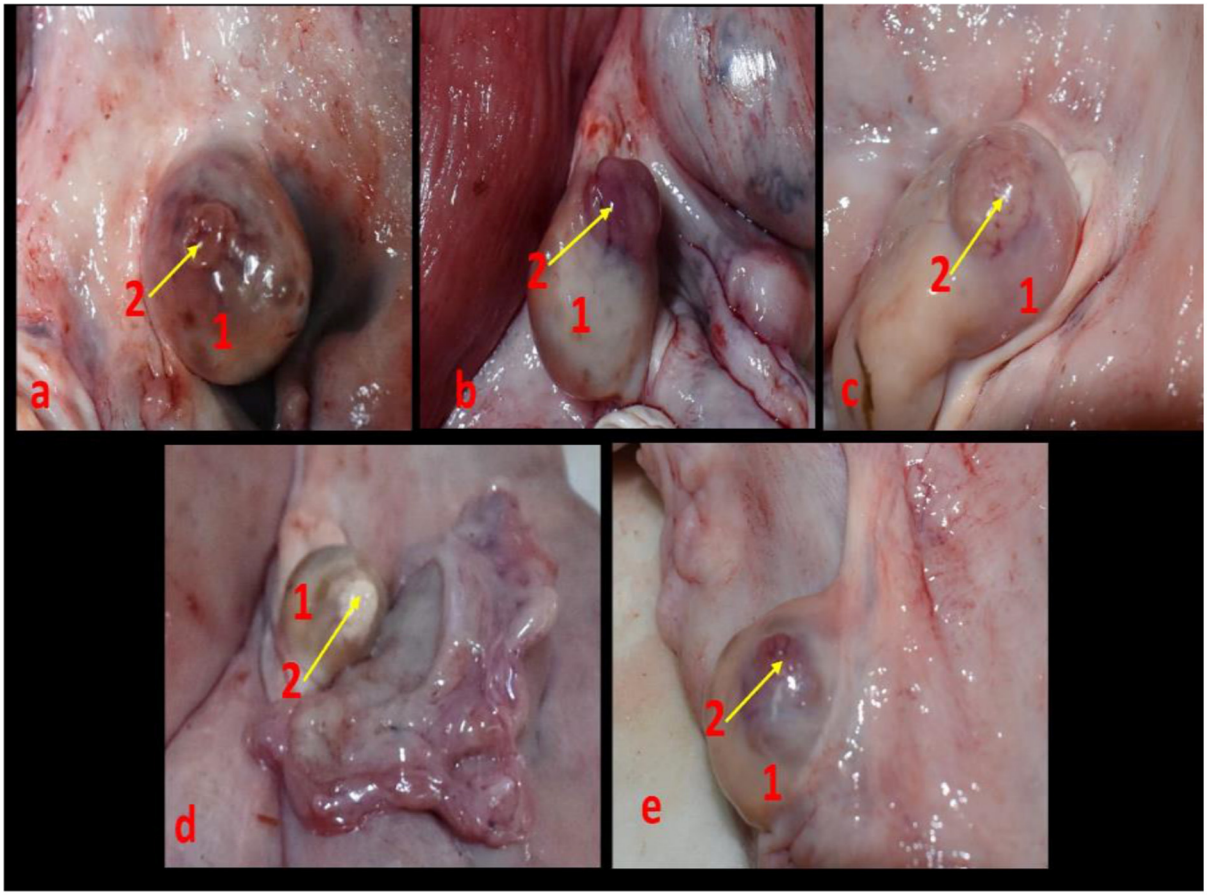

FIGURE 2
Corpus luteum in the buffalo ovary at different luteal stages as **(a)** represented an early luteal (stage I, 1-5 days), **(b)** demonstrated a mid-luteal (stage II, 6-10 days), **(c)** showed a mid-luteal (stage III, 11–16 days), **(d)** showed a late luteal (stage IV, 17-20 days), and **(e)** demonstrated corpus luteum gravidities at early stage of pregnancy. N.B: 1, ovary and 2, corpus luteum.

pregnant and non-pregnant animals. Moreover, this luteal classification was also confirmed by the progesterone levels at these stages.

CL area (cm^2) determination by B-mode ultrasonography

The CL area (cm^2) in both groups showed an elevation beginning from day 5, and with each examination time point, there was an additional increase till day 15 after ovulation. Also, the CL area in non-pregnant buffalos showed a similar pattern but a non-significant decline was observed on days 20, 25, and 30, then the CL area was significantly ($p < 0.05$) elevated on days 35 and 40. The differences between the pregnant and non-pregnant groups reach a significant ($p < 0.05$) level from day 20 (1.87 ± 0.02 cm^2) until day 40 (2.75 ± 1.85 cm^2). The time and interaction between the time with the group showed a significant ($p < 0.05$) difference in the CL area (Figure 7).

Luteal artery Doppler parameter evaluations

The luteal artery was the second division of the ovarian branch of the main ovarian artery and lodged within the meso-ovarian ligament (Figure 3). The spectral mode of the luteal artery was measured to determine both luteal Doppler indices that were expressed by RI and PI. Luteal PI in both groups showed a decrease beginning from day 5, and with each examination time point, there was an additional decrease till day 15. Also, the PI in non-pregnant buffalos showed a similar pattern with a maximum elevation on day 30. The differences between the pregnant and non-pregnant groups reach a significant ($p < 0.05$) level on day 20 (1.33 ± 0.01) and continue to be significant till day 40 (0.89 ± 0.01; Figure 8A). The interaction between time with the group had shown a significant ($p < 0.05$) difference in luteal PI, while the time did not show any significant difference.

Luteal RI in both groups showed a decrease beginning from day 5, and with each examination time point, there was an

10.3389/fvets.2022.896581

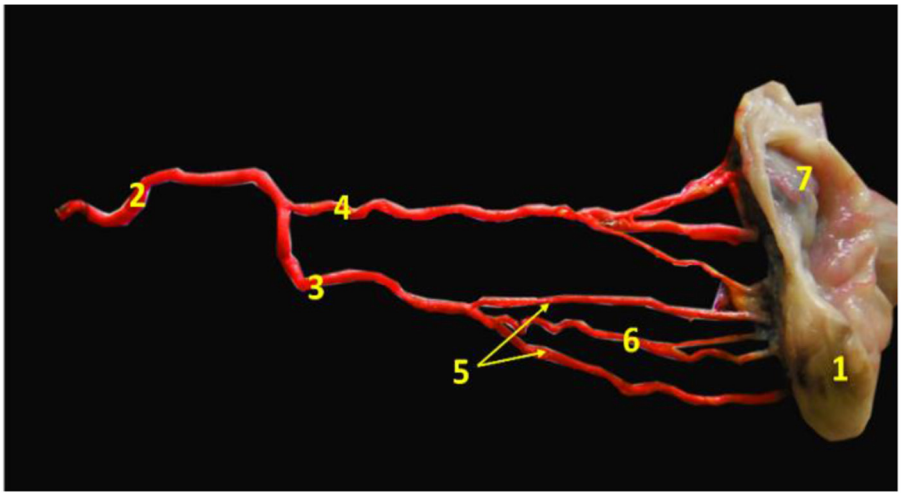

FIGURE 3
Image revealed the main ovarian artery of the ovary. 1- ovary, 2- main ovarian artery, 3- ovarian branch of the main ovarian artery, 4- tubal branch of the main ovarian artery, 5- ovarian twigs of the ovarian branch, 6- luteal branch of the ovarian branch, and 7- mesoslphenix.

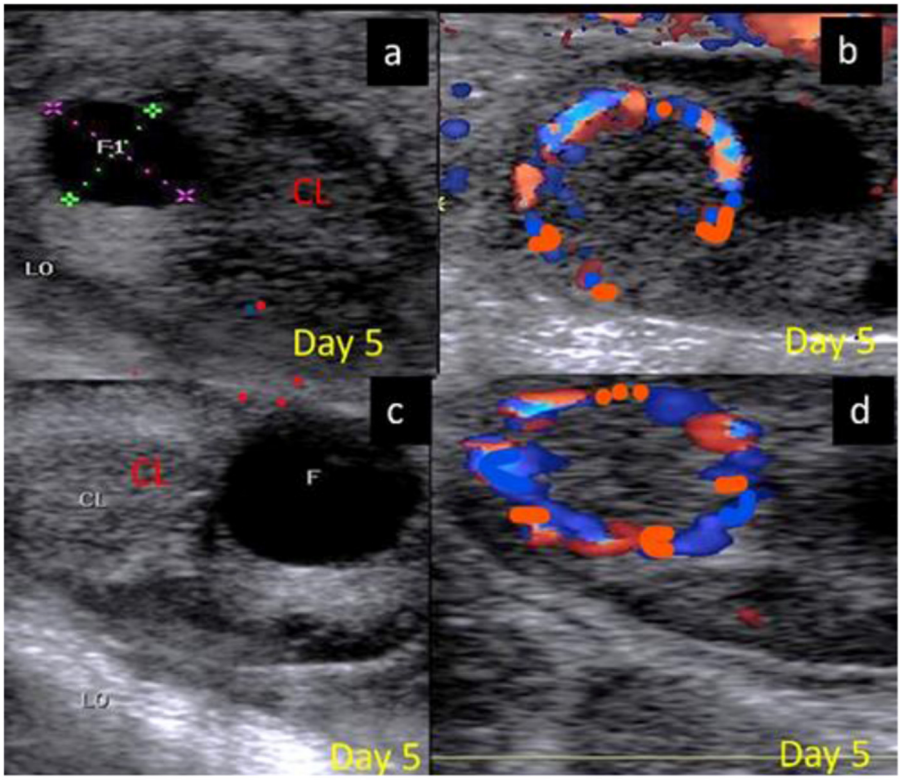

FIGURE 4
B-mode and colored ultrasonograms of a 9-year-old buffalos at the early luteal phase (stage I; from 1 to 5 days) as **(A,B)** images showed an early formed corpus luteum in non-pregnant female on day 5 in gray and color modes and **(C,D)** images showed an early formed corpus luteum in suspected pregnant one on day 5 in gray and color modes. CL, corpus luteum.

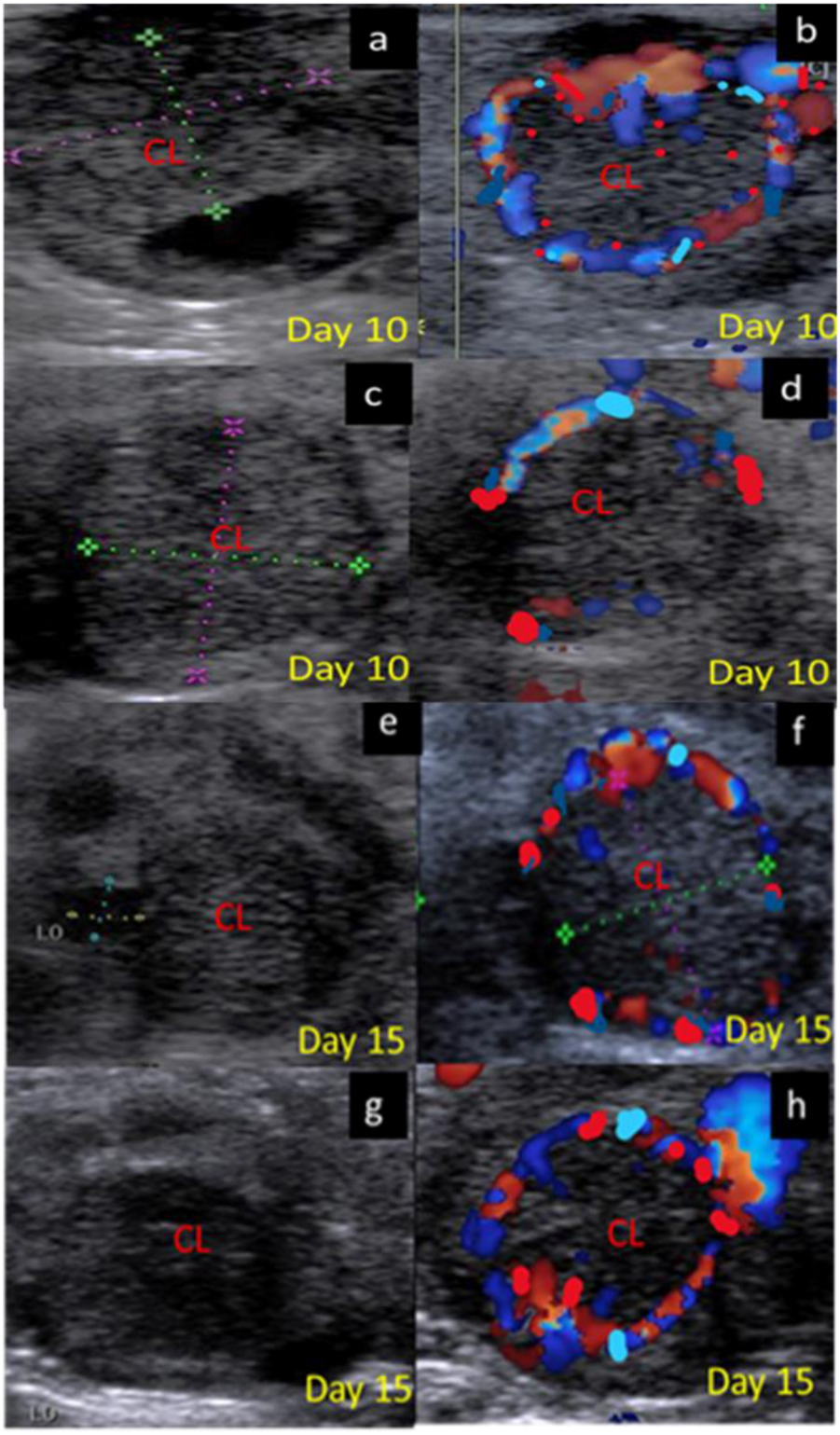

FIGURE 5
B-mode and colored ultrasonograms of a 9-year-old buffalos at the mid luteal phase with two stages stage II; from 6 to 10 days and stage; III from 11 to 16 days, as **(a,b)** images showed the corpus luteum in non-pregnant female on day 10 in gray and color modes, **(c,d)** images showed the formed corpus luteum in suspected pregnant one on day 10 in gray and color modes, **(e,f)** images showed the corpus luteum in non-pregnant female on day 15 in gray and color modes, and **(g,h)** images showed the formed corpus luteum in suspected pregnant one on day 15 in gray and color modes. CL, corpus luteum.

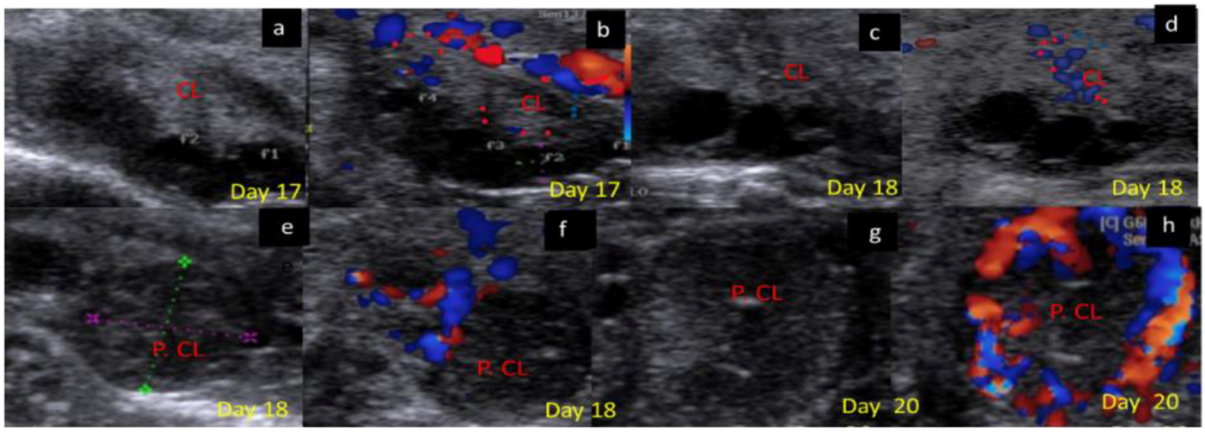

FIGURE 6
B-mode and colored ultrasonograms of 9-year-old buffalos at the late luteal in non-pregnant compared to pregnant one (Stage IV vs. Stage I suspected pregnant from 17 to 20 days). As **(a,b)** images showed the regressed corpus luteum on day 17 in gray and color modes and **(c,d)** images showed the more regressed corpus luteum on day 18 in gray and color modes compared to **(e,f)** images showed the corpus luteum in suspected pregnant females on day 18 in gray and color modes, and **(g,h)** images showed the corpus luteum in suspected pregnant females on day 20 in gray and color modes. CL, corpus luteum.

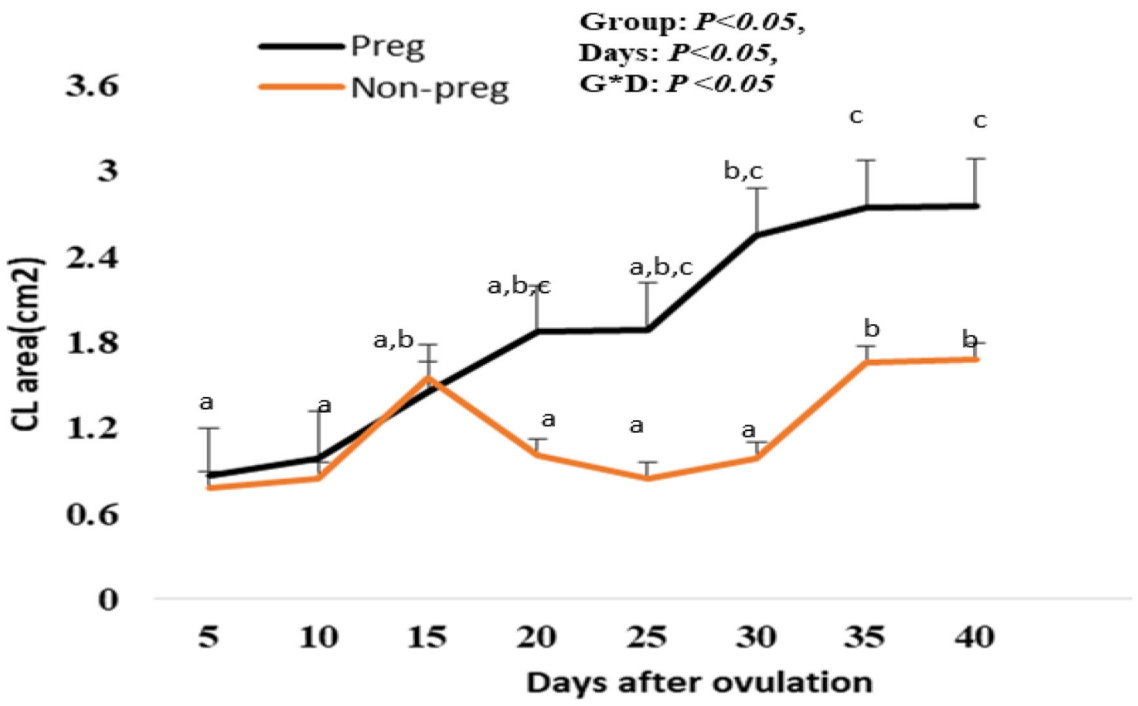

FIGURE 7
Area of the corpus luteum (CL area; cm^2) presented in pregnant (Preg) and non-pregnant (Non-preg) buffalos from day 5 till day 40 after ovulation. Data are obtained as mean with standard error of mean. [a,b] Values are significantly different at $P < 0.05$ compared with day 5 in both groups, while [c]value is significantly different at $P < 0.05$ between two groups at the indicated same time point.

additional decrease. Also, in non-pregnant buffalos, the luteal RI showed a similar pattern with a maximum elevation on day 30. The differences between the pregnant and non-pregnant groups reach a significant ($p < 0.05$) reduction from day 25 (0.69 ± 0.01) until day 40 (0.48 ± 0.01) in the pregnant group compared to that in the non-pregnant group (Figure 8B). The time and interaction between the time with the group show a significant ($p < 0.05$) difference in luteal RI.

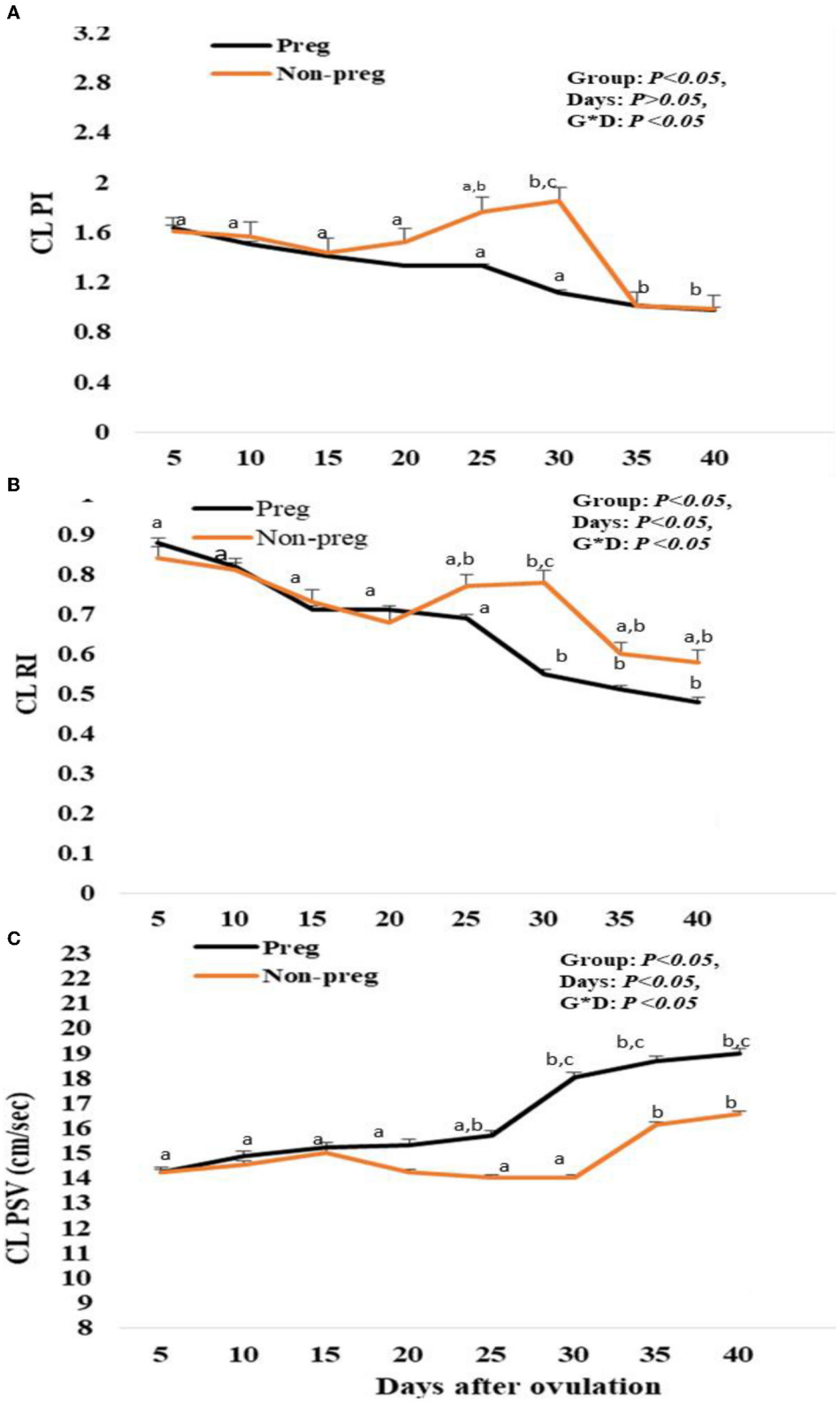

FIGURE 8
Pulsatility index (PI; **A**), resistance index (RI; **B**) and luteal peak systolic velocity (PSV; cm/sec; **C**) values presented in pregnant (Preg) and non-pregnant (Non-preg) buffalos from day 5 till day 40 after ovulation. Data are obtained as mean with standard error of mean. [a,b] Values are significantly different at $P < 0.05$ compared with day 5 in both groups, while [c]value is significantly different at $P < 0.05$ between two groups at the indicated same time point.

Finally, the spectral luteal PSV (cm/s) was elevated in both groups, but the elevation was significant ($p < 0.05$) from day 25 (15.88 ± 0.33) to day 40 (18.97 ± 0.74) in the pregnant group, while in the non-pregnant group, the PSV was elevated until day 15 (15.05 ± 0.85) after ovulation and then subsequently declined at days 20, 25, and 30, and then elevated at day 35 and day 40, as the time and interaction between time with the group showed a significant ($p < 0.05$) difference in luteal PSV (Figure 8C).

Progesterone and nitric oxide levels

Plasma progesterone levels in both groups showed an increase beginning from day 5, and with each examination time point, there was an additional increase. Plasma progesterone levels in pregnant females were elevated ($p < 0.05$) from day 20 (1.34 ± 0.01) until day 40 (2.21 ± 0.01), while those in non-pregnant females significantly decreased at days 25 and 30 (0.23 ± 0.01 and 0.21 ± 0.02) (Figure 9A). The time and interaction between time with the group showed a significant ($p < 0.05$) difference in progesterone level. Serum NOM levels in both groups increased from day 5 till day 15. In the pregnant group, NOM levels were elevated significantly ($p < 0.05$) from day 20 to day 40 compared to the non-pregnant group (Figure 9B), in addition, the time and interaction between time with both groups showed a significant ($p < 0.05$) difference in NOM. A positive correlation ($p < 0.01$) was observed for both pregnant and non-pregnant buffalos between plasma levels of P4 and CL PSV (cm/s), while there was a negative correlation ($p < 0.01$) between P4 levels and both Doppler indices (RI and PI).

Uterine blood flow in live animals

Both blue and red colored area/pixels were seen to be significant ($p < 0.05$) elevated from day 20 (764.12 ± 4.21 and 644.21 ± 2.51) till day 40 (948.12 ± 12.42 and 766.32 ± 3.55) in pregnant females compared to non-pregnant females as shown in Figure 10. There was no time and group interaction in the red and blue uterine blood flow.

Histological investigation

CL of non-pregnant buffalos demonstrated different stages of activity. In the early luteal stage (Stage I), the CL was covered by a fibrous connective tissue capsule, which formed septae that divided the CL into lobules. In this stage, both the capsule and septae appeared highly vascularized with many dilated and engorged blood vessels (Figure 11A). Some lutein cells were large, ovoid, or polyhedral in shape with large spherical vesicular eccentrically situated nuclei and prominent nucleoli [large lutein cells (LLCs)], while others were small and irregular in shape with eccentrically spherical lightly stained nuclei [small granulosa lutein cells (SLCs)]. LLCs possessed more cytoplasmic: nuclear ratio and lipid droplets than that of SLCs. The LLCs occupied a more central portion of CL in a close association with blood capillaries, while SLCs occupied the periphery portion and were distributed among the large ones (Figure 11B). The mid-luteal stage (stage II) was similar to stage I, except for the presence of numerous fibroblast cells and a high number of vacuolated cells with large vacuoles and an increasing number of lutein cells (Figures 11C,D). Moreover, most cells appeared in close association with engorged blood capillaries (Figure 11E). The mid-luteal (Stage III) was characterized by the presence of a high amount of collagen fibers in the capsule surrounding CL, septae, and interstitial tissue in addition to increasing the thickness of the blood vessels enclosed in both capsule and septae (Figures 11F,G). Furthermore, some luteal cells appeared to be generated with shrunken condensed nuclei, while others showed the apocrine mode of secretion. In this mode of secretion, the remaining part of the cells appeared with deep acidophilic cytoplasm and condensed nucleus. Moreover, LLCs appeared with abundant large vacuoles distributed among numerous fibroblast cells. These vacuoles were represented by narrow strands in some cells (Figures 11G,H). Conversely, the late luteal stage (Stage IV) was characterized by a substantial increase in the amount of fibrous CT mainly collagen, thickening of the CT capsule, CT septae, and blood vessels (Figure 11I) in addition to regressed capillaries and arterioles like remnants with an onion-skin arrangement of surrounding myofibroblast and heavily condensed and rounded endothelial cells (Figure 11J). Furthermore, most luteal cells appeared shrunken, degenerated, and highly vacuolated with small, condensed spherical or oval peripherally situated nuclei (Figure 11K). Additionally, the CL of pregnant buffalos revealed the same structure of CL at stage II with abundant LLCs surrounded by highly vascularized connective tissue capsules (Figure 11L).

Discussion

The current study compares the complete growth and development of CL in domestic buffalos from day 5 until day 40 after ovulation. CL plays a critical role in the gestation maintenance and establishment in many species because of its ability to produce an adequate P4 level (10, 45), therefore, any decline of this mechanism could affect embryonic mortality as previously demonstrated in cows (46). This study shows a significant elevation in CL area from day 20 until day 40 in pregnant buffalos compared to non-pregnant buffalos with a marked elevation of plasma P4 levels in the same group, which could help determine the importance of adequate CL diameter and area to establish the first early stage of pregnancy (47). Additionally, some studies reported a higher CL area in early pregnant females compared to non-pregnant ones (25), but others did not show a significant difference between the two

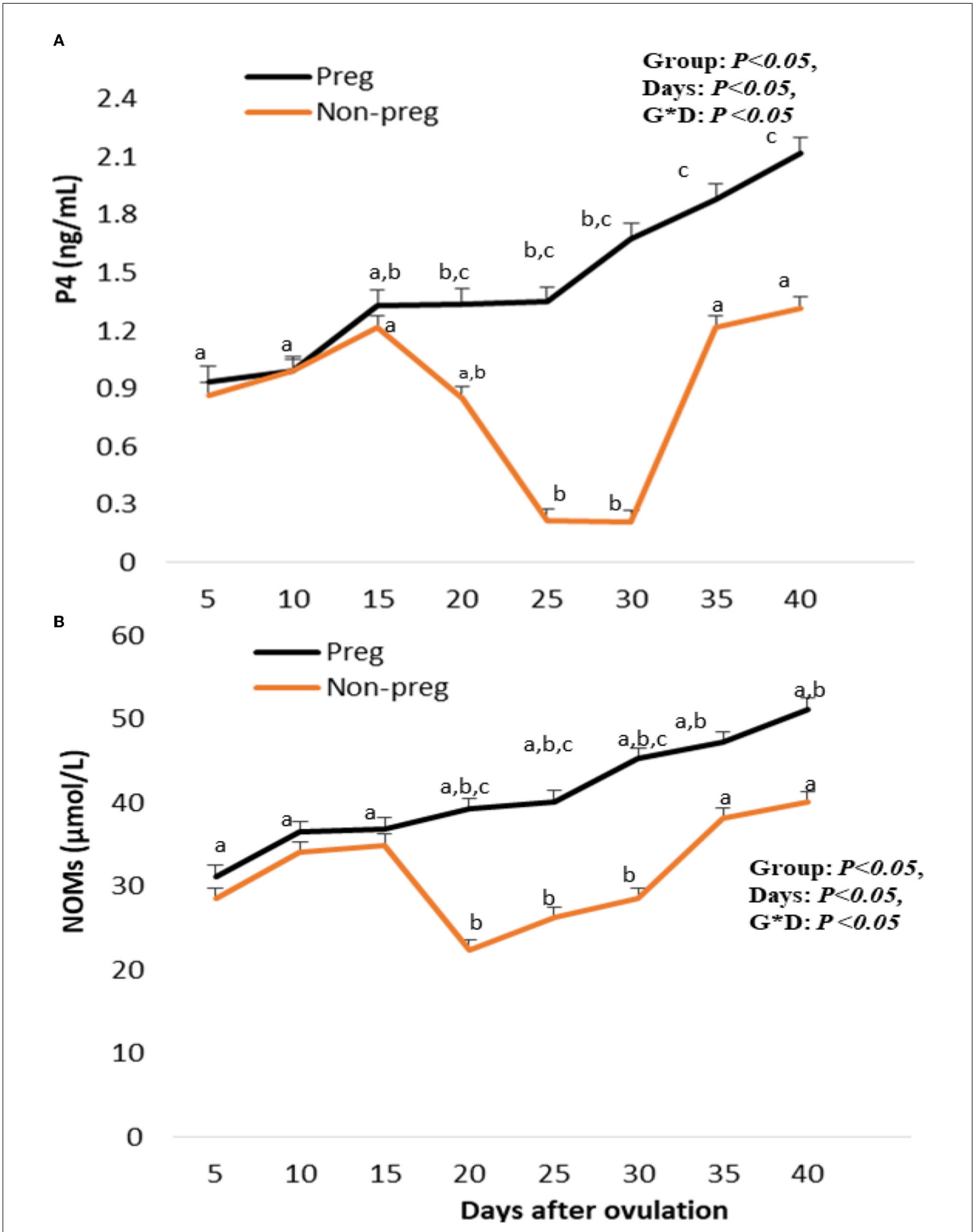

FIGURE 9
Plasma progesterone (P4; ng/mL; **A**), and serum nitric oxdie metabolites (NOMs; µmol/L; **B**) levels presented in pregnant (Preg) and non-pregnant (Non-preg) buffalos from day 5 till day 40 after ovulation. Data are obtained as mean with standard error of mean. [a,b] Values are significantly different at $P < 0.05$ compared with day 5 in both groups, while [c] value is significantly different at $P < 0.05$ between two groups at the indicated same time point.

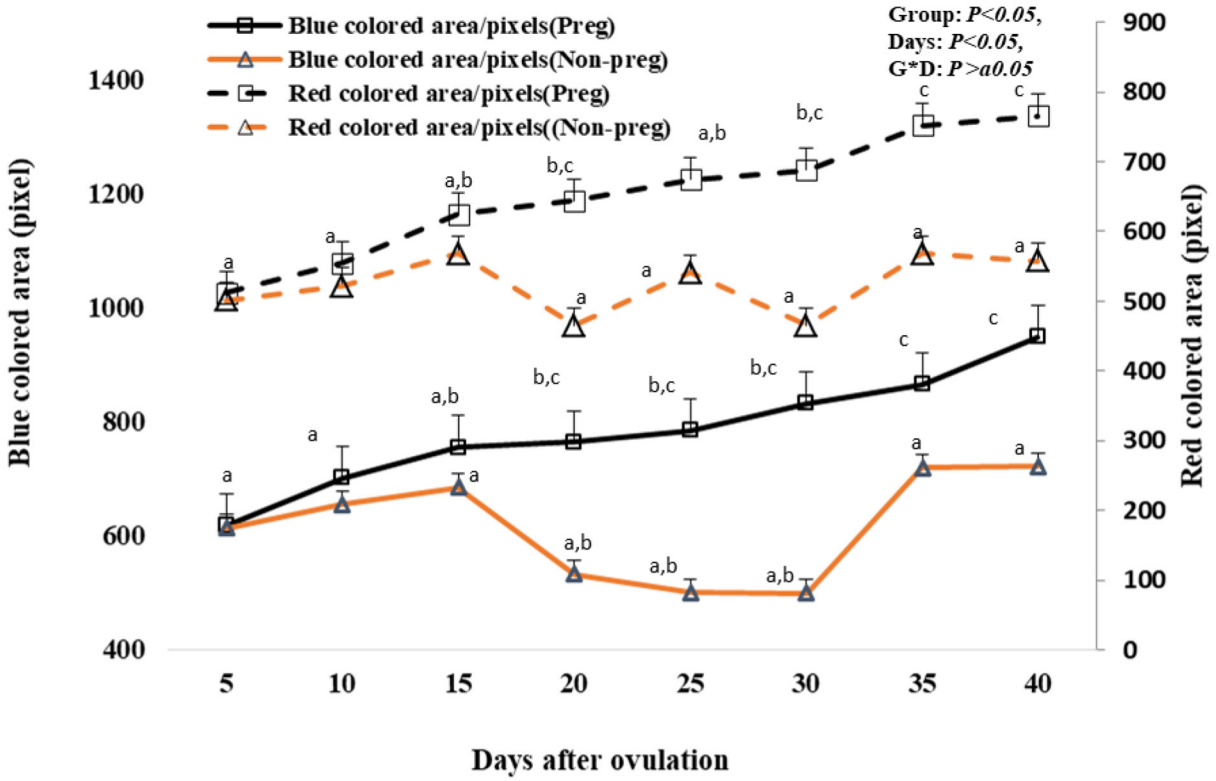

FIGURE 10
Uterine blood flow area expressed by blue and red colored area/pixels presented in pregnant (Preg) and non-pregnant (Non-preg) buffalos from day 5 till day 40 after ovulation. Data are obtained as mean with standard error of mean. [a,b] Values are significantly different at $P < 0.05$ compared with day 5 in both groups, while [c] value is significantly different at $P < 0.05$ between two groups at the indicated same time point.

groups (48). Similarly, some studies reported an elevation in plasma P4 levels from day 7 to day 10 after mating in pregnant females (25, 47) as high P4 levels were responsible mainly for greater embryonic development (23). In addition, the P4 levels remained elevated in some studies until 6–8 months of pregnancy (49).

Increases in CL diameter and progesterone level were greater in pregnant than in non-pregnant buffalos, indicating the importance of adequate CL size for maintenance of pregnancy (47). Lesser plasma progesterone levels from day 10 to 20 after AI in buffalos were associated with the death of an embryo (22), demonstrating the pivotal role of CL for pregnancy stage development and maintenance. The variation in the serum P4 concentrations throughout the estrous cycle of non-pregnant and pregnant buffalos is primarily dependent on the blood flow, CL area, amount of steroidogenic tissue (number and size of luteal cells), and its capacity to synthesize progesterone (10), in addition to its lipid contents (50). The development, maintenance, and regression of CL involved remarkable morphological and functional changes during the estrous cycle (51–53). The current study showed that CL had steroidogenic cells involving LLCs and SLCs with morphological characteristics that were reported by Baithalu et al. (14) in buffalo and Ozen et al. (54) and Xavier et al. (55) in a cow. The presence of large lightly stained nuclei of LLCs throughout stages I, II, and III may indicate the activity and hypersecretory LLCs during these phases of the cycle and pregnancy, while luteal cells of Stage IV revealed small more dense nuclei, which is an indication of luteolysis. Furthermore, the presence of vacuolated cytoplasm of LLCs was caused by their lipid contents that vary throughout the estrous cycle and appear in a close association with the synthesis and secretion of progesterone. Kapoor et al. (50) demonstrated that the variations in lipid distribution within the cyclic and regressed CL were inversely associated with the activity of the 3β-hydroxysteroid dehydrogenase enzyme involved in the synthesis of steroid hormones. Our results exhibited lutein cells of stage IV with highly vacuolated cytoplasm. Increasing accumulation of lipids in the regressed luteal cells with a significant decline in production of P4 hormone might be due to degenerated smooth endoplasmic reticulum resulting in absence of 3β-HSD in addition to degenerated mitochondria containing P450 side-chain cleavage (50, 56). Both 3β-HSD and P450 side-chain cleavage were involved in the biosynthesis of progesterone (50).

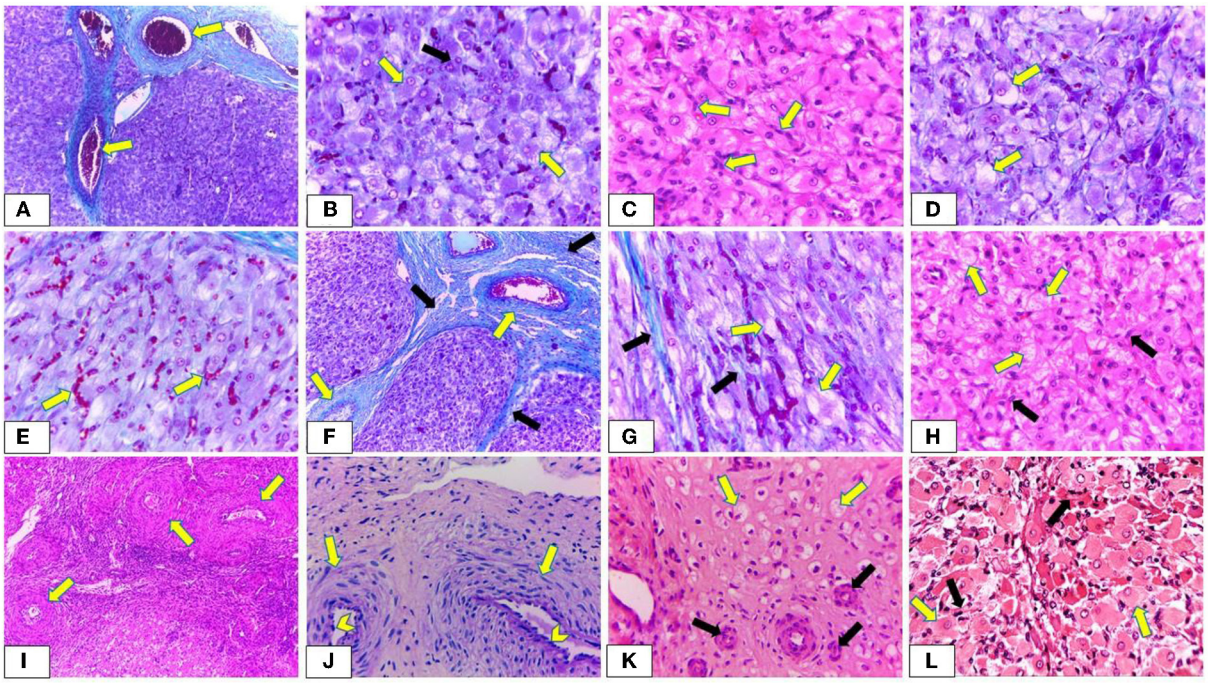

FIGURE 11
Photomicrograph showing the histological structure of corpus luteum (CL) during oestrus cycle and pregnancy. **(A,B)** Demonstrating early luteal stage (Stage I). **(A)** The CL is covered by a highly vascularized connective tissue capsule and septa. The blood vessels are dilated and engorged with blood (arrow) (Crossman's trichrome stain, x100). **(B)** Large lutein cells (LLCs) are ovoid, or polyhedral in shape with large spherical vesicular eccentrically situated nuclei and prominent nucleoli (yellow arrow) while small lutein cells are irregular in shape with eccentrical spherical lightly stained nuclei (SLCs) (black arrow). Furthermore, LLCs possessed more cytoplasmic: nuclear ratio and lipid droplets than that of SLCs (Crossman's trichrome stain, x400). **(C,E)** Showing mid luteal stage (stage II). **(C)** Presence of numerous fibroblast cells (arrow) with increasing the size of LLCs (H & E, x400). **(D)** Revealing a high number of vacuolated lutein cells with large vacuoles (arrow) (Crossman's trichrome stain, x400). **(E)** Most lutein cells appear in a close association with engorged blood capillaries (arrow) (Crossman's trichrome stain, x400). **(F,H)** Revealing mid luteal stage (stage III). **(F)** Presence of a high amount of collagen fibers in the capsule surrounding CL and C.T. septae (black arrow) in addition to increasing the thickness of the blood vessels enclosed in both capsule and septae (yellow arrow) (Crossman's trichrome stain, x100). **(G)** Presence of a high amount of collagen fibers in the interstitial tissue (black arrow). Furthermore, LLCs appear with abundant large vacuoles which are represented by narrow strands in some cells (yellow arrow) (Crossman's trichrome stain, x400). **(H)** LLCs (yellow arrow) appear with abundant large vacuoles distributed among numerous fibroblast cells (black arrow) (H & E, x400). **(I,K)** Exhibiting late luteal stage (stage IV). **(I)** A substantial increase in the thickening of blood vessels enclosed within the C.T. capsule (arrow) (H & E, x400). **(J)** Showing regressed capillaries and arterioles like remnants with an onion-skin arrangement of surrounding myofibroblast (arrow) and heavily condensed and rounded endothelial cells (chevron) (PAS, x400). **(K)** Most lutein cells appear shrunken, degenerated, highly vacuolated with small, condensed spherical or oval peripherally situated nuclei (yellow arrow). Moreover, presence of regressed blood vessels (black arrow) (H & E, x400). **(L)** Showing CL of pregnant buffalos has the same structure of CL at stages I and II with abundant LLCs (yellow arrow) in close association with blood capillaries (black arrow) (H & E, x400). The yellow arrows indicate the prominent nuclei with some LLCs.

Additionally, during the estrus cycle, the luteal cell population and the size of luteal cells increased and then regressed at stage IV. These results were consistent with references (14, 57, 58). Therefore, these findings reflect the variation in the serum P4 concentrations throughout the estrous cycle of non-pregnant and pregnant buffalos.

Hence, the present study was designed to study the cellular composition of the mature buffalo CL with its functional characterization in relation to progesterone secretory ability and nitric oxide during the normal luteal and pregnancy phases. In the normal luteal phase the level of NOMs was critical as it was related to the luteal vascularization and functionality (59), as after ovulation nitric oxide affects oocyte activation by regulating the calcium channel during the process of fertilization (60), while in the normal early pregnant stage, nitric oxide contributes to the elevation of maternal blood and reduction of blood pressure (61). Moreover, nitric oxide was extremely important in the embryo's multiple divisions (62) as some studies showed that embryonic growth was delayed due to the presence of inhibitory mediators in the blastocyst stage that adversely affects nitric oxide levels (63). Besides nitric oxide, some mediators have been concerned with this phenomenon, such as estradiol and prostacyclin (64).

The elevation in uterine blood flow that was expressed by red and blue colored areas in the pregnant group compared to non-pregnant buffalos could be associated with the buffalo maternal

pregnancy recognition that began once the early embryo moved in the fallopian tube and then entered the uterus after 5–6 days post-mating, as the uterine vascularization is included in the implantation procedures expressed by the growth and development of new blood vessels (65, 66). Furthermore, increased serum levels of NOMs in early pregnancy were very important in the vasodilator mechanisms as nitric oxide is shared in the blood pressure regulations and coronary artery vasomotion, therefore any abnormalities in nitric oxide and its metabolites levels could adversely affect pregnancy (67) in form of hypertension and angiogenesis problems (68).

Besides progesterone's important function, CL functionality could also be assessed by luteal vascularization (36). In this study, the CL vascularization was determined using both Doppler indices and PSV (cm/s), as both Doppler indices decreased in pregnant females compared to those in non-pregnant females, while the luteal artery PSV was elevated in the same pregnant group, this could be explained by the inverse relationship between both Doppler indices and Doppler velocities with time average point (TAV) as previously reported in other studies (69–72), in addition, an inverse relationship was observed between blood flow rate and Doppler indices especially PI (73–75). In accordance with our finding, a study reported an increase in both peak and time average velocities (PSV and TAV cm/s) on day 7 after time artificial insemination in pregnant cows (76), as the determination of luteal blood flow total area with Doppler velocities could increase the accuracy of pregnancy prediction (26). Consistent with our Doppler measurements, cyclic CL (stage I, II, and III) and CL of pregnancy were characterized by high vascularization, and most lutein cells were adjacent to engorged blood capillaries that were in harmony with Xavier et al. (55) in the pregnant cow. These results might be due to the high metabolic demand for CL. Moreover, the growth and maintenance of CL and its adequate endocrine function were mainly associated with increasing luteal vascularization and angiogenesis (77, 78). Many studies found a similar positive correlation between CL vascularization in its blood flow and plasma P4 levels after ovulation (79). However, during luteal regression, all lutein cells decreased in their number and shrunk until they disappeared, leaving arteriole-like remnants of blood vessels with an onion-skin arrangement of surrounding myofibroblast and heavily condensed and rounded endothelial cells with dense connective tissue in the residual CL. This finding was in accordance with observations reported by Augustin et al. (80). Increasing thickness of the CT capsule, CT septae, and blood vessels led to reduced blood flow, which in turn resulted in decreased progesterone secretion as observed in the current study.

Moreover, this study revealed the presence of non-steroidogenic cells, mainly fibroblast and endothelial cells. In stages III and IV, the number of fibroblasts notably increased, which was consistent with the results of Baithalu et al. (14) as the fibroblasts were responsible for the synthesis of connective tissue fibers and extracellular matrix (81), and collagen fibers were required to alternate the degenerated and regressed luteal cells. Baithalu et al. (14) reported that, during the late luteal stage, the greater number of macrophages and fibroblasts could serve as a cellular marker of luteal regression. Furthermore, our results revealed a high rate of deposition of collagen fibers in stages III and IV which comes in accordance with Jaglan et al. (53), who observed changes in the collagen concentration with the development and regression of cyclic buffalo CL during the estrous cycle. Iwahashi et al. (82) showed that alterations in the synthesis and distribution of collagen played a primary role in determining the CL structure and function.

Conclusion

The histological structure of CL and assessment of its hemodynamics depending on anatomical identifications could be used extensively to get useful data about CL functional status in both luteal and early pregnant phases. Finally, the evaluation of the luteal artery could be extremely helpful as the artery showed a wave pattern to determine the potential benefits of colored and pulsed Doppler in CL vascularization assessment.

Data availability statement

The original contributions presented in the study are included in the article/supplementary material, further inquiries can be directed to the corresponding author.

Ethics statement

The animal study was reviewed and approved by Faculty of Veterinary Medicine, Cairo University.

Author contributions

EA, IE, YA, AT, NY, and SD designed the protocol and collected the samples. NY worked on the histological examinations. EA and IE performed Doppler and ultrasonographical images, while YA, AT, and SD performed the anatomical vascular architecture. All authors drafted the manuscript, reviewed it, and approved the last version of the manuscript.

Conflict of interest

The authors declare that the research was conducted in the absence of any commercial or financial relationships that could be construed as a potential conflict of interest.

Publisher's note

References

1. Selokar NL, Saini M, Palta P, Chauhan MS, Manik RS, Singla SK. Cloning of buffalo, a highly valued livestock species of South and Southeast Asia: any achievements? *Cell Reprogram.* (2018) 20:89–98. doi: 10.1089/cell.2017.0051

2. Fahim NH, Abdel-Salam SAM, Mekkawy W, Ismael A, Abou-Bakr S, El Sayed M, et al. Upper Egypt buffalo farming systems: a survey comparison Egyptian. *Anim Prod.* (2018) 55:95–106. doi: 10.21608/ejap.2018.93242

3. Perera BMAO. Reproductive cycles of buffalo. *Anim Reprod Sci.* (2011) 124:4–9. doi: 10.1016/j.anireprosci.2010.08.022

4. Warriach HM, McGill DM, Bush RD, Wynn PC, Chohan KR. A review of recent developments in buffalo reproduction - a review. *Asian Australas J Anim Sci.* (2015) 28:451–5. doi: 10.5713/ajas.14.0259

5. Abouelela YS, Yasin NAE, El Karmoty AF, Khattab MA, El-Shahat KH, Abdelnaby EA. Ovarian, uterine and luteal hemodynamic variations between pregnant and non-pregnant pluriparous Egyptian buffalos with special reference to their anatomical and histological features. *Theriogenology.* (2021) 173:173–82. doi: 10.1016/j.theriogenology.2021.06.022

6. Kumar P, Dayal S, Tiwari R, Sengupta D, Barari SK, Dey A. Vaginal prolapse in peri-partum primiparous murrah buffalo complicated into endometritis and cystitis: a case report. *Buffalo Bull.* (2015) 34:153–9.

7. Suthar VS, Dhami AJ. Estrus detection methods in buffalo. *Rev Vet World.* (2010) 3:94–6.

8. Dash S, Chakravarty AK, Singh A, Upadhyay A, Singh M, Yousuf S. Effect of heat stress on reproductive performances of dairy cattle and buffalos: a review. *Vet World.* (2016) 9:235–44. doi: 10.14202/vetworld.2016.235-244

9. Lohan IS, Malik RK, Kaker ML. Uterine involution and ovarian follicular growth during early postpartum period of murrah buffalos (Bubalus bubalis). *Asian Aust J Anim Sci.* (2004) 17:313–6. doi: 10.5713/ajas.2004.313

10. Niswender GD, Juengel JL, Silva PJ, Rollyson MK, McIntush EW. Mechanisms controlling the function and life span of the corpus luteum. *Physiol Rev.* (2000) 80:1–29. doi: 10.1152/physrev.2000.80.1.1

11. Skarzynski DJ, Piotrowska-Tomala KK, Lukasik K, Galvão A, Farberov S, Zalman Y, et al. Growth and regression in bovine corpora lutea: regulation by local survival and death pathways. *Reprod Domest Anim.* (2013) 48:25–37. doi: 10.1111/rda.12203

12. Yoshioka S, Abe H, Sakumoto R, Okuda K. Proliferation of luteal steroidogenic cells in cattle. *PLoS ONE.* (2013) 8:e84186. doi: 10.1371/journal.pone.0084186

13. Care AS, Diener KR, Jasper MJ, Brown HM, Ingman WV, Robertson SA. Macrophages regulate corpus luteum development during embryo implantation in mice. *J Clin Invest.* (2013) 123:3472–87. doi: 10.1172/JCI60561

14. Baithalu RK, Singh SK, Gupta C, Raja AK, Saxena A, Kumar Y, et al. Cellular and functional characterization of buffalo (Bubalus bubalis) corpus luteum during the estrous cycle and pregnancy. *Anim Reprod Sci.* (2013) 140:138–46. doi: 10.1016/j.anireprosci.2013.06.008

15. Skarzynski DJ, Ferreira-Dias G, Okuda K. Regulation of luteal function and corpus luteum regression in cows: hormonal control, immune mechanisms and intercellular communication. *Reprod Domest Anim.* (2008) 43:57–65. doi: 10.1111/j.1439-0531.2008.01143.x

16. Abdelnaby A, Abo El-Maaty AM. Luteal blood flow and growth in correlation to circulating angiogenic hormones after spontaneous ovulation I mares. *Bulg J Vet Med.* (2017) 20:97–109. doi: 10.15547/bjvm.998

17. Chandrahasan C, Rajasekaran J. Biometry of buffalo ovaries in relation to different stages of estrus cycle. *Ind J Anim Reprod.* (2004) 25:87–90.

18. Ojeda AR, Ricardo Londoño O, Carlos Gutierrez R. Gonella-Diaza A. Follicular dynamics, corpus luteum growth and regression in multiparous buffalo cows and buffalo heifers. *Rev MVZ Cordoba.* (2014) 19:4130–40. doi: 10.21897/rmvz.106

19. Sartori R, Rosa GJ, Wiltbank MC. Ovarian structures and circulating steroids in heifers and lactating and dry cows in winter. *J Dairy Sci.* (2002) 85:2813–22. doi: 10.3168/jds.S0022-0302(02)74368-3

20. Mondal S, Kumar V, Reddy IJ, Singh K. Progesterone and nucleic acid contents of buffalo corpus luteum in relation to stages of estrous cycle. *Ind J Anim Sci.* (2004) 74:710–2.

21. Robinson RS, Hammond AJ, Wathes DC, Hunter MG, Mann GE. Corpus luteum-endometrium-embryo interactions in the dairy cow: underlying mechanisms and clinical relevance. *Reprod Domest Anim.* (2008) 43:104–12. doi: 10.1111/j.1439-0531.2008.01149.x

22. Campanile G, Neglia G, D'Occhio MJ. Embryonic and fetal mortality in river bu_alo (Bubalus bubalis). *Theriogenology.* (2016) 86:207–13. doi: 10.1016/j.theriogenology.2016.04.033

23. Balestrieri ML, Gasparrini B, Neglia G, Vecchio D, Strazzullo M, Giovane A, et al. Proteomic profiles of the embryonic chorioamnion and uterine caruncles in buffalos (Bubalus bubalis) with normal and retarded embryonic development. *Biol Reprod.* (2013) 88:119. doi: 10.1095/biolreprod.113.108696

24. Abdelnaby EA, Abo El-Maaty AM, Ragab RSA, Seida AA. Dynamics of uterine and ovarian arteries flow velocity waveforms and their relation to follicular and luteal growth and blood flow vascularization during the estrous cycle in Friesian cows. *Theriogenology.* (2018) 121:112–21. doi: 10.1016/j.theriogenology.2018.08.003

25. Neglia G, Restucci B, Russo M, Vecchio D, Gasparrini B, Prandi A, et al. Early development and function of the corpus luteum and relationship to pregnancy in the buffalo. *Theriogenology.* (2015) 83:959–67. doi: 10.1016/j.theriogenology.2014.11.035

26. Esposito L, Salzano A, Russo M, de Nicola D, Prandi A, Gasparrini B, et al. Corpus luteum color Doppler ultrasound and pregnancy outcome in buffalo during the transitional period. *Animals.* (2020) 10:1181. doi: 10.3390/ani10071181

27. Abdelnaby EA, Abo El-Maaty AM. Effect of the side of ovulation on the uterine morphometry, blood flow, progesterone, oestradiol and nitric oxide during spontaneous and induced oestrus in lactating dairy cows. *Reprod Domest Anim.* (2020) 55:851–60. doi: 10.1111/rda.13693

28. Abdelnaby EA, Abo El-Maaty AM, Ragab RSA, Seida AA. Assessment of uterine vascular perfusion during the estrous cycle of mares in connection to circulating leptin, and nitric oxide concentrations. *J Equine Vet Sci.* (2016) 39:25–32. doi: 10.1016/j.jevs.2015.08.021

29. HodŽić J, Izetbegović S, Muračević B, Iriškić R, Štimjanin Jović HS. Nitric oxide biosynthesis during normal pregnancy and pregnancy complicated by preeclampsia. *Med Glas.* (2017) 14:211–7. doi: 10.17392/915-17

30. Abdelnaby EA, Abo El-Maaty AM, Ragab RSA, Seida AA. Ovsynch produced larger follicles and corpora lutea of lower blood flow associated lower ovarian and uterine blood flows, estradiol and nitric oxide in Cows. *J Adv Vet Res.* (2020) 10:165–76. Available online at: https://advetresearch.com/index.php/AVR/article/view/477/426

31. Neglia G, Gasparrini B, Salzano A, Vecchio D, De Carlo E, Cimmino R, et al. Relationship between the ovarian follicular response at the start of an Ovsynch-TAI program and pregnancy outcome in the Mediterranean river buffalo. *Theriogenology.* (2016) 86:2328–33. doi: 10.1016/j.theriogenology.2016.07.027

32. Siregar TN, Hafizuddin H, Akmal M, Sayuti A, Aliza D. Follicle dynamics of aceh cattle during estrous cycle. *Global Vet.* (2016) 17:424–9. doi: 10.5829/idosi.gv.2016.424.429

33. Lasheen ME, Badr HM, Kandiel MM, Abo El-Maaty AM, Samir H, Farouk M, et al. Predicting early pregnancy in Egyptian buffalo cows via measuring uterine and luteal blood flows, and serum and saliva progesterone. *Trop Anim Health Prod.* (2018) 50:137–42. doi: 10.1007/s11250-017-1413-6

34. Kanazawa T, Seki M, Ishiyama K, Kubo T, Kaneda Y, Sakaguchi M, et al. Pregnancy prediction on the day of embryo transfer (Day 7) and Day 14 by measuring luteal blood flow in dairy cows. *Theriogenology.* (2016) 86:1436–44. doi: 10.1016/j.theriogenology.2016.05.001

35. Abdelnaby EA, Abo El-Maaty AM. Dynamics of follicular blood flow, antrum growth, and angiogenic mediators in mares from deviation to ovulation. *J Equine Vet Sci.* (2017) 55:51–9. doi: 10.1016/j.jevs.2017.04.003

36. Abo El-Maaty AM, Abdelnaby EA. Follicular blood flow, antrum growth and angiogenic mediators in mares from ovulation to deviation. *Anim Reprod.* (2017) 14:1043–56. doi: 10.21451/1984-3143-AR848

37. Farghali HA, Abdelkader NA, Fathi M, Emam IA, Abubakr HO, Alijuaydi SH, et al. The efficiency of intrauterine infusion of platelet-rich plasma in the treatment of acute endometritis as assessed by endoscopic, Doppler, oxidative, immunohistochemical, and gene expression alterations in jennies. *Theriogenology.* (2022) 181:147e160. doi: 10.1016/j.theriogenology.2022.01.023

38. Abdelnaby EA, El-Maaty AMA, El-Badry DA. Evaluation of ovarian hemodynamics by color and spectral Doppler in cows stimulated with three sources of follicle-stimulating hormone. *Reprod Biol.* (2021) 21:100478. doi: 10.1016/j.repbio.2020.100478

39. Siqueira LG, Arashiro EK, Ghetti AM, Souza ED, Feres LF, Pfeifer LF, et al. Vascular and morphological features of the corpus luteum 12 to 20 days after timed artificial insemination in dairy cattle. *J Dairy Sci.* (2019) 102:5612–22. doi: 10.3168/jds.2018-15853

40. Abdelkhalek KG, Badawy ABA, Fathi M, Abdelnaby EA. Reproductive hormonal levels and nitric oxide levels as guides of pubertal reproductive development in relation to testicular width and hemodynamics in Baladi bucks. *Adv Anim Vet Sci.* (2022) 10:236–43. doi: 10.17582/journal.aavs/2022/10.2.236.243

41. EL-Sherbiny H, EL-Shahat KH, Abo El-Maaty AM, Abdelnaby EA. Ovarian and uterine haemodynamics and their relation to steroid hormonal levels inpostpartum egyptian buffaloe. *Bulg J Vet Med.* (2022) 25:262–273. doi: 10.15547/bjvm.2020-0091

42. Abdelnaby EA, Abouelela YS, Yasin NAE. Evaluation of penile blood flow in dogs with tvt before and after chemotherapeutic treatment with special reference to its angioarchitecture. *Adv Anim Vet Sci.* (2021) 9:1159–68. doi: 10.17582/journal.aavs/2021/9.8.1159.1168

43. El-Bably SH, Abouelela YS. Anatomical and radiographical studies on heart of red fox (vulpes vulpes) with special references to its coronary arteries. *Adv Anim Vet Sci.* (2021) 9:754–60. doi: 10.17582/journal.aavs/2021/9.5.754.760

44. Bancroft JD, Gamble M. *Theory and Practice of Histological Techniques. 6th ed.* Churchill Livingstone: Elsevier Health Sciences Philadelphia (2008).

45. Wiltbank MC, Salih SM, Atli MO, Luo W, Bormann CL, Ottobre JS, et al. Comparison of endocrine and cellular mechanisms regulating the corpus luteum of primates and ruminants. *Anim Reprod.* (2012) 9:242–59.

46. Nyman S, Gustafsson H, Berglund B. Extent and pattern of pregnancy losses and progesterone levels during gestation in Swedish red and Swedish Holstein dairy cows. *Acta vet scand.* (2018) 60:68. doi: 10.1186/s13028-018-0420-6

47. Vecchio D, Neglia G, Gasparrini B, Russo M, Pacelli C, Prandi A, et al. Corpus luteum development and function and relationship to pregnancy during the breeding season in the Mediterranean bu_alo. *Theriogenology.* (2012) 77:1811–5. doi: 10.1016/j.theriogenology.2011.12.025

48. Kanazawa T, Seki M, Ishiyama K, Araseki M, Izaike Y, Takahashi T. Administration of gonadotropin-releasing hormone agonist on day 5 increases luteal blood flow and improves pregnancy prediction accuracy on Day 14 in recipient Holstein cows. *J Reprod Dev.* (2017) 63:389–99. doi: 10.1262/jrd.2016-128

49. Abdelnaby EA. Hemodynamic changes in arterial flow velocities throughout the first six months of pregnancy in buffalo heifers by Doppler ultrasonography. *Asian Pac J Reprod.* (2020) 9:204. doi: 10.4103/2305-0500.288589

50. Kapoor K, Singh O, Pathak D. Lipid distribution variations in different stages of cyclic corpus luteum of indian buffalo. *J Anim Res.* (2018) 8:379–85. doi: 10.30954/2277-940X.06.2018.7

51. Hazzard TM, Stouffer RL. Angiogenesis in ovarian follicular and luteal development. In: Arulkumaran S, editor. *Clinical Obstetrics & Gynaecology. Angiogenesis in the Female Reproductive Tract*. London: Bailliere Tindall (2000). p. 883–900. doi: 10.1053/beog.2000.0133

52. Neves MM, Marques AP, Santana CV, Lima FPC, Zambrano WJ. Características de ovários de fêmeas zebu (Bos taurus indicus) colhidos em abatedouro. *Arq bras med vet zootec.* (2002) 54:651–4. doi: 10.1590/S0102-09352002000600016

53. Jaglan P, Das GK, Kumar BV, Kumar R, Khan FA, Meur SK. Cyclical changes in collagen concentration in relation to growth and development of buffalo corpus luteum. *Vet Res Commun.* (2010) 34:511–8. doi: 10.1007/s11259-010-9422-1

54. Ozen A, Ergun L, Ergun E, Simsek N. Cytology of the corpus luteum during pregnancy and sexual cycle in cows. *Ind Vet J.* (2007) 84:1075–8.

55. Xavier PR, Leão RAC, Oliveira e Silva PVD, Marques Júnior AP. Histological characteristics of the corpus luteum of Nelore cows in the first, second and third trimester of pregnancy. *Arq bras med vet zootec.* (2012) 64:505–9. doi: 10.1590/S0102-09352012000200036

56. Christenson LK, Devoto L. Cholesterol transport and steroidogenesis by the corpus luteum. *Reprod Biol Endocrinol.* (2003) 90:1–9. doi: 10.1186/1477-7827-1-90

57. Elvaraju S, Raghavendra BS, Siva Subramani T, Priyadharsini R, Reddy IJ, Ravindra JP. Changes in luteal cells distribution, apoptotic rate, lipid peroxidation levels and antioxidant enzyme activities in buffalo (Bubalus bubalis) corpus luteum. *Anim Reprod Sci.* (2010) 120:39–46. doi: 10.1016/j.anireprosci.2010.02.017

58. Mishra GK, Patra MK, Sheikh PA, Teeli AS, Kharayat NS, Karikalan M, et al. Functional characterization of corpus luteum and its association with peripheral progesterone profile at different stages of estrous cycle in the buffalo. *J Anim Res.* (2018) 8:507–12. doi: 10.30954/2277-940X.06.2018.28

59. Shirasuna K. Nitric oxide and luteal blood flow in the luteolytic cascade in the cow. *J Reprod Dev.* (2010) 56:9–14. doi: 10.1262/jrd.09-206E

60. Luo Y, Zhu Y, Basang W, Wang X, Li C, Zhou X. Roles of nitric oxide in the regulation of reproduction: a review. *Front Endocrinol.* (2021) 12:752410. doi: 10.3389/fendo.2021.752410

61. Soma-Pillay P, Nelson-Piercy C, Tolppanen H, Mebazaa A. Physiological changes in pregnancy. *Cardiovasc J Afr.* (2016) 27:89–94. doi: 10.5830/CVJA-2016-021

62. Nishikimi A, Matsukawa T, Hoshino K, Ikeda S, Kira Y, Sato EF, et al. Localization of nitric oxide synthase activity in unfertilized oocytes and fertilized embryos during preimplantation development in mice. *Reproduction.* (2001) 122:957–63. doi: 10.1530/rep.0.1220957

63. Gouge RC, Marshburn P, Gordon BE, Nunley W, Huet-Hudson YM. Nitric oxide as a regulator of embryonic development. *Biol Reprod.* (1998) 58:875–9. doi: 10.1095/biolreprod58.4.875

64. Darkwa EO, Djagbletey R, Sottie D, Owoo C, Vanderpuye NM, Essuman R, et al. Serum nitric oxide levels in healthy pregnant women: a case- control study in a tertiary facility in Ghana. *Matern Health Neonatol Perinatol.* (2018) 4:1–5. doi: 10.1186/s40748-017-0072-y

65. Silva LA, Gastal EL, Beg MA, Ginther OJ. Changes in vascular perfusion of the endometrium in association with changes in location of the embryonic vesicle in mares. *Biol Reprod.* (2005) 72:755–61. doi: 10.1095/biolreprod.104.036384

66. Varughese EE, Brar S, Dhindsa SS. Uterine blood flow during various stages of pregnancy in dairy buffalos using transrectal Doppler ultrasonography. *Anim Reprod Sci.* (2913) 140:34–9 doi: 10.1016/j.anireprosci.2013.05.011

67. Zhao Y, Vanhoutte PM, Leung SWS. Vascular nitric oxide: beyond eNOS. *J Pharmacol Sci.* (2015) 129:83–94. doi: 10.1016/j.jphs.2015.09.002

68. Busing CB, Longo-Mbenza B, Kengne AP. Iodine deficiency in pregnancy along a concentration gradient is associated with increased severity of preeclampsia in rural Eastern Cape, South Africa. *BMC Pregnancy Childbirth.* (2022) 22:98. doi: 10.1186/s12884-021-04356-6

69. El-Sherbiny HR, Fathi M, Samir H, Abdelnaby EA. Supplemental dietary curcumin improves testicular hemodynamics, testosterone levels, and semen quality in Baladi bucks in the non-breeding season. *Theriogenology.* (2022) 188:100–7. doi: 10.1016/j.theriogenology.2022.05.020

70. Hashem NM, EL-Sherbiny HR, Fathi M, Abdelnaby EA. Nanodelivery system for ovsynch protocol improves ovarian response, ovarian blood flow Doppler velocities, and hormonal profile of goats. *Animals.* (2022) 12:1442. doi: 10.3390/ani12111442

71. Abdelnaby EA, Abo El-Maaty AM. Melatonin and CIDR improved the follicular and luteal haemodynamics, uterine and ovarian arteries vascular perfusion, ovarian hormones and nitric oxide in cyclic cows. *Reprod Domest Anim.* (2021) 56:498–510. doi: 10.1111/rda.13888

72. Abdelnaby EA, Emam IA, Salem NY, Ramadan ES, Khattab MS, Farghali HA, Abd El Kader NA. Uterine hemodynamic patterns, oxidative stress, and chromoendoscopy in mares with endometritis. *Theriogenology.* (2020) 158:112–20. doi: 10.1016/j.theriogenology.2020.09.012

73. Abdelnaby EA. Hemodynamic changes evaluated by Doppler ultrasonographic technology in the ovaries and uterus of dairy cattle after the puerperium. *Reprod Biol.* (2020) 20:202–9. doi: 10.1016/j.repbio.2020.03.001

74. Abdelnaby EA. Higher doses of melatonin affect ovarian and middle uterine arteries vascular blood flow and induce oestrus earlier in acyclic ewes. *Reprod Domest Anim.* (2020) 55:763–9. doi: 10.1111/rda.13678

75. Abdelnaby EA. Testicular haemodynamics, plasma testosterone and oestradiol concentrations, and serum nitric oxide levels in the Egyptian buffalo bull after a single administration of human chorionic gonadotropin. *Reprod Domest Anim.* (2022) 57:754-60. doi: 10.1111/rda.14117

76. Hafez SA. *Advanced Studies in Veterinary Anatomy: Angiogenesis in Caprine Reproductive Organs of Non-Pregnant and Pregnant Normal and Swainsonine-Treated Does* (Ph.D. thesis). USA: Virgina tech (2005).

77. Wiltbank MC. Cell types and hormonal mechanisms associated with mid-cycle corpus luteum function. *J Anim Sci.* (1994) 72:1873–83. doi: 10.2527/1994.7271873x

78. Geva E, Jaffe RB. Role of vascular endothelial growth factor in ovarian physiology and pathology. *Fertil Steril.* (2000) 74:429–38. doi: 10.1016/S0015-0282(00)00670-1

79. Matsui M, Miyamoto A. Evaluation of ovarian blood flow by colour Doppler ultrasound: practical use forreproductive management in the cow. *Vet J.* (2009) 181:232–40. doi: 10.1016/j.tvjl.2008.02.027

80. Augustin HG, Braun K, Telemenakis I, Modlich U, Kuhn W. Ovarian angiogenesis. Phenotypic characterization of endothelial cells in a physiological model of blood vessel growth and regression. *Am J Pathol.* (1995) 147:339–51.

81. Fields MJ, Fields PA. Morphological characteristics of the bovine corpus luteum during the estrus cycle and pregnancy. *Theriogenology.* (1996) 45:1295–325. doi: 10.1016/0093-691X(96)00099-4

82. Iwahashi M, Muragaki Y, Ooshima A, Umesaki N. Immunohistochemical analysis of collagen expression in human corpora lutea during the menstrual cycle and early pregnancy. *Fertil Steril.* (2006) 85:1093–6. doi: 10.1016/j.fertnstert.2005.10.022

frontiers | Frontiers in Veterinary Science

TYPE Case Report
PUBLISHED 29 July 2022
DOI 10.3389/fvets.2022.959526

OPEN ACCESS

EDITED BY
Haney Samir,
Cairo University, Egypt

REVIEWED BY
Alexandros Chardas,
Royal Veterinary College (RVC),
United Kingdom
Hossam R. El-Sherbiny,
Cairo University, Egypt

*CORRESPONDENCE
Michael Nappier
mtnapp1@vt.edu

SPECIALTY SECTION
This article was submitted to Veterinary Imaging, a section of the journal Frontiers in Veterinary Science

RECEIVED 01 June 2022
ACCEPTED 07 July 2022
PUBLISHED 29 July 2022

CITATION
Gomes T, Harmon C and Nappier M (2022) Ultrasonographic and endoscopic guidance in diagnosis of Helicobacter gastritis presenting as a mass lesion in a dog: A case report. *Front. Vet. Sci.* 9:959526. doi: 10.3389/fvets.2022.959526

Ultrasonographic and endoscopic guidance in diagnosis of Helicobacter gastritis presenting as a mass lesion in a dog: A case report

Thomas Gomes, Cecelia Harmon and Michael Nappier*

Department of Small Animal Clinical Sciences, Virginia-Maryland College of Veterinary Medicine, Blacksburg, VA, United States

This case documents a previously undescribed presentation of *Helicobacter* spp. gastritis. An 8-year-old female spayed golden retriever with chronic vomiting was found to have a cluster of multiple, round, well-defined, hypoechoic foci of varying sizes surrounded by gas within the lumen of the stomach on ultrasonographic examination. Further endoscopic examination revealed multiple raised mass-like lesions in the fundus on endoscopic examination. Histopathological findings were consistent with *Helicobacter* spp. infection. The dog was treated with both amoxicillin 400 mg and clarithromycin 180 mg BID for 21 days and omeprazole 20 mg SID for 34 days. After the treatment, the vomiting and fundic lesions were resolved on ultrasonographic examination. This case represents a novel gross morphologic presentation for *Helicobacter* spp. gastritis that responded to appropriate therapy and highlights how early intervention with advanced imaging can aid in diagnosis and treatment.

KEYWORDS

gastric mass, *Helicobacter*, antibiotics, fundus, lymphocytic-plasmacytic gastritis, ultrasound, endoscopy, dog

Background

Helicobacter spp. have long been known to be associated with canine gastritis, although the exact causes are not described. On pathological survey, *Helicobacter* spp., or non-*Helicobacter pylori Helicobacter* species (NHPHs), have been identified in the cardia, fundus, body, and pylorus of infected dogs (1). Infected canines have been described to be asymptomatic or exhibit clinical signs, such as vomiting and diarrhea (2). Unlike in humans, infection by NHPHs in canines rarely causes ulcerative lesions; more often, they are present in or on the gastric mucosa with no associated pathology, and, in some cases, are associated with lymphoplasmacytic gastritis (1, 3). Previous descriptions of NHPHs gastric infections in dogs have shown no gross lesions or tissue inflammation (2). Histologically, *Helicobacter* spp. infections are described to be associated with lymphoplasmacytic infiltrates, inflammatory infiltrates, and degeneration

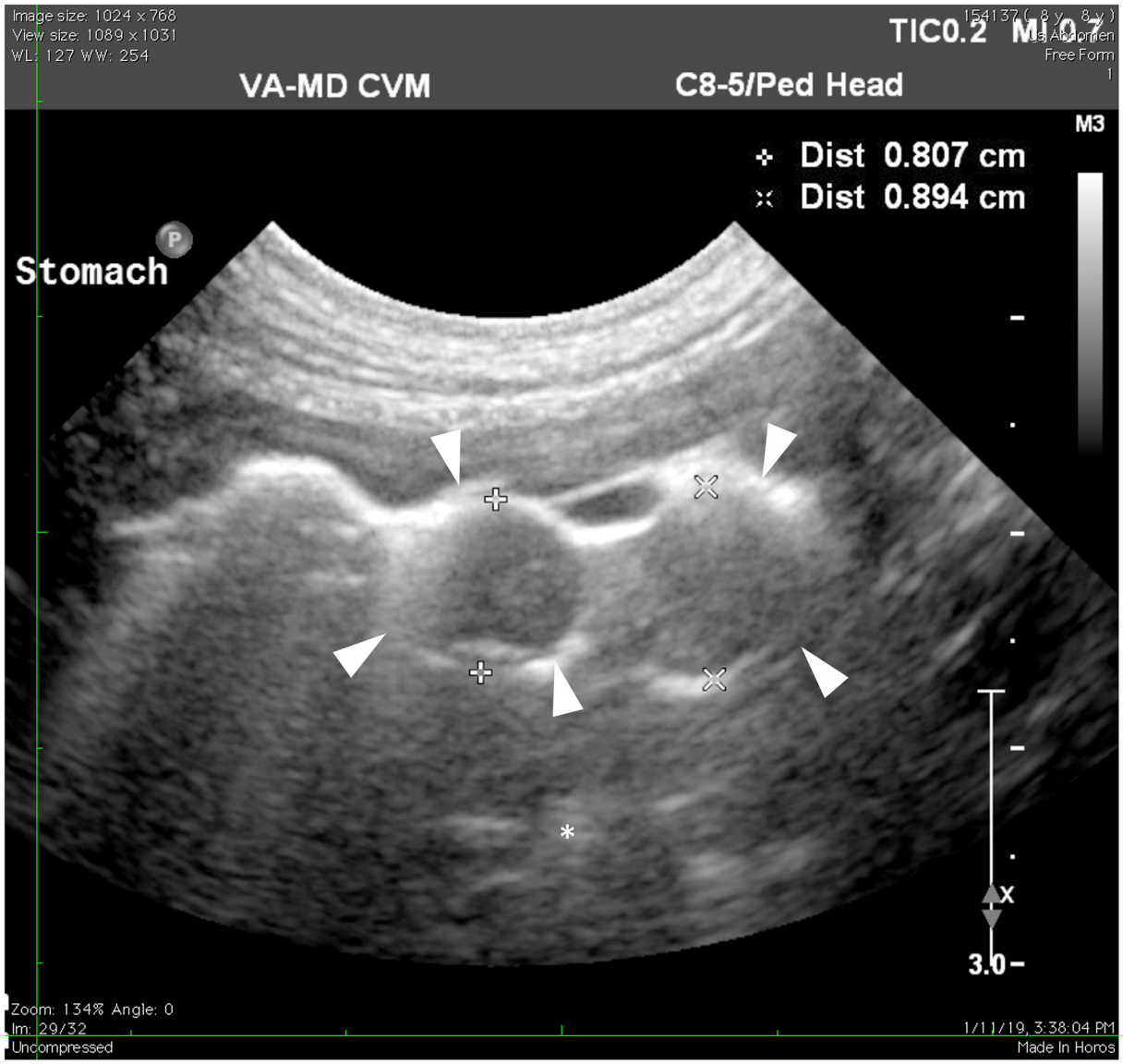

FIGURE 1
Ultrasonography of the stomach. The hypoechoic masses (arrowheads) protruding toward the lumen of the stomach are less echogenic than stomach contents (asterisk).

of the gastric crypts (1, 3). Diagnosis of NHPHs infections has primarily been made through mucosal biopsies of multiple regions of the stomach, which are submitted for tests, such as rapid urease test, histopathology, or PCR (3). Non-invasive techniques for diagnosis have proven to be limited in canines as the number of *Helicobacter* species canines host makes serology challenging, while urea breath and blood tests are most helpful following antimicrobial therapy as they demonstrate eradication of the *Helicobacter* spp. colonies (3). Empiric treatments for NHPHs-associated gastritis in dogs include amoxicillin, metronidazole, and an optional gastroprotectant with a good prognosis (3, 4). This report aims to describe a novel gross mass-like lesion presentation of *Helicobacter* spp. gastritis in a canine on ultrasonographical and endoscopic examination, yet, had typical clinical signs, histopathologic appearance, and response to therapy for NHPHs-associated gastritis.

Case report

An 8-year-old spayed female Golden Retriever was presented to the Virginia-Maryland College of Veterinary Medicine (VMCVM) community practice for intermittent

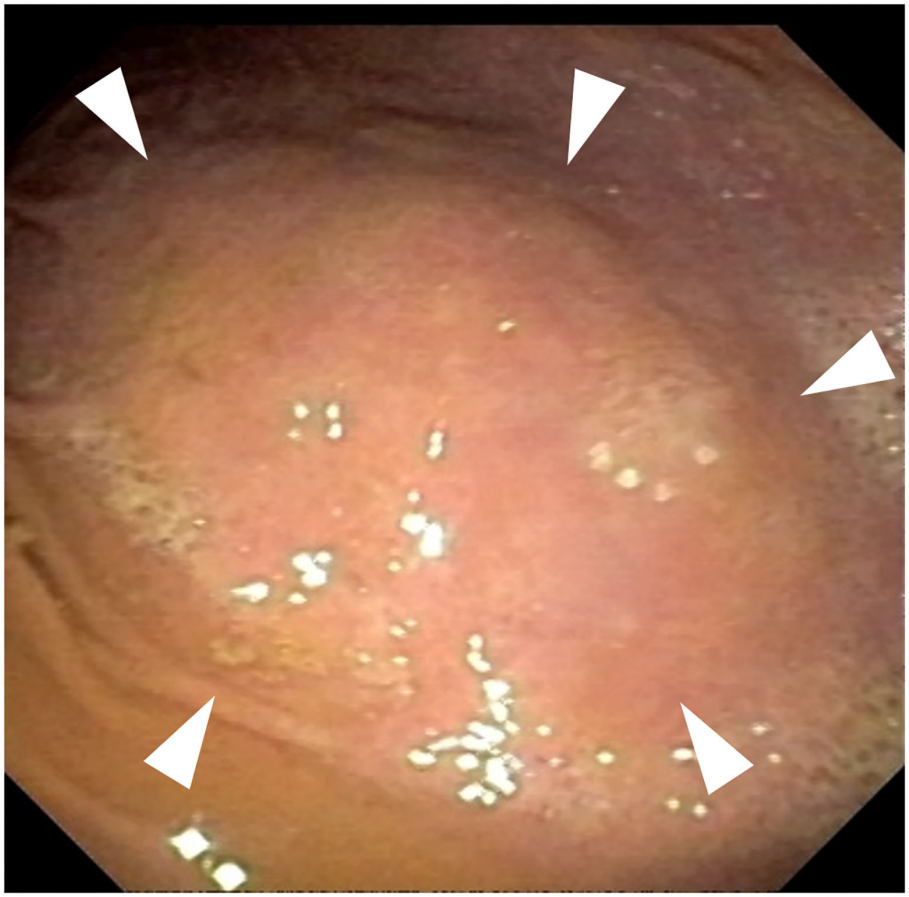

FIGURE 2
Endoscopy of the fundic region of the stomach. Gross thickened areas (arrowheads) appear to be from the stomach wall and do not involve the gastric lumen.

vomiting for 1-month duration. The owner reported that the dog had similar bouts of vomiting approximately 5 months earlier.

On presentation, the patient was in good condition and vital parameters were normal. No abnormalities were found on the physical exam with no pain or other abnormalities on abdominal palpation. Blood was sampled for hematology, biochemistry, thyroid hormone, and serum cortisol to help rule out multiple differentials for chronic vomiting in a dog, such as hypoadrenocorticism, hepatic disease, inflammatory bowel disease, neoplasia, and hyperthyroidism. Hematology revealed a mild microcytosis (58.2 fl) and hypochromia (20.1 pg). Serum biochemistry showed a mild increase in ALT (91 U/L). Serum cortisol (1.01 µg/dl) and thyroid hormone (21.8 nmol/L) were within the reference intervals. Radiographs revealed a focal soft tissue opacity that appeared to fill most of the gastric fundus not identified on lateral views. Other abdominal contents were found to be normal. Transabdominal ultrasonography revealed a cluster of multiple, round, well-defined, hypoechoic foci of varying sizes (~0.7–1.8 cm) surrounded by gas within the lumen toward the fundus of the stomach (Figure 1). These foci were not associated with the wall along the greater curvature. Other abdominal structures were found to be normal.

Endoscopy revealed several areas of thickening (1 cm) noted in the area of the fundus (Figure 2). These lesions grossly appeared to be involving the stomach wall and not intraluminal. Cup biopsy forceps were used to take multiple samples of the most prominent area of abnormality in two separate areas. Yellow-white fluid was noted from the biopsy sites in addition to blood. Espophageal endoscopy revealed normal structures. Histopathologic examination showed large lymphocytic aggregates in 3 out of the 4 samples. All four samples had a mild multifocal inflammation of lymphocytes, plasma cells, and eosinophils with few *Helicobacter*-like organisms (HLO) on the epithelial surface (Figure 3). Histologic diagnosis was lymphocytic-plasmacytic gastritis with *Helicobacter* spp. Further workup on isolating and specifying the *Helicobacter* species was not performed.

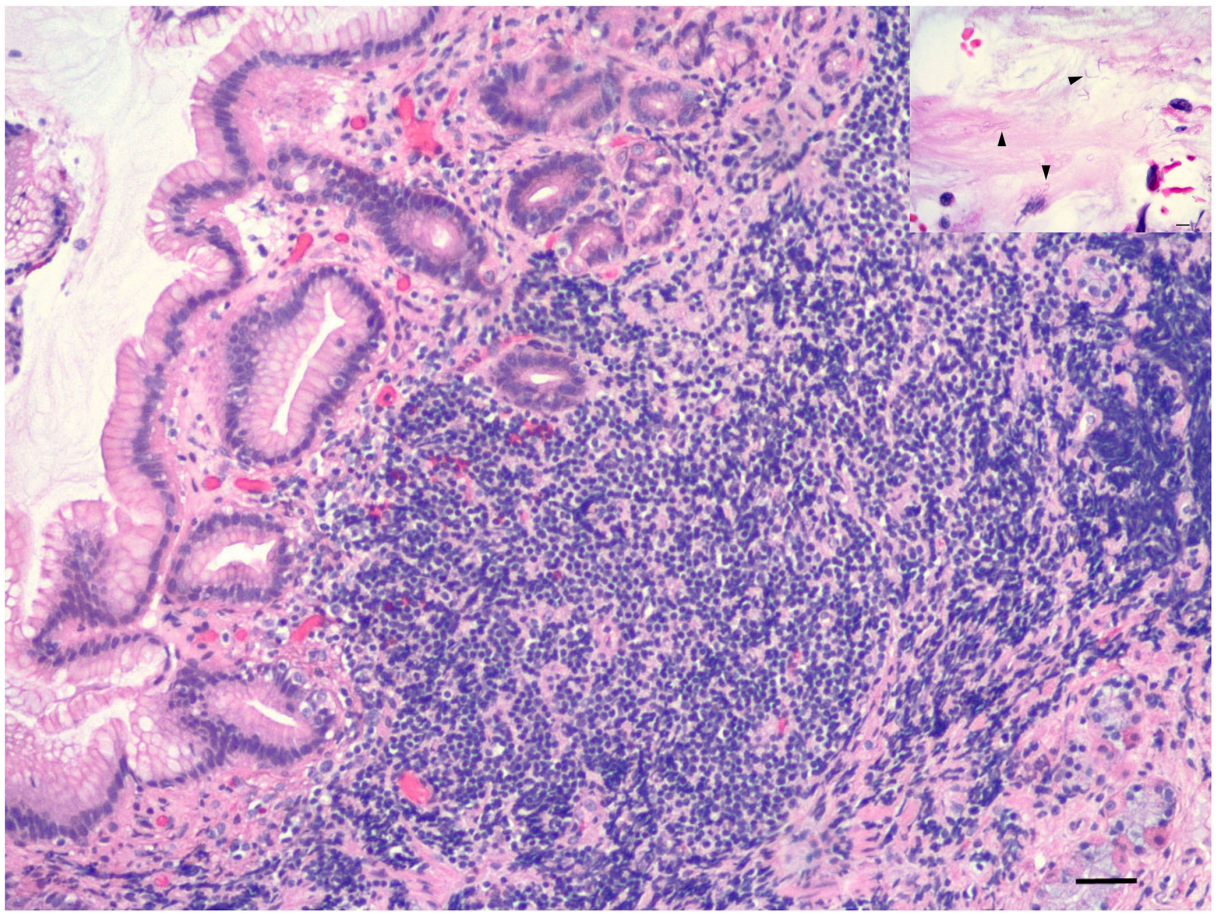

FIGURE 3
Histopathology of fundic cup biopsies. Stomach with lymphoplasmacytic gastritis, 10x magnification, scale bar: 100 μm. Inset shows spiral bacteria (*Helicobacter* spp.) (arrowheads) in surface mucus of stomach, 60x magnification, scale bar: 15 μm.

Based on the diagnostic findings, the patient was prescribed amoxicillin 400 mg BID for 21 days, clarithromycin 180 mg BID for 21 days, omeprazole 20 mg SID for 34 days, and Purina FortiFlora®, and Royal Canin® GI diet.

Nine days after the onset of medications, on follow-up telephone communications, the owner reported that the patient's vomiting had greatly decreased with only two instances of vomiting at home. Twenty-seven days after the onset of medications, the patient was re-evaluated at the community practice. The owner reported that the dog was doing very well at home with only one instance of vomiting. No abnormalities were found on the recheck physical examination. Transabdominal ultrasonography revealed that the previously described hypoechoic foci within the fundic lumen were no longer present, indicating that the gastric lesion was resolved (Figure 4).

The patient lived for another 2 years before dying of unrelated causes. At that time, the owner did not report any recurrence of the clinical signs.

Discussion

In this case, the dog had multifocally raised mass-like nodules associated with *Helicobacter* spp. gastritis, which has not been previously documented in a canine. The mechanisms by which NHPHs were able to form raised lesions in this canine are unknown, but a potential theory that the authors have hypothesized would be through the formation of a biofilm. *Helicobacter* biofilm formation has been described *in vitro* and is suspected to play a role in human cases of chronic *Helicobacter pylori* gastritis (5). In human studies, *Helicobacter pylori* infection and growth consistent with biofilm formation have been found in gastric glands (5). Such a mechanism would account for the focal gross appearance of the current case. *Helicobacter* biofilms associated with chronic gastritis have been minimally described in veterinary species and warrant further investigation.

In human patients, nodular lesions associated with *Helicobacter pylori* have been described as a precursor to

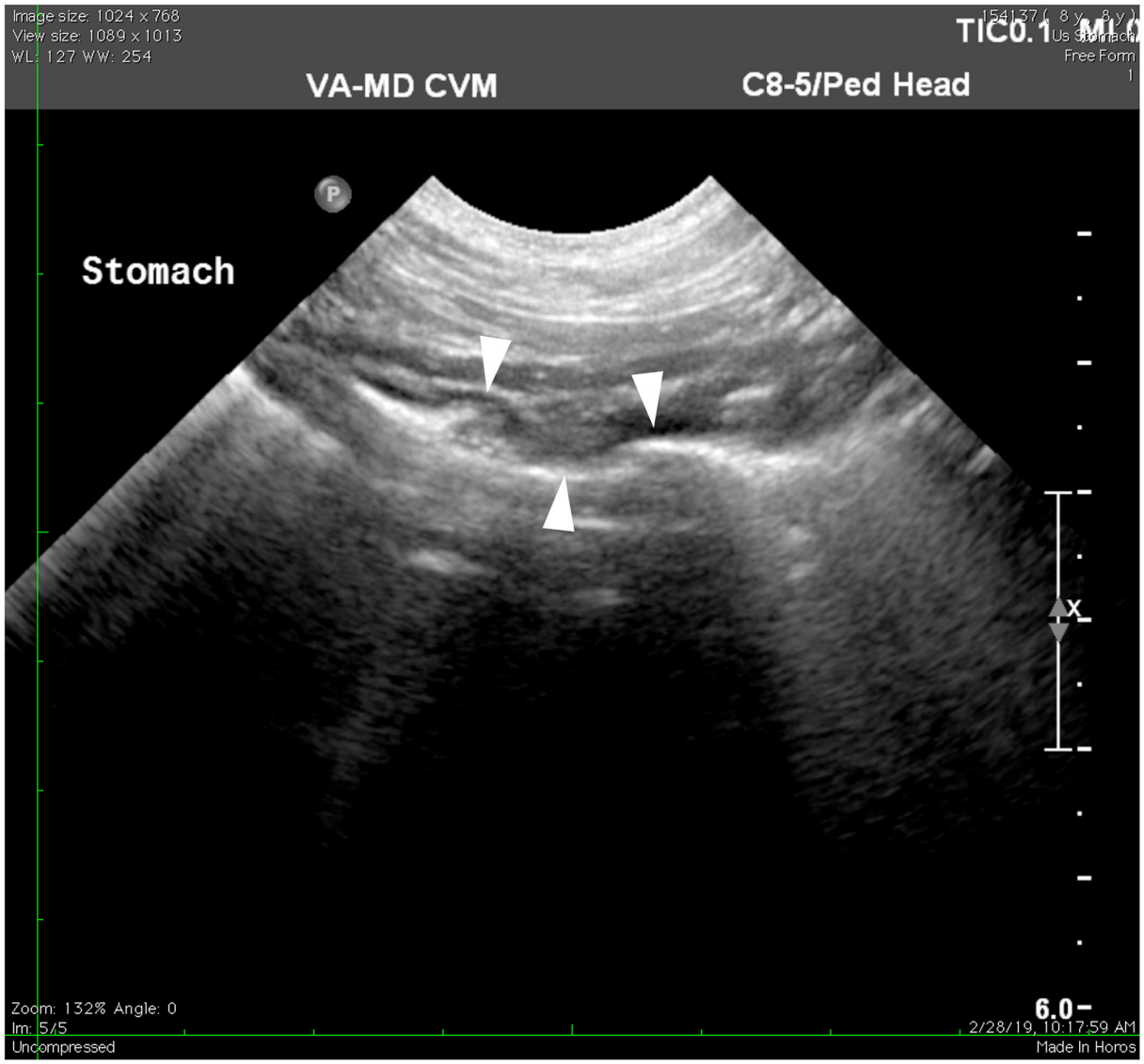

FIGURE 4
Ultrasonography of the stomach 27 days after starting antimicrobial therapy. Previously described fundic lesions appear to no longer be present in the stomach wall (arrowheads).

gastric neoplasia (6). However, progression to neoplasia can be avoided when timely *Helicobacter pylori* therapy is applied (6). In canines, *Helicobacter* spp. are often found in conjunction with gastric neoplasia (7). However, the infection has not been previously associated with nodular neoplastic precursors, and its role, if any, in the pathogenesis of gastric neoplasia in canines remains undiscovered (7, 8).

In this case, exact speciation of the NHPHs was not performed nor was a rapid urease test performed. *Helicobacter* species commonly isolated from canine gastric mucosa, include *H. felis*, *H. bizzozeronii*, *H. salomonis*, *H. bilis, H. heilmannii*, and *Flexispira rappini,* a closely related spirochete (3). Current knowledge of these species is that they behave similarly and cause similar lesions and clinical signs. Bacterial culture and PCR testing were not performed in this case as collecting the samples would have added another invasive procedure for this patient and was not deemed clinically necessary by the authors. *Helicobacter* spp. infections can be reliably diagnosed based on histologic appearance with the observation of the presence of the organism (3).

Abdominal ultrasonography was pursued early in this case as other non-invasive diagnostic tests failed to rule in the authors' differentials. The lesions found on ultrasound moved neoplasia higher up in the list of differentials based on the patient's signalment and lack of other findings. Endoscopy, with the intent to collect a biopsy sample for histopathology,

followed suit, with the type of gross lesion in the present case being consistent with gastric adenocarcinoma, leiomyoma, leiomyosarcoma, and extramedullary plasmacytoma among others (8). Many of these differentials carry a poor-to-guarded long-term prognosis and may require surgical intervention (8). When the histopathology results did not support a neoplastic etiology, instead supporting NHPHs-associated lymphocytic-plasmacytic gastritis as the diagnosis, the authors pursued medical management as it was less invasive than performing another biopsy or surgical excision. Fortunately, the lesions showed resolution *via* ultrasonographical examination and clinical signs had resolved with the empirical treatment, so no further diagnostics nor interventions were clinically necessary. Even in the face of a gross nodular appearance, histopathology remains an important diagnostic tool for gastric lesions to determine the etiology and prognosis. In this case, histopathologic results showed lesions consistent with typical *Helicobacter* spp. gastritis and lacked findings associated with primary gastric neoplasia.

The potential limitation of this case is that endoscopy and endoscopic biopsy are not always readily available in the average general practice. Identifying the species of NHPHs involved may have bolstered the impact of this case for the betterment of understanding the role of *Helicobacter* spp. in canine gastritis; however, this was not proven clinically relevant in this patient.

There are still areas of discovery regarding NHPHs infections and canine gastritis. Based on the authors findings, *Helicobacter* spp. gastritis should remain on a differential list for canine patients experiencing chronic vomiting or those with mass-like gastric lesions on ultrasonographical or endoscopic examination and should not be ruled out by gross lesion appearance alone.

Data availability statement

The original contributions presented in the study are included in the article/supplementary material, further inquiries can be directed to the corresponding author/s.

Ethics statement

Ethical review and approval was not required for the animal study because of the animal was seen as a clinical patient at the Veterinary Teaching hospital and all documentation occurred within normal treatment/care for the patient. Written informed consent was obtained from the owners for the participation of their animals in this study.

Author contributions

TG and CH contributed to writing the manuscript and literature review. MN contributed to the critical revision of the manuscript and managed the clinical case. TG and MN contributed to the final review. All authors contributed to the article and approved the submitted version.

Funding

Open access publication fees provided by Virginia Tech University Libraries.

Acknowledgments

We are grateful to Dr. Michelle Greer for conducting the ultrasound imaging and providing the images, and to Dr. Geoff Saunders for the histopathologic findings and pictures.

Conflict of interest

The authors declare that the research was conducted in the absence of any commercial or financial relationships that could be construed as a potential conflict of interest.

Publisher's note

References

1. Prachasilpchai W, Nuanualsuwan S, Chatsuwan T, Techangamsuwan S, Wangnaitham S, Sailasuta A. Diagnosis of Helicobacter spp. infection in the canine stomach. *J Vet Sci.* (2007) 8:139–45. doi: 10.4142/jvs.2007.8.2.139

2. Simpson KW, Strauss-Ayali D, McDonough PL, Chang YF, Valentine BA. Gastric function in dogs with naturally acquired gastric Helicobacter spp. Infection. *J Vet Intern Med.* (1999) 13:507–15. doi: 10.1111/j.1939-1676.1999.tb02203.x

3. Neiger R, Simpson KW. Helicobacter infection in dogs and cats: facts and fiction. *J Vet Intern Med.* (2000) 14:125–33. doi: 10.1111/j.1939-1676.2000.tb02225.x

4. Leib MS, Duncan RB, Ward DL. Triple antimicrobial therapy and acid suppression in dogs with chronic vomiting and gastric Helicobacter spp. *J Vet Intern Med.* (2007) 21:1185–92. doi: 10.1111/j.1939-1676.2007.tb01936.x

5. Hathroubi S, Servetas SL, Windham I, Merrell DS, Ottemann KM. Helicobacter pylori biofilm formation and its potential role in pathogenesis. *Microbiol Mol Biol Rev.* (2018) 82:1–18. doi: 10.1128/MMBR.00001-18

6. Nishikawa I, Kato J, Terasoma S, Matsutani H, Tamaki H, Tamaki T, et al. Nodular gastritis in association with gastric cancer development before and after Helicobacter pylori eradication. *JGH Open.* (2018) 2:80–6. doi: 10.1002/jgh3.12049

7. Hardas A, Suárez-Bonnet A, Beck S, Becker WE, Ramírez GA, Priestnall SL. Canine gastric carcinomas: a histopathological and immunohistochemical study and similarities with the human counterpart. *Animals (Basel).* (2021) 11:1409. doi: 10.3390/ani11051409

8. Amorim I, Taulescu MA, Day MJ, Catoi C, Reis CA, Carneiro F, et al. Canine gastric pathology: a review. *J Comp Pathol.* (2016) 154:9–37. doi: 10.1016/j.jcpa.2015.10.181

frontiers | Frontiers in Veterinary Science

TYPE Case Report
PUBLISHED 11 August 2022
DOI 10.3389/fvets.2022.930210

OPEN ACCESS

EDITED BY
Haney Samir,
Cairo University, Egypt

REVIEWED BY
Kate English,
University of Surrey, United Kingdom
Sirilak Disatian Surachetpong,
Chulalongkorn University, Thailand
Carlos Fernando Agudelo,
University of Veterinary and Pharmaceutical Sciences Brno, Czechia

*CORRESPONDENCE
Tomohiko Yoshida
Tomohiko7731-yoshida@yahoo.co.jp
Ahmed S. Mandour
dr_mandour@vet.suez.edu.eg

SPECIALTY SECTION
This article was submitted to Veterinary Imaging, a section of the journal Frontiers in Veterinary Science

RECEIVED 27 April 2022
ACCEPTED 18 July 2022
PUBLISHED 11 August 2022

CITATION
Yoshida T, Mandour AS, Sato M, Hirose M, Kikuchi R, Komiyama N, Hendawy HA, Hamabe L, Tanaka R, Matsuura K and Uemura A (2022) Pulmonary thromboembolism due to immune-mediated hemolytic anemia in a cat: A serial study of hematology and echocardiographic findings. *Front. Vet. Sci.* 9:930210. doi: 10.3389/fvets.2022.930210

Pulmonary thromboembolism due to immune-mediated hemolytic anemia in a cat: A serial study of hematology and echocardiographic findings

Tomohiko Yoshida[1,2]*, Ahmed S. Mandour[2,3]*, Manami Sato[1], Miki Hirose[1,2], Rina Kikuchi[1], Norihiro Komiyama[1], Hanan A. Hendawy[2], Lina Hamabe[2], Ryou Tanaka[2], Katsuhiro Matsuura[2] and Akiko Uemura[4]

[1]VCA JAPAN-Mitaka Veterinary Group, Tokyo, Japan, [2]Department of Veterinary Surgery, Tokyo University of Agriculture and Technology, Tokyo, Japan, [3]Department of Animal Medicine (Internal Medicine), Faculty of Veterinary Medicine, Suez Canal University, Ismailia, Egypt, [4]Department of Clinical Veterinary Medicine, Obihiro University of Agriculture and Veterinary Medicine, Hokkaido, Japan

Pulmonary thromboembolism (PTE) secondary to immune-mediated hemolytic anemia (IMHA) is rarely diagnosed in cats. In this report, a 3-year-old cat was referred to our private hospital with dyspnea, anorexia, and anemia. On the thoracic radiography, cardiac enlargement and pulmonary edema were noted. Echocardiography revealed right ventricular and right atrium enlargement with mild tricuspid regurgitation (tricuspid regurgitation velocity 3.28 m/s). A thrombus was recognized in the main pulmonary artery on the right parasternal short-axis view. Blood examination suggested regenerative anemia and autoagglutination. The findings suggested immune-mediated hemolytic anemia and PTE. Antithrombotic therapy (dalteparin) and immunosuppressive therapy (prednisolone) were administered under oxygen supplementation in the ICU cage. After treatment, regenerative anemia and right-heart failure were improved. During follow-up, the cat remained hemodynamically stable, and the owner reported no cardiac-related clinical signs. Further blood examination confirmed the anemia was improved. Prednisolone was discontinued on Day 56, and the cat continues in good health, administered only mycophenolate mofetil. The clinical outcome of PTE secondary to the IMHA throughout 100 days of periodical observation was reported.

KEYWORDS

cat, pulmonary thromboembolism, immune-mediated hemolytic anemia, echocardiography, hematobiochemical

Introduction

Immune-mediated hemolytic anemia (IMHA) in cats is considered to occur less frequently than in dogs (1). Early reports suggested that IMHA is more likely to be secondary to underlying disease in cats. However, more recent studies suggest that the proportion of cats with primary IMHA is higher, similar to that reported in dogs (2–7). Clinically, as in dogs, IMHA causes rapid erythrocyte destruction by autoimmunity, resulting in mucosal pallor, jaundice, hemoglobinuria, and abdominal distention due to splenomegaly, which can be fatal if progressing rapidly (7). In canine IMHA, disseminated intravascular coagulation syndrome (DIC) and pulmonary thromboembolism (PTE) are the most common causes of death, and antithrombotic therapy has been stated to play a significant role in prognosis (8, 9). In cats, two cases of PTE secondary to IMHA were reported (10). However, the occurrence of thrombosis in the pulmonary artery and the necessity of antithrombotic therapy in the treatment protocol have not been clarified. In the present study, we diagnosed IMHA and secondary PTE in a 3-year-old cat with respiratory distress and visible mucosal pallor. The cat was treated for IMHA with prednisolone and mycophenolate mofetil, and with antithrombotic therapy. The case description, steps of diagnosis, the treatment strategy, and patient follow-ups for 100 days are reported here.

Case presentation

A 3-year-old spayed munchkin (Body weight 2.6 kg) was referred with the primary complaints of respiratory distress, loss of energy, loss of appetite, and visible mucosal pallor. She had already been treated with antibiotics at another hospital, and blood tests revealed anemia and auto-agglutination of the red blood cells. Haemoglobinuria was noted on urination, stool observations were unremarkable, with no evidence of melena or fresh blood. Body temperature on admission was 37.4°C, with a heart rate of 180 beats/min, and a respiratory rate of 60 breaths/min. The patient presented jaundiced on visible mucosa, light pigmentation of the nasal speculum, no enlarged peripheral lymph nodes, and a capillary refill time of <2 s. The cat showed a palpable femoral artery and a systolic apical murmur on the right chest wall. The patient had a subcutaneous hemorrhage at the site of blood sampling at another hospital. A complete blood count (CBC), blood coagulation tests, and hematology and biochemistry test was performed as part of a systemic screening examination (Table 1, day 0). Blood typing was performed in consideration of blood transfusion. To exclude the infectious causes of hemolytic anemia, testing for common hemolytic anemia inducing pathogens was also performed. Because of profound dyspnea, the thorax and abdomen were evaluated by X-rays and ultrasonography.

Laboratory examination revealed severe regenerative anemia, increased white blood cell count, and decreased platelet count (ProCyte Dx Hematology Analyzer, IDEXX Laboratories, Japan). In addition, the auto-agglutination of red blood cells on the slide was observed (Figure 1). Blood chemistry tests showed elevated total bilirubin and phosphorus concentration (DRI-CHEM 7000V, Fujifilm, Japan). Blood coagulation tests are also shown in Table 1 (PT, APTT, Fib). The blood fibrinolytic system test revealed a normal D-dimer level (Fujifilm Monolith, reference value: 0–2.0 μg/ml). The blood type was determined to be type B. There was no evidence of infectious disease-causing hemolytic anemia: negative feline vector-borne pathogens (FeVBPs), feline leukemia virus antigen (FeLV), and feline immunodeficiency virus antibody (FIV) tests (IDEXX Laboratories, Japan). Also, the antiglobulin antibody (Coombs test, Fujifilm Monolith, Japan) and the anti-nuclear antibody test (IDEXX Laboratories, Japan) were negative. On thoracic and abdominal radiographs, the right lateral view showed the increased pulmonary opacity in the anterior lung lobes and the disappearance of the ventral waist of the cardiac shadow, suggesting right heart enlargement and pulmonary edema (Figure 2A). In the dorsoventral view, the interlobar fissure in the posterior lung lobe was clear, suggesting pleural effusion (Figure 2B). Abdominal radiography showed no significant alteration. Echocardiography revealed an enlarged right ventricle and right atrium with tricuspid regurgitation (TR flow 3.28 m/s) in the right parasternal long-axis view (Figures 3A,B). The right parasternal short-axis view showed flattening of the interventricular septum on B-mode images (Figure 3C). In the right parasternal short-axis view at the base of the heart, dilatation of the main pulmonary artery was observed (PA/Ao 1.1), and the pulmonary arterial flow velocity was 0.8 m/s with a shortened acceleration time to ejection time ratio (AT/ET 0.25). Hyperechoic structure, which was suspected thrombus, was observed in the pulmonary artery bifurcation (Figure 3D). Early diastolic mitral inflow (E wave) was 0.5 m/s. Right ventricular fractional area change (RV-FAC) was 18%, obtained by tracing the RV endocardial border at end-diastole and end-systole from the left parasternal long axis 4-chamber view. The right atrial area (RAA) was 2.75 cm^2, measured by tracing from the lateral aspect of the tricuspid annulus to the septal aspect, excluding the area between the leaflets and annulus, following the RA endocardium at the end of the ventricular systole. A small amount of pleural effusion was observed, however, thoracentesis was not performed due to the low platelet count and bleeding tendency. There was no evidence of short-circuit disease or structural abnormality of the tricuspid valve. Abdominal ultrasonography showed a trace amount of ascites which was difficult to collect. There were no other significant findings, and no tumor lesions were observed.

10.3389/fvets.2022.930210

TABLE 1 Hematological and biochemical analysis in a cat with immune-mediated hemolytic anemia.

Variables		Examination intervals						Reference range (11, 12)
	Unit	Day 0	Day 2	Day 14	Day 28	Day 35	Day 100	
WBC	$10^3/\mu\ell$	21.2	9.8	20.0	6.6	24.5	17.6	7.73–18.6
RBC	$10^6/\mu\ell$	1.58	5.20	6.4	8.00	7.36	9.11	5.9–11.2
HGB	g/dℓ	3.8	8.2	8.5	11.2	10.4	12.5	8.2–15.3
HCT	%	12	28.2	31.1	33.9	33.2	35.1	24–46
MCV	fL	79.7	50.4	42.6	42.4	44.0	46.1	35.9–53.1
MCHC	g/dl	31.7	30.4	32.9	33.0	33.2	34	28.1–35.8
Reticulocyte	$10^3/\mu\ell$	78.2	132.0	10.3	13.0	5.12	4.4	3.0–50.0
Reticulocyte	%	5.0	2.5	0.2	0.2	0.7	0.5	0.2–1.0
PLT	$10^3/\mu\ell$	43	19.2	16.3	22.6	26.3	20.7	13.0–62.6
PT	second	9	8	-	-	-	-	6.0–8.6
APTT	second	31	32	-	-	-	-	12.0–51.3
Fib	mg/dl	108	202	-	-	-	-	120–400
D-dimer	μg/ml	1.22	-	-	-	-	-	<2.0
FeLV		Negative	-	-	-	-	-	-
FIV		Negative	-	-	-	-	-	-
Coombs test		Negative	-	-	-	-	-	-
ANA		Negative	-	-	-	-	-	-
FeVBPs		Negative	-	-	-	-	-	-
TP	g/dℓ	6.5	6.7	6.8	7.0	7.5	7.0	5.4–7.8
Alb	g/dℓ	2.7	2.8	3.2	3.6	3.6	3.4	2.1–3.3
GLU	mg/dℓ	99	180	148	132	131	161	64–152
GGT	IU/l	4	-	-	2	3	-	1–7
BUN	mg/dℓ	43.7	34.6	20.3	17.2	21	20.6	15–37
Cre	mg/dℓ	1.26	0.95	0.71	0.43	0.52	0.51	0.8–1.8
ALT	IU/ℓ	50	-	62	>2000	121	77	19–90
AST	IU/ℓ	66	-	66	>1000	61	57	12–45
ALP	IU/ℓ	75	-	34	155	110	90	9–50
Na	mEq/ℓ	155	149	152	154	153	155	145–159
K	mEq/ℓ	3.7	4.1	4.0	4.6	4.2	4.0	3.0–4.8
Cl	mg/dℓ	114	104	107	104	105	105	111–125
IP	mg/dℓ	6.0	3.6	3.0	4.3	4.2	3.7	2.2–6.5
Ca	mg/dℓ	9.6	9.0	10.5	12.5	11.5	11.1	8.0–11.1
T-Bil	mg/dℓ	1.0	0.1	0.1	1.1	0.1	0.1	0.1–0.5

WBC, white blood cells; RBC, red blood cells, HGB, hemoglobin; HCT, hematocrit; PLT, platelet count; PT, prothrombin time; APTT, activated prothrombin time; Fib, fibrinogen; FeLV, feline lentivirus; FIV, feline immune virus; TP, total protein; Alb, albumin; GLU, glucose; GGT, gamma-glutamyl transferase; BUN, blood urea nitrogen; Cre, creatinine; ALT, alanine aminotransferase; AST; aspartate transferase; ALP, alkaline phosphatase; Na, sodium; K; potassium; Cl, chloride; IP, inorganic phosphorus; Ca, calcium; T-Bil, total bilirubin; ANA, antinuclear antibody; FeVBPs, feline vector born pathogens.

In the present report, blood tests and imaging studies revealed no underlying disease, infection, or disease-causing regenerative anemia. The diagnosis of primary IMHA was made based on the presence of auto-agglutination as a sign of immune mediated destruction as well as the presence of jaundice and haemoglobinuria. These two signs suggesting the prescence of hemolysis. Our diagnosis also was confirmed as IMHA by the absence of another underlying cause for the anemia. Besides, observation of a structure in the pulmonary artery was thought to be a thrombus, potentially a complication of PTE. As the patient presented with severe anemia and respiratory distress, a CT scan was not performed. Instead, a blood transfusion and improvement of respiratory symptoms were prioritized.

The treatment protocol was initiated based on the previously published report including blood transfusion, diuretic, anticoagulant, immunosuppressant, antibiotic, and antiacid (4). The blood transfusion consisted of 40 ml of whole fresh blood, given to the recipient over 24 h to avoid

FIGURE 1
Results of in-saline slide agglutination test (SAT). Self-agglutination was positive.

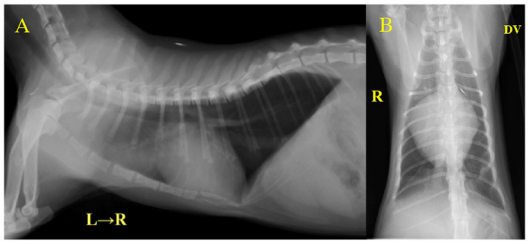

FIGURE 2
Thoracic radiography at initial examination. **(A)** Right lateral view, **(B)** Dorsoventral view. The increased pulmonary opacity was observed in the bilateral anterior lobe of the lungs. VHS = 9.4 v and CTR = 81% indicated a clear cardiac enlargement.

rapid volume loading. Since the right ventricular volume increased after the transfusion, risking a worsening respiratory condition, furosemide 0.5 mg/kg IV (Lasix Injection, Nichi-Iko Co., Ltd., Japan) was administered at the beginning of the transfusion; the respiratory condition stabilized after a few minutes. Echocardiography and blood pressure were measured every 6 h in the first 48 h. Dalteparin sodium, a low molecular weight anticoagulant, 100 IU/kg TID SC (IV Fragmin, Kissei Pharmaceutical Company, Nagano, Japan) was administered for PTE; prednisolone 4 mg/kg/day SC (prednisolone injection solution, Kyoritsu Pharmaceutical Company, Tokyo, Japan) for IMHA treatment, and famotidine (antiacid) 1 mg/kg BID IV (Gaster, LTL Corporation, Tokyo, Japan) was administered to protect the digestive tract. Enrofloxacin 5 mg/kg SID SC (Baytril, Bayer Yakuhin, Ltd., Japan) was also administered to treat possible causes of feline infectious anemia. After the transfusion, on day two, the anemia improved. The respiratory condition was enhanced a little but respiratory frequency remained high, necessitating the administration of furosemide 0.5 mg/kg SC BID (Gaster, LTL Corporation, Tokyo, Japan). On day four, the respiratory condition was improved and the patient was able to feed independently with increased activity. During hospitalization, she continued to receive dalteparin sodium, prednisolone, famotidine, and enrofloxacin. On Day 14, as the respiratory symptoms had calmed down and anemia had not progressed, the patient was treated with prednisolone 4 mg/kg/day PO (prednisone 5 mg tablet, Shionogi, Japan); furosemide 0.5 mg/kg BID PO (Furosemide tablet 10 mg, Nipro K.K., Japan); lansoprazole 1 mg/kg BID PO (Lansoprazole, Daiko Pharmaceutical, Japan); rivaroxaban 1 mg/kg SID PO (Igzarelto tablets 10 mg, Bayer Yakuhin, Japan); leflunomide 2 mg/kg SID PO (Arava tablets 10 Sanofi K.K., Japan), and the patient was discharged from hospital. On Day 21, echocardiography showed a reversible reduction in the right ventricle and right atrium size, disappearance of the TR (Figures 4A,B), no flattening of the interventricular septum (Figure 4C), and improvement of RV-FAC (39.1%) and RAA (0.74 cm^2). Besides, the thrombus in the pulmonary artery had disappeared and the patient's respiratory condition became stable (Figure 4D). At this moment, the dose of furosemide was reduced to 0.5 mg/kg SID. On Day 28, the visible mucosa showed a slightly jaundiced color. Blood chemistry tests showed elevated ALT, AST, ALP, GGT, and T-Bil. The cat's activity was decreased but no decrease in appetite was observed. There was no increase in serum amyloid A (<3.75) (DRI-CHEM IMMUNO AU10V, Fujifilm, Japan) or progression of anemia. Since leflunomide or the high-dose prednisolone was considered a cause of the liver disorder, leflunomide was withdrawn and mofetil mycophenolate 10 mg/kg BID (CellCept suspension spray 31.8%, Chugai, Japan) was additionally prescribed. The prednisolone was reduced to 3 mg/kg/day, and acetic acid ringer's solution (1 ml/kg/h) (Fuso Pharmaceutical Industries, Osaka, Japan) was administered under hospitalization. On Day 35, an improvement in bilirubin and liver enzymes was observed. On Day 44, further improvement of bilirubin and liver enzymes was observed. On Day 56, anemia was completely resolved, and the dose of prednisolone was reduced to 2 mg/kg/day. Further, the dose of prednisolone was decreased to 0.5 mg/kg every 2–4 weeks, and on Day 100, both prednisolone and reversaloxaban were withdrawn. At present, the cat is continuing her IMHA treatment solely with mycophenolate mofetil 10 mg/kg BID.

Discussion

The IMHA diagnostic criteria in the ACVIM consensus statement include the saline agglutination test (SAT) and the direct antiglobulin test (Coombs test). According to the ACVIM guidelines, biomarkers of immune destruction including flow cytometry are evaluated, and at least two of these must be present to make a definite diagnosis. The presence of one of the above and at least two haemolytic findings (when only one indication of immune mediated destruction is present) such as hyperbilirubinemia/hyperbilirubinuria,

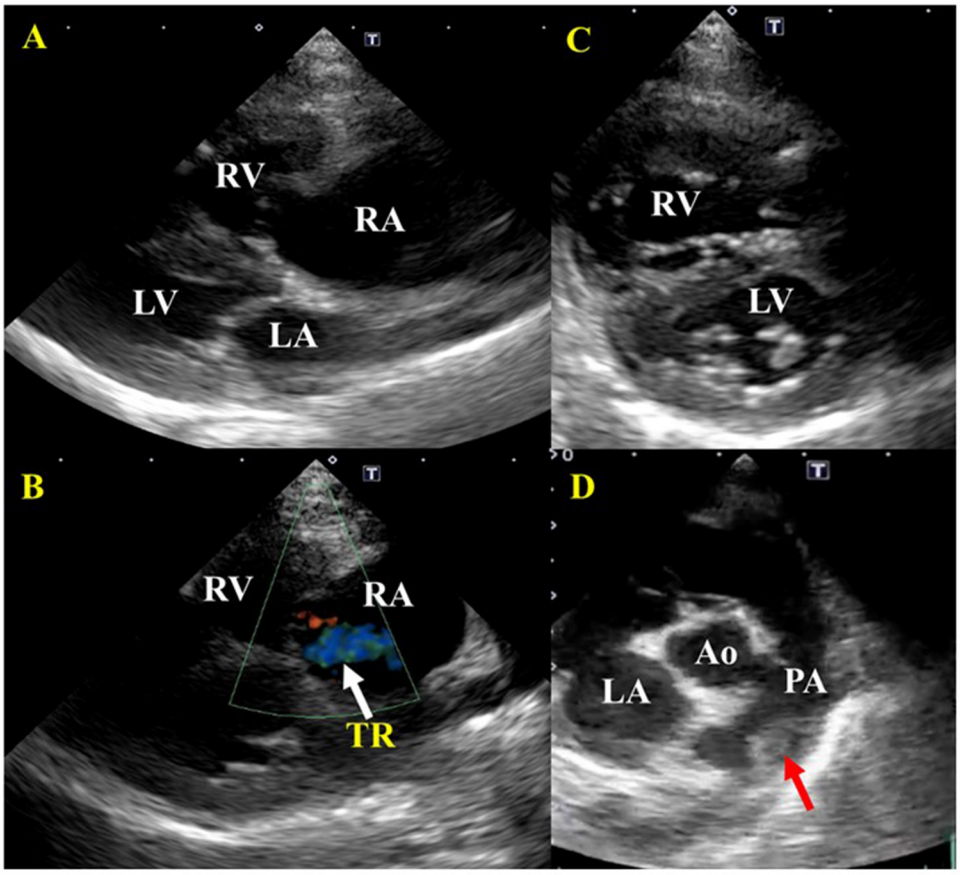

FIGURE 3
Echocardiographic images before treatment of a cat diagnosed with IMHA and pulmonary thromboembolism. **(A)** Right parasternal long-axis view. Enlargement of the right atrium and right ventricle were found. There was no dysplasia of the tricuspid valve, patent ductus arteriosus, atrial septal defect, or ventricular septal defect. **(B)** Right parasternal long-axis view (Color Doppler imaging). Tricuspid regurgitation was recognized. **(C)** Right parasternal short-axis view (Apical level). The flattening of the interventricular septum was observed. **(D)** Right parasternal short-axis view (Basal level). A thrombus was found between the main pulmonary artery and the bifurcation of the right and left pulmonary arteries. RA, right atrium; RV, right ventricle; LA, left atrium; LV, left ventricle; PA, pulmonary artery. Red arrows indicate a thrombus; white arrows indicate tricuspid regurgitation (TR).

hemoglobinemia, hemoglobinuria, or erythrocyte ghosting with no abnormalities in the hepatobiliary system, can also support the diagnosis of IMHA (1). In this case, the diagnosis of IMHA was made presumptively based on the presence of jaundice, regenerative anemia, and hemoglobinuria, as well as the auto-agglutination of red blood cells. Since various diseases cause hemolytic anemia, it may be important to fulfill the diagnostic criteria, especially in cats, where the incidence of primary IMHA has historically been considered to be lower than in dogs. In dogs, thromboembolism has been reported to occur in association with the onset of IMHA, either by the activation of coagulation factors or by the formation of erythrocyte auto-aggregates (13, 14). There are, however, few reports on IMHA and thromboembolism in cats, and the incidence of thromboembolism is still unknown. In the present case, PTE secondary to IMHA was suspected in the patient presented with respiratory distress; echocardiography showed a thrombus in the right and left pulmonary artery branches, and right heart enlargement disappeared after several days of treatment with antithrombotic drugs. The sensitivity and specificity of D-dimer in the diagnosis of thrombosis in cats are lower than those in dogs (15, 16), and in this case, D-dimer was normal despite the presence of a thrombus in imaging studies. Therefore, a comprehensive diagnosis of thrombosis in cats, including imaging and blood tests, is necessary. If thrombosis is largely suspected from the results of imaging tests, it is worthwhile to start antithrombotic therapy if there is no bleeding tendency or findings that suggest blood loss. As treatment for PTE in this patient, low molecular weight heparin was administered subcutaneously on admission, as the patient was unable to take oral medication due to her worsening respiratory condition, and rivaroxaban was prescribed at the

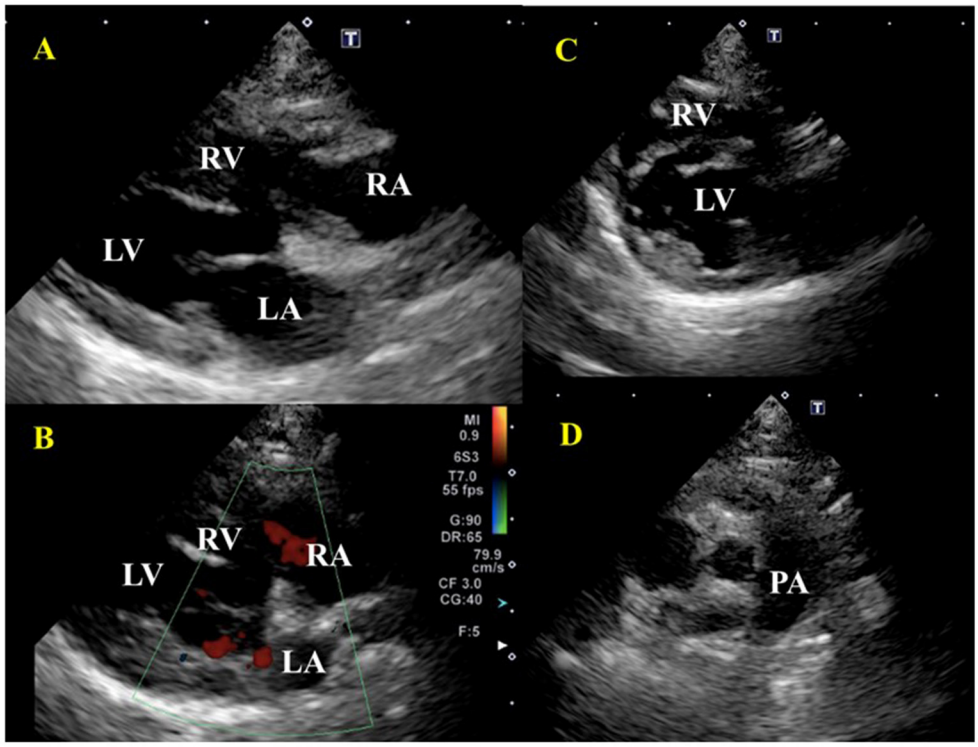

FIGURE 4
Echocardiographic images after treatment of a cat diagnosed with IMHA and pulmonary thromboembolism on Day 21. **(A)** Right parasternal long-axis view. There was no enlargement of the right atrium and right ventricle. **(B)** Right parasternal long-axis view (Color Doppler imaging), tricuspid valve regurgitation had disappeared. **(C)** Right parasternal short-axis view (Apical level). Right ventricular enlargement and flattening of the ventricular septum disappeared. **(D)** Right parasternal short-axis view (Basal level). A thrombus in the pulmonary artery had disappeared. RA, right atrium; RV, right ventricle; LA, left atrium; LV, left ventricle; PA, pulmonary artery.

time of discharge from the hospital because of improved general condition. In addition, a diuretic was administered to reduce the right ventricular capacitance load, and the patient's respiratory condition improved to a good standard (17). It has been reported that a good course of treatment for PTE in dogs has been achieved by administering antithrombotic drugs and oxygen inhalation (16). As such, we decided to follow the same protocol by administering antithrombotic drugs under oxygen inhalation. In this case, factor Xa inhibitor, reversaloxaban, was the antithrombotic therapy of choice. Although there are fewer reports on the use of rivaroxaban for thrombosis in cats than clopidogrel and other drugs, we chose rivaroxaban as the patient was relatively small in stature; the smaller tablet size of rivaroxaban made it easier for the owner to administer the drug. However, the dosage of rivaroxaban for cats has not been clearly defined, and setting the dosage could be a significant challenge in the future (18). The PTE is a cause of pulmonary edema by inducing pulmonary hypertension (19). This may have been the case in our patient since her respiratory urgency was reduced in response to increased impermeability in the lung fields and diuretics on imaging examination. In such patients in poor general condition, diuretics may decrease blood pressure and lead to a potentially fatal situation; as such, it is recommended that diuretics be administered while measuring blood pressure and monitoring the right and left ventricular cavity size, and the left ventricular inflow tract waveform (E waveform) by echocardiography, to maintain hemodynamic status. The treatment of pulmonary edema could be effectively performed while preserving the patient's health. Pulmonary vasodilators were also considered in the current case but were not administered as they are not a fundamental treatment for addressing hypertension. For the treatment of IMHA in cats, we used prednisolone and leflunomide as immunosuppressive therapy. On Day 28 of treatment, leflunomide was withdrawn after a possible leflunomide-related adverse reaction was observed, i.e., elevated liver enzymes and bilirubin. The patient quickly improved, although ALP remained persistently elevated. Since there are few reports on adverse reactions to immunosuppressive drugs in cats (20), it is unclear whether leflunomide causes such adverse reactions specifically in cats or just in this case, but it should be used with caution. In addition, the possibility

of hepatic injury due to prednisolone cannot be ruled out, and regular monitoring of liver enzyme levels is necessary when high-dose prednisolone is used. Since the cause of low creatinine, and low chloride also were unclear, these values also should be monitored. Although no serious adverse reactions have occurred with immunosuppressive therapy using mycophenolate mofetil, the lack of large-scale studies in cats suggests the need for further careful monitoring of these patients.

In the future, when long-term remission is achieved, mofetil mycophenolate will also be withdrawn.

Conclusion

We reported a case of primary IMHA complicated by PTE in a cat. Blood transfusion, immunosuppressive therapy, antithrombotic therapy, and diuretics are effective treatment strategies for patients with IMHA and PTE, but detailed hemodynamic monitoring, including echocardiography and blood pressure measurement, is necessary during the induction, due to significant hemodynamic changes.

Data availability statement

The raw data supporting the conclusions of this article will be made available by the authors, without undue reservation.

Ethics statement

Ethical review and approval was not required for the animal study, given there was only one case, for which written informed consent for participation was obtained from the owners. Written informed consent was obtained from the owners for the participation of their animals in this study.

Author contributions

TY, AM, and MS designed the report and drafted the manuscript. KM, MH, and RK acquired and analyzed the data. NK, LH, and AU critically reviewed the manuscript. HH and RT summarized in this report. All authors contributed to the article and approved the submitted version.

Acknowledgments

The authors would like to thank all the hospital staff involved in the care of this cat, as well as the owner, who showed remarkable commitment.

Conflict of interest

The authors declare that the research was conducted in the absence of any commercial or financial relationships that could be construed as a potential conflict of interest.

The handling editor HS, declared past co-authorships with the author, AM.

Publisher's note

Supplementary material

The Supplementary Material for this article can be found online at: https://www.frontiersin.org/articles/10.3389/fvets.2022.930210/full#supplementary-material

References

1. Garden OA, Kidd L, Mexas AM, Chang YM, Jeffery U, Blois SL, et al. ACVIM consensus statement on the diagnosis of immune-mediated hemolytic anemia in dogs and cats. *J Vet Internal Med.* (2019) 33:313–34. doi: 10.1111/jvim.15441

2. Scott DW, Schultz RD, Post JE. Autoimmune hemolytic anemia in the cat. *J Am Animal Hospital Assoc.* (1973) 9:530–9.

3. Werner LL, Gorman NT. Immune-mediated disorders of cats. *Vet Clin North Am: Small Animal Practice.* (1984) 14:1039–64. doi: 10.1016/S0195-5616(84)50106-5

4. Kohn B, Weingart C, Eckmann V, Ottenjann M, Leibold W. Primary immune-mediated hemolytic anemia in 19 cats: Diagnosis, therapy, and outcome (1998–2004). *J Vet Internal Med.* (2006) 20:159–66. doi: 10.1111/j.1939-1676.2006.tb02836.x

5. Tasker S, Murray JK, Knowles TG, Day DJ. Coombs', haemoplasma and retrovirus testing in feline anaemia. *J Small Animal Practice.* (2010) 51:192–9. doi: 10.1111/j.1748-5827.2009.00869.x

6. Piek CJ, Junius G, Dekker A, Schrauwen E, Slappendel RJ, Teske E. Idiopathic immune-mediated hemolytic anemia: Treatment outcome and prognostic factors in 149 dogs. *J Vet Internal Med.* (2008) 22:366–73. doi: 10.1111/j.1939-1676.2008.0060.x

7. Swann JW, Szladovits B, Glanemann B. Demographic characteristics, survival and prognostic factors for mortality in cats with primary immune-mediated

hemolytic anemia. *J Vet Internal Med.* (2016) 30:147–56. doi: 10.1111/jvim.13658

8. Swann JW, Skelly BJ. Canine autoimmune hemolytic anemia: management challenges. *Vet Med (Auckl).* (2016) 7:101–12. doi: 10.2147/VMRR.S81869

9. Weinkle TK, Center SA, Randolph JF, Warner KL, Barr SC, Erb HN. Evaluation of prognostic factors, survival rates, and treatment protocols for immune-mediated hemolytic anemia in dogs: 151 cases (1993–2002). *J Am Vet Med Assoc.* (2005) 226:1869–80. doi: 10.2460/javma.2005.226.1869

10. Norris CR, Griffey SM, Samii VF. Pulmonary thromboembolism in cats: 29 cases (1987-1997). *J Am Vet Med Assoc.* (1999) 215:1650–4.

11. Granat F, Geffré A, Bourgès-Abella N, Mortier J, Théron ML, Fauchon E, et al. Feline reference intervals for the Sysmex XT-2000iV and the ProCyte DX haematology analysers in EDTA and CTAD blood specimens. *J Feline Med Surg.* (2014) 16:473–82. doi: 10.1177/1098612X13511811

12. Kaneko JJ, Harvey JW, Bruss ML. *Clinical Biochemistry of Domestic Animals*. Academic Press (2008).

13. Carr AP, Panciera DL, Kidd L. Prognostic factors for mortality and thromboembolism in canine immune-mediated hemolytic anemia: a retrospective study of 72 dogs. *J Vet Internal Med.* (2002) 16:504–9. doi: 10.1111/j.1939-1676.2002.tb02378.x

14. Klein MK, Dow SW, Rosychuk RA. Pulmonary thromboembolism associated with immune-mediated hemolytic anemia in dogs: ten cases (1982-1987). *J Am Vet Med Assoc.* (1989) 195:246–50.

15. Brazzell JL, Borjesson DL. Evaluation of plasma antithrombin activity and D-dimer concentration in populations of healthy cats, clinically ill cats, and cats with cardiomyopathy. *Clin Pathol.* (2007) 36:79–84. doi: 10.1111/j.1939-165X.2007.tb00186.x

16. Tholen I, Weingart C, Kohn B. Concentration of D-dimers in healthy cats and sick cats with and without disseminated intravascular coagulation (DIC). *J Feline Med Surg.* (2009) 11:842–6. doi: 10.1016/j.jfms.2009.04.008

17. Morita T, Nakamura K, Osuga T, Hanazono K, Morishita K, Takiguchi M. Change in right ventricular function in an American cocker spaniel with acute pulmonary thromboembolism. *J Vet Med Sci.* (2019) 81:1259–65. doi: 10.1292/jvms.19-0082

18. Dixon-Jimenez AC, Brainard BM, Brooks MB, Nie B, Arnold RD, Loper D, et al. Pharmacokinetic and pharmacodynamic evaluation of oral rivaroxaban in healthy adult cats. *J Vet Emerg Crit Care.* (2016) 26:619–29. doi: 10.1111/vec.12524

19. Kellihan HB, Waller KR, Pinkos A, Steinberg H, Bates ML. Acute resolution of pulmonary alveolar infiltrates in 10 dogs with pulmonary hypertension treated with sildenafil citrate: 2005-2014. *J Vet Cardiol.* (2015) 17:182–91. doi: 10.1016/j.jvc.2015.04.002

20. Mehl ML, Tell L, Kyles AE, Chen YJ, Craigmill A, Gregory CR. Pharmacokinetics and pharmacodynamics of A77 1726 and leflunomide in domestic cats. *J Vet Pharmacol Therap.* (2012) 35:139–46. doi: 10.1111/j.1365-2885.2011.01306.x

frontiers | Frontiers in Veterinary Science

TYPE Original Research
PUBLISHED 26 September 2022
DOI 10.3389/fvets.2022.991148

OPEN ACCESS

EDITED BY
Ayman Abdel-Aziz Swelum,
Zagazig University, Egypt

REVIEWED BY
Louis Charles Penning,
Utrecht University, Netherlands
Noboru Sasaki,
Hokkaido University, Japan

*CORRESPONDENCE
Merle Toom
repseps@gmail.com

†These authors have contributed equally to this work and share last authorship

SPECIALTY SECTION
This article was submitted to Veterinary Imaging, a section of the journal Frontiers in Veterinary Science

RECEIVED 11 July 2022
ACCEPTED 31 August 2022
PUBLISHED 26 September 2022

CITATION
Toom M, Saunders JH, Duchateau L, Serrano G, De Rooster H, Devriendt N and Stock E (2022) Shear wave elastography measurements in dogs treated surgically for congenital extrahepatic portosystemic shunts. *Front. Vet. Sci.* 9:991148. doi: 10.3389/fvets.2022.991148

Shear wave elastography measurements in dogs treated surgically for congenital extrahepatic portosystemic shunts

Merle Toom[1]*, Jimmy H. Saunders[1], Luc Duchateau[2], Goncalo Serrano[3], Hilde De Rooster[3], Nausikaa Devriendt[3†] and Emmelie Stock[1†]

[1]Department of Morphology, Imaging, Orthopedics, Rehabilitation and Nutrition, Faculty of Veterinary Medicine, Merelbeke, Belgium, [2]Department of Veterinary and Biosciences, Faculty of Veterinary Medicine, Merelbeke, Belgium, [3]Department of Small Animals, Faculty of Veterinary Medicine, Merelbeke, Belgium

Assessing the postoperative surgical success of congenital extrahepatic portosystemic shunt (EHPSS) attenuation can be challenging and involve invasive imaging methods. Elastography is an ultrasound technique that allows qualitative and quantitative estimation of tissue stiffness and has extensively been used in people with liver disease. In recent years, increased interest in this technique has developed in veterinary medicine due to its non-invasive nature, availability, and low cost. The objective of this study was to compare liver stiffness values between dogs with closed EHPSS and those with multiple acquired portosystemic shunts (MAPSS) after gradual surgical attenuation and to assess whether shear wave elastography could be used to determine EHPSS closure. As a secondary objective, measurements obtained from both intercostal and subxiphoidal views were compared. Mean values for the average, median, and maximum two-dimensional shear wave velocities (2D SWV) for the closed EHPSS were 2.88 +/−0.11 m/s; 2.83 +/−0.11 m/s; and 3.75 +/−0.16 m/s, respectively. In the MAPSS dogs, mean values for the average, median, and maximum 2D SWV were 2.77 +/− 0.17 m/s; 2.71 +/− 0.17 m/s; and 3.66 +/−0.24 m/s, respectively. No significant differences in 2D SWV were present between dogs with closed EHPSS and those with MAPSS ($P = 0.33$; $P = 0.33$; $P = 0.42$, respectively). When assessing potential differences between intercostal and subxiphoidal 2D SWV measurements, no effect was observed for the average and median 2D SWV ($P = 0.06$; $P = 0.07$, respectively). Yet, a significant difference was identified for the maximum 2D SWV between intercostal 4.00 +/−0.20 m/s and subxiphoidal 3.41 +/−0.17 m/s measurements ($P = 0.02$). The relevance of this finding is uncertain as many other studies about liver elastography only report mean and not maximum values.

KEYWORDS

elastography, 2D SWE, liver, dog, portosystemic shunt

Introduction

Portosystemic shunts (PSS) are vascular anomalies that connect the portal vein to the systemic circulation, bypassing the hepatic sinusoids and the liver parenchyma (1). When blood bypasses the liver, trophic factors (particularly insulin and glucagon) are not available to encourage hepatic growth, resulting in poor hepatic development, and altered fat and protein metabolism, hepatic atrophy, and eventually liver failure (2, 3). Liver histology of dogs suffering from congenital PSS demonstrates many changes such as microscopic bile duct proliferation, hypoplasia of portal tributaries, arteriolar proliferation, and smooth muscle hypertrophy, with some dogs also showing evidence of fibrosis (4, 5). In one recent study, some degree of liver fibrosis was present in about 90% of dogs with congenital extrahepatic PSS (EHPSS), with some even categorized as an advanced stage of fibrosis (6). The degree of portal fibrosis has been suggested to increase with advanced age with a resolution of hepatic changes in dogs with closed EHPSSs (4). In the latter study, liver samples collected before and 8 to 272 days (median 48.5 days) after partial ligation of the shunting vessel were compared; however, confirmation of the surgical success of PSS closure was not described.

As shorter life expectancy is reported in dogs where PSS attenuation is not performed, it is important to try to gradually attenuate PSS without causing multiple acquired PSS (MAPSS) to develop (7–11). No ideal non-invasive test exists to discriminate between different surgical outcomes (closed PSS vs. shunt patency through the original PSS or development of MAPPS) (12–15). Computed tomography angiography (CTA), transsplenic portal scintigraphy (TSPS), splenoportovenography, and magnetic resonance imaging (MRI) are considered reliable techniques, but they are invasive, require anesthesia, hospitalization, are high in costs, and are associated with potential morbidity (16–18).

Sonoelastography evaluates the firmness of tissues through which differences between normal and pathological tissue could be made (19, 20). It is a convenient way to visualize, record, and report tissue stiffness parameters. There are four types of US-based elastography techniques available: strain elastography, transient elastography, point-shear wave elastography, and two-dimensional shear-wave elastography (2D SWE)(19, 21). Two-dimensional shear wave elastography uses the acoustic radiation force impulse (ARFI) technique to provide a quantitative assessment of tissue stiffness. The ARFI push generates a transverse (shear) wave that moves slowly in soft tissues and more rapidly in stiffer tissues. Consequently, 2D SWE provides information complementary to conventional ultrasound and is of particular interest due to its non-invasiveness, wide availability, and relatively low cost (21–23).

In human hepatic diseases, elastography has been used primarily to diagnose and monitor the degree of hepatic fibrosis to guide treatment decisions (20) but liver stiffness has also been linked to many other physiological and pathological conditions such as hepatic inflammation, obstructive cholestasis, hepatic congestion, acute toxic hepatitis, amyloidosis, lymphoma, and extramedullary hematopoiesis (20). In recent years, there have been numerous studies pertaining to liver elasticity in dogs and cats (23–31), but no studies describe such modality in dogs with PSS.

The objectives of this study were to compare liver 2D SWE measurements in dogs with successfully closed EHPSS and those with multiple acquired portosystemic shunts (MAPSS) after gradual EHPSS attenuation. Furthermore, the location of the ultrasound probe (intercostal vs. subxiphoidal) for taking the measurements as well as dog characteristics (sex, breed, body weight, and age both at time of surgery and at time of 2D SWE) were analyzed to determine the effect of these values on liver 2D SWE measurements. We hypothesized that patients with MAPPS would have increased tissue stiffness and therefore increased measured velocities. Additionally, we hypothesized that the location of the measurements and dog characteristics would not significantly influence the measured results.

Materials and methods

Animals

All procedures were approved by and conducted in accordance with the local ethical and deontological committee (EC 2018-77 and DWZ/ER/1.15/28).

Dogs that underwent gradual surgical treatment for congenital EHPSS in our institution (Faculty of Veterinary Medicine of Ghent University) between 2013 and 2018 were prospectively recruited. To be eligible, the dogs had to have the outcome of surgical attenuation of the EHPSS confirmed *via* TSPS and/or CTA minimally 3 months after the surgical procedure and had to have a postoperative follow-up period of at least 6 months. Signalment, sex, breed, body weight, and age both at the time of surgery and at the time of 2D SWE were recorded at the time of recruitment.

Measurement of two-dimensional shear wave elastography

Ultrasound examination was performed between July 2019 and January 2020 by a board-certified veterinary radiologist (E.S). In all the dogs, 2D SWE was performed without sedation using Philips ElastQ Imaging (ElastQ, software version 3.0.3, Philips, Brussels, Belgium) and a linear probe (Pure Wave eL18-4 ultra–broadband linear array transducer, Philips). In accordance with the guidelines for the clinical use of elastography of the liver in humans (20, 21, 32) and the published results in dogs (23, 25, 27, 29–31), the subxiphoidal

and left lateral recumbency intercostal approach for acquiring the elastography measurements from the right liver lobe was used. The provided confidence map highlighted areas with optimal shear wave propagation for improved ROI (region of interest) placement. Within the confidence map, every pixel in the ROI is assigned a confidence value from 0 to 100 and a corresponding color between red and green. Low values (red) indicate that the stiffness value for a given pixel is less reliable. High values (green) indicate that the stiffness value for a given pixel is more reliable (Figure 1). The confidence threshold was set at 50%, as recommended by the manufacturer (Philips, Brussels, Belgium), meaning that regions with a confidence value of < 50% were rendered transparent and not measurable. Measurements were recorded either in kPa (pressure) or m/s (velocity). For the consistency of measurements, the interquartile range (IQR)/median was set to be < 30%. The IQR is the spread of 50% of the measurements around the median and thus the IQR/median is an effective way to assess the quality of the range of measurements (32). Using the visual control of the 2D B-mode image, an artifact-free image of the liver parenchyma was chosen for subsequent SWE measurements. A circular shape sample area within the ROI was set at 5 to 10 mm in diameter and excluded regions that were not color coded. The sample area was positioned in the parenchyma of the liver at least 10 mm deep to the liver capsule and at least 5 to 10 valid measurements were obtained, and the resultant mean 2D SWV was calculated and used as representatives. The scanner software calculates simultaneously the average, median, and maximal 2D SWV in m/s or kPa (Young's modulus). The measurements were recorded and used for further analysis.

Statistical analysis

Statistical analysis was performed with SAS (SAS V.9.4, SAS institute). Two-dimensional shear wave velocities were compared between dogs with closed EHPSS and those with MAPSS using a mixed model with the animal as random effect and outcome (closed EHPSS vs. MAPPS), and location (sub-xiphoidal vs. intercostal) and their interaction as categorical fixed effect factors.

Results

Study population

Fifteen dogs with closed EHPSS and 6 patients with MAPSS met the inclusion criteria. Out of the 21 patients from the initial cohort, one dog from the EHPSS group was excluded due to poor cooperation and inability to acquire good quality 2D SWE images.

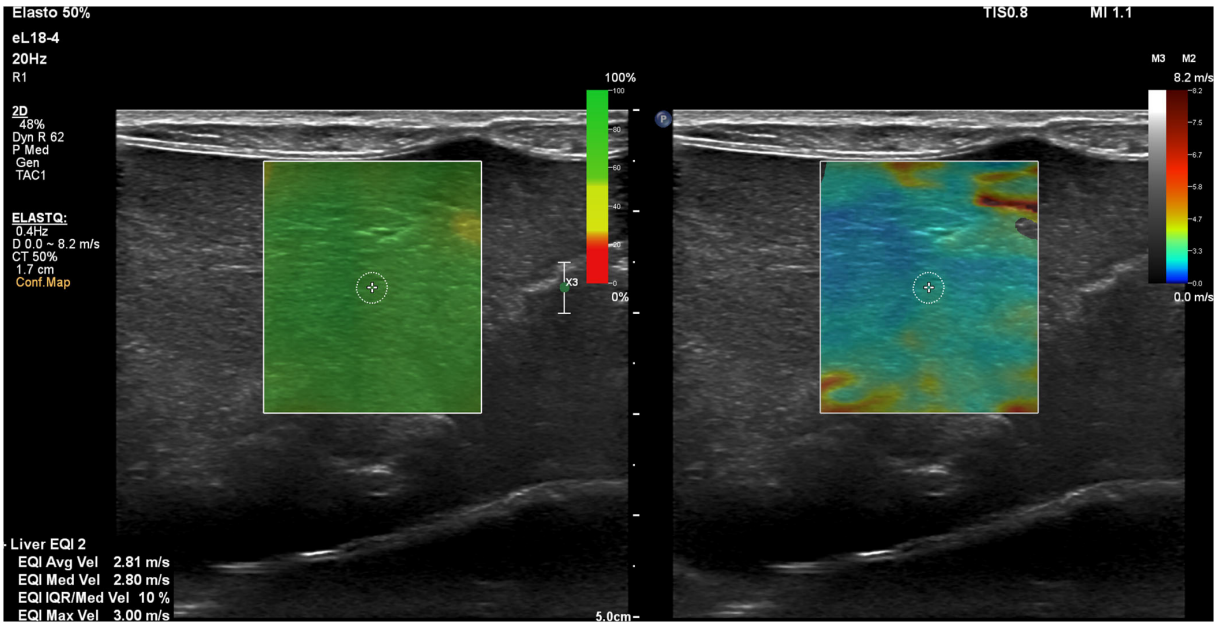

FIGURE 1
Representative two-dimensional shear wave elastography (2D SWE) image of the right lobe of the liver using the subxiphoidal approach for a speed mode in a dog with a closed extrahepatic portosystemic shunt. The green confidence map and the elastogram image are displayed concurrently over the B-mode image. A small circular shape sample area within the ROI is selected to produce the 2D SWE measurements.

10.3389/fvets.2022.991148

TABLE 1 Mean two-dimensional shear wave velocity (2D SWV) of dogs with closed extrahepatic portosystemic shunts (EHPSS) and multiple acquired portosystemic shunts (MAPSS).

2D SWV	Average (m/s)	Median (m/s)	Maximum (m/s)
Closed EHPSS ($n = 14$)	2.88 +/−0.11	2.83 +/−0.11	3.75 +/−0.16
MAPSS ($n = 6$)	2.77 +/−0.17	2.71 +/−0.17	3.66 +/-0.24
P-value	0.33	0.33	0.42

Of the 20 dogs included in study, 1 was intact male, 6 were neutered male, and 13 were neutered female. The mean body weight at the time of elastography on the closed EHPSS group was 5.8 kg (+/−0.67), ranging from 2.2 to 9 kg. The mean body weight in dogs with MAPPS was 5.3 kg (+/-0.98), ranging from 2.8 to 9.2 kg. The mean age at the time of surgery in the closed EHPSS group was 31 months (+/−5,6), ranging from 4 to 72 months. The mean age at the time of surgery in the MAPSS group was 16 months (+/−5.2), ranging from 5 to 38 months. The mean age at the time of 2D SWE in the closed EHPSS group was 72 months (+/−7.5) and 62 months (+/−12) in the MAPPS group. The represented breeds were as follows: 3 Chihuahuas, 3 Maltese dogs, 3 Yorkshire Terriers, 2 Bichon Frise dogs, 2 cross breed dogs, 2 Dachshunds, 2 Miniature Schnauzers, and 1 German Spitz, Norwich Terrier, and Pug.

Comparison of two-dimensional shear wave elastography between closed EHPSS and MAPSS

Results of the study are provided in Table 1 and are illustrated in boxplot diagrams (Figures 2, 3).

No significant differences in 2D SWVs between dogs with closed EHPSS and those with MAPSS were identified (Table 1) regarding average, median, and maximum SWV ($P = 0.33$; $P = 0.33$; $P = 0.42$, respectively).

There was a significant difference between the maximum 2D SWV measurement of the intercostal (4.00 +/−0.20) and the subxiphoidal (3.41 +/−0.17) approach ($P = 0.02$). Regarding the average and median SWVs, the difference was not statistically significant ($P = 0.06$ and $P = 0.07$, respectively).

No significant effects on the average, median, and maximum SWV by sex ($P = 0.18$; $P = 0.19$; $P = 0.21$, respectively), body weight ($P = 0.32$; $P = 0.35$; $P = 0,24$, respectively), age at time of surgery ($P = 0.53$; $P = 0.53$; $P = 0.45$, respectively), or age at time of elastography ($P = 0.42$; $P = 0.42$; $P = 0.59$, respectively) were observed.

Discussion

The objective of the present study was to compare the long-term postoperative liver stiffness measurements in dogs that underwent gradual surgical attenuation of congenital EHPSS and had successful closure of the EHPSS and those that developed MAPSS. The goal was to determine if non-invasive 2D SWE could potentially predict the success of surgical attenuation. Despite the current literature (8, 10) contradicting the relevance of persistent subclinical postoperative shunting on the life quality of dogs, establishing the surgical outcome would help to better compare survival time, quality of life, and best surgical techniques between these dogs. Many retrospective studies analyzing the long-term clinical outcome of surgical shunt attenuation have presumed shunt closure with no actual post-operative imaging to support that (9, 33). Thus far, CTA has been used as a method for quantifying changes in liver volume and hepatic perfusion after surgery and found to be useful as a quantitative marker of shunt fraction postoperatively (34, 35). Similarly, TSPS can determine the surgical outcome (36, 37). Both imaging techniques allow shunt fractions to be calculated and assessed pre–and post-operatively. Nevertheless, both these modalities require anesthesia and are associated with radiation exposure; therefore, the potential of elastography was investigated in the light of many recent studies demonstrating its usefulness in animals (23, 26, 38, 39).

As portal fibrosis development along with other pathological histomorphological hepatic changes is suggested to be associated with prolonged shunt patency and MAPSS (4–6), it would be expected for MAPPS dogs to have increased liver stiffness which might be demonstrated with non-invasive 2D SWE (2, 33, 39). Tamura et al. in their recent study showed the correlation between liver stiffness and the clinical stage of hepatic fibrosis in dogs (23). However, their velocity measurements overlapped between healthy controls, necroinflammatory hepatic conditions, and those with clinically insignificant liver fibrosis stages, making it only possible to differentiate advanced stages of liver fibrosis.

The mean 2D SWV between dogs with closed EHPSS and those with MAPSS did not differ significantly in our study. Multiple studies detailing MAPPS formation following PSS attenuation have shown that there is a subset of dogs that have the potential for long-term survival and overall favorable clinical outcome (33, 40, 41). The similar results between our two groups might suggest that the persistent shunting *via* MAPPS does not cause sufficient liver fibrosis to alter liver stiffness measurements with 2D SWE significantly. The mean age at the time of 2D SWE in our dogs was similar in both groups (closed EHPSS 72 months vs. 62 months in MAPPS). The mean time from surgery to elastography between the two groups was also similar (closed EHPSS 40.0+/−4.3 months vs. MAPPS 39.6 +/−8.1 months). At the time of surgery, MAPPS dogs were younger in comparison to dogs in the closed EHPSS group (16

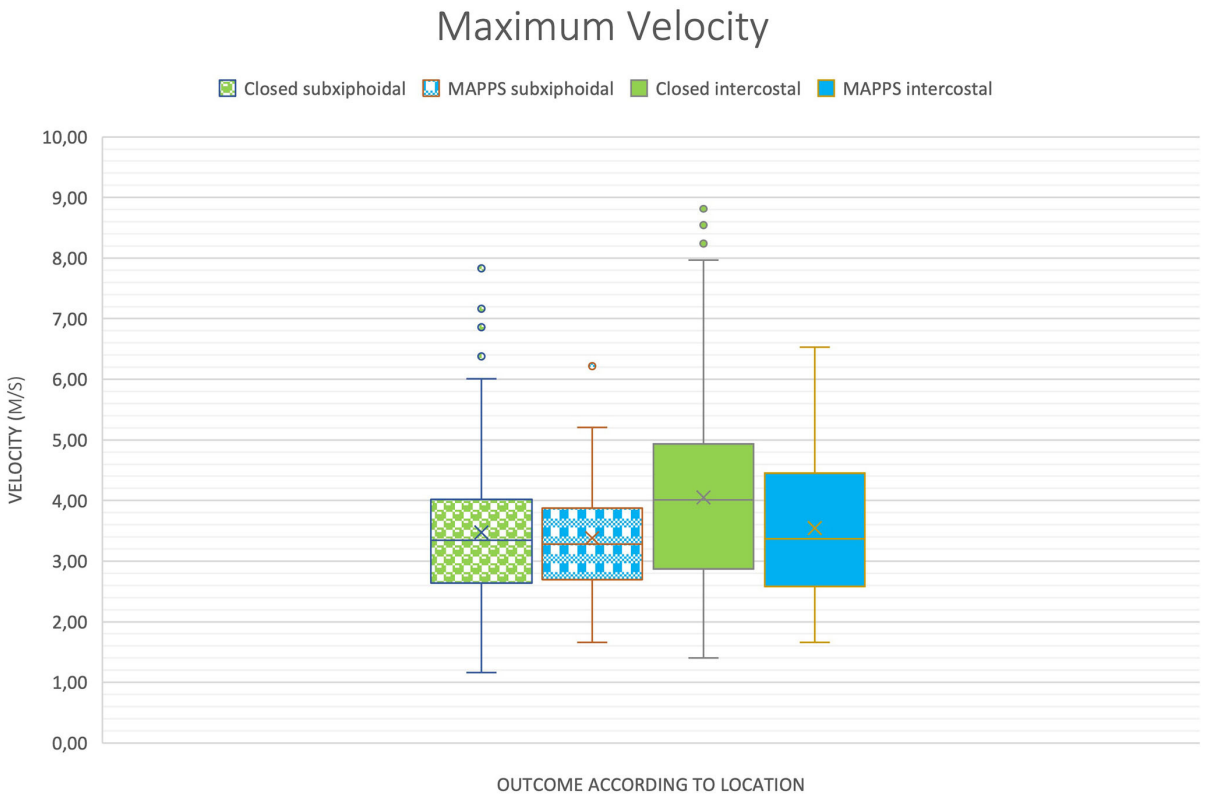

FIGURE 2
Boxplot of two-dimensional shear wave velocities (2D SWV) depending on location and outcome, demonstrating similar means between the groups, except for maximum shear wave velocity (SWV).

vs. 31 months). This could suggest earlier presentation due to more severe clinical signs consequent to the advanced disease process or due to the known association of clinical signs and age of presentation with different shunt morphology types (42). Unfortunately, we do not have comparative pre-operative 2D SWE measurements to corroborate if any dynamic changes between the pre–and post-operative elastography results were present. This would be an interesting area for future research. However, evaluating 2D SWV measurements later in life might be able to demonstrate differences in liver stiffness between these groups as aging itself has been considered a risk factor for the progression of fibrosis, at least in people. In people, it has been suggested that aging increases the susceptibility to liver fibrosis (43, 44).

Our measurements differ significantly from findings obtained in studies performed on healthy dogs (31, 45). In the study by Tamura et al., the mean SWV for the right lobe of the liver in healthy dogs was 1.51 m/s and in the study by Holdsworth et al., the interquartile range for values obtained from the liver at 0 to 2 cm of depth was 1.18 to 1.88 m/s. It is known that the data comparability between the different elastography technologies, system settings, and parameters will vary as many technical factors are not standardized. Several system factors, in particular, shear wave vibration frequency and bandwidth (20) between different commercial systems and equipment, make measurements comparison and data pooling from different studies difficult. Additionally, many other factors such as the examination procedure itself (use of anesthesia, fasting and resting, selection of ROI), breathing, and cardiac motion can cause variability in the measurements (25). An experiment on phantoms between different commercially available systems demonstrated the difference in measurements between machines and observers in the order of 12% (21). It would be interesting to compare the current results with measurements obtained from a control group of healthy dogs using the same ultrasound system.

Shear wave elastography measurements can be affected by body weight, sex, measurement approach, and depth of the measured organ, with normal canine liver, spleen, and kidney measurements being affected by these variables in one study (31). Our study did not see any significant influence of body weight, sex, or age on the liver stiffness results, but considering the congenital nature of the disease and the predilection for small breed dogs (3), our population was

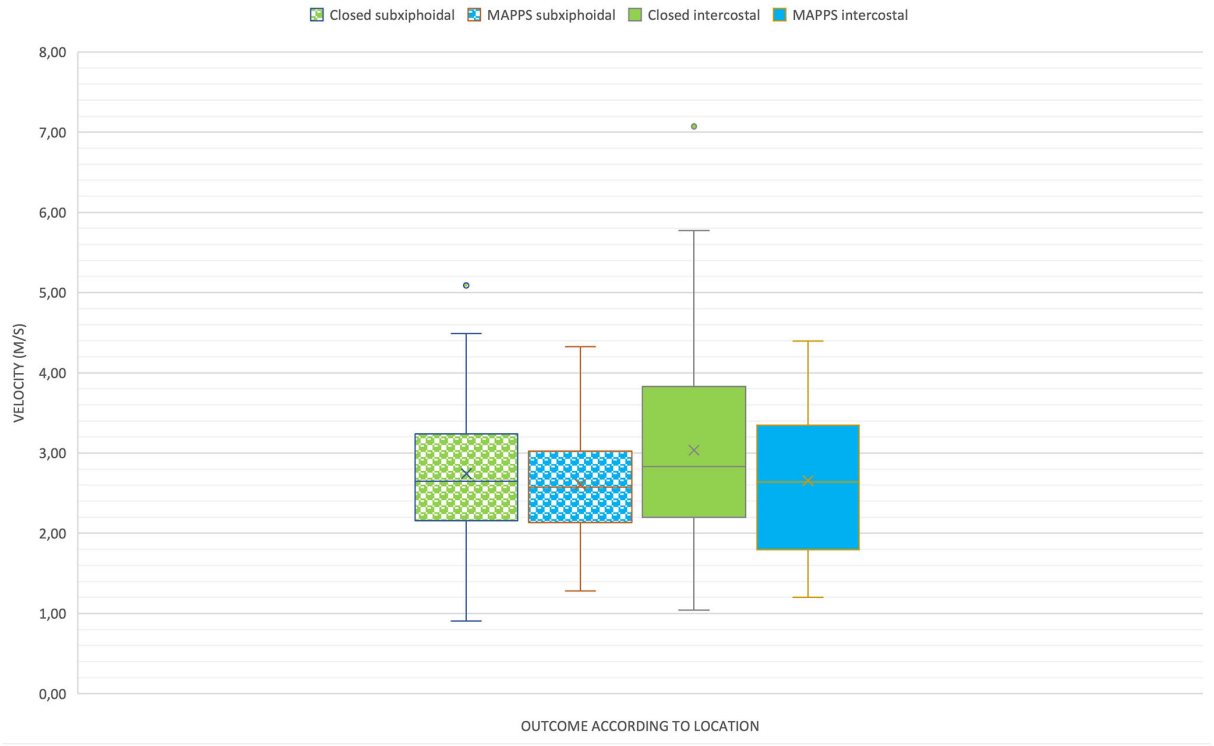

FIGURE 3
Boxplot of two-dimensional shear wave velocities (2D SWV) depending on location and outcome, demonstrating similar means between the groups.

homogenous. Regarding the location of the measurements, a statistically significant difference in the subxiphoidal vs. intercostal approach was identified; however, this was only the case for the maximum velocity. In human medicine, the intercostal approach is recommended as the highest intra–and interobserver agreement was obtained through that approach (20). One veterinary study in healthy Beagle dogs also showed a difference in liver elastography measurements according to approach (46), whereas another study with healthy Beagles did not find any correlation (25). Comparison of the outcomes between different studies is hindered as explained before; furthermore, while our method of recording velocities differentiates average, median, and maximum results, it is often not specified how the mean elastographic velocities in other studies are derived.

Our study had some limitations. The sample size was small, especially for dogs with MAPSS, which may have decreased statistical power and led to type II error. Further studies with a larger number of dogs would allow us to possibly show differences between the two populations. This would most likely require a multi-institutional study design; however, as sonoelastographic technical aspects are ultrasound system specific, pooling and comparing data from different institutions would be unreliable. For data uniformity, it would have been better to implement the liver 2D SWE measurements at the same postoperative time point in all the dogs, especially as shunt recanalization 3 and 5 years postoperatively has been described (47) and as age is suggested to be associated with progression of liver fibrosis in people (44).

The severity of hepatic histologic lesions in dogs with congenital PSSs is believed to be related to the degree of shunting and may vary among liver lobes, especially in patients with intrahepatic shunts (3, 5, 48). Another study showed that hepatic lesions were mostly uniformly distributed in dogs suffering from congenital EHPSS (4); however, in three dogs with EHPSS, they found that the left lobes were slightly more affected than the right ones. As all our measurements were performed on the right liver lobe, it is still possible that these measurements are not fully representative of the entire liver parenchyma. Liver histology at the time of 2D SWE performance would have been interesting, as it would allow us to correlate the degree of fibrosis and other histological liver changes to the measured variables. Due to the invasive nature of obtaining a liver biopsy, this was not considered justifiable.

Conclusion

Real-time 2D SWE was unable to differentiate between dogs with closed EHPSS and those with MAPSS long-term after gradual attenuation of EHPSS. No previous studies have described the liver stiffness measurements in a population of dogs with hepatic vascular anomalies and our results could serve as a baseline and reference for future studies.

Data availability statement

The raw data supporting the conclusions of this article will be made available by the authors, without undue reservation.

Ethics statement

The animal study was reviewed and approved by Institutional Animal Care and Use Committee (EC 2018–77) and the deontological committee of the Federal Public Service Health, Food Chain Safety and Environment (DWZ/ER/1.15/28). Written informed consent was obtained from the owners for the participation of their animals in this study.

Author contributions

Concept and design: ES, MT, HD, ND, and GS. Acquisition of data: ES, MT, and LD. Analysis and interpretation: MT and LD. Revising article for intellectual content: JS, LD, GS, ND, HD, and ES. Drafting the article: MT. Final approval of completed article: JS, LD, GS, ND, HD, ES, and MT. All authors contributed to the article and approved the submitted version.

Conflict of interest

The authors declare that the research was conducted in the absence of any commercial or financial relationships that could be construed as a potential conflict of interest.

Publisher's note

All claims expressed in this article are solely those of the authors and do not necessarily represent those of their affiliated organizations, or those of the publisher, the editors and the reviewers. Any product that may be evaluated in this article, or claim that may be made by its manufacturer, is not guaranteed or endorsed by the publisher.

References

1. Suter PF. Portal vein anomalies in the dog: their angiographic diagnosis. *Vet Radiol.* (1975) 16:84–97. doi: 10.1111/j.1740-8261.1975.tb01324.x

2. Berent AC, Tobias KM. Portosystemic vascular anomalies. *Vet Clin North Am Small Anim Pract.* (2009) 39:513–41. doi: 10.1016/j.cvsm.2009.02.004

3. Cullen JM, van den Ingh TSGAM, Bunch SE, Rothuizen J, Washabau RJ, Desmet VJ. Morphological classification of circulatory disorders of the canine and feline liver. In: *WSAVA Standards for Clinical and Histological Diagnosis of Canine and Feline Liver Diseases*. Elsevier Ltd (2006). p. 41–59. doi: 10.1016/B978-0-7020-2791-8.50008-3

4. Baade S, Aupperle H, Grevel V, Schoon HA. Histopathological and immunohistochemical investigations of hepatic lesions associated with congenital portosystemic shunt in dogs. *J Comp Pathol.* (2006) 134:80–90. doi: 10.1016/j.jcpa.2005.07.003

5. Powers BE, Twedt DC. Histologic examination of hepatic biopsy samples as a prognostic indicator in dogs undergoing surgical correction of congenital portosystemic shunts: 64 cases (1997–2005). *JAVMA.* (2005) 232. doi: 10.2460/javma.232.10.1511

6. Sobczak-Filipiak M, Szarek J, Badurek I, Padmanabhan J, Trębacz P, Januchta-Kurmin M, et al. Retrospective liver histomorphological analysis in dogs in instances of clinical suspicion of congenital portosystemic shunt. *J Vet Res (Poland).* (2019) 63:243–9. doi: 10.2478/jvetres-2019-0026

7. Greenhalgh SN, Reeve JA, Johnstone T, Goodfellow MR, Dunning MD, O'Neill EJ, et al. Long-term survival and quality of life in dogs with clinical signs associated with a congenital portosystemic shunt after surgical or medical treatment. *J Am Vet Med Assoc [Internet].* (2014) 245:527–33. doi: 10.2460/javma.245.5.527

8. Falls EL, Milovancev M, Hunt GB, Daniel L, Mehl ML, Schmiedt CW. Long-term outcome after surgical ameroid ring constrictor placement for treatment of single extrahepatic portosystemic shunts in dogs. *Vet Surgery.* (2013) 42:951–7. doi: 10.1111/j.1532-950X.2013.12072.x

9. Otomo A, Singh A, Jeong J, Dobberstein R, Lundhild A, Peter E, et al. Long-term clinical outcomes of dogs with single congenital extrahepatic portosystemic shunts attenuated with thin film banding or ameroid ring constrictors. *Vet Surgery.* (2020) 49:436–44. doi: 10.1111/vsu.13384

10. Hottinger HA, Walshaw R, Hauptman JG. Long-Term results of complete and partial ligation of congenital portosystemic shunts in dogs. *Vet Surgery.* (1995) 24:331–6. doi: 10.1111/j.1532-950X.1995.tb01339.x

11. Tivers MS, Lipscomb VJ, Bristow P, Brockman DJ. Intrahepatic congenital portosystemic shunts in dogs: short- and long-term outcome of suture attenuation. *J Small Animal Pract.* (2018) 59:201–10. doi: 10.1111/jsap.12788

12. D'Anjou MA, Penninck D, Cornejo L, Pibarot P. Ultrasonographic diagnosis of portosystemic shunting in dogs and cats. *Vet Radiol Ultrasound.* (2004) 45:424–37. doi: 10.1111/j.1740-8261.2004.04076.x

13. Devriendt N, Serrano G, Paepe D, de Rooster H. Liver function tests in dogs with congenital portosystemic shunts and their potential to determine persistent shunting after surgical attenuation. *Vet Journal.* (2020) 261:105478. doi: 10.1016/j.tvjl.2020.105478

14. Schaub S, Hartmann A, Schwarz T, Kemper K, Pueckler KH, Schneider MA. Comparison of contrast-enhanced multidetector computed tomography angiography and splenoportography for the evaluation of portosystemic-shunt occlusion after cellophane banding in dogs. *BMC Vet Res [Internet].* (2016) 12:5–8. doi: 10.1186/s12917-016-0910-6

15. van den Bossche L, van Steenbeek FG, Weber MF, Spee B, Penning LC, van Sluijs FJ, et al. Genome-wide based model predicting recovery from portosystemic shunting after liver shunt attenuation in dogs. *J Vet Intern Med.* (2018) 32:1343–52. doi: 10.1111/jvim.15140

16. Broome CJ, Walsh VP, Braddock JA. Congenital portosystemic shunts in dogs and cats. *N Z Vet J.* (2004) 52:154–62. doi: 10.1080/00480169.2004.10749424

17. Bille C, Auvigne V, Libermann S, Bomassi E, Durieux P, Rattez E. Risk of anaesthetic mortality in dogs and cats: an observational cohort study of 3546 cases. *Vet Anaesth Analg.* (2012) 39:59–68. doi: 10.1111/j.1467-2995.2011.00686.x

18. Bille C, Auvigne V, Bomassi E, Durieux P, Libermann S, Rattez E. An evidence-based medicine approach to small animal anaesthetic mortality in a referral practice: the influence of initiating three recommendations on subsequent anaesthetic deaths. *Vet Anaesth Analg.* (2014) 41:249–58. doi: 10.1111/vaa.12116

19. Ozturk A, Grajo RJ, Dhyani M, Anthony WB, Samir EA. Principles of ultrasound elastography. *Abdominal Radiol (NY).* (2018) 43:773–85. doi: 10.1007/s00261-018-1475-6

20. Dietrich CF, Bamber J, Berzigotti A, Bota S, Cantisani V, Castera L, et al. EFSUMB Guidelines and Recommendations on the Clinical Use of Liver Ultrasound Elastography, Update 2017 (Long Version). *Ultraschall Med.* (2017) 38:16–47. doi: 10.1055/s-0043-103952

21. Sigrist RMS, Liau J, Kaffas A. el, Chammas MC, Willmann JK. Ultrasound elastography: review of techniques and clinical applications. *Theranostics.* (2017) 7:1303–29. doi: 10.7150/thno.18650

22. Wells PNT, Liang HD. Medical ultrasound: imaging of soft tissue strain and elasticity. *J R Soc Interface.* (2011) 8:1521–49. doi: 10.1098/rsif.2011.0054

23. Tamura M, Ohta H, Shimbo G, Osuga T, Sasaki N, Morishita K, et al. Usefulness of noninvasive shear wave elastography for the assessment of hepatic fibrosis in dogs with hepatic disease. *J Vet Intern Med.* (2019) 33:2067–74. doi: 10.1111/jvim.15598

24. Lee D, Park S, Ang MJC, Park JG, Yoon S, Kim C, et al. Evaluation of liver lesions by use of shear wave elastography and computed tomography perfusion imaging after radiofrequency ablation in clinically normal dogs. *Am J Vet Res.* (2018) 79:1140–9. doi: 10.2460/ajvr.79.11.1140

25. Jung JW, Je H, Lee SK, Jang Y, Choi J. Two-Dimensional shear wave elastography of normal soft tissue organs in adult beagle dogs; interobserver agreement and sources of variability. *Front Bioeng Biotechnol.* (2020) 8:1–15. doi: 10.3389/fbioe.2020.00979

26. Facin AC, Uscategui RAR, Maronezi MC, Pavan L, Menezes MP, Montanhim GL, et al. Liver and spleen elastography of dogs affected by brachycephalic obstructive airway syndrome and its correlation with clinical biomarkers. *Sci Rep [Internet].* (2020) 10:1–10.

27. Rivero-Juárez A, Morgaz J, Camacho A, Muñoz-Rascón P, Dominguez JM, Sánchez-Céspedes R, et al. Liver stiffness using transient elastography is applicable to canines for hepatic disease models. *PLoS ONE.* (2012) 7:1–4. doi: 10.1371/journal.pone.0041557

28. White J, Gay J, Farnsworth R, Mickas M, Kim K, Mattoon J. Ultrasound elastography of the liver, spleen, and kidneys in clinically normal cats. *Vet Radiol Ultrasound.* (2014) 55:428–34. doi: 10.1111/vru.12130

29. Huaijantug S, Yatmark P, Phophug P, Worapakdee M, Phutrakul A, Julapanthong P, et al. Quantitative ultrasound elastography and serum ferritin level in dogs with liver tumors. *J Adv Vet Anim Res.* (2020) 7:575–84. doi: 10.5455/javar.2020.g455

30. Jeon S, Lee G, Lee SK, Kim H, Yu D, Choi J. Ultrasonographic elastography of the liver, spleen, kidneys, and prostate in clinically normal beagle dogs. *Vet Radiol Ultrasound.* (2015) 56:425–31. doi: 10.1111/vru.12238

31. Holdsworth A, Bradley K, Birch S, Browne WJ, Barberet V. Elastography of the normal canine liver, spleen and kidneys. *Vet Radiol Ultrasound.* (2014) 55:620–7. doi: 10.1111/vru.12169

32. Barr RG. Elastography in clinical practice. *Radiol Clin North Am [Internet].* (2014) 52:1145–62. doi: 10.1016/j.rcl.2014.07.002

33. Hunt GB, Kummeling A, Tisdall PLC, Marchevsky AM, Liptak JM, Youmans KR, et al. Outcomes of cellophane banding for congenital portosystemic shunts in 106 dogs and 5 cats. *Vet Surgery.* (2004) 33:25–31. doi: 10.1111/j.1532-950x.2004.04011.x

34. Zwingenberger AL, Daniel L, Steffey MA, Mayhew PD, Mayhew KN, Culp WTN, et al. Correlation between liver volume, portal vascular anatomy, and hepatic perfusion in dogs with congenital portosystemic shunt before and after placement of ameroid constrictors. *Vet Surgery.* (2014) 43:926–34. doi: 10.1111/j.1532-950X.2014.12193.x

35. Kummeling A, Vrakking DJE, Rothuizen J, Gerritsen KM, van Sluijs FJ. Hepatic volume measurements in dogs with extrahepatic congenital portosystemic shunts before and after surgical attenuation. *J Vet Intern Med.* (2010) 24:114–9. doi: 10.1111/j.1939-1676.2009.0439.x

36. Morandi F, Sura PA, Sharp D, Daniel GB. Characterization of multiple acquired portosystemic shunts using transsplenic portal scintigraphy. *Vet Radiol Ultrasound.* (2010) 51:466–71. doi: 10.1111/j.1740-8261.2010.01687.x

37. Morandi F, Cole RC, Tobias KM, Berry CR, Avenell J, Daniel GB. Use of 99mTcO4- trans-splenic portal scintigraphy for diagnosis of portosystemic shunts in 28 dogs. *Vet Radiol Ultrasound.* (2005) 46:153–61. doi: 10.1111/j.1740-8261.2005.00030.x

38. Glińska-Suchocka K, Jankowski M, Kubiak K, Spuzak J, Dzimira S, Nicpon J. Application of shear wave elastography in the diagnosis of mammary gland neoplasm in dogs. *Pol J Vet Sci.* (2013) 16:477–82. doi: 10.2478/pjvs-2013-0066

39. Feliciano MAR, Maronezi MC, Pavan L, Castanheira TL, Simões APR, Carvalho CF, et al. ARFI elastography as a complementary diagnostic method for mammary neoplasia in female dogs - preliminary results. *J Small Animal Pract.* (2014) 55:504–8. doi: 10.1111/jsap.12256

40. Bristow P, Lipscomb V, Kummeling A, Packer R, Gerrits H, Homan K, et al. Health-related quality of life following surgical attenuation of congenital portosystemic shunts versus healthy controls. *J Small Animal Pract.* (2019) 60:21–6. doi: 10.1111/jsap.12927

41. Anglin E v., Lux CN, Sun X, Folk CA, Fazio C. Clinical characteristics of, prognostic factors for, and long-term outcome of dogs with multiple acquired portosystemic shunts: 72 cases (2000-2018). *J Am Vet Med Assoc.* (2022) 260:30–9. doi: 10.2460/javma.20.12.0703

42. Fukushima K, Kanemoto H, Ohno K, Takahashi M, Fujiwara R, Nishimura R, et al. Computed tomographic morphology and clinical features of extrahepatic portosystemic shunts in 172 dogs in Japan. *Vet J [Internet].* (2014) 199:376–81. doi: 10.1016/j.tvjl.2013.11.013

43. Sirli R, Sporea I, Tudora A, Deleanu A, Popescu A. Transient elastographic evaluation of subjects without known hepatic pathology: does age change the liver stiffness? *J Gastrointestinal Liver Dis.* (2009) 18:57–60.

44. Kim IH, Kisseleva T, Brenner DA. Aging and liver disease. *Curr Opin Gastroenterol.* (2015) 31:184–91. doi: 10.1097/MOG.0000000000000176

45. Tamura M, Ohta H, Nisa K, Osuga T, Sasaki N, Morishita K. et al. Evaluation of liver and spleen stiffness of healthy dogs by use of two-dimensional shear wave. *Elastography.* (2019) 80:378–84. doi: 10.2460/ajvr.80.4.378

46. Cha J, Kim J, Ko J, Kim J, Eom K. Effects of confounding factors on liver stiffness in two-dimensional shear wave elastography in beagle dogs. *Front Vet Sci.* (2022) 9:1–10. doi: 10.3389/fvets.2022.827599

47. Matiasovic M, Chanoit GPA, Meakin LB, Tivers MS. Outcomes of dogs treated for extrahepatic congenital portosystemic shunts with thin film banding or ameroid ring constrictor. *Vet Surgery.* (2020) 49:160–71. doi: 10.1111/vsu.13273

48. Kemp SD, Zimmerman KL, Panciera DL, Monroe WE, Leib MS. Histopathologic variation between liver lobes in dogs. *J Vet Intern Med.* (2015) 29:58–62. doi: 10.1111/jvim.12520

frontiers | Frontiers in Veterinary Science

TYPE Original Research
PUBLISHED 06 October 2022
DOI 10.3389/fvets.2022.935437

OPEN ACCESS

EDITED BY
Fazul Nabi,
Lasbela University of Agriculture, Water and Marine Sciences, Pakistan

REVIEWED BY
Hakan Salci,
Uludag University, Turkey
Sayed Haidar Abbas Raza,
Northwest A&F University, China

*CORRESPONDENCE
Ahmed S. Mandour
dr_mandour@vet.suez.edu.eg
Ryou Tanaka
ryo@vet.ne.jp

SPECIALTY SECTION
This article was submitted to Veterinary Imaging, a section of the journal Frontiers in Veterinary Science

RECEIVED 03 May 2022
ACCEPTED 22 August 2022
PUBLISHED 06 October 2022

CITATION
Mandour AS, Samir H, Yoshida T, Matsuura K, Hamabe L, Shimada K, Abdelmageed HA, Elbadawy M, Uemura A, Takahashi K, Watanabe G and Tanaka R (2022) Novel color M-mode echocardiography for non-invasive assessment of the intraventricular pressure in goats: Feasibility, repeatability, and the effect of sedation. *Front. Vet. Sci.* 9:935437. doi: 10.3389/fvets.2022.935437

Novel color M-mode echocardiography for non-invasive assessment of the intraventricular pressure in goats: Feasibility, repeatability, and the effect of sedation

Ahmed S. Mandour[1,2]*, Haney Samir[3], Tomohiko Yoshida[2], Katsuhiro Matsuura[2], Lina Hamabe[2], Kazumi Shimada[2], Hend A. Abdelmageed[4], Mohamed Elbadawy[5,6], Akiko Uemura[7], Ken Takahashi[8], Gen Watanabe[9] and Ryou Tanaka[2]*

[1]Department of Veterinary Medicine (Internal Medicine), Faculty of Veterinary Medicine, Suez Canal University, Ismailia, Egypt, [2]Laboratory of Veterinary Surgery, Department of Veterinary Medicine, Tokyo University of Agriculture and Technology, Tokyo, Japan, [3]Department of Theriogenology, Faculty of Veterinary Medicine, Cairo University, Giza, Egypt, [4]Ismailia Laboratory, Animal Health Research Institute, Agriculture Research Center, First District, Ismailia, Egypt, [5]Department of Pharmacology, Faculty of Veterinary Medicine, Benha University, Toukh, Egypt, [6]Laboratory of Pharmacology, Tokyo University of Agriculture and Technology, Tokyo, Japan, [7]Division of Veterinary Research, Department of Veterinary Surgery, Obihiro University of Agriculture and Veterinary Medicine, Obihiro, Japan, [8]Department of Pediatrics and Adolescent Medicine, Juntendo University Graduate School of Medicine, Tokyo, Japan, [9]Laboratory of Veterinary Physiology, Tokyo University of Agriculture and Technology, Tokyo, Japan

Background: The intraventricular pressure difference (IVPD) and intraventricular pressure gradients (IVPG), estimated from color M-mode echocardiography (CMME) of the transmitral flow, have been introduced as novel indices for the evaluation of heart functions. Until now, no study demonstrated the feasibility of the CMME approach to measure IVPD and IVPG in any farm animals. The aim of this study was to assess the feasibility and repeatability of CMME-derived IVPD and IVPG variables in goats and explore the effect of sedation on the measured variables.

Materials and methods: Sixteen male Shiba goats were included in this study and underwent conventional echocardiography. Eight goats were used in the repeatability of IVPD/IVPG variables. Another eight goats were used to evaluate the effect of sedation by xylazine on IVPD/IVPG measurements. CMME between the base and the apex of the left ventricle was carried out. The IVPD and IVPG were analyzed using in-house code software. The IVPD and IVPG were expressed as total, basal, mid-to-apical, mid, and apical segments. Data analysis including the imaging quality score (IQS), repeatability, variability, intraclass correlation coefficient (ICC), as well as the effect size of sedation on the measured variables was calculated.

Results: IVPD and IVPG variables from CMME were feasible in all goats. Low to moderate variability of IVPD and IVPG variables was observed (CV 95% <25%) except for the apical IVPD and apical IVPG. The IVPD/IVPG measurements

were repeatable without a significant effect of animal or time on the obtained measurements. The overall ICC was higher than 0.75 in all variables except for the apical segment. Xylazine administration reduced the total, basal, and mid parts of IVPD and IVPG with a large effect size (biserial ranked correlation; $rc > 0.8$).

Conclusion: We reported, for the first time, IVPD and IVPG measurements by CMME in goats. The assessment of IVPD and IVPG by CMME is feasible in goats which can be evaluated in further cardiovascular or pharmacological studies in this species.

KEYWORDS

color M-mode echocardiography, intraventricular pressure, heart function, sedation, feasibility, goats

Introduction

Echocardiography is the most common cardiac function evaluation technique utilized in the clinical setting in both human and animal species because of its feasibility and noninvasiveness. The establishment of new echocardiographic techniques for the early detection of cardiac dysfunction is helpful for early interference and better patient outcomes (1). Currently, the assessment of diastolic function is thought to be an important issue for in-depth understanding and early detection of cardiac disorders (2, 3). The diastolic function of the left ventricle (LV) is affected by the heart rate, preload, myocardial relaxation, recoil, and untwist, as well as ventricular compliance and myocardial stiffness. Therefore, the evaluation of diastolic function using traditional echocardiography is somewhat challenging and a combination of various echocardiographic techniques is necessary to avoid the overestimation of the measurements (2–4). Cardiac catheterization is the basic method to diagnose diastolic dysfunction through pressure–volume (PV) analysis and interpretation of the pressure inside the LV, but the technique is invasive and difficult to use in serial studies when longitudinal observation of the same individuals is needed (5).

Recently, the benefit of spatiotemporal maps of the LV hemodynamics has been applied in the context of diastolic function assessment. The velocity pattern along the transmitral scanline can be efficiently evaluated from the analysis of color M-mode echocardiographic (CMME) recordings after processing of images (6, 7) depending principally on Euler's equation (8). By this method, the LV is divided into basal, mid, and apical parts. This segmentation allows for studying the normal stratification of the intraventricular pressure which is known as the intraventricular pressure difference (IVPD, the pressure difference between LV segments), and the intraventricular pressure gradients (IVPG, obtained when the IVPD is divided by the LV length) (9, 10). In early diastole, the negative pressure gradients created by the LV are necessary to restore the LV shape and have an important role in diastolic function evaluation. This pressure gradient comes from the interaction between convective, inertial, and viscous forces in the LV (11).

The IVPD variables derived from CMME have been well-correlated with the same indices measured by the invasive catheterization method (12). Therefore, CMME-derived indices can non-invasively evaluate heart function. Studies revealed that the IVPD and IVPG as novel echocardiographic indices could reflect the diastolic function changes that could differentiate subtypes of heart failure (13). In addition, CMME variables showed more advantages regarding repeatability and continuous data acquisition for better interpretation of the segmental pressure (14–16). To date, the utility of IVPD and IVPG is still under research consideration as a promising tool for the detection of cardiac dysfunction in animal models. Experimental studies revealed that IVPG/IVPD segments could determine the changes in heart function in response to loading states (16), chemotherapy-induced cardiomyopathy (1), LV ventricular hypertrophy (17) in addition to uremic and diabetic cardiomyopathies in animal models (18–20). Other clinical studies were explored IVPD/IVPG in healthy dogs and cats (21, 22), as well as in dogs with patent ductus arteriosus (7, 21, 22).

The anatomical segmentation of the LV in small ruminants was previously reported (23); however, the physiology of intraventricular blood flows in ruminants is still unclear. The assessment of IVPD and IVPG in goats may be important since goats are considered useful candidates in cardiology research because of reasonable heart size and blood flow dynamics (24, 25). They are also regarded as an intermediate model between small animals, large animals, and humans. Besides, goats as a ruminant species can efficiently reflect the physiological, pathological, and pharmacological aspects when used as a model for ruminants (26–29). To date, the evaluation of IVPD/IVPG *via* CMME in any farm animals is lacking. Therefore, this study aimed to evaluate the IVPD and IVPG in goats using CMME. We will describe the technical procedures, and repeatability

of measurements, and evaluate the IVPD/IVPG changes after sedation. The results of this study would provide fundamental background on the usability of CMME for the assessment of IVPD/IVPG in goats to refine further cardiovascular research studies in goats or similar species.

Materials and methods

Animals

Sixteen male Shiba goats, 2 to 3 years old and weighing 30±5 kg, were enrolled in this study. Animals were kept in a special barn where they received alfalfa hay cubes as a basic diet, while water and mineral blocks were kept *ad libitum*. Detailed physical examination was performed, and the enrolled goats were considered healthy and free from any cardiac abnormalities based on the medical record, cardiac auscultation, routine electrocardiography, echocardiography, and standard hemato-biochemical profile. Two weeks before the study, neither medications nor vaccination was administered. Animals were acclimatized to the hospital to avoid stress-induced erroneous imaging. First, conventional and CMME were performed on eight goats for CMME repeatability. Second, we examined the effect of sedation on heart function through the evaluation of conventional echocardiography and CMME in another eight goats.

Conventional echocardiography

The echocardiography was carried out from the right and left sides, while goats were maintained on the lateral recumbency position. The right and left precordial areas were prepared with ultrasound gel after shaving. Animals were restrained on the echocardiographic table by two assistants and the forelegs were kept anteriorly. A ProSound Alpha 10 ultrasonography system (Hitachi Aloka Medical, Tokyo, Japan) supplied with a sector probe of 5 MHz was used. A lead II electrocardiogram was arranged and attached to the skin surface to measure the duration of echocardiographic variables. The average of the same echocardiographic variables was obtained from five different consecutive heart cycles by the same operator (A.S.M). The recorded measurements and image orientation were according to the veterinary echocardiography guidelines described by Boon (30).

First, each animal underwent conventional two-dimensional, M-mode, spectral Doppler, and tissue Doppler imaging (TDI) from the standard right and left parasternal views. The right transthoracic long axis four- and five-chamber views were observed. After that, the M-mode short-axis view at the papillary muscle level was viewed to trace the LV measurements which include LV end-diastolic and end-systolic diameters (LVIDd, LVIDs), diastolic and systolic interventricular septal thickness (IVSd, IVSs), diastolic and systolic LV free wall thickness (LVPWd, LVPWs), ejection fraction (EF), and fractional shortening (FS). Aortic root diameter (Ao) was measured at end-diastole and left atrial (LA) dimension was measured at end-systole from the right parasternal short-axis view at the level of heart base, and LA/Ao ratio was calculated. The right ventricular outflow tract (RVOT) was obtained through an assessment of the pulmonary artery using pulsed-wave Doppler echocardiography. The left transthoracic echocardiography was initiated from the left parasternal apical four-chamber view. Aortic blood flow was assessed from the left apical five-chamber view and the the left ventricular outflow tract (LVOT) and cardiac output (CO) were measured. Dual Doppler function of the mitral inflow and tissue Doppler imaging (TDI) was switched on for simultaneous assessment of mitral inflow and tissue Doppler velocity. Diastolic indices including early (E) and late (A) mitral inflow velocities, E/A ratio, and deceleration time were obtained by pulsed-wave Doppler echocardiography. The early and late diastolic myocardial velocities (e', a') were measured at both lateral and septal annuli using pulsed TDI. The ratio of early mitral inflow and early tissue velocity (E/e'), as well as annular tissue velocities (e'/a'), were calculated.

Color M-mode echocardiography

The apical four-chamber view was consistently optimized, which was used to capture CMME images for IVPD/IVPG calculation. First, the mitral inflow was visualized by two-dimensional echocardiography then the IVPG setting of the ultrasound machine was initiated (1). A sweep speed of 300 mm/s and a color baseline shift of −64 were maintained. The M-mode cursor was positioned along the streamline of the transmittal inflow and good quality imaging which showed perfect mitral inflow and mitral valve movement was saved for further analysis. The CMME and image analysis were performed by two observers, once by each observer at a one-day interval (A.S.M and T.Y). Images used in the analysis showed three consecutive heart cycles to ensure consistent mitral inflow and at least five images were saved for analysis by the software. Four images from consecutive heart cycles were selected from each animal to calculate IVPD and IVPG.

Assessment of the intraventricular pressure

After CMME image acquisition, the IVPD was calculated using in-house code written in MATLAB (The MathWorks, Natick, MA, USA). In each goat, by using the conventional echocardiography images and the displayed ECG, the time

from aortic opening to aortic closure (aortic flow images) and the time from Q wave on ECG to the start of mitral valve opening as well as the time from Q wave to peak mitral inflow (mitral inflow images) were obtained and manually inserted into the software during each photo processing by MATLAB (7). Automatic and manual correction of the resulting curves using specific software codes was applied when required to enhance the quality of analysis. The IVPD of each corresponding part was calculated from the following Euler equation.

$$(\partial P)/(\partial s) = -\rho((\partial v)/(\partial t) + v(\partial v)/(\partial\, s))$$

where ∂ is the change in element followed, P is the pressure, ρ is the constant blood density (1,060 kg/m^3), v is the velocity, s is the position along with the color M-mode line, and t is the time. v, s, and t are obtained by MATLAB which is further used to measure the relative pressures within the region of interest (14, 20, 21). The Euler equation assuming laminar blood flow across the mitral valve and the ultrasound scanline is related to the inflow blood streamline and the IVPD and IVPG can be estimated by solving the equation (12).

Previously, Takahashi and colleagues (31) measure the IVPD and IVPG in young children after the modification of the method used in adult humans (32, 33). Later, the same method was used in dogs and cats (21, 22). We used the same method for IVPD and IVPG calculation. This method assumes the dividing of the LV into three segments (basal, mid, and apical) on the long axis, and the respective IVPD and IVPG were calculated. The data of IVPD obtained from CMME were previously validated against direct measurements using a micromanometer (12). For IVPG calculation, the same image used to assess the IVPD was used to measure the LV length on the long axis, from the level of mitral annulus to the LV apex. The IVPG was calculated by dividing the IVPD by the left ventricular length (34). As previously described (20), the LV was trisected into apical, mid, and basal parts. Mid-to-apical segments of IVPD/IVPG were calculated by adding the mid and apical segments. Both total IVPD and IVPG and their corresponding pressure at the anatomical position in the LV were calculated and expressed as basal IVPD and IVPG; mid IVPD and IVPG; mid-to-apical IVPD and IVPG; and apical IVPD and IVPG (mmHg).

Sedation of goats

The echocardiography was performed before and after xylazine administration (0.05 mg/kg BW/IM, xylazine hydrochloride, Fujita-Pharm, Japan). Echocardiography was started 10 min after the observation of the signs of xylazine sedation (35). The duration of ultrasonography ranged between 20 and 30 min and no other medication was used during the experiment.

Statistical analysis

The normality of the data was tested by the Shapiro–Wilk test. The repeatability of IVPD and IVPG variables was assessed by the analysis of variance using two-way ANOVA. Two factors (goat and time), as well as the interaction between goat and time, were considered. The coefficient of variation for each parameter was measured between randomly selected four consecutive cardiac cycles to assess the intraobserver variability and between observers (scans A and B). All measurements from the four heart cycles were pooled from each goat regardless of the examination time to determine the within-goat variability using one-way ANOVA considering only animals as a factor. Moreover, the intraclass correlation coefficient (ICC) was calculated for each variable. The reproducibility of the technique is acceptable when the ICC is equal to or higher than 0.75. Lastly, all images captured from CMME and after CMME image processing by MATLAB were blindly evaluated by another two observers to obtain the imaging quality score (IQS; from zero to five) which was further analyzed using Fisher's exact test. According to the degree of variability, the obtained measurements were classified as low variability (CV$<$15%), moderate variable (CV% 15–25%), and high variable (CV%$>$ 25%) as previously described (16, 19). The confidence interval of the mean (95% CI) for each variable was calculated to determine the interval within the absolute value which had a 95% of probability being included. CMME variables were considered acceptable if both a non-significant result of the two-way ANOVA and low or moderate variability (95% CV $<$ 25%) were observed.

For comparison between normal and sedated goats, the Wilcoxon matched-pairs signed-rank test was calculated between measurements of baseline and after xylazine administration. Analyzed variables showing $p < 0.05$ were considered statistically significant. To quantify the strength of xylazine administration on echocardiographic data, the effect size estimator (Rank-Biserial Correlation, rc) for the Wilcoxon signed-rank test was calculated. Interpretation of the effect size was classified into small, medium, and large depending on cutoffs of 0.1, 0.4, and 0.6, respectively (36). Spearman's rank correlation (r_s) was expressed as a whole value between measured conventional variables and CMME-derived measurements before and after xylazine injection. The ICC was evaluated by SPSS software version 26.0 (Chicago, IL, USA). The effect size was calculated using a free JASP software version 0.13 (JASP Team, Amsterdam, Netherlands). Other Statistical analyses and graphs were conducted using GraphPad Prism 8.4 (GraphPad Software, San Diego, CA).

Results

Conventional echocardiography

The echocardiographic data are presented in Table 1. A significant reduction in HR after sedation compared with the baseline was observed ($P < 0.05$); meanwhile, EF and FS did not show a significant difference. LA/AR, LVOT, and RVOT were slightly increased after xylazine administration. The mitral inflow measurements, as well as the TDI indices, were reduced after xylazine administration. Early (E) and late (A) mitral inflow velocities and deceleration time were significantly reduced, while the E/A ratio did not change. Septal annular wall velocity (a′) and lateral annular velocity (e′) were significantly reduced post-xylazine administration ($P = 0.02, 0.03$, respectively). The ratio of septal e′/a′ was significantly decreased after xylazine administration, while the lateral e′/a′ was reduced but not significant. The LV length was increased after xylazine treatment compared with the baseline ($P = 0.008$). The magnitude of echocardiographic measurements difference between the baseline and post-xylazine administration was clinically relevant and associated with a large effect size on HR, LVOT, E velocity, A velocity, deceleration time, a′ septal, e′/a′ septal, E/e′ septal, and e′ lateral (rc = 0.944, 0.833, 0.778, 1.0, 0.944, 0.833, 0.833, 0.722, 0.611), respectively.

Color M-mode echocardiography for the assessment of IVPD and IVPG

Feasibility of imaging and repeatability of CMME indices

The CMME was feasible in all examined goats (100%) (Figure 1). The estimated time to get the entire streamline of the left ventricular inflow from the left atrium to the LV apex across the mitral valve, excluding the MATLAB analysis, was 13 ± 5 min. The IQS of CMME images was done by the qualitative examination of echo- and MATLAB-derived photos. Examination of goats by CMME was excellent (12 goats, 75%) or very good (4 goats, 25%). The LV free wall was not entirely visualized in these four goats; however, the mitral inflow was optimized for CMME. On MATLAB analysis, all goats showed an excellent presentation of the IVPD curves.

TABLE 1 Conventional echocardiographic measurements before and after xylazine administration in male goats.

Variables	Unit	Baseline	Post-xylazine	*P* value	Effect size (rc)
EDV	ml	38.5 (22.5–57)	40 (26–57.5)	0.72	0.167
ESV	ml	10.4 (2.5–14.5)	9.4 (5.1–14.5)	0.30	0.333
EF	%	76.8 (49.9–91.3)	74.2 (60.9–85)	0.71	0.056
FS	%	39.2 (31.9–55.7)	36.45 (27–46.6)	0.09	0.786
LA/Ao		1.55 (1.2–1.7)	1.6 (1.2–2.2)	0.05	0.751
RVOT	mm	15.0 (12.7–16.7)	15.75 (13.5–18.6)	0.17	0.556
LVOT	cm	14.1 (10.5–15.7)*	16.75 (15–17.9)	0.02	0.833
HR	pbm	112.5 (100–166)*	94.5 (73–103)	0.03	0.944
CO	l/min	2.5 (1.9–4.1)	2.35 (1.2–3.6)	0.42	0.222
E	cm/s	57.1 (37.7–69.7)*	44.65 (37–55.7)	0.048	0.778
A	cm/s	54.65 (43.8–57.5)*	39.3 (28.1–51.3)	0.013	1.0
E/A		1.01 (0.8–1.6)	1.25 (0.8–1.5)	0.15	0.667
DecT	ms	99.8 (62–162)*	160.6 (111.7–222)	0.02	0.944
e′ Sep	cm/s	8.52 (5.5–11.3)	8.55 (6.8–9.7)	0.97	0.056
a′ Sep	cm/s	10.1 (5.2–13.8) *	6.5 (4.7–10.5)	0.03	0.833
e′/a′ Sep		0.83 (0.5–1.8) *	1.4 (0.8–1.8)	0.04	0.833
E/e′ Sep		6.25 (5.1–10.4)	5.75 (4.1–6.5)	0.06	0.722
e′ Lat	cm/s	12.4 (9.3–15.2) *	10.6 (6.7–13)	0.03	0.611
a′ Lat	cm/s	10.57 (7–16.6)	9.22 (5.6–11.3)	0.23	0.722
e′/a′ Lat	cm/s	1.4 (0.6–2.1)	1.25 (0.71–1.97)	0.81	0.028
E/e′ Lat	cm/s	4.55 (2.8–7.0)	4.35 (3.4–5.9)	0.83	0.056
LVL	mm	36.10 (29.76–40.14)**	42.01 (40.1–47.2)	0.008	0.889

Values are presented as median (data range). The comparison was done between the obtained measurements in the same individuals at the baseline and 20 min post-xylazine injection (n = 8). *p < 0.05. rc, ranked biserial correlation. EDV, end-diastolic volume; ESV, end-systolic volume; EF, ejection fraction; FS, fractional shortening; LA/Ao, left atrial diameter to aortic diameter ratio; RVOT, right ventricular outflow tract; LVOT, left ventricular outflow tract; HR, heart rate; CO, cardiac output; E, the early diastolic velocity of mitral inflow; A, late diastolic velocity of mitral inflow; E/A early to late mitral inflow ratio; DecT, deceleration time; e′ and a′, annular tissue velocity, Sep, septal, Lat, lateral. LVL, left ventricular length.

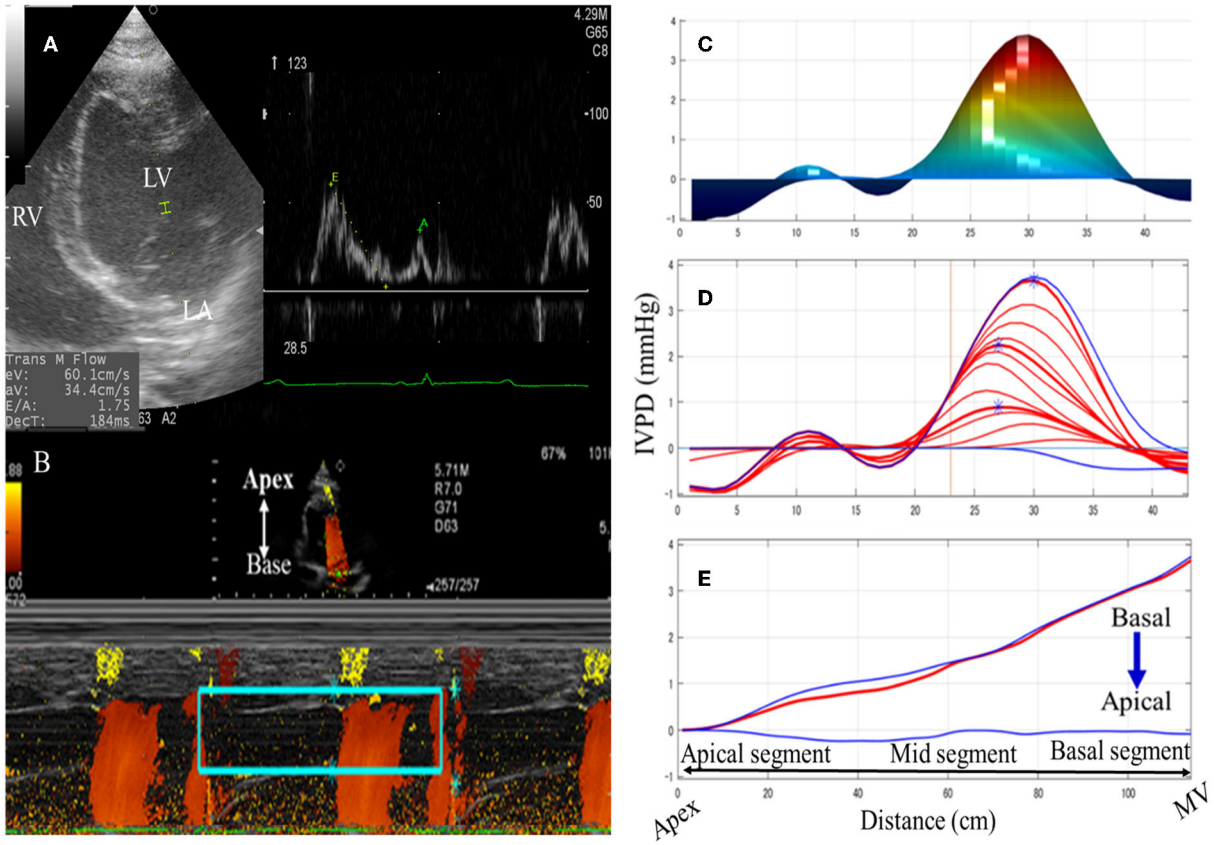

FIGURE 1
Schematic illustration of color M-mode echocardiographic (CMME) in goats. The left apical four-chamber view was optimized to evaluate the mitral inflow **(A)**. After that, the proper machine setting was started to initiate CMME. IVPG tracing was switched on to trace the entire left ventricular inflow tract from the LV base to the apex. Captured CMME images **(B)** were used for IVPD/IVPG measurements of the area of interest (mitral inflow, rectangular green box) using MATLAB software based on Euler's equation. Measurements of the time from q wave to the start of mitral inflow, from q wave to the peak mitral inflow, and from q wave to the end of aortic flow were separately added to the software's dialog box using ECG displayed on the ultrasound machine. Manual correction of the analysis was limited to noisy photos so that the measurement area matches the IVPD/IVPG position by the software. Temporal and spatial profiles of IVPD **(C)**, and IVPD time distribution **(D,E)** were automatically calculated. MV, mitral valve; LV, left ventricle; LA, left atrium.

Overall, the average CMME imaging and software analysis scores obtained by the two observers were 4.2 ± 0.5 and 3.9 ± 0.7, respectively.

Table 2 summarizes the repeatability of CMME indices. The intraobserver variability of all CMME data displayed low to moderate variability considering different heart cycles (95% CV: 11.96–23.9) except for apical IVPD and apical IVPG which showed high variability (CV = 31.81, 29.5), respectively. Between observers, the data revealed low to moderate variability (95% CV range: 4.11–23.67). By two-way ANOVA, the goat factor, the time factor, as well as the goat X time interaction showed no significant effect on the obtained IVPD and IVPG measurements (Figures 2, 3). Within goats, there were no significant differences in all measurements. The average ICC for the obtained data was acceptable in all measurements (ICC > 0.75) except for apical IVPD and apical IVPG (ICC = 0.601, 0.698), respectively.

Effect of sedation on IVPG and IVPD analysis

The time required to perform CMME, excluding the MATLAB analysis, was shorter after sedation (range: 8–14 min) compared with that at the baseline (range: 10–17 min). Regarding the IVPD (Figure 4), the data revealed a significant reduction in total IVPD (median: 3.28 vs. 2.29; $P = 0.005$), basal IVPD (median: 1.21 vs. 0.87; $P = 0.023$), mid-to-apical IVPD (median: 1.86 vs. 1.47; $P = 0.008$), and mid-IVPD (median: 1.29 vs. 0.98; $P = 0.008$) after xylazine administration compared with their values at the baseline. In the same way, significant reduction in total IVPG (median: 1.17 vs. 0.81; $P = 0.016$), basal IVPG (median: 0.45 vs. 0.33; $P = 0.015$), and mid-IVPG (median: 0.54 vs. 0.33; $P = 0.008$) was also observed post-xylazine administration (Figure 5). Meanwhile, apical IVPD, mid-to-apical IVPG, and apical IVPG showed no significant changes ($P > 0.05$). The difference between baseline and post-xylazine measurements was clinically relevant and associated

10.3389/fvets.2022.935437

TABLE 2 Repeatability of color M-mode echocardiographic measurements in adult healthy male Shiba goats.

Variables	Mean±SD	95% CI of mean (L-U)	95 % CV		ICC
			Between cycles	Between time	
Total IVPD	2.02 ± 0.41	1.55–2.49	20.24	23.04	0.91
Basal IVPD	0.67 ± 0.14	0.55–0.80	20.54	11.63	0.80
Mid-to-apical IVPD	1.14 ± 0.24	0.91–1.36	21.29	13.66	0.94
Mid IVPD	0.82 ± 0.17	0.66–0.97	20.52	14.11	0.94
Apical IVPD	0.32 ± 0.10	0.24–0.41	31.81	17.27	0.70
Total IVPG	0.78 ± 0.13	0.67–0.88	16.22	4.72	0.82
Basal IVPG	0.29 ± 0.07	0.24–0.35	23.90	12.22	0.81
Mid-to-apical IVPG	0.49 ± 0.06	0.44–0.53	11.69	6.81	0.77
Mid IVPG	0.36 ± 0.06	0.30–0.41	17.95	10.99	0.70
Apical IVPG	0.15 ± 0.04	0.11–0.18	29.52	19.66	0.69

Color M-mode echocardiography-derived variables in goats (n = 8). CV, coefficient of variation; CI, confidence interval; ICC, intraclass correlation coefficient. All variables are measured by mmHg.

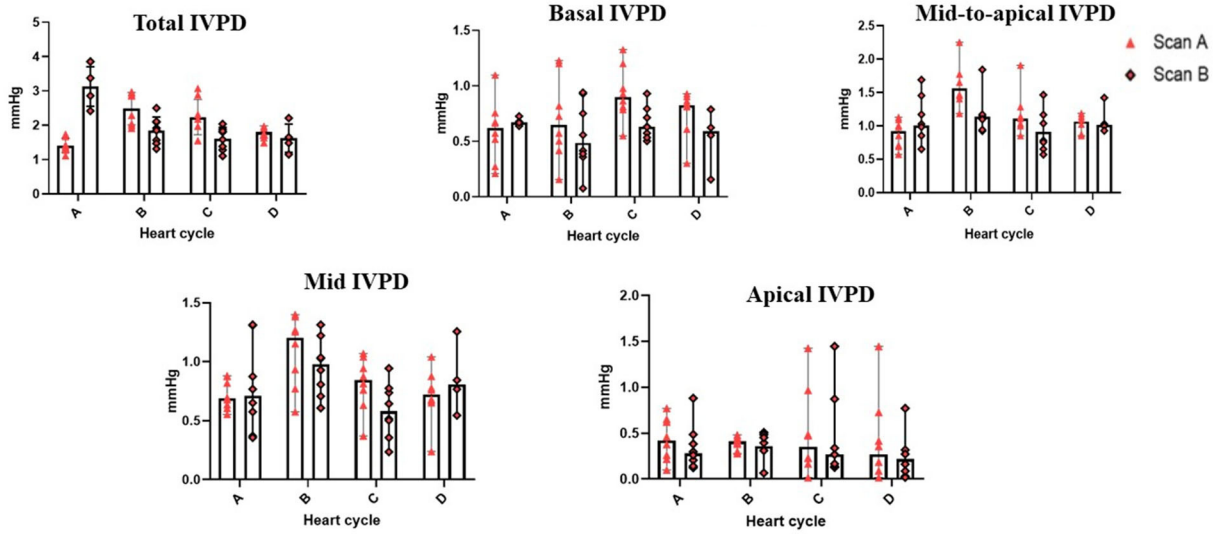

FIGURE 2
Variability of CMME-derived intraventricular pressure difference (IVPD). Variability was calculated within goats between heart cycles (four heart cycles were selected) and between time by two observers (scans A and B); *n* = 8.

with a large effect size on total IVPD, basal IVPD, mid-to-apical IVPD, and mid-IVPD (rc: 1.0, 0.889, 1.0, 1.0, respectively) as well as total IVPG, basal IVPG, and mid IVPG (rc: 0.94, 1.0, 1.0, respectively).

Correlation between IVPD/IVPG and conventional echocardiographic variables

Table 3 shows Spearman's correlation between IVPD/IVPG indices and conventional echocardiographic measurements. Total IVPD was positively correlated with HR ($r_s = 0.615$, $P = 0.013$) and negatively correlated with LV length ($r_s = -0.506$, $P = 0.046$). Mid IVPD found a significant positive correlation with lateral annular velocity a′ ($r_s = 0.567$, $P = 0.022$); meanwhile, basal IVPD was positively correlated with lateral annular e′ ($r_s = 0.539$, $P = 0.031$). The apical IVPD showed a positive correlation with HR, mitral A velocity, and septal a′ velocity ($r_s = 0.521$, 0.724, 0.512; $P = 0.041$, 0.002, 0.043, respectively) and negative correlation with E/A ratio and deceleration time ($r_s = -0.601$, −0.509, $P = 0.014$, 0.044, respectively). Moreover, total IVPG showed a positive correlation with HR and mitral A velocity ($r_s = 0.675$,

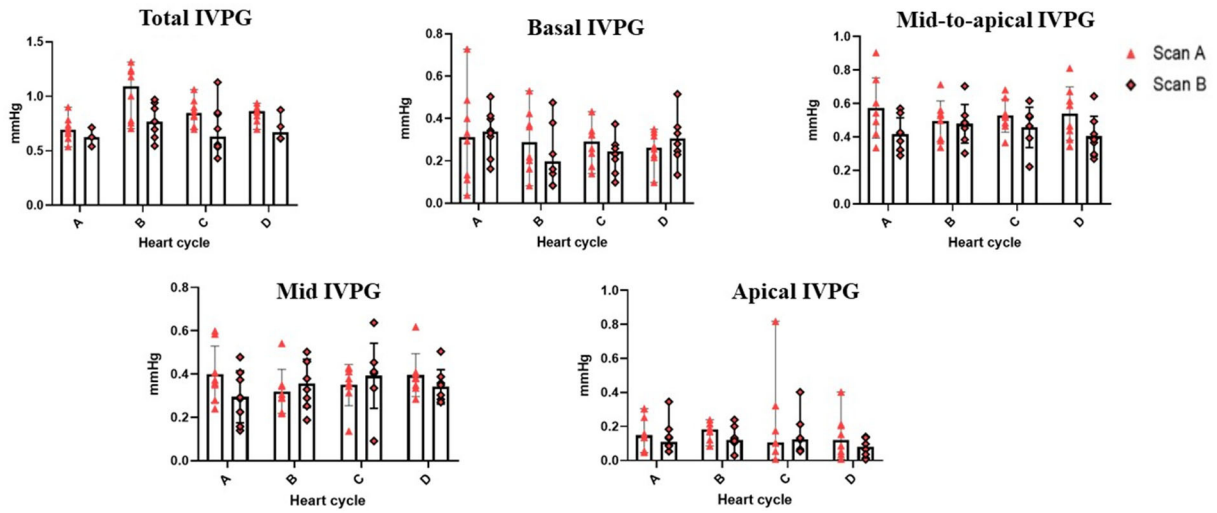

FIGURE 3
Variability of CMME-derived intraventricular pressure gradients (IVPG). Variability was calculated within goats between heart cycles and between time by two observers (scans A and B); $n = 8$.

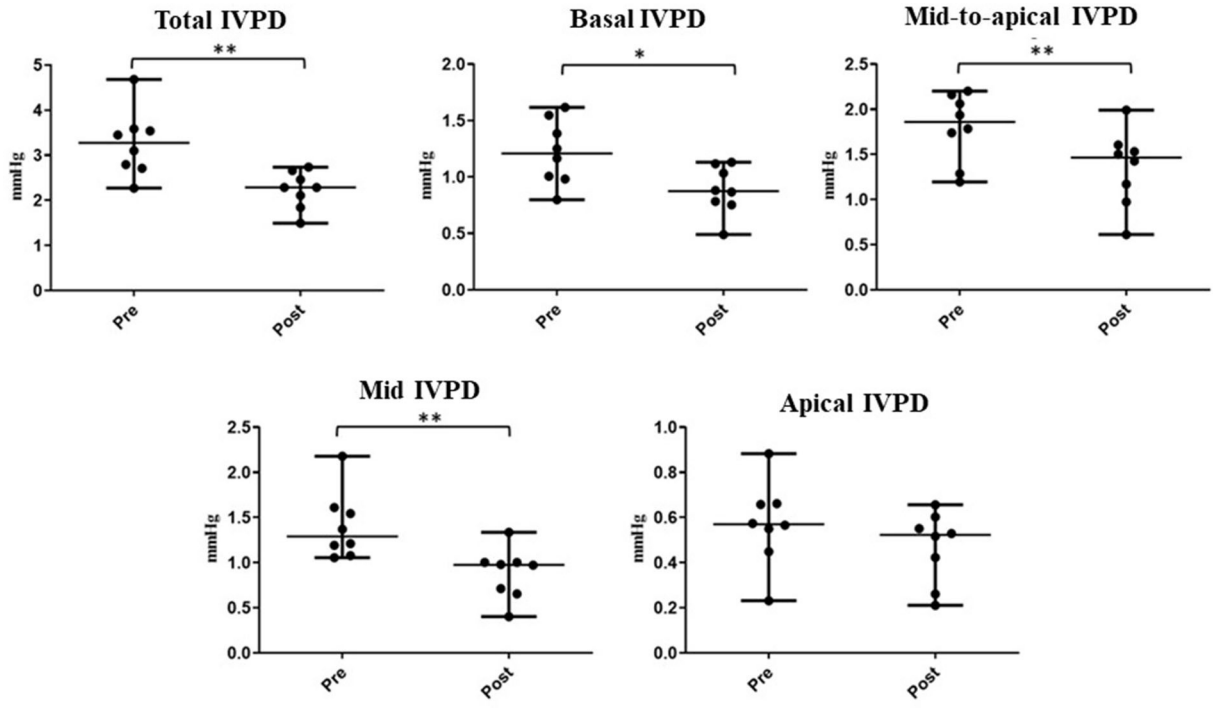

FIGURE 4
Changes in IVPD indices measured by color M-mode echocardiography before and after sedation with xylazine in goats ($n = 8$). Plots showing the median (central horizontal line) and range (upper and lower lines). *$p < 0.05$, **$p < 0.01$.

0.671; $P = 0.005$, 0.004, respectively) and significant adverse correlation with E/A ratio and deceleration time ($r_s = -0.736$, -0.600; $P = 0.001$, 0.014, respectively). Mid-to-apical IVPG showed a significant positive correlation with annular lateral e′ ($r_s = 0.514$, $P = 0.042$). Moreover, the relationship between total IVPD and A velocity; basal IVPD and HR; apical IVPD

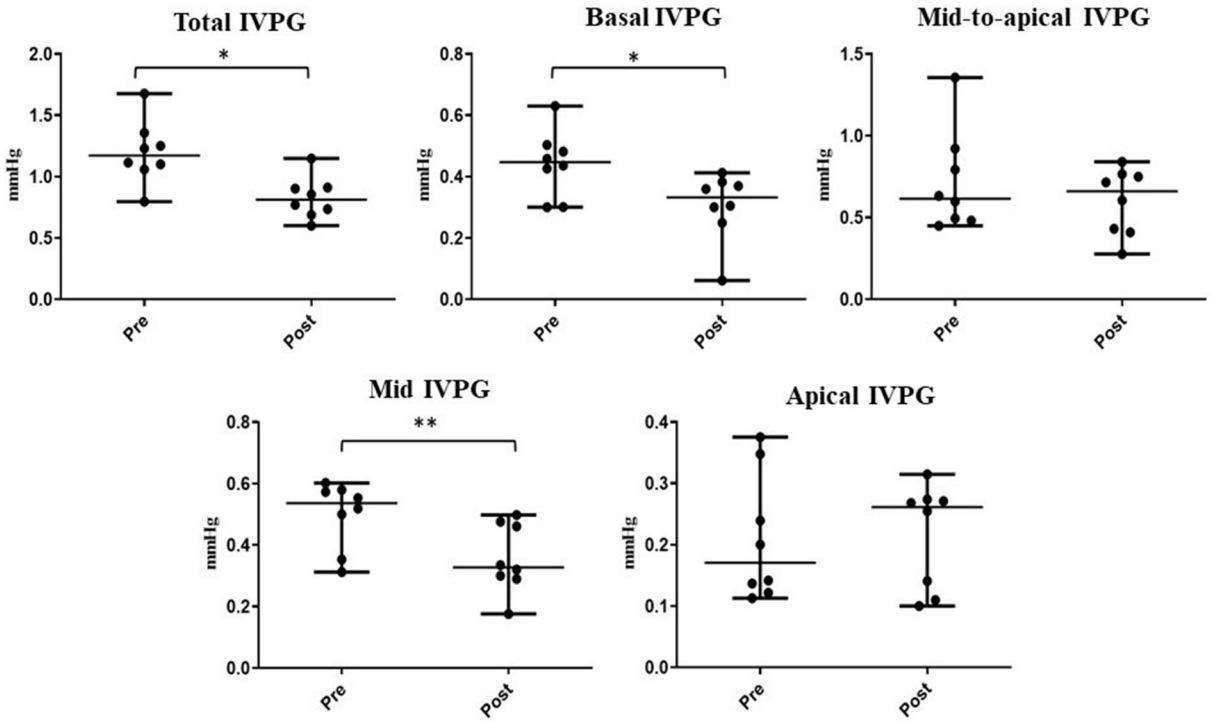

FIGURE 5
Changes in IVPG indices before and after sedation with xylazine in goats ($n = 8$). Plots showing the median (central horizontal line) and range (upper and lower lines). *$p < 0.05$, **$p < 0.01$.

and LV length; total IVPG and LV length; mid IVPG and HR, mitral A velocity and E/A; as well as the relationship among mid-to-apical IVPG and HR, mitral A velocity, and E/A ratio were significant ($P < 0.10$).

Discussion

The establishment of new technology regarding cardiac function evaluation in ruminants is a point of interest for both clinical and research purposes (24, 37, 38). In this study, we examined the use of the novel CMME-specific variables (IVPD and IVPG) in goats. Furthermore, we reported the normal values of IVPG and IVPD indices and explored the effect of sedation by xylazine on the obtained measurements.

Visualization of different cardiac windows from standard views was optimized in all goats. In the current study, systolic function indices (FS% and EF%) showed no significant changes between pre- and post-xylazine administration although the heart function was significantly reduced (39). Pulsed TDI was used to evaluate the regional wall velocity at both sides of mitral valve attachment (40, 41). TDI at the septal and posterior walls yield two negative diastolic velocities (e′, a′) which are representative of myocardial relaxation and atrial contraction, respectively (42). For the interpretation of the diastolic cardiac function, the annular velocity e′ wave is considered an indicator for relaxation and elastic recoil of the LV; meanwhile, the E/e′ ratio is crucial for the diagnosis of congestion (41).

In our study, diastolic function measurements were not homogenous based on conventional echocardiography examination. In this regard, the E/A ratio did not significantly change after xylazine administration, and the tissue Doppler velocities showed variations at the septal and free walls of the LV walls. Thus, septal a′ velocity, lateral e′ velocity, and septal E/e′ were significantly reduced after sedation. In contrast, the velocity of septal e′, lateral a′, and E/e′ of the free wall did not significantly change. The assessment of mitral inflow and myocardial tissue velocity is frequently used to evaluate diastolic function. Nevertheless, accurate diagnosis of diastolic dysfunction is a controversial issue that requires a combination of different diagnostic approaches (2, 4).

Recent studies revealed that CMME-derived IVPD/IVPG is significantly related to the *Tau* (a reliable index of left ventricular diastolic function) (43), and hence could non-invasively evaluate the diastolic function (1, 12). To our knowledge, the current study is the first to investigate the validity of IVPD and IVPG in goats. The left parasternal long axis four-chamber view was optimized for adequate Doppler alignment using CMME as

TABLE 3 Correlation between CMME indices and conventional echocardiographic measurements in goats.

Variables	IVPD										IVPG									
	Total		Basal		Mid-to-apical		Mid		Apical		Total		Basal		Mid-to-apical		Mid		Apical	
	r_S	*P*	r_S	*P*	r_S	*P*	r_S	*P*	r_S	*P*	r_S	*P*	r_S	*P*	r_S	*P*	rs	*P*	r_S	*P*
HR	0.615*	0.013	0.472	0.066	0.266	0.316	0.135	0.615	0.521*	0.041	0.675*	0.005	−0.009	0.976	0.492	0.055	0.492	0.055	−0.078	0.773
EDV	−0.115	0.672	−0.250	0.349	−0.103	0.705	0.068	0.805	−0.129	0.633	−0.169	0.528	0.238	0.373	−0.150	0.579	−0.150	0.579	0.121	0.656
E	0.226	0.399	0.256	0.339	0.141	0.602	−0.147	0.587	0.229	0.393	0.011	0.700	−0.371	0.158	0.100	0.713	0.100	0.713	−0.409	0.116
A	0.453	0.078	0.297	0.264	0.176	0.513	−0.038	0.888	0.724*	0.002	0.671*	0.004	−0.124	0.649	0.432	0.094	0.432	0.094	−0.332	0.209
E/A	−0.219	0.416	−0.018	0.947	0.078	0.774	0.138	0.611	−0.601*	0.014	−0.736*	0.001	−0.133	0.623	−0.456	0.076	−0.456	0.076	−0.012	0.965
DecT	−0.326	0.217	−0.076	0.778	0.088	0.745	0.168	0.535	−0.509*	0.044	−0.600*	0.014	0.226	0.399	−0.221	0.412	−0.221	0.412	0.306	0.249
e′ Sep	−0.165	0.542	−0.330	0.212	−0.159	0.556	−0.156	0.564	0.180	0.506	−0.043	0.873	−0.161	0.553	0.156	0.564	0.156	0.564	−0.082	0.761
a′ Sep	0.168	0.535	−0.149	0.583	0.202	0.454	0.162	0.549	0.512*	0.043	0.406	0.119	0.090	0.741	0.241	0.368	0.241	0.368	−0.091	0.737
e′/a′ Sep	−0.283	0.289	−0.034	0.901	−0.287	0.281	−0.265	0.322	−0.396	0.128	−0.412	0.113	−0.176	0.514	−0.172	0.525	−0.172	0.525	0.016	0.952
E/e′ Sep	0.279	0.296	0.404	0.121	0.311	0.241	0.202	0.453	0.050	0.854	−0.163	0.546	−0.158	0.560	−0.156	0.563	−0.156	0.563	−0.307	0.248
e′ Lat	0.361	0.170	0.539*	0.031	0.277	0.300	0.246	0.359	0.196	0.468	0.395	0.130	0.411	0.114	0.514*	0.042	0.514	0.042	0.212	0.431
a′ Lat	0.373	0.155	0.090	0.741	0.409	0.115	0.567*	0.022	0.343	0.193	0.064	0.814	0.274	0.305	0.031	0.910	0.031	0.910	0.243	0.365
e′/a′ Lat	0.027	0.922	0.251	0.349	−0.093	0.732	−0.181	0.502	−0.178	0.509	0.161	0.552	0.111	0.684	0.318	0.230	0.318	0.230	0.085	0.753
E/e′ Lat	−0.150	0.579	−0.296	0.266	−0.050	0.854	−0.121	0.656	−0.004	0.987	−0.362	0.168	−0.362	0.168	−0.281	0.292	−0.281	0.292	−0.322	0.223
LVL	−0.506*	0.046	−0.224	0.405	−0.226	0.399	−0.141	0.602	−0.438	0.090	−0.452	0.079	0.000	0.901	−0.265	0.322	−0.265	0.322	0.012	0.966

Spearman's correlation (r_s) between IVPD and IVPG indices and conventional echocardiographic measurements in goats (n = 8). *$p < 0.05$.

10.3389/fvets.2022.935437

previously described in other animals (8, 21). The imaging quality and software analysis scores for CMME obtained in the current study were acceptable. All CMME variables, except apical IVPD and apical IVPG, showed acceptable repeatability with low to moderate variability. These results are quite reasonable particularly when we consider that these data were calculated before sedation. The higher CV of apical indices may be related to variation in the color resolution of the apical part of CMME images compared with the basal and mid parts (7). Therefore, CMME can be used for further evaluation of heart function in goats and the apical variables should be considered with caution.

The present study also intended to explore the agreement of the IVPG/IVPD findings with other studies conducted in dogs, the largest animal species in which CMME was previously studied. As previously described, MATLAB-specific software (MathWorks) classifies the IVPD/IVPG into basal, mid-to-apical, mid, and apical parts (1, 8, 21). In the current study, the reported IVPD and IVPG ranges were comparable to recently published studies on anesthetized Beagle dogs under various loading conditions (8), during chemotherapy treatment (1), and non-anesthetized client-owned dogs (21). In the later study ($n = 58$, BW 1.3–42.3 kg), this classification yielded 0.92 ± 2.86, 0.39 ± 1.13, 0.47 ± 1.41 and 0.25 ± 0.33 for total, basal, mid, and apical IVPD, respectively, and 0.30 ± 0.94, 0.12 ± 0.36, 0.14 ± 0.44 and 0.11 ± 0.09 for total, basal, mid and apical IVPG parts (21). Another study in Beagle dogs yielded 0.12 ± 0.86, 0.09 ± 0.35, 0.11 ± 0.51, 0.08 ± 0.48 and 0.03 ± 0.03 for total, basal, mid-to-apical, mid, and apical IVPG parts (1). Our study elected not to focus only on normal goats but to investigate the CMME in goats after an alteration of heart function. This was different than the other published studies on IVPG in dogs since the net effect of sedation or anesthesia on CMME indices in dogs has not been reported. Despite the difference in species and body weight between our study and other canine studies (1, 8), there was an acceptable similarity in the obtained CMME measurements in dogs and goats. However, the study sample in our study had subjectively fewer goats and was treated with xylazine when compared to case numbers and conditions in the previous studies. Overall, this indicates that the CMME-derived IVPD/IVPG is comparatively acceptable in goats as another species to study this novel echocardiographic approach. Moreover, our findings suggested that the CMME technique may be possible to use in other farm animals for further physiological and pharmacological studies.

In ruminants, xylazine is used for pre-anesthesia and induction. The safety margin of xylazine is comparatively narrow which could induce rapid collapse in animals if the dose is not properly adjusted (44). In the current study, as in previous reports, xylazine administration reduced HR and Doppler measurements of the pulmonary artery, and aorta as well as the mitral inflow (E and A waves) from the baseline. These reductions in the pressure, heart rate and cardiac contraction, and elevation in afterload are caused by its chronotropic properties (39, 45, 46).

In this study, xylazine was selected as a simple medicine to induce alteration in the heart function for subsequent evaluation of the response of IVPG/IVPD to the hemodynamic changes in goats. In this regard, xylazine administration resulted in significantly reduced IVPD and IVPG indices; meanwhile, the E/A ratio was not significantly changed. This indicates the potential importance of IVPG and IVPD to detect preload changes as confirmed by a significant reduction in E and A waves of the mitral inflow. The importance of IVPG and IVPD as indicators of diastolic function has been demonstrated (16). It has been evidenced that each IVPD or IVPG part could reflect a specific function during heart function evaluation. For example, basal IVPD is positively related to the increased volume load in case of congestion (16, 33), advanced diastolic dysfunction reduce mid IVPG (33, 42), left ventricular active relaxation correlated well with mid-to-apical IVPG, and apical IVPG is related to the active power of blood withdrawal from the left atrium by LV (11, 15). In our study, changes in IVPD and IVPG indices could be ascribed to reduced contractility and blood flow and increased LV length after xylazine injection.

In the current study, xylazine administration exerted a profound effect on atrial contractility as observed by reduced late mitral velocity (A, rc = 1.0) and a annular tissue velocity values. However, the E/e' ratio (left atrial pressure indicator), which was measured at both septal and lateral mitral annulus (47), was not significantly changed. Previous studies reported that the evaluation of left atrial pressure using E/e' has certain limitations and basal IVPG could be more suitable for the monitoring of the preload in response to medication. In this regard, a previous study (16) reported inconsistent results of TDI in loading changes and found only that septum E/e' was significantly increased after colloidal solution infusion in contrast to the IVPG which was significantly responding to the infusion. In the present work, apical IVPD and total IVPG were negatively and significantly correlated with late mitral inflow (A) wave velocity, E/A ratio, and deceleration time of the mitral inflow. The presence of significant correlation between CMME indices and conventional parameters might enforce the usefulness of CMME-derived IVPG/IVPD to evaluate heart function especially diastolic one away from invasive procedures. However, proper interpretation of these relationships should be cautiously considered because of small sample size and short-term evaluation.

In this study, the LV length was slightly increased after xylazine administration. However, only total IVPD was negatively correlated with the LV length. This was in agreement with a previous study in sheep which showed a linear relationship between the decrease in intraventricular pressure and LV length (48). In contrast, the study by Popović et al. (34) revealed that LV length was positively correlated with IVPD but not associated with IVPG. In the latter study, the authors

investigated different species with different heart sizes. However, upon the examination of their results, we found that the goat was almost close to the dog and human values that almost show a negative relationship of LV length with IVPG values in contrast to smaller heart size species. IVPD was also reported to be related to the LV length in dogs (21), but this study used many dogs in which small breed dogs were predominant. IVPG is calculated from IVPD to exclude the effect of the LV length. Although both IVPD and IVPG approximately showed a similar trend of results before and after xylazine medication, IVPG will be more reliable when there is a great variation in LV length, or when the LV length significantly changes due to medication as in the current study. However, a combination between IVPD and IVPG may be better to explore the actual pressure difference and the pressure slope in the LV. Our results revealed positively correlated HR with total IVPD and apical IVPD, as well as total IVPG. During restraint of animals, the HR can be increased, and subsequently, the pressure increases (49), and the reverse is true after medication with xylazine.

Cardiac tissue damages in ruminants due to various infectious diseases and nutritional disorders are frequently occurring without expressing clear clinical signs in the early stage but they rather can be detected in the late stages of cardiac diseases or during necropsy (50). IVPD and IVPG assessments are useful in the early detection of cardiac dysfunction in animal models, such as dogs and rats. In farm animals too, especially goats, IVPD and IVPG could deepen the understanding of the pathophysiological and pharmacological aspects of intraventricular flow. Also, clinical trials are warranted to evaluate whether this technique helps detect cardiac pathologies earlier to decide whether to treat or cull those animals.

Limitations

The present study includes only adult male goats with small sample size. The number of goats in Japan has a limited distribution since goats are infrequently accepted as food for humans and are mostly used for research and educational purposes by elementary students (51, 52). Male goats were selected to avoid the biased results from female reproductive cycles that should be addressed in another study. Simultaneous assessment of IVPD/IVPG using invasive catheterization and CMME was not provided.

Conclusion

To the best of the author's knowledge, this is the first study of the quantitative measurement of the IVPD and IVPG in goats using a novel CMME technique. The CMME-derived IVPD and IVPG are valid methods in awake and sedated goats. A translational lens of this novel study, in conjunction with conventional echocardiographic methods, might deepen understanding of the LV hemodynamics in goats as well as other farm animals for further experimental and clinical studies.

Data availability statement

The raw data supporting the conclusions of this article will be made available by the authors, without undue reservation.

Ethics statement

The animal study was reviewed and approved by the Ethical Committee of the Animal Medical Center, Tokyo University of Agriculture and Technology, and Technology (Ethical No: 30–78).

Author contributions

ASM and RT: experiment design. ASM, HS, TY, and KM: echocardiography. ASM, HS, TY, and ME: investigation. ASM, TY, HS, KS, HAA, KT, KM, LH, and AU: software and data analysis. ASM, LH, and KS: data collection. ASM and HAA: writing and drafting. HS, ME, LH, KT, and GW: critical editing. GW and RT: supervision. All authors reviewed and edited the final version. All authors contributed to the article and approved the submitted version.

Acknowledgments

We would like to extend our best regards to the Mission Sector, Ministry of High Education—Egypt, for their support of the current study.

Conflict of interest

The authors declare that the research was conducted in the absence of any commercial or financial relationships that could be construed as a potential conflict of interest.

Publisher's note

References

1. Matsuura K, Shiraishi K, Mandour AS, Sato K, Shimada K, Goya S, et al. The utility of intraventricular pressure gradient for early detection of chemotherapy-induced subclinical cardiac dysfunction in dogs. *Animals (Basel).* (2021) 11:1122. doi: 10.3390/ani11041122

2. Nagueh SF. Left ventricular diastolic function. *JACC Cardiovasc Imaging.* (2020) 13:228–44. doi: 10.1016/j.jcmg.2018.10.038

3. Nagueh SF, Smiseth OA, Appleton CP, Byrd BF 3rd, Dokainish H, Edvardsen T, et al. Recommendations for the Evaluation of Left Ventricular Diastolic Function by Echocardiography: An Update from the American Society of Echocardiography and the European Association of Cardiovascular Imaging. *J Am Soc Echocardiogr.* (2016) 29:277–314. doi: 10.1016/j.echo.2016.01.011

4. Flachskampf FA, Biering-Sørensen T, Solomon SD, Duvernoy O, Bjerner T, Smiseth OA. Cardiac imaging to evaluate left ventricular diastolic function. *JACC: Cardiovasc Imaging.* (2015) 8:1071–93. doi: 10.1016/j.jcmg.2015.07.004

5. Bastos MB, Burkhoff D, Maly J, Daemen J, den Uil CA, Ameloot K, et al. Invasive left ventricle pressure–volume analysis: overview and practical clinical implications. *Eur Heart J.* (2019) 41:1286–97. doi: 10.1093/eurheartj/ehz552

6. Nakamura M, Wada S, Mikami T, Kitabatake A, Karino T. Relationship between Intraventricular Flow Patterns and the Shapes of the Aliasing Area in Color M-mode Doppler Echocardiograms. *JSME Int J Ser.* (2001) 44:1013–20. doi: 10.1299/jsmec.44.1013

7. Hirose M, Mandour AS, Goya S, Hamabe L, Matsuura K, Yoshida T, et al. Color M-mode echocardiography for non-invasive assessment of the intraventricular pressure in dogs before and after ductus arteriosus occlusion: a retrospective study. *Front Vet Sci.* (2022) 9:908829. doi: 10.3389/fvets.2022.908829

8. Matsuura K, Shiraishi K, Sato K, Shimada K, Goya S, Uemura A, et al. Left ventricular vortex and intraventricular pressure difference in dogs under various loading conditions. *Am J Physiol Heart Circ Physiol.* (2019) 316:H882–8. doi: 10.1152/ajpheart.00686.2018

9. Cerqueira MD, Weissman NJ, Dilsizian V, Jacobs AK, Kaul S, Laskey WK, et al. Standardized Myocardial Segmentation and Nomenclature for Tomographic Imaging of the Heart. *Circulation.* (2002) 105:539–42. doi: 10.1161/hc0402.102975

10. Guerra M, Amorim MJ, Mota JC, Vouga L, Leite-Moreira A. Rationale, design and methodology for Intraventricular Pressure Gradients Study: a novel approach for ventricular filling assessment in normal and falling hearts. *J Cardiothorac Surg.* (2011) 6:67. doi: 10.1186/1749-8090-6-67

11. Notomi Y, Popovic ZB, Yamada H, Wallick DW, Martin MG, Oryszak SJ, et al. Ventricular untwisting: a temporal link between left ventricular relaxation and suction. *Am J Physiol Heart Circ Physiol.* (2008) 294:H505–13. doi: 10.1152/ajpheart.00975.2007

12. Yotti R, Bermejo J, Antoranz JC, Desco MM, Cortina C, Rojo-Alvarez JL, et al. A noninvasive method for assessing impaired diastolic suction in patients with dilated cardiomyopathy. *Circulation.* (2005) 112:2921–9. doi: 10.1161/CIRCULATIONAHA.105.561340

13. Londono-Hoyos F, Segers P, Hashmath Z, Oldland G, Koppula MR, Javaid K, et al. Non-invasive intraventricular pressure differences estimated with cardiac MRI in subjects without heart failure and with heart failure with reduced and preserved ejection fraction. *Open Heart.* (2019) 6:e001088. doi: 10.1136/openhrt-2019-001088

14. Greenberg NL, Vandervoort PM, Firstenberg MS, Garcia MJ, Thomas JD. Estimation of diastolic intraventricular pressure gradients by Doppler M-mode echocardiography. *Am J Physiol Heart Circ Physiol.* (2001) 280:H2507–15. doi: 10.1152/ajpheart.2001.280.6.H2507

15. Shigemitsu S, Takahashi K, Yazaki K, Kobayashi M, Yamada M, Akimoto K, et al. New insight into the intraventricular pressure gradient as a sensitive indicator of diastolic cardiac dysfunction in patients with childhood cancer after anthracycline therapy. *Heart Vessels.* (2019) 34:992–1001. doi: 10.1007/s00380-018-01332-7

16. Yairo A, Mandour AS, Matsuura K, Yoshida T, Ma D, Kitpipatkun P, et al. Effect of loading changes on the intraventricular pressure measured by color m-mode echocardiography in rats. *Diagnostics.* (2021) 11:1403. doi: 10.3390/diagnostics11081403

17. Ma D, Mandour AS, Yoshida T, Matsuura K, Shimada K, Kitpipatkun P, et al. Intraventricular pressure gradients change during the development of left ventricular hypertrophy: Effect of salvianolic acid B and beta-blocker. *Ultrasound.* (2021) 29:229–40. doi: 10.1177/1742271X20987584

18. Ma D, Mandour AS, Elfadadny A, Hendawy H, Yoshida T, El-Husseiny HM, et al. Changes in cardiac function during the development of uremic cardiomyopathy and the effect of salvianolic acid B administration in a rat model. *Front Vet Sci.* (2022) 9:905759. doi: 10.3389/fvets.2022.905759

19. Kitpipatkun P, Matsuura K, Shimada K, Uemura A, Goya S, Yoshida T, et al. Key factors of diastolic dysfunction and abnormal left ventricular relaxation in diabetic rats. *J Med Ultrason (2001).* (2020) 47:347–56. doi: 10.1007/s10396-020-01021-x

20. Kobayashi M, Takahashi K, Yamada M, Yazaki K, Matsui K, Tanaka N, et al. Assessment of early diastolic intraventricular pressure gradient in the left ventricle among patients with repaired tetralogy of Fallot. *Heart Vessels.* (2017) 32:1364–74. doi: 10.1007/s00380-017-1011-6

21. Matsuura K, Sato K, Shimada K, Goya S, Uemura A, Iso T, et al. Changes in left ventricular blood flow during diastole due to differences in chamber size in healthy dogs. *Sci Rep.* (2020) 10:1106. doi: 10.1038/s41598-019-57180-6

22. Matsuura K, Bach MBT, Takahashi K, Willesen JL, Koch J, Tanaka R. Non-invasive assessment of left ventricular relaxation property using color M-mode-derived intraventricular pressure gradients in cats. *J Vet Cardiol.* (2022) 41:236–48. doi: 10.1016/j.jvc.2022.03.006

23. Giao DM, Wang Y, Rojas R, Takaba K, Badathala A, Spaulding KA, et al. Left ventricular geometry during unloading and the end-systolic pressure volume relationship: Measurement with a modified real-time MRI-based method in normal sheep. *PLoS ONE.* (2020) 15:e0234896. doi: 10.1371/journal.pone.0234896

24. Berli AS, Jud Schefer R, Steininger K, Schwarzwald CC. The use of strain, strain rate, and displacement by 2D speckle tracking for assessment of systolic left ventricular function in goats: applicability and influence of general anesthesia. *Cardiovasc Ultrasound.* (2015) 13:11. doi: 10.1186/s12947-015-0005-8

25. Kim WG, Cho SR, Sung SH, Park HJ. A chronic heart failure model by coronary artery ligation in the goat. *Int J Artif Organs.* (2003) 26:929–34. doi: 10.1177/039139880302601010

26. Leroux AA, Farnir F, Moonen ML, Sandersen CF, Deleuze S, Amory H. Repeatability, variability and reference values of pulsed wave Doppler echocardiographic measurements in healthy Saanen goats. *BMC Vet Res.* (2012) 8:190. doi: 10.1186/1746-6148-8-190

27. Mandour AS, Mahmoud AE, Ali AO, Matsuura K, Samir H, Abdelmageed HA, et al. Expression of cardiac copper chaperone encoding genes and their correlation with cardiac function parameters in goats. *Vet Res Commun.* (2021) 45:305–17. doi: 10.21203/rs.3.rs-457799/v1

28. Samir H, Nyametease P, Elbadawy M, Fathi M, Mandour AS, Radwan F, et al. Assessment of correlations and concentrations of salivary and plasma steroids, testicular morphometry, and semen quality in different climatic conditions in goats. *Theriogenology.* (2020) 157:238–44. doi: 10.1016/j.theriogenology.2020.08.002

29. Tsang HG, Rashdan NA, Whitelaw CBA, Corcoran BM, Summers KM, MacRae VE. Large animal models of cardiovascular disease. *Cell Biochem Funct.* (2016) 34:113–32. doi: 10.1002/cbf.3173

30. Boon JA. *Veterinary Echocardiography*. Ames, IA: John Wiley & Sons. (2011).

31. Takahashi K, Nii M, Takigiku K, Toyono M, Iwashima S, Inoue N, et al. Development of suction force during early diastole from the left atrium to the left ventricle in infants, children, and adolescents. *Heart Vessels.* (2019) 34:296–306. doi: 10.1007/s00380-018-1239-9

32. Iwano H, Kamimura D, Fox E, Hall M, Vlachos P, Little WC. Altered spatial distribution of the diastolic left ventricular pressure difference in heart failure. *J Am Soc Echocardiogr.* (2015) 28:597–605.e1. doi: 10.1016/j.echo.2015.01.002

33. Ohara T, Niebel CL, Stewart KC, Charonko JJ, Pu M, Vlachos PP, et al. Loss of adrenergic augmentation of diastolic intra-LV pressure difference in patients with diastolic dysfunction: evaluation by color M-mode echocardiography. *JACC Cardiovasc Imaging.* (2012) 5:861–70. doi: 10.1016/j.jcmg.2012.05.013

34. Popović ZB, Richards KE, Greenberg NL, Rovner A, Drinko J, Cheng Y, et al. Scaling of diastolic intraventricular pressure gradients is related to filling time duration. *Am J Physiol Heart Circ Physiol.* (2006) 291:H762–9. doi: 10.1152/ajpheart.00081.2006

35. Grant C, Upton RN. Cardiovascular and haemodynamic effects of intramuscular doses of xylazine in conscious sheep. *Aust Vet J.* (2001) 79:58–60. doi: 10.1111/j.1751-0813.2001.tb10642.x

36. Fritz CO, Morris PE, Richler JJ. Effect size estimates: Current use, calculations, and interpretation. *J Exp Psychol Gen.* (2012) 141:2–18. doi: 10.1037/a0024338

37. Leroux AA, Moonen M, Farnir F, Deleuze S, Sandersen C, Amory H. Two-dimensional speckle tracking echocardiography in goats: repeatability,

variability, and validation of the technique using an exercise test and an experimentally induced acute ischemic cardiomyopathy. *BMC Vet Res*. (2020) 16:56. doi: 10.1186/s12917-020-02277-8

38. Lecoq L, Moula N, Amory H, Rollin F, Leroux A. Two-dimensional speckle tracking echocardiography in calves: feasibility and repeatability study. *J Vet Cardiol*. (2018) 20:45–54. doi: 10.1016/j.jvc.2017.10.008

39. Abouelfetouh MM, Liu L, Salah E, Sun R, Nan S, Ding M, et al. The effect of xylazine premedication on the dose and quality of anesthesia induction with alfaxalone in goats. *Animals*. (2021) 11:723. doi: 10.3390/ani11030723

40. De Madron E, Chetboul V, Bussadori C. *Clinical Echocardiography of the Dog and Cat-E-Book*. The Netherlands: Elsevier Health Sciences (2015).

41. Kadappu KK, Thomas L. Tissue Doppler imaging in echocardiography: value and limitations. *Heart Lung Circ*. (2015) 24:224–33. doi: 10.1016/j.hlc.2014.10.003

42. Mandour AS, Samir H, Yoshida T, Matsuura K, Abdelmageed HA, Elbadawy M, et al. Assessment of the cardiac functions using full conventional echocardiography with tissue doppler imaging before and after xylazine sedation in male shiba goats. *Animals*. (2020) 10:2320. doi: 10.3390/ani10122320

43. Bai X, Wang Q. Time constants of cardiac function and their calculations. *Open Cardiovasc Med J*. (2010) 4:168–72. doi: 10.2174/1874192401004010168

44. Greene SA, Thurmon JC. Xylazine–a review of its pharmacology and use in veterinary medicine. *J Vet Pharmacol Ther*. (1988) 11:295–313. doi: 10.1111/j.1365-2885.1988.tb00189.x

45. Stypmann J, Engelen MA, Breithardt AK, Milberg P, Rothenburger M, Breithardt OA, et al. Doppler echocardiography and Tissue Doppler Imaging in the healthy rabbit: Differences of cardiac function during awake and anaesthetised examination. *Int J Cardiol*. (2007) 115:164–70. doi: 10.1016/j.ijcard.2006.03.006

46. Yang XP, Liu YH, Rhaleb NE, Kurihara N, Kim HE, Carretero OA. Echocardiographic assessment of cardiac function in conscious and anesthetized mice. *Am J Physiol*. (1999) 277:H1967–74. doi: 10.1152/ajpheart.1999.277.5.H1967

47. Fraysse B, Weinberger F, Bardswell SC, Cuello F, Vignier N, Geertz B, et al. Increased myofilament Ca2+ sensitivity and diastolic dysfunction as early consequences of Mybpc3 mutation in heterozygous knock-in mice. *J Mol Cell Cardiol*. (2012) 52:1299–307. doi: 10.1016/j.yjmcc.2012.03.009

48. Asada-Kamiguchi J, Jones M, Greenberg NL, Popovic ZB, Tsujino H, Zetts AD, et al. Intraventricular pressure gradients in left ventricular aneurysms determined by color M-mode doppler method: an animal study. *J Am Soc Echocardiogr*. (2006) 19:1112–8. doi: 10.1016/j.echo.2006.04.015

49. Matsui K, Takahashi KEN, Tanaka N, Kobayashi M, Yamada M, Kishiro M, et al. Relationship between left ventricular deformation and early diastolic intraventricular pressure difference during rest and exercise. *Juntendo Med J*. (2016) 62:26–33. doi: 10.14789/jmj.62.26

50. Bexiga R, Mateus A, Philbey AW, Ellis K, Barrett DC, Mellor DJ. Clinicopathological presentation of cardiac disease in cattle and its impact on decision making. *Vet Rec*. (2008) 162:575–80. doi: 10.1136/vr.162.18.575

51. Mandour AS, Samir H, El-Beltagy MA, Hamabe L, Abdelmageed HA, Watanabe I, et al. Monthly dynamics of plasma elements, hematology, oxidative stress markers, and hormonal concentrations in growing male shiba goats (Capra hircus) reared in Tokyo-Japan. *Animals*. (2022) 12:645. doi: 10.3390/ani12050645

52. Koda N, Kutsumi S, Hirose T, Watanabe G. Educational possibilities of keeping goats in elementary schools in Japan. *Front Vet Sci*. (2016) 3:118. doi: 10.3389/fvets.2016.00118

frontiers | Frontiers in Veterinary Science

TYPE Original Research
PUBLISHED 12 October 2022
DOI 10.3389/fvets.2022.969304

OPEN ACCESS

EDITED BY
Haney Samir,
Cairo University, Egypt

REVIEWED BY
Sirilak Disatian Surachetpong,
Chulalongkorn University, Thailand
Toshiharu Fukayama,
Teikyo University of Science, Japan

*CORRESPONDENCE
Ahmed S. Mandour
dr_mandour@vet.suez.edu.eg
Ryou Tanaka
ryo@vet.ne.jp

†These authors have contributed equally to this work

SPECIALTY SECTION
This article was submitted to Veterinary Imaging, a section of the journal Frontiers in Veterinary Science

RECEIVED 14 June 2022
ACCEPTED 29 August 2022
PUBLISHED 12 October 2022

CITATION
Enokizono M, Mandour AS, Komeda S, Goya S, Takeuchi A, Katoh K, Yairo A, Yilmaz Z, Shimada K and Tanaka R (2022) Hemodynamic effect of pimobendan following intramuscular and intravenous administration in healthy dogs: A pilot study. *Front. Vet. Sci.* 9:969304. doi: 10.3389/fvets.2022.969304

Hemodynamic effect of pimobendan following intramuscular and intravenous administration in healthy dogs: A pilot study

Masayuki Enokizono[1†], Ahmed S. Mandour[1,2*†], Syunta Komeda[1], Seijirow Goya[3], Aki Takeuchi[1], Konosuke Katoh[1], Akira Yairo[1], Zeki Yilmaz[4], Kazumi Shimada[1] and Ryou Tanaka[1*]

[1]Department of Veterinary Surgery, Faculty of Veterinary Medicine, Tokyo University of Agriculture and Technology, Tokyo, Japan, [2]Department of Animal Medicine (Internal Medicine), Faculty of Veterinary Medicine, Suez Canal University, Ismailia, Egypt, [3]Department of Bioresource Sciences, Nihon University, Fujisawa, Japan, [4]Department of Internal Medicine, Faculty of Veterinary Medicine, Uludag University, Bursa, Turkey

Background: Pimobendan is widely used for the treatment of dogs with heart failure *via* the oral route. A new injectable form of pimobendan is now available and its potential usefulness *via* intravenous route has been recently demonstrated in dogs. However, the cardiovascular effects of intramuscular (IM) administration of injectable pimobendan have not been investigated yet.

Hypothesis: IM administration of pimobendan may have the same hemodynamic effect as the IV route.

Methods: Six healthy Beagle dogs underwent a placebo-controlled double-blind crossover study. The early cardiovascular effects after a single dose of IM and IV injections of pimobendan (0.2 ml/kg; Pimo IM and Pimo IV, respectively) were compared to the same volume of IM placebo (Saline IM) in anesthetized dogs. Clinical [heart rate (HR) and blood pressure (BP)] and echocardiographic hemodynamic parameters [left ventricular (LV) inflow waveforms of diastolic early wave (eV), atrial systolic wave (aV), diastolic early mitral ring velocity (e′), peak velocity (pV), stroke volume (SV), cardiac output (CO), and systemic vascular resistance (SVR)] were monitored with 15 min intervals for 120 min.

Results: Diastolic BP decreased significantly at 30 min in Pimo IM compared to Saline IM. Mean eV and CO values significantly increased from 75 min, e′ from 60 min, pV from 75 min, and SV from 15 to 120 min, whereas SVR significantly decreased at 30–60 min in Pimo IM compared to those of Saline IM ($P < 0.05$). Compared with the Pimo IV, eV and pV were significantly lower at 30–60 min ($P < 0.05$) while SV was significantly higher at 90–105 min in Pimo IM ($P < 0.05$). Other hemodynamic parameters (BP, HR, SVR, CO, e′, and E/e′) did not significantly change between Pimo IM and IV.

Conclusions: The hemodynamic effect of pimobendan following IM and IV injection was described. Our results suggested that IM administration

of pimobendan is equally comparable and possibly interchangeable with IV administration. This warrant further studies to investigate the clinical effectiveness of IM pimobendan in treating dogs with congestive heart failure or in heart failure cases unable to receive IV or oral administration.

KEYWORDS

pimobendan injection, echocardiography, hemodynamics, phosphodiesterase III inhibitor, cardiotonic, dogs

Introduction

Mitral valve disease (MVD) is the most common acquired heart disease in dogs which accounts for 75–80% of congestive heart failure (1, 2). Pimobendan has long been used as a treatment of choice in dogs suffering from MVD (3–5) and dilated cardiomyopathy (DCM) (6). ACVIM Specialists of Cardiology recommended the use of pimobendan for hospital-based acute care to improve the survival rate and patient outcomes (7, 8). Moreover, pimobendan medication delays the onset of congestive heart failure (CHF) in dogs with preclinical MVD with enlarged left atrium and left ventricle (ACVIM Stage B2) by 15 months (3). Pimobendan has cardiotonic, myocardial relaxing, and vasodilatory effects by calcium sensitivity enhancing (9–11) and phosphodiesterase III (PDE-III) inhibitory effects (12–14) in a dose-dependent manner (15).

Oral administration of pimobendan is the most preferred method when the MVD condition is stable and for chronic medication strategy (16). The pharmacokinetics of pimobendan during oral medication considering the drug form vary among studies. This difference is essential to predict the onset of the peak effect of pimobendan during the treatment of patients, particularly in severe cases (17–20). In addition, many dogs with acute heart failure cases due to MDV have little reserve cardiorespiratory function, hemoptysis, and respiratory distress (2). Oral administration in such cases is more difficult than parenteral routes, and the desired effect of the drug occurs slowly when used per os (17), making it an inappropriate route of administration in emergency cases such as in acute heart failure or severe CHF.

Currently, injectable pimobendan has been formulated and became available for IV injection (17, 21), suggesting an alternative live-saving route of administration in case of advanced stages of MVD to rapidly reduce the left ventricular end-diastolic pressure (17, 22). Recent studies revealed that the IV administration of pimobendan, but not SC, may be useful in patients with acute heart failure caused by MVD (23, 24). Until now, there is no data regarding the IM route of pimobendan administration in dogs. In severe cases, injection of medicine is a lifesaving choice because of getting the desired effect after a short time compared with the oral route. In light of previous literature, there are certain cases of emergency where the IV route can be accessed easily. However, in some cases, like vasogenic shock, IV is very difficult due to the collapse of peripheral veins (25). Also, in small breed dogs, the peripheral veins are not so easily accessed and IV injection should perform with caution. When we consider these points, the IM route of pimobendan administration is worth studying. Practically, IM injection is easier, and safer, and may serve as an alternative route of administration in urgent cases when the IV route is difficult. Besides, the desired effect of the medication is generally more rapid when used *via* IM than the SC (26, 27).

The current study aims to investigate the cardiovascular effect of injectable pimobendan through the IM route. We will demonstrate the prolonged effect of pimobendan IM injection on cardiovascular functions through evaluation of hemodynamic changes, evaluating the start time of action, the duration for maximum activity, and the strength of the action in comparison with the IV route in healthy dogs.

Abbreviations: aV, The left ventricular inflow waveforms of the atrial systolic wave; BP, Blood pressure; CHF, Congestive heart failure; CO, Cardiac output; DBP, Diastolic blood pressure; DCM, Dilated cardiomyopathy; E/e′, early mitral inflow to the diastolic early mitral ring velocity; eV, The left ventricular inflow waveforms of the diastolic early wave; HR, Heart rate; LAP, Left atrial pressure; LV, Left ventricular; LVEDP, The left ventricular end-diastolic pressure; MAP, Mean blood pressure; MVD, Mitral valve disease; $PaCO_2$, Expiratory terminal carbon dioxide partial pressure; PDE-III, Phosphodiesterase III; Pimo IM, Intramuscular administration of pimobendan; Pimo IV, Intravenous administration of pimobendan; pV, Peak velocity; SBP, Systolic blood pressure; SpO_2, Saturation of percutaneous oxygen; SV, Stroke volume; SVR, Systemic vascular resistance; VTI, Velocity-time integral.

Materials and methods

Animals

A group of six female beagle dogs aged 1–3 years old and weighing 7.6–8.4 kg (median: 7.9 kg) was studied. No abnormalities were found in their health, based on clinical,

hematological, and serum biochemical examinations, as well as the cardiologic evaluation by electrocardiography and transthoracic echocardiography.

Study design

This is a placebo-controlled, double-blinded, crossover study. In this study, the cardiovascular effect of pimobendan treatment *via* IM route (Pimo IM) was investigated which was compared with pimobendan IV (Pimo IV) and placebo administered IM (normal saline; saline IM).

For each examined dog, the supervisors randomly prepared the dose of injectable pimobendan and the same volume of saline as Drugs A and B. Additionally, the other supervisor selected either Drug A or B for IM administration and subsequent measurements of heart function parameters in anesthetized animals. The IM injections were performed in the longissimus muscle of the lower back. None of the supervisors who prepared and administered the drug/placebo knew which substance was administered until all experiments were finished. In addition, the preparation and administration of the drug were overseen by the designated supervisors. Moreover, the effect of intravenous administration of pimobendan (Pimo IV) was compared with that of the Pimo IM, using the same individual animals as in the Pimo IM vs. saline IM test. The drugs were prepared at doses of pimobendan 0.15 mg/kg (0.2 ml/kg; Vetmedin® 0.75 mg/ml, Boehringer Ingelheim, Germany) for IM and IV routes, and saline 0.2 ml/kg (Otsuka normal saline, Otsuka Pharmaceutical Factory, Inc., Japan), respectively, according to the previously published protocol (23). The IV route was injected over 1 min in the cephalic vein.

In this experiment, all dogs were subjected to the same route of administration. After one week's lag, another route was started to avoid overlapping and ensure complete clearance of the medicine (23).

Anesthesia and preparation

A catheter (SURFLO 22-gauge, 25 mm, TERUMO, Japan) was placed in the cephalic vein for pre-medication and infusion. Each dog was pre-medicated with butorphanol (0.2 mg/kg, IV; Vetorphale, Meiji Seika, Japan). Anesthesia was slowly introduced with propofol IV (6.0 mg/kg; propofol IV 1% "FK", Fresenius Kabi Japan K.K., Japan) and endotracheal intubation was performed (28, 29). General anesthesia was maintained by isoflurane (isoflurane, Pfizer Inc., NY, United States) to 100% oxygen, supplied *via* mechanical ventilation (Aestiva/5, Datex-Ohmeda, GE Healthcare, Japan). The concentration of isoflurane during the experiment was determined for each dog (1.0–1.8%), and the concentration was maintained within a range of ±0.1%. The dog was placed in the left lateral position, and the heart rate (HR), expiratory terminal carbon dioxide partial pressure ($PaCO_2$), expiratory terminal isoflurane concentration, blood pressure [BP; systolic blood pressure (SBP), mean blood pressure (MAP), diastolic blood pressure (DBP)], esophageal temperature, and saturation of percutaneous oxygen (SpO_2) were continuously monitored using an anesthesia monitor (Life Scope A BSM-5192, Nihon Kohden, Japan). Samples for expiratory terminal $PaCO_2$ and expiratory terminal isoflurane concentration were collected from the Y piece of the ventilator respiratory system, and expiratory terminal $PaCO_2$ was maintained at 35–45 mmHg. BP was monitored with a transducer (DX-300, Nihon Kohden, Japan) connected with a catheter (SURFLO 24-gauge, 19 mm, TERUMO, Japan) placed in the dorsalis pedis artery. Esophageal temperature was maintained at 37.0–37.5°C using a warm air mat (Bair hugger™, 3M™, Minnesota, United States). The SpO_2 was measured with a pulse oximeter clipped to the tongue and levels were maintained at 98% or higher. Lactated Ringer's solution was infused at a flow rate of 3.0 mL/kg/h throughout the experiment.

Measurements of cardiovascular and hemodynamic parameters

After confirming the stability of the hemodynamic parameters following anesthesia, the baseline parameters before drug administration (Time 0) were measured from the anesthesia monitor and by using conventional echocardiography (Prosound F75, Hitachi Aloka Med., Japan). Subsequently, while dogs were still under anesthesia, drug administration was started, and the data were measured every 15 min up to 120 min (eight-time points: T15, T30, T45, T60, T75, T90, T105, T120) after the acquisition of the baseline measurements (T0). This protocol has been modified from previously published studies (17, 23). For echocardiography (30), a cross-sectional image of the apex of the heart was visualized. By the left parasternal approach, the left ventricular inflow waveforms of the diastolic early wave (eV) and atrial systolic wave (aV) were measured using the pulse Doppler method, and the early diastolic mitral annular velocity (assessed by TDI) (e') on the lateral wall was measured using the tissue Doppler echocardiography. The eV/e' (E/e') was calculated from the measured eV and e'. Subsequently, the five-chamber view with color flow Doppler was acquired, and the peak velocity (pV), velocity-time integral (VTI), and tract diameter (d, cm) of LV outflow was measured by the Pulsed-wave Doppler echocardiography of the aorta. The following values were calculated from the following formulas (31):

$$\text{Stroke volume (SV)} = (d/2)^2 \times \pi \times \text{VTI}$$
$$\text{Cardiac output (CO)} = \text{SV} \times \text{HR}$$

TABLE 1 Heart rate and blood pressure measurements after pimobendan injection in comparison with measurements at the baseline (Time 0).

Time (min)	Saline IM				Pimobendan IM				Pimobendan IV			
	Mean	95%CI		*P*-value	Mean	95%CI		*P*-value	Mean	95%CI		*P*-value
HR (beats/min)												
15	2.14	−1.09	5.37	0.18	0.20	−3.04	3.43	0.90	2.50	−0.73	5.72	0.12
30	4.04	0.97	7.11	**0.01**	3.79	0.72	6.86	**0.02**	3.17	0.11	6.24	**0.04**
45	3.62	0.00	7.23	**0.05**	3.40	−0.22	7.01	0.06	1.66	−1.95	5.26	0.34
60	6.50	1.70	11.30	**0.01**	3.90	−0.90	8.70	0.10	−0.40	−5.19	4.39	0.86
75	6.32	−0.31	12.96	0.06	−0.76	−7.39	5.88	0.81	4.60	−2.02	11.22	0.16
90	8.26	3.45	13.07	**0.002**	5.96	1.14	10.77	**0.02**	3.79	−1.01	8.59	0.11
105	8.78	2.69	14.88	**0.01**	9.00	2.90	15.10	**0.01**	6.55	0.47	12.64	**0.04**
120	10.31	2.83	17.80	**0.01**	10.83	3.34	18.32	**0.01**	6.86	−0.61	14.33	0.07
SBP (mmHg)												
15	−2.10	−8.26	4.06	0.48	−2.02	−8.43	4.39	0.51	−0.88	−7.32	5.56	0.78
30	0.58	−4.15	5.32	0.80	−2.90	−7.82	2.03	0.23	−4.35	−9.30	0.59	0.08
45	−3.85	−9.39	1.70	0.16	−4.85	−10.62	0.92	0.09	−1.30	−7.10	4.50	0.64
60	−3.82	−11.67	4.03	0.31	−3.81	−11.97	4.35	0.33	0.46	−7.74	8.67	0.91
75	−3.16	−11.25	4.93	0.42	−4.03	−12.44	4.38	0.32	−1.31	−9.76	7.15	0.75
90	0.00	−7.36	7.37	1.00	−6.13	−13.79	1.53	0.11	−2.71	−10.40	4.99	0.46
105	−0.97	−9.64	7.70	0.81	−2.74	−11.75	6.28	0.53	−0.62	−9.69	8.44	0.89
120	0.86	−7.17	8.89	0.82	−3.79	−12.13	4.56	0.35	0.76	−7.63	9.15	0.85
MAP (mmHg)												
15	0.93	−2.37	4.23	0.55	0.25	−3.06	3.57	0.87	0.32	−3.11	3.74	0.85
30	3.08	−0.28	6.43	0.07	−0.45	−3.82	2.92	0.78	−1.30	−4.78	2.19	0.44
45	2.19	−1.19	5.56	0.19	−0.59	−3.99	2.80	0.71	−1.26	−4.77	2.25	0.45
60	1.64	−2.78	6.06	0.44	−1.18	−5.62	3.26	0.58	−0.46	−5.05	4.13	0.83
75	1.99	−1.88	5.86	0.29	−1.96	−5.86	1.93	0.30	−0.52	−4.54	3.50	0.78
90	2.64	−1.31	6.59	0.17	−2.31	−6.28	1.66	0.23	−0.99	−5.10	3.11	0.61
105	2.31	−2.48	7.10	0.32	0.15	−4.67	4.97	0.95	−0.62	−5.60	4.35	0.79
120	3.23	−1.08	7.54	0.13	−0.78	−5.12	3.55	0.70	0.56	−3.92	5.03	0.79
DBP (mmHg)												
15	0.69	−3.47	4.85	0.73	−2.17	−6.19	1.86	0.27	1.47	−2.68	5.63	0.46
30	3.54	−0.90	7.99	0.11	−3.00	−7.30	1.30	0.16	−0.21	−4.65	4.23	0.92

(Continued)

10.3389/fvets.2022.969304

TABLE 1 (Continued)

Time (min)	Saline IM				Pimobendan IM				Pimobendan IV			
	Mean	95%CI		*P*-value	Mean	95%CI		*P*-value	Mean	95%CI		*P*-value
45	3.02	−0.91	6.94	0.12	−2.17	−5.96	1.63	0.24	−1.85	−5.78	2.07	0.33
60	1.51	−2.23	5.25	0.40	−3.67	−7.28	−0.05	**0.05**	−1.18	−4.92	2.56	0.51
75	1.57	−1.93	5.08	0.35	−4.33	−7.72	−0.94	**0.02**	−1.57	−5.08	1.93	0.35
90	2.72	−1.25	6.69	0.16	−4.67	−8.50	−0.83	**0.02**	−1.39	−5.35	2.58	0.47
105	1.56	−2.48	5.60	0.42	−1.00	−4.91	2.91	0.59	−1.56	−5.60	2.48	0.42
120	1.64	−2.20	5.48	0.37	−2.17	−5.88	1.55	0.23	−0.48	−4.32	3.36	0.79

Test for change from Time 0 in the repeated measures ANCOVA (time effect, group effect, and time*group interaction) (least significant difference). P-value of 0.05 is considered significant. 95% CI: 95% confidence interval. HR, heart rate; SBP, systolic blood pressure; DBP, diastolic blood pressure; MBP, mean blood pressure. Bold values idicated that the P value < 0.05.

Systemic vascular resistance (SVR) = 80.0 × (MAP – central venous pressure).

Since the healthy dogs had no right atrial enlargement or transvenous distension, the central venous pressure was assumed to be 5 mmHg (32).

Statistical analysis

The statistical analysis was performed by SATISTA (Kyoto, Japan). SPSS for Windows version 24.0 (IBM Japan, Tokyo, Japan) was used for the statistical analysis. For each time series outcome, the time (every 15 min), group (saline IM, Pimo IM, Pimo IV), and their interactions were fixed effects; additionally, RM-ANCOVA was performed with the initial value of the dependent variable (Time 0) corrected as a covariant. The estimated mean value at each time and its 95% confidence interval (CI) were calculated. For the pairwise comparison, the Pimo IM vs. saline IM test and the Pimo IV vs. IM test were performed. Since the comparative tests of the above two hypotheses were performed independently of each other, multiplicity was not corrected. Since each outcome was researched on the assumption that it followed a normal distribution from the preliminary survey, a parametric method was adopted. $P < 0.05$ was considered statistically significant.

Results

Hemodynamic changes caused by pimobendan IM in comparison with the baseline

All hemodynamic measurements obtained from the current study are submitted as additional data (Supplementary Tables 1, 2). Tables 1, 2 summarizes the changes in hemodynamic parameters after pimobendan administration in comparison with the baseline (Time 0). The HR was significantly higher than the baseline 30 and 90 min after administration of Pimo IM. The SBP and MAP did not change significantly during the monitoring period ($P > 0.05$); however, DBP showed a significant decrease at 60, 75, and 90 min compared to its baseline ($P < 0.05$, Table 1).

The echocardiographic data showed significant increases in pV, SV, and CO following Pimo IM at all measurement time points compared with the baseline (Time 0) and reach the maximum values at 90 min (Table 2). The pV was increased from the baseline (mean: 81.4 ± 5.4 cm/s) to (mean: 106.2 ± 8.3 cm/s) after 15 min and continued to increase until 90 min (mean: 152.0 ± 13.1 cm/m). Concomitantly, SV and CO were elevated from the baseline (mean: 13.7 ± 1.2 mL, 1.3 ± 0.1 L/min) to (mean: 15.9 ± 1.2 mL, 1.5 ± 0.1 L/min) after

TABLE 2 Hemodynamic parameters after pimobendan injection in comparison with the baseline (Time 0).

Time	Saline IM				Pimobendan IM				Pimobendan IV			
	Mean	95%CI		*P*-value	Mean	95%CI		*P*-value	Mean	95%CI		*P*-value
aV (cm/s)												
15	1.71	−2.83	6.25	0.43	3.24	−1.50	7.98	0.17	4.34	−0.40	9.07	0.07
30	3.03	−1.36	7.42	0.16	2.13	−2.45	6.71	0.34	6.39	1.82	10.97	**0.01**
45	2.47	−1.80	6.75	0.24	4.75	0.29	9.21	**0.04**	8.36	3.90	12.81	**0.001**
60	2.89	−2.33	8.11	0.26	6.93	1.48	12.38	**0.02**	7.23	1.78	12.67	**0.01**
75	3.79	−1.87	9.44	0.17	7.66	1.76	13.57	**0.02**	7.89	2.00	13.79	**0.01**
90	4.59	0.40	8.78	**0.03**	9.03	4.66	13.41	**<0.001**	11.73	7.36	16.10	**<0.001**
105	4.43	−1.72	10.58	0.15	12.44	6.02	18.86	**<0.001**	15.18	8.77	21.60	**<0.001**
120	7.55	2.67	12.42	**0.01**	13.18	8.10	18.27	**<0.001**	12.07	6.99	17.15	**<0.001**
eV (cm/s)												
15	2.84	−3.04	8.72	0.32	7.23	1.28	13.17	**0.02**	12.35	7.07	17.62	**<0.001**
30	3.33	−5.92	12.59	0.45	7.35	−2.01	16.71	0.11	20.33	12.03	28.63	**<0.001**
45	3.03	−9.07	15.14	0.60	12.39	0.14	24.63	**0.05**	26.09	15.23	36.94	**<0.001**
60	6.65	−5.17	18.47	0.25	19.20	7.25	31.16	**0.004**	31.05	20.45	41.66	**<0.001**
75	3.60	−5.14	12.33	0.39	34.89	26.05	43.73	**<0.001**	33.51	25.68	41.35	**<0.001**
90	6.04	−5.79	17.86	0.29	23.87	11.91	35.83	**<0.001**	31.22	20.61	41.82	**<0.001**
105	7.51	−4.19	19.22	0.19	35.28	23.44	47.11	**<0.001**	34.88	24.38	45.38	**<0.001**
120	4.75	−4.34	13.83	0.28	28.63	19.44	37.81	**<0.001**	35.61	27.46	43.75	**<0.001**
e′ (cm/s)												
15	0.07	−0.36	0.50	0.74	0.41	−0.03	0.84	0.06	0.75	0.31	1.18	**0.002**
30	0.41	−0.58	1.39	0.39	0.64	−0.35	1.64	0.19	1.94	0.94	2.93	**0.001**
45	0.16	−0.94	1.26	0.76	0.76	−0.35	1.87	0.16	2.14	1.03	3.25	**0.001**
60	−0.04	−1.18	1.10	0.94	1.85	0.70	3.00	**0.004**	2.85	1.71	4.00	**<0.001**
75	−0.04	−1.48	1.40	0.95	1.68	0.23	3.13	**0.03**	2.96	1.51	4.41	**0.001**
90	0.51	−0.61	1.62	0.34	2.59	1.47	3.71	**<0.001**	2.95	1.83	4.07	**<0.001**
105	0.06	−1.26	1.37	0.93	2.13	0.81	3.45	**0.004**	3.28	1.96	4.60	**<0.001**
120	0.01	−1.18	1.20	0.99	2.51	1.31	3.71	**0.001**	2.78	1.58	3.99	**<0.001**
E/e′												
15	0.7	0.0	1.4	**0.04**	0.15	−0.51	0.81	0.63	0.75	0.10	1.40	**0.03**
30	0.3	−1.0	1.5	0.66	0.08	−1.10	1.27	0.88	0.74	−0.43	1.92	0.19
45	0.5	−0.5	1.4	0.29	0.45	−0.48	1.37	0.32	1.15	0.24	2.06	**0.02**

(Continued)

10.3389/fvets.2022.969304

TABLE 2 (Continued)

Time	Saline IM				Pimobendan IM				Pimobendan IV			
	Mean	95%CI		*P*-value	Mean	95%CI		*P*-value	Mean	95%CI		*P*-value
60	1.2	−0.1	2.4	0.06	0.00	−1.18	1.18	0.99	1.08	−0.08	2.25	0.07
75	1.0	−0.2	2.3	0.11	1.51	0.27	2.75	**0.02**	1.31	0.09	2.54	**0.04**
90	0.5	−0.4	1.4	0.24	0.00	−0.85	0.85	0.99	0.85	0.01	1.69	**0.05**
105	1.1	−0.1	2.3	0.07	1.42	0.23	2.61	**0.02**	0.94	−0.23	2.12	0.11
120	0.6	−0.2	1.5	0.13	0.71	−0.12	1.53	0.09	1.23	0.41	2.04	**0.01**
pV (cm/s)												
15	7.95	2.45	13.44	**0.01**	9.95	4.55	15.34	**0.001**	13.49	8.17	18.81	**<0.001**
30	12.94	4.47	21.41	**0.01**	24.88	16.56	33.20	**<0.001**	28.26	20.06	36.46	**<0.001**
45	16.05	5.88	26.21	**0.004**	28.62	18.63	38.61	**<0.001**	48.58	38.74	58.42	**<0.001**
60	11.61	−5.20	28.42	0.16	33.02	16.50	49.53	**<0.001**	60.08	43.81	76.35	**<0.001**
75	15.00	0.54	29.45	**0.04**	60.45	46.25	74.65	**<0.001**	63.69	49.70	77.68	**<0.001**
90	15.46	2.05	28.87	**0.03**	70.63	57.45	83.80	**<0.001**	55.21	42.23	68.19	**<0.001**
105	22.72	6.71	38.72	**0.01**	68.68	52.95	84.40	**<0.001**	55.25	39.76	70.74	**<0.001**
120	26.72	16.94	36.50	**<0.001**	59.90	50.29	69.51	**<0.001**	63.88	54.41	73.35	**<0.001**
SV (mL)												
15	0.46	−0.73	1.65	0.42	2.24	1.00	3.47	**0.002**	1.58	0.39	2.76	**0.01**
30	1.19	−0.43	2.81	0.14	3.86	2.18	5.53	**<0.001**	4.27	2.65	5.88	**<0.001**
45	2.22	0.60	3.83	**0.01**	4.69	3.01	6.37	**<0.001**	6.24	4.63	7.86	**<0.001**
60	1.28	−1.14	3.69	0.28	5.73	3.22	8.24	**<0.001**	7.70	5.28	10.11	**<0.001**
75	2.32	−0.35	4.99	0.08	9.37	6.60	12.15	**<0.001**	7.12	4.45	9.79	**<0.001**
90	1.96	−0.11	4.02	0.06	11.69	9.55	13.84	**<0.001**	6.63	4.56	8.69	**<0.001**
105	2.57	1.26	3.88	**<0.001**	8.73	7.37	10.10	**<0.001**	6.27	4.96	7.58	**<0.001**
120	2.26	0.31	4.20	**0.03**	9.33	7.31	11.35	**<0.001**	6.95	5.00	8.89	**<0.001**
CO (L/min)												
15	0.16	0.01	0.32	**0.04**	0.22	0.05	0.39	**0.01**	0.24	0.08	0.40	**0.01**
30	0.17	−0.05	0.40	0.12	0.49	0.24	0.73	**<0.001**	0.50	0.27	0.73	**<0.001**
45	0.32	−0.17	0.80	0.18	0.83	0.31	1.34	**0.004**	0.67	0.18	1.16	**0.01**
60	0.24	−0.07	0.56	0.12	0.62	0.29	0.96	**0.001**	0.76	0.44	1.08	**<0.001**
75	0.34	−0.07	0.75	0.10	1.09	0.65	1.53	**<0.001**	0.82	0.40	1.23	**<0.001**
90	0.39	0.06	0.72	**0.02**	1.21	0.86	1.56	**<0.001**	0.90	0.57	1.23	**<0.001**
105	0.47	0.18	0.76	**0.004**	1.03	0.72	1.33	**<0.001**	0.90	0.60	1.19	**<0.001**
120	0.42	0.07	0.77	**0.02**	1.15	0.77	1.52	**<0.001**	0.92	0.56	1.28	**<0.001**

(Continued)

10.3389/fvets.2022.969304

10.3389/fvets.2022.969304

TABLE 2 (Continued)

Time	Saline IM				Pimobendan IM				Pimobendan IV			
	Mean	95%CI		*P*-value	Mean	95%CI		*P*-value	Mean	95%CI		*P*-value
SVR (dyne·s/cm^{-5})												
15	−180.5	−472.2	111.2	0.21	−393.7	−714.3	−73.0	**0.02**	−512.5	−818.2	−206.8	**0.003**
30	−168.6	−432.6	95.3	0.19	−682.8	−972.9	−392.7	**<0.001**	−985.0	−1261.6	−708.4	**<0.001**
45	−414.9	−726.0	−103.9	**0.01**	−833.7	−1175.7	−491.8	**<0.001**	−1283.7	−1609.8	−957.7	**<0.001**
60	−337.8	−657.0	−18.7	**0.04**	−853.6	−1204.4	−502.7	**<0.001**	−1315.7	−1650.2	−981.1	**<0.001**
75	−442.4	−891.6	6.8	0.05	−1270.4	−1764.2	−776.6	**<0.001**	−1306.4	−1777.2	−835.6	**<0.001**
90	−427.1	−749.0	−105.2	**0.01**	−1404.5	−1758.4	−1050.7	**<0.001**	−1368.9	−1706.3	−1031.5	**<0.001**
105	−483.0	−853.8	−112.2	**0.01**	−1193.0	−1600.6	−785.4	**<0.001**	−1353.8	−1742.4	−965.1	**<0.001**
120	−537.4	−774.6	−300.2	**<0.001**	−1300.2	−1561.0	−1039.4	**<0.001**	−1358.9	−1607.6	−1110.3	**<0.001**

Test for change from Time 0 in the repeated measures ANCOVA (time effect, group effect, and time*group interaction) (least significant difference). P-value of 0.05 is considered significant. 95% CI: 95% confidence interval.
aV, atrial systolic wave; eV, the early diastolic wave; e′, the diastolic early mitral ring velocity; The eV/e′ (E/e′) early mitral inflow to diastolic annular tissue velocity; pV, the peak aortic velocity; SV, stroke volume; Co, cardiac output; SVR, systemic vascular resistance. The bold values indicate the values which are less than 0.05.

15 min and reach their maximum values at 90 min (mean: 25.4 ± 2.1 mL, 2.5 ± 0.3 L/min), respectively. The eV increased significantly at 15 min and 45 min after IM administration and reached the maximum value at 105 min after administration. Meanwhile, a significant increase in aV was observed from 45 min after administration, and the increase continued until 120 min. Subsequently, e′ was significantly increased 60 min after administration, and reached a maximum value 90 min after administration. E/e′ index was significantly increased 75 min and 105 min after administration.

Finally, SVR showed a regular manner of a significant decrease in overall measurement time points, showing a minimum reduction at 90 min (mean: 1693 ± 353 dyne·s/cm^5) after administration compared with the baseline (mean: 3098.4 dyne·s/cm^{-5}).

Hemodynamic changes caused by IV administration of pimobendan in comparison with the baseline

The HR was significantly higher than the baseline at 30 and 105 min after administration. No significant changes were observed in the SBP, MAP, and DBP compared to the baseline. There was a significant increase in the pV, SV, and CO at all measurement points compared with the baseline. The data revealed increased pV from baseline (81.41 ± 5.32 cm/s) and reach its maximum at 75 min (145.10 ± 13.99 cm/s). Besides, the LVOT revealed a continuous increment of SV and CO from Time 0 (13.73 ± 1.19 mL, 1.3 ± 0.16 L/min; respectively) until 60 min for SV (21.43 ± 2.42 mL); while CO continued to increase until 90 min (2.20 ± 0.33 L/min).

While eV and e′ were significantly increased at all measurement points, E/e′ was significantly increased at five measurement points (15, 45, 75, 90, and 120 min) and aV was only significantly increased after 30 min of IV administration.

Furthermore, SVR was significantly reduced at all the measurement points following IV administration of pimobendan and the reduction was continuously observed from the baseline until 90 min (3098.4± 305.7 vs. 1729.5 ± 337.4 dyne·s/cm^{-5}).

Comparison between pimobendan IM and saline IM

No significant difference between groups was observed at all measurement points in HR, SBP, or MAP (Figures 1A–C). However, a significant decrease was observed in DBP in Pimo IM at 30 min [difference between groups ("Pimo IM," "Saline IM"):

−6.54 (95% CI: −12.72 - −0.36), $P = 0.040$], 75 min [−5.91 (CI: −10.78 - −1.03), $P = 0.021$], and 90 min [−7.39 (CI: −12.91 - −1.87), $P = 0.012$] after administration compared with those of Saline IM (Figure 1D).

In the Pimo IM group, a significant increase in pV was observed at 75 min [45.45 (CI: 24.69 - 66.21), $P < 0.001$; Figure 2E], for SV at 15 min [1.77 (0.02 - 3.5), $P = 0.048$; Figure 2F], and for CO at 75 min [0.75 (CI: 0.13 - 1.37), $P = 0.022$; Figure 2G] after administrations compared with the saline IM.

No significant difference between groups was observed in late mitral velocity (aV) at all measurement points; however, early mitral velocity (eV) was significantly increased at 75 min [31.30 (CI: 17.65 - 44.94), $P < 0.001$], 105 min [27.76 (CI: 9.49 - 46.04), $P = 0.006$], and 120 min [23.88 (CI: 9.70 - 38.06), $P = 0.003$] after Pimo IM administration compared with saline IM (Figures 2A,B).

In the Pimo IM group, mitral annulus velocity (e') was significantly reduced at 60 min [1.89 (0.27 - 3.51), $P = 0.025$] and 90 min [2.08 (0.50 - 3.66), $P = 0.014$] after administration compared with the placebo (Figure 2C). There was no significant difference in E/e' ratio between Pimo IM and saline IM at all measurement points (Figure 2D). Finally, SVR showed a significant decrease in the Pimo IM group after 30 min [−514.2 (CI: −917.6 - −110.8), $P = 0.016$] and 60 min [−515.7 (CI: −1003.6 - −27.9), $P = 0.040$] of administration (Figure 2H).

Comparison between the two routes of pimobendan administration

In the Pimo IM and IV groups, significant changes were observed in eV 30 min after administration [difference between groups ("Pimo IM," "Pimo IV"): Time 30: −12.98 (CI: −25.57 - −0.39), $P = 0.044$; Figure 2B] and in pV at 45 min [−19.96 (CI: −33.88 - −6.05), $P = 0.008$] and 60 min [−27.07 (CI: −50.07 - −4.06), $P = 0.024$] after administration (Figure 2E), with a significant increase in the Pimo IV group. On the other hand, SV was significantly increased in Pimo IM at 90 min [5.07 (CI: 2.02 - 8.12), $P = 0.003$] and 105 min [2.47 (CI: 0.53 - 4.40), $P = 0.016$] compared with Pimo IV (Figure 2F). In addition, there was no significant difference in BP, HR, aV, SVR, CO, e', and E/e' between IM and IV routes of pimobendan injection (Figures 1A–D, 2A,C,D,G,H).

Discussion

Pimobendan is a drug known to enhance the systolic force and vasodilator effects, and so, is defined as an inodilator (11). In the present study, we measured parameters that represent systolic contractile and diastolic relaxing functions of LV myocardium and BP to verify whether IM injectable pimobendan works safely and effectively in healthy dogs. Our results showed that the two routes of pimobendan administration affected the LV myocardial diastolic and systolic functions by increasing eV of the mitral inflow and pV values of LV outflow (relaxation) and increasing SV and CO (positive inotropy), along with the superiority of pimobendan IM over IV. Also, IM pimobendan produced vasodilator effects due to decreasing SVR and diastolic BP within 120 min of a single dose in healthy dogs.

Pimobendan, a benzimidazole-pyridazinone derivative, is a non-sympathomimetic, and non-glycoside inotropic agent that presents vasodilator effects by inhibiting PDE-III, a regulator of cardiac and vascular smooth muscle contractility (11). Additionally, pimobendan has a Ca^{+2}-sensitizing effect and directly increases the affinity of the regulatory site on cardiac troponin C for Ca^{+2}, giving rise to a positive inotropic activity (12–14). Pimobendan increases CO and decreases SVR (inodilation) in a dose-dependent manner. In the current study, the observed increases in CO and decreases in SVR following IM pimobendan administration were consistent with a previous study (24). These results show that the inodilator effect of pimobendan is maintained after IM injection.

Rapid fluctuations in the HR and BP may be a high risk for acute heart failure patients who are already in shock with hypotension. In the present study, a significant increase in HR was observed in Pimo IM and saline IM groups, but the amount of change from the baseline in those two groups was almost the same (∼10 beats). This finding indicated that the increase in HR was related to factors other than the effect of pimobendan, such as the effect of long-term anesthesia. Isoflurane was maintained at ±0.1% during the experiment, ETCO2 was 35–45 mmHg, and body temperature was maintained at 37.0–37.5°C. However, the T1/2 of propofol used in the anesthetic preadministration was 4.2 ± 2.2 min (33) and the T1/2 of butorphanol was 1.3–3.6 h. It is possible that the attenuation of these effects led to a decrease in anesthetic depth, which in turn led to an increase in heart rate. Therefore, IM (and IV) administrations of pimobendan (0.15 mg/kg) were considered not to affect the HR, SBP, or MBP. This is in agreement with a previous study in which pimobendan was administered intravenously (23). On the other hand, some studies have reported an increase in HR and a decrease in systolic LV pressure (34, 35). Other studies also stated that the increase in HR and decrease in BP after pimobendan administration is dose-dependent (36, 37). The differential effect of pimobendan on HR and BP may be due to the differences in the dose of pimobendan among the studies. When used at high doses as in later studies, the effect of pimobendan on HR and BP will be more than the net effect observed in the present study.

Reducing the afterload of the LV is an important target during the treatment of acute heart failure. The afterload is mainly due to the resistance applied to the LV wall and the resistance of the arterial system. The resistance applied

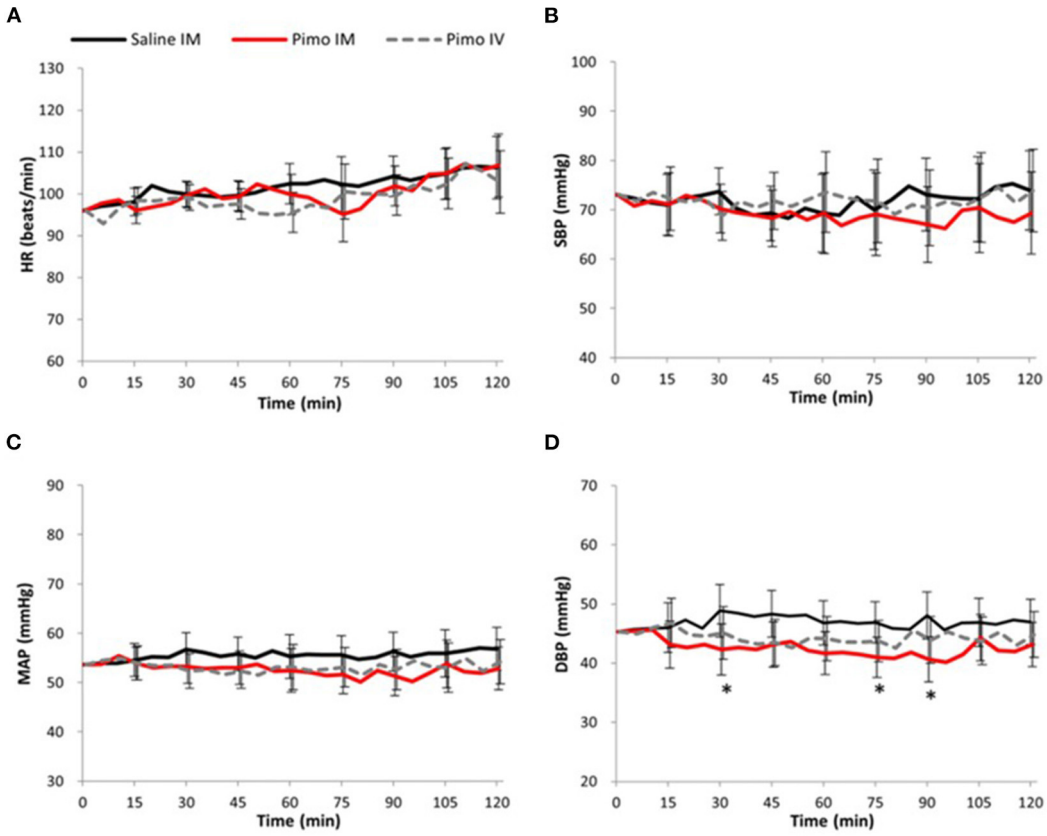

FIGURE 1
Data are presented as mean ± 95% confidence interval (error bar). Black line: Saline IM; Red line: Pimobendan IM (Pimo IM); Gray dot line: Pimobendan IV (Pimo IV). (*) fitted to indicate the significance difference between Pimo IM Saline IM, [for the repeated measures ANCOVA (model: time, group, and time*group)]; $P < 0.05$. **(A)** Heat rate (HR, beat/min), **(B)** systolic blood pressure (SBP, mmHg), **(C)** mean arterial pressure (MAP, mmHg), **(D)** diastolic blood pressure (DBP, mmHg).

to the LV wall is defined by SBP, while the resistance of the arterial system is defined by SVR (2). In the present study, although no significant change was observed in SBP, a significant decrease was observed in the SVR, indicating that IM pimobendan leads to vasodilation. In addition, the vasodilator effect was rapidly observed (after 15 min) and was maximized 90 min after administration, the same as observed *via* the IV route. Pimobendan is given primarily to increase CO (11). Hypotension is frequently observed in cases of cardiogenic shock in which an immediate increase in CO should be considered to maintain effective circulation (25, 29). Our findings suggested that IM pimobendan is not a hypotensive drug, and therefore will not worsen the blood pressure in case of hypotension.

Active relaxation of the LV myocardium occurs when the LV pressure drops below LAP, the pressure difference becomes the driving pressure and the mitral valve opens, causing blood inflow from the left atrium to the LV; this is eV (38). In the present study, pimobendane IM administration resulted in a significant increase in eV. The potential reasons for eV increase are the active relaxation of the LV or increased LAP (39). Previous studies have reported that pimobendan significantly reduces the trans LAP (15) and LV end-diastolic pressure (23). Moreover, the present study showed a significant increase in e'; e' represents myocardial movement during diastole (40). Therefore, this result indicated that the IM pimobendan was effective regarding cardiotonic action. In addition, there was no difference in E/e' in the present study. Previous studies reported a significant correlation between E/e' and mean LAP (40, 41). There was no significant change in LAP in dogs treated with pimobendan in the current study. Nevertheless, Ohte et al. (35) found a significant decrease in LAP when pimobendan was administered at a high dose (0.25 mg/kg). Lowering LAP is necessary in heart failure treatment. However, the low dose of pimobendan (0.15 mg/kg) in our study did not decrease LAP. Therefore, the absence of reduced LAP in our study could be attributed to the difference in pimobendan doses used in this study compared with other studies (36).

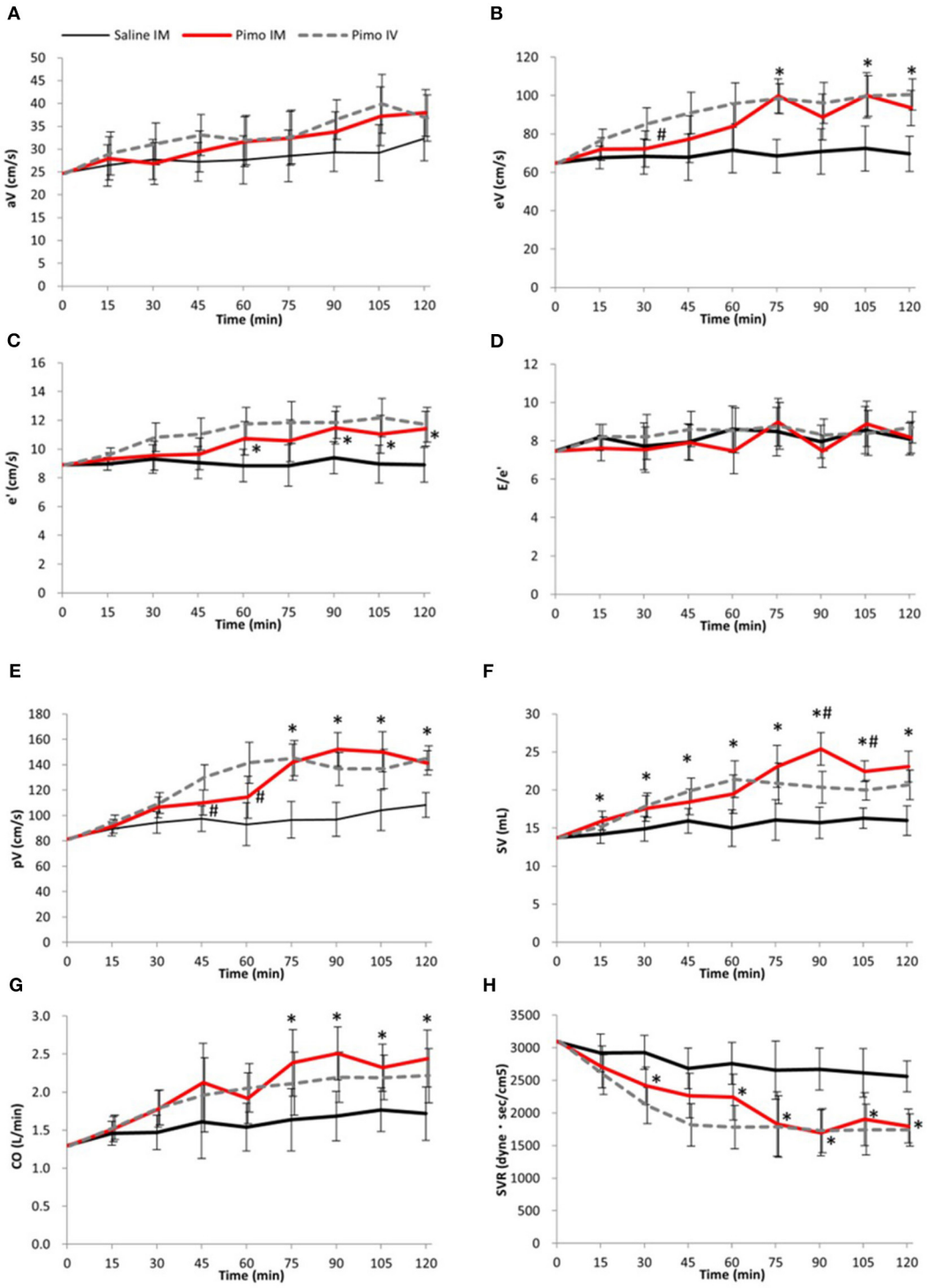

FIGURE 2
Data are presented as mean ± 95% confidence interval (error bar). Black line: Saline IM; Red line: Pimobendan IM (Pimo IM); Gray dot line: Pimobendan IV (Pimo IV). (*) fitted to indicate the significant difference between Pimo IM and Saline IM, while (#) fitted to compare Pimo IM vs. Pimo IV [for the repeated measures ANCOVA (model: time, group, and time*group)]; $P < 0.05$. **(A)** Peak atrial filling velocity (aV, cm/s), **(B)** Early diastolic left ventricular filling velocity (eV, cm/s), **(C)** Peak early diastolic velocity of the mitral annulus (e', cm/s), **(D)** Early diastolic left ventricular filling velocity/Peak early diastolic velocity of the mitral annulus ratio (E/e'), **(E)** Peak velocity (pV, cm/s), **(F)** Stroke volume (SV, mL), **(G)** Cardiac output (CO, L/min), **(H)** Systemic vascular resistance (SVR, dyne·s/cm^5).

Cardiac output is a result of the synergistic action of cardiotonic activity, preload, and afterload (2). The results of the present study demonstrated a rapid and marked increase in CO after IM administration of pimobendan, most probably due to either increased cardiotonic action, increased preload, decreased afterload, or the synergistic effect (11, 16). The present study did not measure factors increasing the preload. As described above, the results of SVR and e′ values were thought to be compatible with a reduction in the afterload and an increase of cardiotonic action, respectively. Therefore, it was considered that the increase in the CO in the present study was due to the enhancement of cardiotonic action and the reduction of afterload. Cardiac output is proportional to the initial length of myocardial fibers as defined by Frank-Starling's law (42). This means that CO depends on the relaxation of the left ventricular myocardium and its ability to contract. The results of pimobendan administration obtained in this study indicated that pimobendan contributes to increased CO by enhancing myocardial relaxation, thereby promoting an increase in blood volume during left ventricular relaxation and enhancing myocardial contractile capacity (35, 43, 44). In addition, the enhanced vasodilatory effects decreased peripheral vascular resistance and reduced afterload, which was thought to be attributable to the increase in CO (35, 43, 45).

In this study, the hemodynamic effect of IM and IV pimobendan has been comparatively described. Significance difference was only observed in eV, SV, and pV while other parameters (BP, HR, SVR, CO, e′, and E/e′) were not significantly changed. However, in comparison with the baseline, while pV, SV, and CO showed statistically significant increases after pimobendan injection *via* the two routes, SVR decreased significantly after 15 min in both groups, indicating that the two routes are approximately expressing the same hemodynamic effect with extended improve in SV after IM administration. Our results suggested that both IM and IV administration of pimobendan nearly induce the same hemodynamic effect and multiple routes of the drug administration will be more beneficial for life-saving therapies, especially in urgent conditions.

Moreover, there were significant differences in eV and e′ values between IM and IV routes of pimobendan administration. Generally, eV and e′ are measured to assess LV myocardial relaxation using echocardiography (38, 40). The IM administration of pimobendan caused a significant increase in the eV after Time 45 and e′ after Time 60, whereas its IV administration caused a significant increase in both eV and e′ after 15 min. From these results, it was speculated that the IM injection of pimobendan might have a milder effect on the LV myocardial relaxation than its IV administration. This was thought to be due to the fact that when pimobendan is administered intramuscularly, it takes time for the drug to move from the intramuscular to the bloodstream (26, 27). In the present study, this difference in time was thought to account for the different effects of IV and IM administration. In this regard, it can be considered that IM is another choice in acute heart failure patients who are already in shock with collapsed peripheral vessels. Because of the availability of oral, IV and IM routes of pimobendan administration, it will be easier for the practitioner to choose a suitable route of its administration depending on the condition of each case particularly in countries where injectable pimobendan solution is available. However, injectable pimobendan may be extended soon to include many countries (17, 24). In the future, further research is needed to accurately evaluate how the effects of cardiotonic action, vasodilatory action, and LV myocardial relaxation action change depending on different methods of pimobendan administration in clinical cases.

Clinical implications

Taken together, our results suggested that the IM route of pimobendan administration is an effective method to provide cardiotonic action, vasodilator effect, and LV myocardial relaxation. At present, IV administrations of cardiotonic drugs have been preferred, especially in the emergency treatment of heart failure in human and veterinary medicine. However, IM pimobendan might be another simple and safe route for cases in which the heart failure is complicated by other factors such as hemoptysis, and when the condition is expected to worsen due to stress—caused, for example, by retention to secure a venous route—and in cases of cardiogenic shock associated with difficulty in securing a venous route. In the current study, anesthesia resulted in some hemodynamic changes as previously reported (46–50), however, our results provided clear evidence for the usefulness of IM pimobendan the same as observed by IV pimobendane to enhance the heart function in healthy dogs.

Limitations

The current study has been conducted on healthy dogs. Hemodynamic properties of pimobendan are different in animals with heart disease compared to healthy dogs and the sensitivity by target site may vary depending on the degree of acidemia and circulatory failure in dogs with CHF. Here we have to say that various routes of injectable pimobendan administration are still under research consideration using animal models or healthy dogs and further clinical studies should be performed (17, 21–23).

We did not measure the plasma concentration of pimobendan and its active metabolite following IM injection. In our protocol, we measured the hemodynamic parameters every 15 minutes. This requires continuous blood sampling at short intervals which may impact the hemodynamics during the study. In addition, it has been reported that pimobendan has altered pharmacokinetics in plasma, whole blood, and intracellularly in dogs (17).

Besides, the effects of pimobendan administration on CO and vasodilation were measured by echocardiography. Despite cardiac catheterization being more accurate than echocardiography in these measurements, cardiac catheterization is more invasive and unsuitable for repeated measurements in each dog (51–53). Moreover, we elected to conduct the study under anesthesia to avoid any fluctuation in cardiac measurements during the handling of animals as previously described (22, 23). However, the isoflurane used in the present study has a dose-dependent antihypertensive effect associated with vasodilation and negative inotropic effects as previously reported (46–49); additionally, isoflurane has been reported to increase the HR and LAP and decrease myocardial contractility (50). This can diminish the effect of pimobendan even though the hemodynamic effect of injectable pimobendan in our study was clear.

Conclusion

The present study showed that intramuscular pimobendan changes cardiovascular functions by enhancing LV myocardial relaxation and LV contractility, producing vasodilation within a short time after its administration in healthy dogs approximately in the same way as the IV route. However, further clinical studies should be performed to explore the usefulness of an intramuscular administration of Pimobendan and whether it is an effective route of administration in case of emergency and when the IV route cannot be applied.

Data availability statement

The raw data supporting the conclusions of this article will be made available by the authors, without undue reservation.

Ethics statement

The present study was carried out according to the standards set by the Tokyo University of Agriculture and Technology (TUAT) and the guide on the use of laboratory animals. All experimental procedures were approved by the TUAT Animal Care and Use Committee (Approval No. R03-180).

Author contributions

ME and RT conceived and designed the experiment. ME, ASM, KS, SK, KK, and AY methodology and data collection. ME, SG, and KS animal preparation and anesthesia. ZY, SG, and KS data validation. ME and ASM statistical analysis, manuscript drafting, and writing the final manuscript. All authors have read and agreed to the published version of the manuscript.

Conflict of interest

The authors declare that the research was conducted in the absence of any commercial or financial relationships that could be construed as a potential conflict of interest.

The handling editor HS declared a past co-authorship with the authors ASM and RT.

Publisher's note

All claims expressed in this article are solely those of the authors and do not necessarily represent those of their affiliated organizations, or those of the publisher, the editors and the reviewers. Any product that may be evaluated in this article, or claim that may be made by its manufacturer, is not guaranteed or endorsed by the publisher.

Supplementary material

The Supplementary Material for this article can be found online at: https://www.frontiersin.org/articles/10.3389/fvets.2022.969304/full#supplementary-material

References

1. Cheng CJ, Mandour AS, Yoshida T, Watari T, Tanaka R, Matsuura K. Changes in renin-angiotensin-aldosterone system during cardiac remodeling after mitral valvuloplasty in dogs. *J Vet Intern Med.* (2022) 36:397–405. doi: 10.1111/jvim.16346

2. Tilley LP. *Manual of Canine and Feline Cardiology*. West Sussex: Elsevier Health Sciences (2008).

3. Boswood A, Häggström J, Gordon SG, Wess G, Stepien RL, Oyama MA, et al. Effect of pimobendan in dogs with preclinical myxomatous mitral valve disease and cardiomegaly: the EPIC study-a randomized clinical trial. *J Vet Intern Med.* (2016) 30:1765–79. doi: 10.1111/jvim.14586

4. Häggström J, Boswood A, O'Grady M, Jöns O, Smith S, Swift S, et al. Longitudinal analysis of quality of life, clinical, radiographic, echocardiographic, and laboratory variables in dogs with myxomatous mitral valve disease receiving pimobendan or benazepril: the QUEST study. *J Vet Intern Med.* (2013) 27:1441–51. doi: 10.1111/jvim.12181

5. Häggström J, Lord PF, Höglund K, Ljungvall I, Jöns O, Kvart C, et al. Short-term hemodynamic and neuroendocrine effects of pimobendan and benazapril in dogs with myxomatous mitral valve disease and congestive heart failure. *J Vet Intern Med.* (2013) 27:1452–62. doi: 10.1111/jvim.12217

6. O'Grady MR, Minors SL, O'Sullivan ML, Horne R. Effect of pimobendan on case fatality rate in Doberman Pinschers with congestive heart failure caused by dilated cardiomyopathy. *J Vet Intern Med.* (2008) 22:897–904. doi: 10.1111/j.1939-1676.2008.0116.x

7. Keene BW, Atkins CE, Bonagura JD, Fox PR, Häggström J, Fuentes VL, et al. ACVIM consensus guidelines for the diagnosis and treatment of myxomatous mitral valve disease in dogs. *J Vet Intern Med.* (2019) 33:1127–40. doi: 10.1111/jvim.15488

8. Iwanuk N, Wall L, Nolte I, Raue J, Rumstedt K, Pilgram A, et al. Effect of pimobendan on physical fitness, lactate and echocardiographic parameters in dogs with preclinical mitral valve disease without cardiomegaly. *PLoS ONE.* (2019) 14:e0223164. doi: 10.1371/journal.pone.0223164

9. Böhm M, Morano I, Pieske B, Rüegg JC, Wankerl M, Zimmermann R, et al. Contribution of cAMP-phosphodiesterase inhibition and sensitization of the contractile proteins for calcium to the inotropic effect of pimobendan in the failing human myocardium. *Circ Res.* (1991) 68:689–701. doi: 10.1161/01.RES.68.3.689

10. Fujino K, Sperelakis N, Solaro RJ. Sensitization of dog and guinea pig heart myofilaments to Ca2+ activation and the inotropic effect of pimobendan: comparison with milrinone. *Circ Res.* (1988) 63:911–22. doi: 10.1161/01.RES.63.5.911

11. Fitton A, Brogden RN. Pimobendan. A review of its pharmacology and therapeutic potential in congestive heart failure. *Drugs Aging.* (1994) 4:417–41. doi: 10.2165/00002512-199404050-00007

12. Brunkhorst D, v der Leyen H, Meyer W, Nigbur R, Schmidt-Schumacher C, Scholz H. Relation of positive inotropic and chronotropic effects of pimobendan, UD-CG 212 Cl, milrinone and other phosphodiesterase inhibitors to phosphodiesterase III inhibition in guinea-pig heart. *Naunyn-Schmiedeberg's Arch Pharmacol.* (1989) 339:575–83. doi: 10.1007/BF00167264

13. Duncker DJ, Hartog JM, Levinsky L, Verdouw PD. Systemic haemodynamic actions of pimobendan (UD-CG 115 BS) and its O-demethylmetabolite UD-CG 212 Cl in the conscious pig. *Br J Pharmacol.* (1987) 91:609–15. doi: 10.1111/j.1476-5381.1987.tb11254.x

14. Lee JA, Ruegg JC, Allen DG. Effects of pimobendan, a novel inotropic agent, on intracellular calcium and tension in isolated ferret ventricular muscle. *Clin Sci.* (1989) 76:609–18. doi: 10.1042/cs0760609

15. Suzuki S, Fukushima R, Ishikawa T, Hamabe L, Aytemiz D, Huai-Che H, et al. The effect of pimobendan on left atrial pressure in dogs with mitral valve regurgitation. *J Vet Intern Med.* (2011) 25:1328–33. doi: 10.1111/j.1939-1676.2011.00800.x

16. Boyle KL, Leech E. A review of the pharmacology and clinical uses of pimobendan. *J Vet Emerg Crit Care.* (2012) 22:398–408. doi: 10.1111/j.1476-4431.2012.00768.x

17. Bell ET, Devi JL, Chiu S, Zahra P, Whittem T. The pharmacokinetics of pimobendan enantiomers after oral and intravenous administration of racemate pimobendan formulations in healthy dogs. *J Vet Pharmacol Ther.* (2016) 39:54–61. doi: 10.1111/jvp.12235

18. Her J, Kuo KW, Winter RL, Cruz-Espindola C, Bacek LM, Boothe DM. Pharmacokinetics of pimobendan and its metabolite O-desmethyl-pimobendan following rectal administration to healthy dogs. *Front Vet Sci.* (2020) 7:423. doi: 10.3389/fvets.2020.00423

19. Pichayapaiboon P, Tantisuwat L, Boonpala P, Saengklub N, Boonyarattanasoonthorn T, Khemawoot P, et al. Pharmacodynamics and pharmacokinetics of injectable pimobendan and its metabolite, O-desmethyl-pimobendan, in healthy dogs. *Front Vet Sci.* (2021) 8:656902. doi: 10.3389/fvets.2021.656902

20. Yata M, McLachlan AJ, Foster DJ, Page SW, Beijerink NJ. Pharmacokinetics and cardiovascular effects following a single oral administration of a nonaqueous pimobendan solution in healthy dogs. *J Vet Pharmacol Ther.* (2016) 39:45–53. doi: 10.1111/jvp.12243

21. Morita T, Nakamura K, Osuga T, Kawamoto S, Miki S, Sasaoka K, et al. Acute effects of intravenous pimobendan administration in dog models of chronic precapillary pulmonary hypertension. *J Vet Cardiol.* (2020) 32:16–27. doi: 10.1016/j.jvc.2020.09.003

22. Miki S, Nakamura K, Morita T, Osuga T, Kawamoto S, Sasaki N, et al. Effects of intravenous administration of pimobendan on hemodynamic indices and indices of left atrial longitudinal strain derived from speckle-tracking echocardiography in healthy dogs. *Am J Vet Res.* (2021) 82:795–801. doi: 10.2460/ajvr.82.10.795

23. Hori Y, Taira H, Nakajima Y, Ishikawa Y, Yumoto Y, Maekawa Y, et al. Inotropic effects of a single intravenous recommended dose of pimobendan in healthy dogs. *J Vet Med Sci.* (2019) 81:22–5. doi: 10.1292/jvms.18-0185

24. Itami T, Hanazono K, Makita K, Yamashita K. Cardiovascular effects of intravenous pimobendan in dogs with acute respiratory acidosis. *J Vet Emerg Crit Care.* (2022) 32:341–9. doi: 10.1111/vec.13178

25. Silverstein DC, Kleiner J, Drobatz KJ. Effectiveness of intravenous fluid resuscitation in the emergency room for treatment of hypotension in dogs: 35 cases (2000–2010). *J Vet Emerg Crit Care.* (2012) 22:666–73. doi: 10.1111/j.1476-4431.2012.00822.x

26. Rebuelto M, Albarellos G, Ambros L, Kreil V, Montoya L, Bonafine R, et al. Pharmacokinetics of ceftriaxone administered by the intravenous, intramuscular or subcutaneous routes to dogs. *J Vet Pharmacol Ther.* (2002) 25:73–6. doi: 10.1046/j.1365-2885.2002.00389.x

27. Schwartz M, Muñana KR, Nettifee-Osborne JA, Messenger KM, Papich MG. The pharmacokinetics of midazolam after intravenous, intramuscular, and rectal administration in healthy dogs. *J Vet Pharmacol Ther.* (2013) 36:471–7. doi: 10.1111/jvp.12032

28. Yoshida T, Mandour AS, Matsuura K, Shimada K, El-Husseiny HM, Hamabe L, et al. Changes in the pulmonary artery wave reflection in dogs with experimentally-induced acute pulmonary embolism and the effect of vasodilator. *Animals Open Access J MDPI.* (2021) 11:977. doi: 10.3390/ani11071977

29. Yoshida T, Matsuura K, Mandour AS, Aboshi Y, Yamada S, Yotsuida H, et al. Hemodynamic effects of protamine infusion in dogs with myxomatous mitral valve disease undergoing mitral valvuloplasty. *Vet Sci.* (2022) 9:178. doi: 10.3390/vetsci9040178

30. Boon JA. *Veterinary Echocardiography*. West Sussex: John Wiley & Sons. (2011).

31. Haskins S, Pascoe PJ, Ilkiw JE, Fudge J, Hopper K, Aldrich J. Reference cardiopulmonary values in normal dogs. *Comp Med.* (2005) 55:156–61.

32. Fukushima R, Kawaguchi T, Yamada S, Yoshimura A, Hirao D, Oomori T. Effects of cilostazol on the heart rate in healthy dogs. *J Vet Med Sci.* (2018) 80:1707–15. doi: 10.1292/jvms.18-0240

33. Cockshott ID, Douglas EJ, Plummer GF, Simons PJ. The pharmacokinetics of propofol in laboratory animals. *Xenobiotica.* (1992) 22:369–75. doi: 10.3109/00498259209046648

34. Asanoi H, Ishizaka S, Kameyama T, Ishise H, Sasayama S. Disparate inotropic and lusitropic responses to pimobendan in conscious dogs with tachycardia-induced heart failure. *J Cardiovasc Pharmacol.* (1994) 23:268–74. doi: 10.1097/00005344-199402000-00014

35. Ohte N, Cheng CP, Suzuki M, Little WC. The cardiac effects of pimobendan (but not amrinone) are preserved at rest and during exercise in conscious dogs with pacing-induced heart failure. *J Pharmacol Exp Ther.* (1997) 282:23–31.

36. Pagel PS, Hettrick DA, Warltier DC. Influence of levosimendan, pimobendan, and milrinone on the regional distribution of cardiac output in anaesthetized dogs. *Br J Pharmacol.* (1996) 119:609–15. doi: 10.1111/j.1476-5381.1996.tb15716.x

37. van Meel JC, Diederen W. Hemodynamic profile of the cardiotonic agent pimobendan. *J Cardiovasc Pharmacol.* (1989) 14(Suppl. 2):S1–6. doi: 10.1097/00005344-198906142-00002

38. Nagueh SF. Left Ventricular diastolic function: understanding pathophysiology, diagnosis, and prognosis with echocardiography. *JACC Cardiovasc Imag.* (2020) 13:228–44. doi: 10.1016/j.jcmg.2018.10.038

39. Masuyama T, Popp RL. Doppler evaluation of left ventricular filling in congestive heart failure. *Eur Heart J.* (1997) 18:1548–56. doi: 10.1093/oxfordjournals.eurheartj.a015134

40. Nagueh SF, Middleton KJ, Kopelen HA, Zoghbi WA, Quiñones MA. Doppler tissue imaging: a noninvasive technique for evaluation of left ventricular relaxation and estimation of filling pressures. *J Am Coll Cardiol.* (1997) 30:1527–33. doi: 10.1016/S0735-1097(97)00344-6

41. Ommen SR, Nishimura RA, Appleton CP, Miller FA, Oh JK, Redfield MM, et al. Clinical utility of Doppler echocardiography and tissue doppler imaging in the estimation of left ventricular filling pressures: a comparative simultaneous Doppler-catheterization study. *Circulation.* (2000) 102:1788–94. doi: 10.1161/01.CIR.102.15.1788

42. Sunagawa K. The pressure-volume relationship of the heart: past, present and future. *Ann Int Conf IEEE Eng Med Biol Soc.* (2010) 2010:3554–5. doi: 10.1109/IEMBS.2010.5627485

43. Hall J, Guyton A. Cardiac muscle; the heart as a pump and function of the heart valves. In: *Guyton and Hall Textbook of Medical Physiology*. New York, NY: Elsevier Inc (2016). p. 12.

44. He KL, Dickstein M, Sabbah HN Yi GH, Gu A, Maurer M, et al. Mechanisms of heart failure with well preserved ejection fraction in dogs following limited coronary microembolization. *Cardiovasc Res.* (2004) 64:72–83. doi: 10.1016/j.cardiores.2004.06.007

45. Isoyama S, Maruyama Y, Koiwa Y, Ishide N, Kitaoka S, Tamaki K, et al. Experimental study of afterload-reducing therapy: the effects of the reduction of systemic vascular resistance on cardiac output, aortic pressure and coronary circulation in isolated, ejecting canine hearts. *Circulation.* (1981) 64:490–9. doi: 10.1161/01.CIR.64.3.490

46. Boban M, Stowe DF, Buljubasic N, Kampine JP, Bosnjak ZJ. Direct comparative effects of isoflurane and desflurane in isolated guinea pig hearts. *Anesthesiology.* (1992) 76:775–80. doi: 10.1097/00000542-199205000-00016

47. Hettrick DA, Pagel PS, Warltier DC. Desflurane, sevoflurane, and isoflurane impair canine left ventricular-arterial coupling and mechanical efficiency. *Anesthesiology.* (1996) 85:403–13. doi: 10.1097/00000542-199608000-00023

48. Rusy BF, Komai H. Anesthetic depression of myocardial contractility: a review of possible mechanisms. *Anesthesiology.* (1987) 67:745–66. doi: 10.1097/00000542-198711000-00020

49. Swanson CR, Muir WW, III. Simultaneous evaluation of left ventricular end-systolic pressure-volume ratio and time constant of isovolumic pressure decline in dogs exposed to equivalent MAC halothane and isoflurane *Anesthesiology.* (1988) 68:764–70. doi: 10.1097/00000542-198805000-00015

50. Seifen E, Seifen AB, Kennedy RH, Bushman GA, Loss GE, Jr., Williams TG. Comparison of cardiac effects of enflurane, isoflurane, and halothane in the dog heart-lung preparation. *J Cardiothor Anesth.* (1987) 1:543–53. doi: 10.1016/0888-6296(87)90041-X

51. Lopes PC, Sousa MG, Camacho AA, Carareto R, Nishimori CT, Santos PS, et al. Comparison between two methods for cardiac output measurement in propofol-anesthetized dogs: thermodilution and Doppler. *Vet Anaesth Analg.* (2010) 37:401–8. doi: 10.1111/j.1467-2995.2010.00552.x

52. Matsuura K, Shiraishi K, Mandour AS, Sato K, Shimada K, Goya S, et al. The utility of intraventricular pressure gradient for early detection of chemotherapy-induced subclinical cardiac dysfunction in dogs. *Animals Open Access J MDPI.* (2021) 11:1122. doi: 10.3390/ani11041122

53. Miki H, Mandour AS, Goya S, Hamabe L, Matsuura K, Yoshida T, et al. Color M-mode echocardiography for non-invasive assessment of the intraventricular pressure in dogs before and after ductus arteriosus occlusion: a retrospective study. *Front Vet Sci.* (2022) 9:908829. doi: 10.3389/fvets.2022.908829

frontiers | Frontiers in Veterinary Science

TYPE Original Research
PUBLISHED 13 October 2022
DOI 10.3389/fvets.2022.991634

OPEN ACCESS

EDITED BY
Ayman Abdel-Aziz Swelum,
Zagazig University, Egypt

REVIEWED BY
Francesco Ferrucci,
University of Milan, Italy
Francesca Beccati,
University of Perugia, Italy

*CORRESPONDENCE
Kate L. Hepworth-Warren
klhepwor@ncsu.edu

SPECIALTY SECTION
This article was submitted to Veterinary Imaging, a section of the journal Frontiers in Veterinary Science

RECEIVED 11 July 2022
ACCEPTED 19 September 2022
PUBLISHED 13 October 2022

CITATION
Hepworth-Warren KL, Nelson N, Dembek KA and Young KAS (2022) Comparison of thoracic ultrasonography and thoracic radiography between healthy adult horses and horses with bacterial pneumonia using a novel, objective ultrasonographic scoring system. *Front. Vet. Sci.* 9:991634. doi: 10.3389/fvets.2022.991634

Comparison of thoracic ultrasonography and thoracic radiography between healthy adult horses and horses with bacterial pneumonia using a novel, objective ultrasonographic scoring system

Kate L. Hepworth-Warren[1]*, Nathan Nelson[2], Katarzyna A. Dembek[1] and Kimberly A. S. Young[1]

[1]Department of Clinical Sciences, College of Veterinary Medicine, North Carolina State University, Raleigh, NC, United States, [2]Department of Molecular Biomedical Sciences, College of Veterinary Medicine, North Carolina State University, Raleigh, NC, United States

Background: Thoracic ultrasonography (TUS) is widely used in equine practice but comparison to radiography is limited in horses.

Objectives: To validate a novel, objective scoring system for TUS in adult horses and to compare ultrasonographic and radiographic findings.

Animals: 13 healthy horses and 9 with confirmed bacterial pneumonia

Methods: Prospective study in which TUS and radiography were performed on healthy horses and those with bacterial pneumonia confirmed by clinical signs and results of transtracheal wash analysis. Ultrasonography was scored utilizing a novel scoring system evaluating number of comet tail lesions, the presence or absence of pleural effusion and/or pulmonary consolidation in each intercostal space. Eighteen horses had thoracic radiographs taken that were scored by a board-certified radiologist utilizing a previously described system. Total scores were recorded and compared between control and diseased patients.

Results/Findings: Ultrasonographic scores were significantly higher in the diseased group (median= 126) than in the control group (median = 20, p = 0.01). Receiver operating characteristics (ROC) analysis identified a sensitivity of 66.7% (95% CI 0.417–1) and specificity of 92.3% (95% CI 0.462–1) for the ability of ultrasonography to identify bacterial pneumonia utilizing a TUS score cutoff of 37.

Conclusions and clinical importance: TUS had moderate sensitivity and high specificity for identification of bacterial pneumonia in adult horses. TUS appears to be an acceptable stand-alone imaging modality for diagnosis of bacterial pneumonia in horses when radiography is not practical.

KEYWORDS

equine pneumonia, thoracic radiography, imaging, equine pleuropneumonia, ultrasonography

Introduction

Thoracic ultrasonography (TUS) is widely used in equine medicine for the diagnosis of bacterial pneumonia due to the simplicity of use, its non-invasive nature, and the high availability of portable machines for field use. In an ambulatory practice setting, thoracic radiography of the adult horse is often not possible, thus TUS is relied upon heavily in the evaluation of horses with signs of bacterial pneumonia (1).

Thoracic ultrasonography in human and small animal medicine is comparable in sensitivity to radiography and computed tomography (CT) for the diagnosis of pneumonia, pulmonary edema, pneumothorax and pulmonary contusions (2–6). While there have been direct comparisons between the sensitivity of TUS and radiography in the identification of *Rhodococcus equi* pneumonia in foals and pneumothorax in the adult horse, the two modalities have not been compared for their diagnostic accuracy in bacterial pneumonia in adult horse (7, 8).

In order to compare ultrasonographic and radiographic images, previous studies in humans, small animals, dairy calves and foals have utilized objective scoring systems (3–6, 9–16). Numerous ultrasonographic and radiographic scores have been proposed for the evaluation of pleural changes associated with *Rhodococcus equi* pneumonia in foals, asthma and exercise-induced pulmonary hemorrhage in adult horses, bronchopneumonia in calves, pulmonary injury in dogs, and pneumonia and pulmonary edema in humans (3–6, 9–18). In addition to providing an objective measure of comparison between different modalities, these scoring systems have been applied clinically in disease screening and to expedite diagnostics and therapy including assessing severity and progression of pneumonia in humans with COVID-19 (11, 19, 20).

An objective scoring system for TUS in adult horses that accounts for the presence of pleural effusion and pulmonary consolidation, in addition to comet tails, has not previously been compared to thoracic radiography. The objectives of this study were to develop a novel scoring system for TUS in adult horses and to compare it to thoracic radiography utilizing a scoring system developed by Mazan et al. and to compare the TUS score and radiographic score in healthy horses to horses diagnosed with bacterial pneumonia (21). We hypothesized that this ultrasonographic scoring system would be an accurate and simple method of assessment of TUS in adult horses, and that ultrasonographic scores would correlate with radiographic scores and be a sensitive diagnostic for the identification of bacterial pneumonia. We hypothesized that horses classified as healthy based on history, physical examination and normal complete blood count would have significantly lower TUS and radiographic scores than those diagnosed with bacterial pneumonia.

Materials and methods

Patient selection and grouping

This was a prospective case-control study that included clinical patients presented to the (NC State College of Veterinary Medicine Veterinary Teaching Hospital) between August of 2020 and September of 2021. Client consent was obtained for the use of each animal, and all protocols were approved by the Institutional Animal Care and Use Committee. Control animals were horses of three or more years of age that were presented for elective magnetic resonance imaging for orthopedic disease and deemed healthy based on physical examination, rebreathing examination and complete blood count. Physical examination was considered normal if vital parameters were within normal limits (temperature $<101.5^{\circ}$F, heart rate 28–48 beats per min, respiration 10–20 breaths per min) and there was no nasal discharge, cough, abnormal lung sounds on auscultation, or increased respiratory effort. Rebreathing exam was considered normal if there was no coughing noted during or after the exam and if the horse returned to a normal resting respiratory rate in fewer than 6 breaths after removal of the rebreathing bag. Exclusion criteria for control animals included history of respiratory or cardiac disease, and any of the following within the 90 days prior to the study: transport of >6 consecutive hours, esophageal obstruction, or general anesthesia. Horses in the diseased group were clinical patients of three or more years of age that were enrolled following diagnosis of bacterial pneumonia. Pneumonia was diagnosed by the attending clinician *via* clinical signs, clinicopathologic data and thoracic imaging, and was confirmed by transtracheal wash cytology (confirming intracellular bacteria and suppurative inflammation) and/or positive bacterial culture of transtracheal wash fluid. All animals in the control group and 6 horses in the diseased group had ultrasonographic exams and right to left lateral radiography performed of the lungs within 6 h of each other.

Scoring of radiographic findings

Radiographs were assessed by a board-certified radiologist (NN who was blinded to the ultrasonographic findings) and the group assignment of each patient. Each series was scored according to the system previously described in detail by Mazan et al. (21). The lungs were divided into 3 regions (cranioventral, caudodorsal, caudoventral) and each region was assessed for the presence of 4 radiographic patterns (vascular, alveolar, interstitial, bronchial). A score of 0 was assigned when regions were considered "not different/normal" or a pattern was absent, a score of 1 for "moderate presence" of a pattern, and a score of 2 was assigned for "marked presence" of a pattern, allowing for a total score range of 0-24.

Scoring of ultrasonographic findings

The initial ultrasonographic examination on each horse was performed by a board-certified internal medicine specialist (KHW) and a subset of horses were evaluated by a second board-certified internal medicine specialist (KHW) blinded to the results of the initial exam, but not to the group assignment of the horse. Examinations performed by two investigators were performed within 6 h of one another. Ultrasonography was performed by scanning each intercostal space (ICS) from dorsal to ventral with a 3.5 MHz curvilinear probe in B-mode with depth adjusted on a case-by-case basis. Each examination was performed with one of two identical machines (Sonoscape S9, Universal Imaging, Bedford Hills, New York, United States). Each ICS was assessed for the presence of comet tail artifacts >5 mm in length from the pleural surface, consolidation, and pleural fluid in the dorsal and ventral portions of the thorax, which were divided by a horizontal line extending caudally from the level of the point of the shoulder (see Figure 1). Comet tails were defined as linear hyperechoic artifacts perpendicular to the pleural surface. Comet tail lesions identified deep to a consolidated region of lung were also quantified. Consolidation was defined as any section of lung where the normal hyperechoic pleura was interrupted, and the tissue was hypoechoic or heterogenous in appearance. An ICS was documented as having pleural fluid if there was expansion with anechoic or hypoechoic fluid noted between the pleura and body wall. If comet tail artifacts were present, they were counted in each ICS and the number recorded. Consolidation and pleural fluid were weighted more heavily than comet tails due to their association with more severe disease and each was given a score of 4 if present and 0 if absent in an ICS (1, 22). In order to maintain ease of use for the TUS score, the weighted score did not take into account the depth of pleural effusion. However, it is the clinical impression of the authors that significant effusion would be more likely to be present in multiple ICS and in both dorsal and ventral subsections and as such would be reflected in the overall score. If lung was not visible in a portion of an ICS, no number was assigned. The score for each hemithorax was totaled for each side, and as an overall score for each horse.

Statistical analysis

Statistical analysis was performed with R software (version 4.1.2, R foundation for Statistical Computing, Vienna, Austria). Age was examined *via* Mann-Whitney-Wilcoxon test while the gender was evaluated *via* Fisher's exact test. Differences in TUS and radiographic scores between control and diseased patients were examined *via* Mann-Whitney-Wilcoxon test. Spearman correlations were used for correlations between scores from different regions of the thorax and total ultrasonographic scores and for correlations between age and total ultrasonographic score where appropriate based on examination of plots for linear trend and homoscedasticity. Reported correlations were Pearson correlations calculated after the removal of extreme outliers. Comparisons of Pearson correlations were done using the Z transformation. The optimal cut-off for the receiver operating characteristics (ROC) analysis of ultrasound scores was determined by the concordance probability method with sensitivity and specificity reported at that point (23). Comparisons of sensitivity and specificity between ultrasound and radiography were made *via* the exact McNemar's test. Intra-class correlation coefficients used a two-way model with random effects for both subjects and raters.

Results

Patient demographics

The control group included 13 horses, 3 mares and 10 geldings, with a median age of 10 years (range: 6–19 years). In the diseased group there were 11 separate exams performed on 9 horses. Two horses in the diseased group were included twice as they were examined multiple weeks apart as part of disease monitoring but were treated as separate horses for purpose of analysis of the imaging findings, but only included once in analysis of signalment data. The diseased group included 1 stallion, 4 mares, and 4 geldings with a median age of 9 years (range: 8–21 years) There were no significant differences in age ($p = 0.81$) or gender ($p = 0.19$) between the two groups.

Ultrasonographic and radiographic scores

Total ultrasonographic score was significantly higher ($p = 0.01$) in the diseased group (median score 126; range: 13–353) than the control group (median score 20; range: 4–50) (see Figure 2). All horses in the control group had thoracic radiographs, and 5 horses in the diseased group. There was no significant difference in total radiographic score between the diseased group (median score 3; range: 0–9) and the control group (median score 0, range: 0–2) ($p = 0.12$) (see Figure 3). Ultrasonographic and radiographic scores for each individual horse are reported in Table 1. There was not a significant correlation between ultrasonographic and radiographic scores in the entire group (Pearson correlation: 0.4, $p = 0.11$, 95% CI −0.09–0.74), nor in the diseased group (Pearson correlation: 0.4, $p = 0.60$, 95% CI −0.91–0.98) or the control group (Pearson correlation: 0.53, $p = 0.07$, 95% CI −0.03–0.84). Interobserver agreement in assignment of ultrasonographic scores was good at 0.79. ROC analysis identified a sensitivity of 67% (95% CI 0.333–1) and specificity of 92.3% (95% CI 0.462–1) for the identification of bacterial pneumonia utilizing

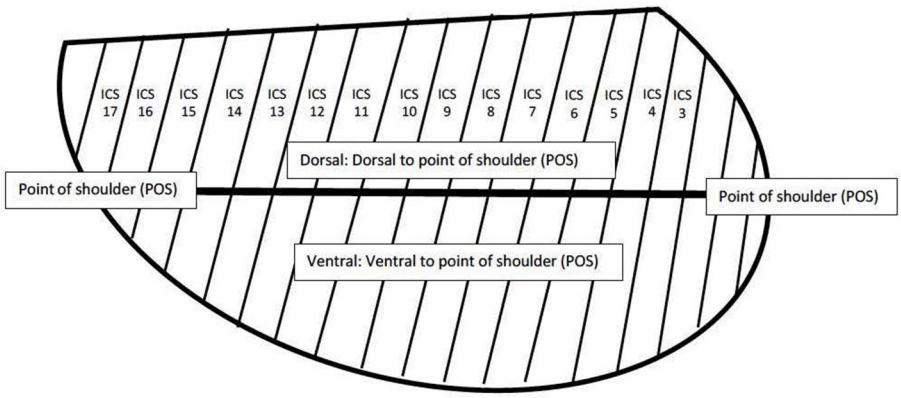

FIGURE 1
Diagram depicting intercostal spaces and dorsal and ventral regions for LUS score.

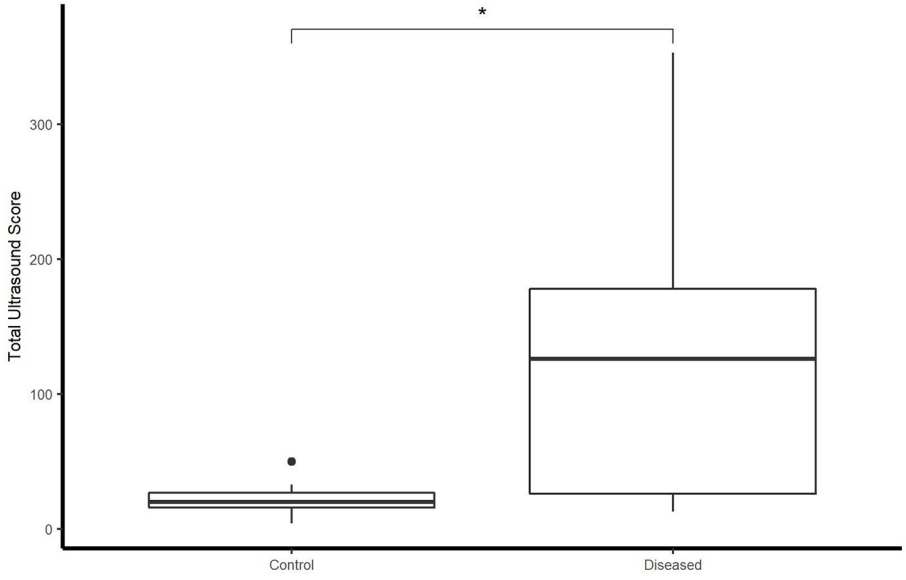

FIGURE 2
Boxplot illustrating LUS score between control and diseased group. *indicates statistical significance. Significance $p < 0.05$.

an ultrasonographic score cutoff of 37 (see Figure 4). This score was applied retroactively to allow for the calculation of accuracy. Accuracy of the ultrasonographic score when compared to clinical diagnosis was 81.8% (95% CI 0.597–0.948). One patient in the control group scored >37 (patient 2), and 3/11 exams in the diseased group scored below 37 (patients 14, 15, 17). Using an ROC cutoff of 2.5 for radiographic score sensitivity was maximized at 57.1% (95% CI 0.286–0.857) and specificity was 100% (95% CI 0.23–1). There was not a significant difference between sensitivity ($p = 1$) and specificity of the ultrasonographic or radiographic scores ($p = 1$) when applying the cutoff values from ROC analysis. See Figure 5 for example of ultrasonographic and radiographic image of a patient in the study.

The cranial and ventral portions of each hemi-thorax tended to be more strongly correlated with the overall score for each side and the total TUS than more caudal and dorsal sub-sections (see Table 2 for all correlations).

Comet tails were the only lesions identified in control horses, with the exception of one horse that had consolidation in 2 intercostal spaces (see Table 1 for complete individual lesion scores). Therefore, only the number of comet tails per ICS and the number of ICS that contained comet tails were compared between groups. There were significantly fewer comet tails per

10.3389/fvets.2022.991634

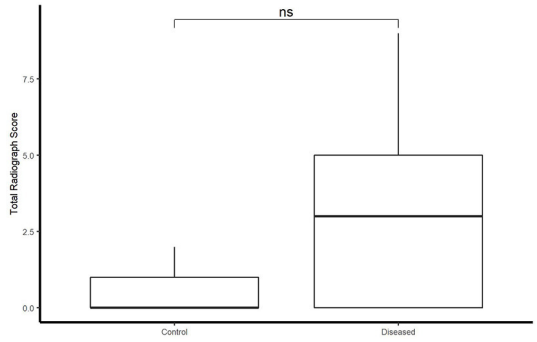

FIGURE 3
Boxplot illustrating radiograph score between control and diseased group. Significance $p < 0.05$.

ICS ($p = 0.01$) in the control group (median 0.67 comet tails per ICS; range 0.16–2.04) when compared to the diseased group (median 1.62 comet tails per ICS; range 0.52–5.2). Control horses did not have a statistically significantly different number of ICS that contained comet tails when compared to the diseased group (control: 11 ICS with comet tails (range 5–17), diseased:13 ICS with comet tails (range 7–26); $p = 0.09$).

TABLE 1 Ultrasonographic and radiographic findings for controls (healthy horses) and diseased horses (horses with bacterial pneumonia).

	Control	Diseased
Ultrasonographic scores median (range)		
Total US score	20 (4–50)	126 (13–353)
Comet tail score	20 (4–48)	65 (13–126)
Consolidation score	0 (0–2)	16 (0–140)
Pleural effusion score	0 (0–0)	0 (0–148)
Frequency of specific ultrasonographic lesions *n* (% of total)		
# of ultrasonographic exams with comet tails	13/13 (100%)	13/13 (100%)
# of exams with consolidation	1/13 (7.7%)	8/11 (72.7%)
# of exams with pleural effusion	0/13 (0%)	3/11 (27.3%)
Radiographic scores median (range)		
Total radiographic score	0 (0–2)	3 (0–9)
Frequency of specific radiographic lesions *n* (% of total)		
# of exams with presence of vascular pattern	0/13 (0%)	0/5 (0%)
# of exams with presence of interstitial pattern	3/13 (23.1%)	4/5 (80.0%)
# of exams with presence of alveolar pattern	0/13 (0%)	2/5 (40.0%)
# of exams with presence of bronchial pattern	2/13 (15.4%)	4/5 (80.0%)

Discussion

The ultrasonographic score developed for this study provided an objective measure for differentiating healthy horses from those with bacterial pneumonia and allowed for correlation between TUS and radiography. The ultrasonographic score had similar sensitivity and specificity for the identification of bacterial pneumonia when compared to radiographic score, suggesting that in many horses the addition of thoracic radiographs may not be necessary to identify evidence of disease.

In human medicine, TUS has been shown to be an effective standalone diagnostic modality for pulmonary disease and injury (24–27). Thoracic ultrasonography is non-invasive and convenient, does not expose patients to radiation and can easily be taught to inexperienced ultrasonographers with adequate diagnostic results (27). When thoracic ultrasonography and radiography were compared to each other and to computed tomography (CT) in 144 adult human patients with acute pneumonia ultrasonography had a significantly higher sensitivity (95%) than chest radiography (60%, $p < 0.01$) (24). Ultrasonography also had 100% accuracy in identifying patients with pneumonia whereas radiography had only 52% accuracy when each was compared to chest CT (24). Severity of lesions identified on TUS also correlate well with chest CT in patients with pneumonia caused by COVID-19 (12, 15, 28).

There have been multiple studies investigating the benefit and diagnostic accuracy of utilizing TUS as the primary imaging modality in non-equine species for the identification of cardiogenic pulmonary edema, bronchopneumonia, and trauma (2–6). Thoracic ultrasonography has high sensitivity (90%) and specificity (93%) when compared to radiography for the identification of cardiogenic pulmonary edema in dogs with chronic valvular heart disease and had higher sensitivity and specificity than thoracic radiography for the diagnosis of pulmonary contusions in dogs following motor vehicle trauma (2, 6). In Holstein calves, TUS had a sensitivity of 94% and specificity of 95% for the identification of subclinical lung lesions that were confirmed on post-mortem examination (3).

Thoracic ultrasonography and radiography have been compared in the diagnosis of *Rhodococcus equi* pneumonia in foals and pneumothorax in adult horses, but not in bacterial pneumonia in adult horses. In foals, TUS has been advocated as a screening tool for diagnosis of pulmonary abscessation caused by *R. equi* pneumonia and was an accurate alternative to radiography in two studies (7, 10). The only direct comparison to date between thoracic radiography and ultrasonography in adult horses evaluated 6 horses in which small-volume pneumothorax was experimentally induced. In that study, the diagnostic sensitivity of M-mode (84%) and 2D-mode (80%) TUS was significantly higher ($p = 0.02$ and 0.04, respectively) than thoracic radiography (48%) (8).

Several scoring systems have been developed to objectively evaluate TUS images and to quantify specific lesions in

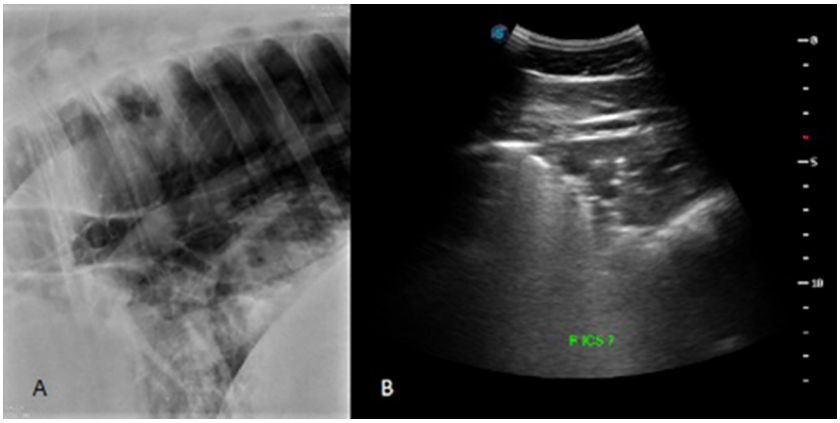

FIGURE 4
Radiographic **(A)** and ultrasonographic **(B)** image from corresponding sites on a patient in the diseased group. In the caudoventral portion of the lung, the radiograph was classified as having normal/not different presence of a vascular pattern (score of 0), a moderate presence for interstitial and alveolar patterns (score of 1 for each pattern), and a marked presence of a bronchial pattern (score of 2). The total radiographic score for this patient was 9. The ventral portion of right ICS 7 was given a comet tail score of 3 and a score of 4 for the presence of pulmonary consolidation. The total US score for this horse was 283.

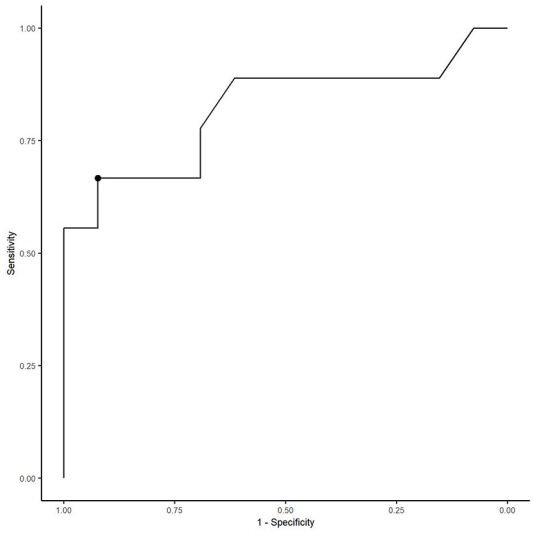

FIGURE 5
Receiver operating characteristic curve for LUS score to predict presence or absence of lower respiratory tract disease. The optimal cutoff score of 37 gave a sensitivity of 67% and specificity of 92.3%.

humans, small animals, dairy calves and horses (3–6, 11–18, 29, 30). The benefit of an objective scoring system is increased consistency of imaging interpretation, more rapid assessment and monitoring of clinical patients, and the ability to compare imaging modalities in research settings. Ultrasonographic scores have been employed in the COVID-19 pandemic to allow for risk assessment, triage, and monitoring of patients with pneumonia (11–15). In veterinary medicine, TUS scores have been developed for use in dogs with cardiac disease, aspiration pneumonia and thoracic trauma, and in bronchopneumonia in calves (3–6, 16). Specifically in horses, TUS scores have been developed to evaluate and describe horses with specific disease processes, including Equine Influenza Virus, *Rhodococcus equi,* and equine asthma syndrome (10, 29, 30). However, no system has been developed to specifically differentiate horses with bacterial pneumonia from healthy controls and to compare TUS to radiography and to account for multiple lesion types.

Ultrasonographic scores in other species focus heavily on the presence and number of B-lines, the artifact referred to as comet tails in equine medicine (31, 32). In the scoring system described here, the authors chose to include comet tails, pulmonary consolidation and pleural effusion to provide a more complete assessment of bacterial pneumonia. Pulmonary consolidation and pleural effusion are observed in more severe pulmonary disease, whereas comet tails may be the only observed lesions in mild disease (22). A score that involves multiple types of lesions can allow for more effective classification of disease and can identify minor changes over the course of clinical disease.

Sporadic comet tail lesions have been documented in healthy horses and were also noted in the control horses in this study (29). With the exception of one control horse that had a focal region of consolidation, the only lesions present in control horses were comet tails. In human medicine, the presence of 3 or more B-lines in one region of the lung is considered abnormal, which supports the clinical impression that a low number of comet tails can be considered normal in the horse (31, 33). Every horse in the control group of this study had at least one intercostal space where comet tail lesions were noted, but the median number of comet tails per intercostal space in the

10.3389/fvets.2022.991634

TABLE 2 Correlation coefficients between specific subsections of each hemithorax and the total overall thoracic ultrasonographic score.

Sub-section	LV ICS 3–9	LV ICS 10–17	LD ICS 3–9	LD ICS 10–17	LV ICS 3–8	LV ICS 9–12	LV ICS 13–17	LD ICS 3–8	LD ICS 9–12	LD ICS 13–17
Correlation coefficient with left-sided score	0.85	0.36	0.74	0.51	0.87	0.48	—	0.72	0.52	0.14
Correlation coefficient with total score	0.75	0.38	0.72	0.64	0.75	0.51	—	0.71	0.61	0.33
Sub-section	**RV ICS 3–9**	**RV ICS 10–17**	**RD ICS 3–9**	**RD ICS 10–17**	**RV ICS 3–8**	**RV ICS 9–12**	**RV ICS 13–17**	**RD ICS 3–8**	**RD ICS 9–12**	**RD ICS 13–17**
Correlation coefficient with right-sided score	0.88	0.36	0.79	0.25	0.88	0.69	—	0.74	0.67	0.27
Correlation coefficient with total score	0.73	0.36	0.84	0.21	0.73	0.64	—	0.80	0.67	0.18

ICS, intercostal space; LV, left ventral; LD, left dorsal; RV, right ventral; RD, right dorsal.

control group was 0.67 (range 0.16–2.04) and did not exceed 3. By applying the cut-off TUS score of 37, an inexperienced ultrasonographer may be able to more readily differentiate a horse with bacterial pneumonia from a healthy horse with a clinically insignificant number of comet tails.

The use of zones or standardized points of evaluation when performing TUS has been applied in human medicine and provides a more rapid and targeted method of assessment than a scan of each individual ICS in emergency settings (30, 31, 34, 35). In the data reported here, scores from the right and left dorsal and ventral ICS 3-8 regions were most highly correlated with the total score for the respective sides and the overall scores than the more caudal regions. The cranioventral region (LV ICS 3-8, RV ICS 3-8, RV ICS 3-9) score on each side was the most highly correlated with the total score for that side (correlation coefficients: R 0.88, L 0.87) suggesting that a brief, targeted examination focused on the cranioventral lung fields may provide sufficient information to rapidly diagnose horses with bacterial pneumonia in an emergency setting.

The main limitation of this study was the small number of subjects. Enrollment of subjects was dependent upon hospital caseload, so varied substantially over the enrollment period. Due to the clinical nature of this study, enrolled horses were often being treated by the investigators, and thus were aware of the diagnosis, which may have biased interpretation of ultrasonographic findings. However, by establishing an objective means of quantifying changes identified on ultrasound, this bias was reduced. Despite knowledge of the patient's diagnosis, ultrasonographers (KHW and KD) were not present for exams performed by the other ultrasonographer and were blinded to each other's scores. Two horses included in the diseased group were enrolled twice leading to a total of 11 ultrasonographic examinations in the diseased group. However, examinations were performed at least 2 weeks apart when their clinical disease was likely to have changed significantly, and earlier scores were not reviewed prior to the examination to avoid bias. Demographic data for these 2 horses was only included in analysis once. Six of 11 ultrasonographic examinations in the diseased group did not have concurrent radiographs performed, which may explain why the difference in radiographic score between healthy (median score 0) and diseased horses (median score 3) did not reach statistical significance. It is possible that with a larger number of subjects, the differences in radiographic score would be statistically significant.

The data presented here supports growing evidence in small animal and human medicine that point-of-care TUS provides a rapid and sensitive method for the diagnosis of pneumonia in adult horses without the addition of radiography. The ultrasonographic score described here was able to readily differentiate horses with confirmed bacterial pneumonia from healthy horses with a calculated accuracy of 81%. Additionally, there was no significant difference in sensitivity and specificity of ultrasonography and radiography.

By utilizing the ultrasonographic scoring system described here and applying the cut-off score of 37, practitioners can readily distinguish healthy horses from those with bacterial pneumonia. Future studies are warranted to compare TUS scores between equine asthma and bacterial pneumonia to assess the utility of the score in differentiating between the two disease processes, but by quantifying multiple types of lesions (comet tails, pulmonary consolidation and pleural effusion), it is plausible that the score could be applied in the evaluation of horses presenting for evaluation of lower respiratory disease. It is important to note that TUS is unable to identify lesions that do not extend to the pleural surface. However, in bacterial pneumonia of adult horses it is rare for deep lesions, such as abscessation, to be present without accompanying comet tails, consolidation or pleural effusion (1, 22). Therefore, TUS can be recommended as an accurate method for the initial identification of bacterial pneumonia in many cases without the need for immediate additional imaging in the field setting where radiography of the thorax is often impractical.

Data availability statement

The raw data supporting the conclusions of this article will be made available by the authors, upon reasonable request, without undue reservation.

Ethics statement

The animal study was reviewed and approved by North Carolina State University Institutional Animal Care and Use Committee. Written informed consent was obtained from the owners for the participation of their animals in this study.

Author contributions

KH-W, NN, and KD designed the study and ultrasonographic scoring system. KH-W performed all initial ultrasonographic examinations. KD served as second ultrasonographer. NN performed radiographic evaluations. KY assisted in data collection and examinations. All authors contributed to manuscript preparation and approved the submitted version.

Funding

This study was funded by North Carolina State University College of Veterinary Medicine start-up funds.

Acknowledgments

The authors would like to acknowledge James Robertson for performing the statistical analysis, and the faculty, staff and students of North Carolina State College of Veterinary Medicine for their contributions to patient recruitment and data collection.

Conflict of interest

The authors declare that the research was conducted in the absence of any commercial or financial relationships that could be construed as a potential conflict of interest.

Publisher's note

References

1. Reuss SM, Giguère S. Update on bacterial pneumonia and pleuropneumonia in the adult horse. *Vet Clin North Am Equine.* (2015) 31:105–20. doi: 10.1016/j.cveq.2014.11.002

2. Vezzosi T, Mannucci T, Pistoresi A, Toma F, Tognett R, Zini E, et al. Assessment of Lung ultrasound B-lines in dogs with different stages of chronic valvular heart disease. *J Vet Intern Med.* (2017) 31:700–4. doi: 10.1111/jvim.14692

3. Ollivett TL, Caswell JL, Nydam DV, Duffield T, Leslie KE, Hewson J, et al. Thoracic ultrasonography and bronchoalveolar lavage fluid analysis in holstein calves with subclinical lung lesions. *J Vet Intern Med.* (2015) 29:1728–34. doi: 10.1111/jvim.13605

4. Berman J, Masseau I, Fecteau G, Buczinski S, Francoz D. Comparison between thoracic ultrasonography and thoracic radiography for the detection of thoracic lesions in dairy calves using a two-stage bayesian method. *Prev Vet Med.* (2020) 184:105–53. doi: 10.1016/j.prevetmed.2020.105153

5. Ward JL, Lisciandro GR, Keene BW, Tou SP, DeFrancesco TC. Accuracy of point-of-care lung ultrasonography for the diagnosis of cardiogenic pulmonary edema in dogs and cats with acute dyspnea. *J Am Vet Med Assoc.* (2017) 250:666–75. doi: 10.2460/javma.250.6.666

6. Dicker SA, Lisciandro GR, Newell SM, Johnson JA. Diagnosis of pulmonary contusions with point-of-care lung ultrasonography and thoracic radiography

compared to thoracic computed tomography in dogs with motor vehicle trauma: 29 cases (2017-2018). *J Vet Emerg Crit Care.* (2020) 30:638–46. doi: 10.1111/vec.13021

7. Ramirez S, Lester GD, Roberts GR. Diagnostic contribution of thoracic ultrasonography in 17 foals with rhodococcus equi pneumonia. *Vet Radiol Ultrasound.* (2004) 45:172–6. doi: 10.1111/j.1740-8261.2004.04028.x

8. Partlow J, David F, Hunt LM, Relave F, Blond L, Pinilaa M, et al. Comparison of thoracic ultrasonography and radiography for the detection of induced small volume pneumothorax in the horse. *Vet Radiol Ultrasound.* (2017) 58:354–60. doi: 10.1111/vru.12480

9. Giguère S, Roberts GD. Association between radiographic pattern and outcome in foals with pneumonia caused by rhodococcus equi. *Vet Radiol Ultrasound.* (2012) 53:601–4. doi: 10.1111/j.1740-8261.2012.01964.x

10. McCracken JL, Slovis NM. Use of Thoracic Ultrasound for the Prevention of Rhodococcus equi Pneumonia on Endemic Farms. In: *Proceedings of the 55th Annual Convention of the American Association of Equine Practitioners*. (2009). Las Vegas, NV.

11. Dargent A, Chatelain E, Kreitmann L, Quenot JP, Cour M, Argaud L, et al. Lung Ultrasound score to monitor COVID-19 pneumonia progression in patients with ARDS. *PLoS ONE.* (2020) 15:1–4. doi: 10.1371/journal.pone.0236312

12. Zieleskiewicz L, Markarian T, Lopez A, Taguet C, Mohammedi N, Boucekine M, et al. Comparative Study of Lung Ultrasound and Chest Computed Tomography Scan in the Assessment of Severity of Confirmed COVID-19 Pneumonia. *Intensive Care Med.* (2020) 46:1707–13. doi: 10.1007/s00134-020-06186-0

13. Ji L, Cao C, Gao Y, Zhang W, Xie Y, Duan Y, et al. Prognostic value of bedside lung ultrasound score in patients with COVID-19. *Crit Care.* (2020) 24:1–12. doi: 10.1186/s13054-020-03416-1

14. Alencar de, Julio Cesar G, Marchini JFM, Marino LO, da Costa Ribeiro SC, Bueno CG, et al. Lung ultrasound score predicts outcomes in COVID-19 patients admitted to the emergency department. *Ann Intensive Care.* (2021) 11:6. doi: 10.1186/s13613-020-00799-w

15. Nouvenne A, Zani M, Milanese G, Parrise A, Baciarello M, Bignami EG, et al. Lung ultrasound in COVID-19 pneumonia: correlations with chest CT on hospital admission. *Respir.* (2020) 99:617–24. doi: 10.1159/000509223

16. Rodrigues NF, Giraud L, Bolen G, Fastres A, Clercx C, Boysen S, et al. Comparison of lung ultrasound, chest radiographs, c-reactive protein, and clinical findings in dogs treated for aspiration pneumonia. *J Vet Intern Med.* (2022) 36:1–10. doi: 10.1111/jvim.16379

17. Ferrucci F, Stancari G, Zucca E, Ayalon S, Falcone C, Ferro E. Specificity and sensitivity of ultrasonography and endoscopy for the diagnosis of exercise-induced pulmonary haemorrhage (EIPH) in 157 race horses. *Vet Res Commun.* (2009) 33:5185–8. doi: 10.1007/s11259-009-9277-5

18. Lo Feudo CM, Stucchi L, Alberti E, Stancari G, Conurba B, Zucca E, et al. The role of thoracic ultrasonography and airway endoscopy in the diagnosis of equine asthma and exercise-induced pulmonary hemorrhage. *Vet Sci.* (2021) 8:1–15. doi: 10.3390/vetsci8110276

19. Lichter Y, Topilsky Y, Taieb P, Banai A, Hochstadt A, Merdler I, et al. Lung Ultrasound predicts clinical course and outcomes in COVID-19 patients. *Intensive Care Med.* (2020) 46:1873–83. doi: 10.1007/s00134-020-06212-1

20. Brattain LJ, Telfer BA, Liteplo AS, Noble VE. Automated B-line scoring on thoracic sonography. *J Med Ultrasound.* (2013) 32:2185–90. doi: 10.7863/ultra.32.12.2185

21. Mazan MR, Vin R, Hoffman AM. Radiographic scoring lacks predictive value in inflammatory airway disease. *Equine Vet J.* (2005) 37:541–5. doi: 10.2746/042516405775314899

22. Ferrucci F, Zucca E, Croci C, Di Fabio V, Martino PA, Ferro E. Bacterial pneumonia and pleuropneumonia in sport horses: 17 Cases (2001–2003). *Equine Vet Educ.* (2008) 20:526–31. doi: 10.2746/095777308X354255

23. Liu X. Classification accuracy and cut point selection. *Stat Med.* (2012) 31:2676–86. doi: 10.1002/sim.4509

24. Bourcier J, Paquet J, Seinger M, Gallard E, Redonnet JP, Cheddadi F, et al. Performance comparison of lung ultrasound and chest X-ray for the diagnosis of pneumonia in the ED. *Am J Emerg Med.* (2014) 32:115–8. doi: 10.1016/j.ajem.2013.10.003

25. Long L, Zhao HT, Zhang ZY, Wang GY, Zhao HL. Lung ultrasound for the diagnosis of pneumonia in adults. *Medicine.* (2017) 96:e5713. doi: 10.1097/MD.0000000000005713

26. Hu QJ, Shen YC, Jia LQ, Guo SJ, Long HY, Pang CS, et al. Diagnostic performance of lung ultrasound in the diagnosis of pneumonia: a bivariate meta-analysis. *Int J Clin Exp Med.* (2014) 7:115–21.

27. Jones BP, Tay ET, Elikashvili I, Sanders JE, Paul AZ, Nelson BP, et al. Feasibility and safety of substituting lung ultrasonography for chest radiography when diagnosing pneumonia in children. *Chest.* (2016) 150:131–8. doi: 10.1016/j.chest.2016.02.643

28. Deng Q, Cao S, Wang H, Zhang Y, Chen L, Yang Z, et al. Application of quantitative lung ultrasound instead of CT for monitoring COVID-19 pneumonia in pregnant women: a single-center retrospective study. *BMC Pregnancy Childbirth.* (2021) 21:259. doi: 10.1186/s12884-021-03728-2

29. Siwinska N, Zak A, Slowikowska M, Krupinska P, Niedzwiedz A. Prevalence and severity of ultrasonographic pulmonary findings in horses with asthma - a preliminary study. *Pol J Vet Sci.* (2019) 22:653–9. doi: 10.24425/pjvs.2019.129977

30. Gross DK, Morley PS, Hinchcliff KW, Reichle JK, Slemons RD. Pulmonary Ultrasonographic abnormalities associated with naturally occurring equine influenza virus infection in standardbred racehorses. *J Vet Intern Med.* (2004) 18:718–27. doi: 10.1111/j.1939-1676.2004.tb02611.x

31. Gullett J, Donnelly JP, Sinert R, Hosek B, Fuller D, Hill H, et al. Interobserver agreement in the evaluation of B-lines using bedside ultrasound. *J Crit Care.* (2015) 30:1395–9. doi: 10.1016/j.jcrc.2015.08.021

32. Wang Y, Zhang Y, He Q, Liao H, Luo J. Quantitative analysis of pleural line and B-lines in lung ultrasound images for severity assessment of COVID-19 pneumonia. *IEEE Trans Ultrason Ferroelectr Freq Control.* (2022) 69:73–83. doi: 10.1109/TUFFC.2021.3107598

33. Rambhia SH, D'Agostino CA, Noor A, Villani R, Naidich JJ, Pellerito JS. Thoracic ultrasound: technique, applications, and interpretation. *Curr Probl Diagn Radiol.* (2016) 46:305–16. doi: 10.1067/j.cpradiol.2016.12.003

34. Volpicelli G, Elbarbary M, Blaivas M, Lichtenstein DA, Mathis G, Kirkpatrick AW, et al. International evidence-based recommendations for point-of-care lung ultrasound. *Intensive Care Med.* (2012) 38:577–91. doi: 10.1007/s00134-012-2513-4

35. Lichtenstein D. BLUE-protocol and FALLS-protocol. *Chest.* (2015) 147:1659–70. doi: 10.1378/chest.14-1313

Frontiers in Veterinary Science

Transforms how we investigate and improve animal health

The third most-cited veterinary science journal, bridging animal and human health with a comparative approach to medical challenges. It explores innovative biotechnology and therapy for improved health outcomes.

Discover the latest Research Topics

See more →

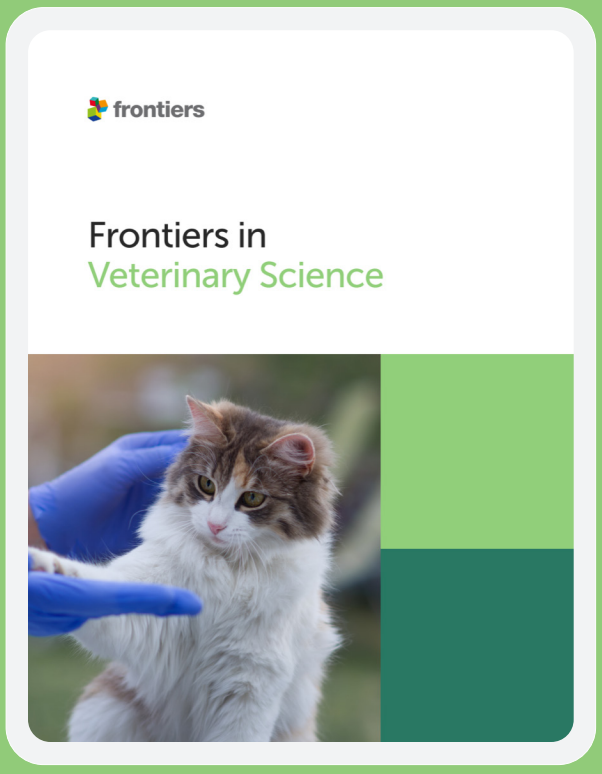

Frontiers

Avenue du Tribunal-Fédéral 34
1005 Lausanne, Switzerland
frontiersin.org

Contact us

+41 (0)21 510 17 00
frontiersin.org/about/contact